arXiv:0810.5226v2 [hep-ex] 2 Jul 2009

# REVIEW OF PROPERTIES OF THE TOP QUARK FROM MEASUREMENTS AT THE TEVATRON

MARC-ANDRÉ PLEIER

*Physikalisches Institut, Universität Bonn*
*Nussallee 12, 53115 Bonn, Germany*
*pleier@fnal.gov*

This review summarizes the program in the physics of the top quark being pursued at Fermilab's Tevatron proton-antiproton collider at a center of mass energy of 1.96 TeV. More than a decade after the discovery of the top quark at the two collider detectors CDF and D0, the Tevatron has been the only accelerator to produce top quarks and to study them directly.

The Tevatron's increased luminosity and center of mass energy offer the possibility to scrutinize the properties of this heaviest fundamental particle through new measurements that were not feasible before, such as the first evidence for electroweak production of top quarks and the resulting direct constraints on the involved couplings. Better measurements of top quark properties provide more stringent tests of predictions from the standard model of elementary particle physics. In particular, the improvement in measurements of the mass of the top quark, with the latest uncertainty of 0.7% marking the most precisely measured quark mass to date, further constrains the prediction of the mass of the still to be discovered Higgs boson.

*Keywords*: Top Quark; Experimental Tests of the Standard Model; Hadron-induced High-energy Interactions

PACS numbers: 14.65.Ha, 12.38.Qk, 13.85.-t, 13.85.Rm, 13.38.Be, 12.60.-i

## Contents

## 1. Introduction

The existence of a third and most massive generation of fundamental fermions was unveiled in 1975 with the discovery of the $\tau$ lepton at SLAC-LBL [1]. In 1977, the discovery of the bottom quark [2] at Fermilab extended the knowledge of a third generation into the quark sector and immediately raised the question of the existence of the top quark as the weak isospin partner of the bottom quark.

To remain self consistent, the standard model (SM) of elementary particle physics required the existence of the top quark, and electroweak precision measurements offered increasingly precise predictions of properties such as its mass. The top quark's large mass prevented its discovery for almost two decades, but by 1994 it was indirectly constrained to be $178 \pm 11 \, {}^{+18}_{-19}$ GeV/c$^2$ [3]. After mounting experimental evidence [4–9], the top quark $(t)$ was finally discovered in 1995 at Fermilab by the CDF and D0 collaborations [10,11] in the mass range predicted by the standard model. The completion of the quark sector once again demonstrated the enormous predictive power of the SM.

By now, the mass of the top quark is measured to be $172.4 \pm 1.2$ GeV/c$^2$ [12], marking the most precisely measured quark mass and the most massive fundamental particle known to date. The consequent lifetime of the top quark in the SM of $\approx 5 \cdot 10^{-25}$ s is extremely short, suggesting that it decays before hadronizing. This makes it the only quark that does not form bound states, allowing the study of an essentially bare quark with properties such as spin undisturbed by hadronization [13].

The measurement of top quark pair $(t\bar{t}\,)$ production probes our understanding of the strong interaction and predictions from perturbative QCD, while the decay of top quarks and the production of single top quarks reflect the electroweak interaction. Measuring other properties of the top quark, such as its electric charge, the helicity of the $W$ boson in $t \rightarrow Wb$ decay, the branching fraction $\mathcal{B}(t \rightarrow Wb)$, *etc.*, and comparing these with predictions of the SM is a very powerful tool in searching for new physics beyond the standard model.

The top quark can also be used to constrain the mass range of the last yet to

be observed particle of the standard model, the Higgs boson, because their masses and the mass of the $W$ boson are linked through radiative corrections [14]. The Higgs boson is a manifestation of the Higgs mechanism [15–20], implemented in the standard model to provide the needed breaking of the electroweak symmetry to which the top quark may be intimately connected because of its large mass.

Because of its fairly recent discovery, the top quark's properties have not yet been explored with the same scrutiny as those of the lighter quarks. However, in the ongoing data taking at Fermilab's Tevatron proton-antiproton collider, an integrated luminosity of more than 4 fb$^{-1}$ has already been recorded by each of the collider experiments CDF and D0, corresponding to an increase of about a factor seventy relative to the data that was available for the discovery of the top quark. The new data can be used to refine previous measurements to higher precision that starts to become limited by systematic rather than statistical uncertainties. In addition, measurements that have never been performed become feasible, such as the first evidence for electroweak production of single top quarks and the consequent first direct measurement of the CKM matrix element $|V_{tb}|$, recently published by D0 [21, 22] and CDF [23].

This article is intended to provide an overview of the current status of the top quark physics program pursued at the Tevatron. Results available until the LHC startup in September 2008 have been included, utilizing samples of data of up to 2.8 fb$^{-1}$ in integrated luminosity. Previous reviews of the top quark are available in Refs. [24–28]. The outline of this article is as follows: The second chapter provides a brief introduction to the standard model, with emphasis on the special role played by the top quark. Chapter 3 describes production and decay modes for top quarks in the framework of the standard model. Chapter 4 outlines the experimental setup used for the measurements described in the following sections. Chapter 5 presents studies of the production of top quarks, including measurements of cross section that form the basis for other measurements of top quark characteristics. Chapter 6 elaborates on the different results for top quark decay properties, followed in Chapter 7 by a discussion of measurements of fundamental attributes of the top quark, such as its charge and mass. The final chapter (8) contains a brief summary of the achievements to date.

## 2. The Standard Model and the Top Quark

### 2.1. *A brief overview of the standard model*

The standard model of elementary particle physics describes very successfully the interactions of the known fundamental spin $J = \frac{1}{2}$ fermion constituents of matter through the exchange of spin $J = 1$ gauge bosons.

As shown in Table 1, both quarks and leptons occur in pairs, differing by one unit of electric charge $e$, and are replicated in three generations that have a strong hierarchy in mass. The fermion masses span at least 11 orders of magnitude, with the top quark being by far the heaviest fundamental particle, which may therefore

Table 1: The known fundamental fermions and their masses [12, 29].

| fermion type | electric charge [$e$] | generation | | |
|---|---|---|---|---|
| | | 1. | 2. | 3. |
| quarks | $+\frac{2}{3}$ | up ($u$) <br> 1.5 - 3.3 MeV/c$^2$ | charm ($c$) <br> 1.27 $^{+0.07}_{-0.11}$ GeV/c$^2$ | top ($t$) <br> 172.4 $\pm$ 1.2 GeV/c$^2$ |
| | $-\frac{1}{3}$ | down ($d$) <br> 3.5 - 6.0 MeV/c$^2$ | strange ($s$) <br> 104 $^{+26}_{-34}$ MeV/c$^2$ | bottom ($b$) <br> 4.20 $^{+0.17}_{-0.07}$ GeV/c$^2$ |
| leptons | 0 | $\nu_e$ <br> < 2 eV/c$^2$ <br> (95% C.L.) | $\nu_\mu$ <br> < 0.19 MeV/c$^2$ <br> (90% C.L.) | $\nu_\tau$ <br> < 18.2 MeV/c$^2$ <br> (95% C.L.) |
| | -1 | $e$ <br> 0.511 MeV/c$^2$ | $\mu$ <br> 105.658 MeV/c$^2$ | $\tau$ <br> 1777 MeV/c$^2$ |

provide further insights into the process of mass generation. The origin of this breaking of the flavor symmetry and the consequent mass hierarchy is still not understood but can be accommodated in the standard model as shown below.

The forces among the fundamental fermions are mediated by the exchange of the gauge bosons of the corresponding quantized gauge fields, as listed in Table 2. The gravitational force is not included in the framework of the standard model, and will not be considered, as its strength is small compared to that of the other interactions among the fundamental fermions at energy scales considered in this article.

The standard model is a quantum field theory based on the local gauge symmetries $SU(3)_{QCD} \times SU(2)_L \times U(1)_Y$. The theory of the strong interaction, coupling three different color charges ("red", "green" and "blue") carried by the quarks and the eight massless gauge bosons (gluons), is called Quantum Chromodynamics (QCD), and is based on the gauge group $SU(3)_{QCD}$ [30–35]. This symmetry

Table 2: The known fundamental interactions and their properties [29]. Gravitation is shown separately as it is not included in the SM of elementary particles.

| interaction type | couples to | affected particles | exchange boson | mass [GeV/c$^2$] | charge [$e$] | spin |
|---|---|---|---|---|---|---|
| strong | color charge | quarks, gluons | gluon (g) | 0 | 0 | 1 |
| weak | weak charge | quarks, $W^\pm$, leptons, $Z^0$ | $W^+$, $W^-$ <br> $Z^0$ | 80.4 <br> 91.2 | +1, -1 <br> 0 | 1 <br> 1 |
| electro-magnetic | electric charge | electrically charged | photon ($\gamma$) | 0 | 0 | 1 |
| gravitation | mass, energy | all | graviton (unobserved) | 0 | 0 | 2 |

is exact, and the gluons carry both a color and an anticolor charge. At increasingly short distances (or large relative momenta), the interaction gets arbitrarily weak (asymptotically free), thereby making a perturbative treatment viable. Via the strong interaction, quarks can form bound color-singlet states called hadrons, consisting of either a quark and an antiquark (mesons) or three quarks respectively antiquarks (baryons). The fact that only color-neutral states and no free quarks are observed is referred to as the confinement of quarks in hadrons. Due to its large mass, the top quark decays faster than the typical hadronization time of QCD ($\Gamma_{top} \gg \Lambda_{QCD}$), and it is therefore the only quark that does not form bound states. Its decay hence offers the unique possibility to study the properties of essentially a bare quark.

The theory of electroweak interactions developed by Glashow [36], Salam [37] and Weinberg [38] is based on the $SU(2)_L \times U(1)_Y$ gauge group of the weak left-handed isospin $T$ and hypercharge $Y$. Since the weak $(V - A)$ interaction only couples to left-handed particles, the fermion fields $\Psi$ are split up into left-handed and right-handed fields $\Psi_{L,R} = \frac{1}{2}(1 \mp \gamma_5)\Psi$ that are arranged in weak isospin $T = \frac{1}{2}$ doublets and $T = 0$ singlets:

$$\begin{pmatrix} u \\ d \end{pmatrix}_L \quad \begin{pmatrix} c \\ s \end{pmatrix}_L \quad \begin{pmatrix} t \\ b \end{pmatrix}_L \qquad\qquad \begin{matrix} u_R & c_R & t_R \\ d_R & s_R & b_R \end{matrix}$$

$$\begin{pmatrix} \nu_e \\ e \end{pmatrix}_L \quad \begin{pmatrix} \nu_\mu \\ \mu \end{pmatrix}_L \quad \begin{pmatrix} \nu_\tau \\ \tau \end{pmatrix}_L \qquad\qquad \begin{matrix} \nu_{eR} & \nu_{\mu R} & \nu_{\tau R} \\ e_R & \mu_R & \tau_R \end{matrix}$$

In the doublets, neutrinos and the up-type quarks $(u, c, t)$ have the weak isospin $T_3 = +\frac{1}{2}$, while the charged leptons and down-type quarks $(d, s, b)$ carry the weak isospin $T_3 = -\frac{1}{2}$. The weak hypercharge Y is then defined via electric charge and weak isospin to be $Y = 2Q - 2T_3$. Consequently, members within a doublet carry the same hypercharge: $Y = -1$ for leptons and $Y = \frac{1}{3}$ for quarks, as implied by the product of the two symmetry groups.

The $SU(2)_L \times U(1)_Y$ gauge group does not accommodate mass terms for the gauge bosons or fermions without violating gauge invariance. A minimal way to incorporate these observed masses is to implement spontaneous electroweak symmetry breaking (EWSB) at energies around the mass scale of the $W$ and $Z$ boson, often referred to as the "Higgs mechanism" [15–20], by introducing an SU(2) doublet of complex scalar fields $\Phi = (\Phi^+, \Phi^0)^T$. When the neutral component obtains a non-zero vacuum expectation value $v/\sqrt{2} \neq 0$, the $SU(2)_L \times U(1)_Y$ symmetry is broken to $U(1)_{QED}$, giving mass to the three electroweak gauge bosons $W^\pm, Z^0$ while keeping the photon massless, and thereby leaving the electromagnetic symmetry $U(1)_{QED}$ unbroken. From the remaining degree of freedom of the scalar doublet, we obtain an additional scalar particle, the Higgs boson.

The Higgs mechanism also provides fermion masses through fermion Yukawa couplings to the scalar field, with masses given by $m_f = \lambda_f v/\sqrt{2}$, for a Yukawa coupling constant $\lambda_f$ for each massive fermion in the standard model. With a Yukawa

coupling close to unity, the top quark may play a special role in the process of mass generation.

The mixing of flavor eigenstates in weak charged-current interactions of quarks is described by the Cabibbo-Kobayashi-Maskawa (CKM) matrix [39,40]. By convention, this is a 3 x 3 unitary matrix $V_{CKM}$ that operates on the negatively-charged flavor states $d, s$ and $b$:

$$
\begin{pmatrix} d' \\ s' \\ b' \end{pmatrix}_L = \begin{pmatrix} V_{ud} & V_{us} & V_{ub} \\ V_{cd} & V_{cs} & V_{cb} \\ V_{td} & V_{ts} & V_{tb} \end{pmatrix} \begin{pmatrix} d \\ s \\ b \end{pmatrix}_L \equiv \mathbf{V_{CKM}} \begin{pmatrix} d \\ s \\ b \end{pmatrix}_L .
\tag{1}
$$

This complex matrix can have 18 independent parameters. However, to conserve the probability, this matrix has to be unitary, which means that there are only nine free parameters. An additional five out of the nine can be absorbed as phases in the quark wave functions. This results in four independent parameters in total – three real Euler angles and one complex phase, the latter implementing CP violation in the standard model. Since the CKM matrix is not diagonal, charged current weak interactions can have transitions between quark generations ("generation mixing") with coupling strengths of the $W^\pm$ boson to the physical up and down type quarks given by the above matrix elements.

From experimental evidence [41–47], neutrinos also have mass, which has led, among other things, to the introduction of an analogue leptonic mixing matrix, the Pontecorvo-Maki-Nakagawa-Sakata (PMNS) matrix [48, 49]. It contains four independent parameters as well if one assumes that neutrinos are not Majorana particles.

In summary, the standard model of elementary particle physics is a unitary, renormalizable theory [50,51], that can be used to perturbatively calculate processes at high energies. It incorporates 25 parameters that have to be provided through measurement:

- 12 Yukawa couplings for the fermion masses
- 8 parameters for the CKM and PMNS mixing matrices
- 3 coupling constants $\alpha_s, g, g'$ of $SU(3)_{QCD}, SU(2)_L$ and $U(1)_Y$, respectively
- 2 parameters from EWSB: $v, m_H$.

At currently accessible energy scales, the standard model describes successfully the interactions of fundamental fermions and gauge bosons, with only the Higgs boson remaining to be observed. For a more detailed introduction to the standard model, the reader is referred to corresponding textbooks, Refs. [52–54] on elementary particle physics and topical reviews such as Ref. [55].

## 2.2.  *The need for the top quark in the standard model*

The existence of the top quark was postulated well before its discovery mainly for three reasons. The first argument reflects the desire to have the standard model
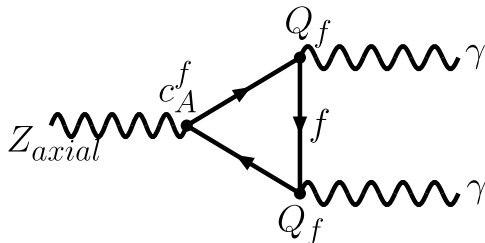
Fig. 1: A "problematic" fermion triangle diagram that could introduce an anomaly.

correspond to a renormalizable theory. When expressed via a perturbation series – usually depicted in Feynman diagrams with first order "tree" diagrams and higher order "loop" terms – certain loop diagrams cause divergences that have to cancel exactly to ensure that the theory is renormalizable. One example is the fermion triangle diagram, as shown in Fig. 1. The contribution for each such diagram is proportional to $c_A^f Q_f^2$, with $c_A^f$ being the weak neutral current axial coupling strength, and $Q_f$ the electric charge for the respective fermion in the loop. Since $c_A^f = T_3$ and neutrinos do not contribute, for the total strength of the anomaly to be cancelled, an equal number of lepton flavors and quark-doublets $N_{families}$, and quarks in three colors ($N_c = 3$) are required [52]:

$$\sum_{i=1}^{N_{families}} \left( -\frac{1}{2}(-1)^2 + \frac{1}{2}N_c \left( +\frac{2}{3} \right)^2 - \frac{1}{2}N_c \left( -\frac{1}{3} \right)^2 \right) \overset{!}{=} 0. \qquad (2)$$

Consequently, the discovery of the $\tau$ lepton already called for an additional quark doublet to be present to keep the standard model renormalizable.

The second argument results from the fact that transitions that change the flavor but not the charge of a fermion ($u \leftrightarrow c \leftrightarrow t$ or $d \leftrightarrow s \leftrightarrow b$) are observed to be strongly suppressed. The absence of such flavor-changing neutral currents (FCNC) for two quark generations could be accommodated through the GIM mechanism [56] by postulating the existence of the charm quark – and thereby completion of the second quark doublet – years before its discovery. This mechanism can be applied in a similar way for three quark generations, requiring a sixth quark as a partner of the $b$ quark to complete the doublet.

The third argument comes from the experimental confirmation that the $b$ quark is not a weak isospin singlet but is part of an isospin doublet carrying the weak isospin $T_3 = -\frac{1}{2}$ and electric charge $Q_b = -\frac{1}{3}e$. The electric charge of the $b$ quark was measured first at the electron-positron storage ring DORIS at DESY operating at the $\Upsilon$ and $\Upsilon'$ resonances through a measurement of the cross section for resonant hadron production $\sigma_h$ [57–59]. The integral over $\sigma_h$ is related to the electronic partial width $\Gamma_{ee}$, the hadronic partial width $\Gamma_h$, the total width $\Gamma_{tot}$ and the resonance mass $M_R$ via $\int \sigma_h \, dM = 6\pi^2 \Gamma_{ee}\Gamma_h/(M_R^2 \Gamma_{tot})$. Assuming that the total width is dominated by the hadronic partial width ($\Gamma_h \approx \Gamma_{tot}$), a measurement of

the integrated cross section and the resonance mass provides the electronic partial width $\Gamma_{ee}$ of the $\Upsilon$ and of the $\Upsilon'$. In the framework of non-relativistic quarkonium potential models [60, 61], this partial width can then be related with the bound quark's charge.

The weak isospin of the $b$ quark was measured via the forward-backward asymmetry $A_{FB}$ in the process $e^+e^- \to b\bar{b} \to \mu^\pm +$ hadrons with the JADE detector at PETRA [62]. The asymmetry originates from electroweak interference effects and is defined as the difference between the number of fermions produced in the forward direction (with polar angle $\theta < 90°$) and the number of fermions produced backward ($\theta > 90°$), divided by their sum. $A_{FB}$ is proportional to the ratio of the weak axial to the electric charge and vanishes for a weak isospin singlet. For a $T_3 = -\frac{1}{2}, Q = -\frac{1}{3}e$ $b$-quark, the predicted asymmetry is $-25.2\%$, in good agreement with the measurement of $-22.8 \pm 6.0$ (stat.) $\pm 2.5$ (syst.)%.

As a result of these measurements, the top quark's weak isospin and electric charge within the standard model were assigned to be $T_3 = +\frac{1}{2}$, $Q_t = +\frac{2}{3}e$, well before its discovery. The mass of the top quark, being a free parameter in the standard model, could not be predicted. Nevertheless, the mass of the top quark can indirectly be constrained by precision electroweak measurements.

### 2.3.  *Top quark mass from precision electroweak measurements*

As discussed above, the standard model comprises a set of free parameters that are a priori unknown. However, once these are measured, all physical observables can be expressed in terms of those parameters. To make optimal use of the predictive power of the theory, it is therefore crucial to measure its input parameters with highest possible precision, and thereby probe the self-consistency of the SM and any contributions beyond its scope. Being a renormalizable theory, predictions for any observable can be calculated to any order and checked with experiment.

Electroweak processes depend mainly on three parameters: the coupling constants $g$ and $g'$ of $SU(2)_L$ and $U(1)_Y$, respectively, and the Higgs vacuum expectation value $v$. Since these input parameters have to be obtained from experiment, it is best to substitute them with the most precisely measured quantities of the electromagnetic fine structure constant $\alpha$ (using electron-positron annihilations into hadrons at low center of mass energies to measure hadronic vacuum polarization corrections [63–65]), the Fermi constant $G_F$ (from the muon lifetime [66, 67]) and the mass of the $Z$ boson $m_Z$ (from electron-positron annihilations around the $Z$ pole [68]).

With these input values, the theoretical framework can be used to predict other quantities such as the $W$ boson mass. Given precision measurements, the $W$ boson mass is sensitive to the mass of the top quark and the mass of the Higgs boson through higher order radiative quantum corrections [69–71].

The most precise electroweak measurements to date have been performed at the Large Electron-Positron (LEP) Collider [72, 73] at CERN by the four experiments
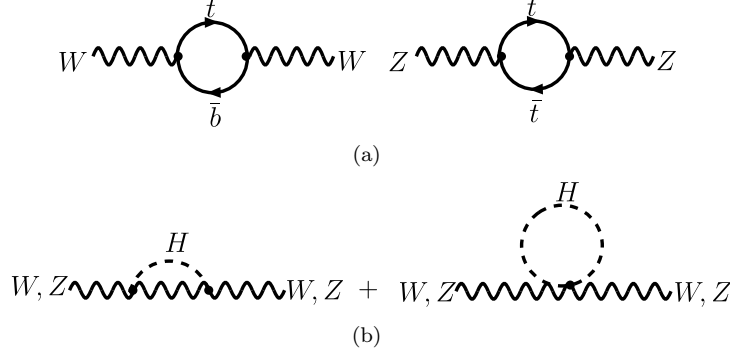
(a)



(b)

Fig. 2: (a) Radiative contributions to the $W$ and $Z$ propagators from the top quark. (b) Radiative corrections to the $W$ and $Z$ propagators from the Higgs boson.

ALEPH [74,75], DELPHI [76,77], L3 [78,79] and OPAL [80,81], and at the Stanford Linear Collider (SLC) [82,83] by the SLD experiment [84,85]. The LEP experiments have analyzed $\approx$17 million $Z$ decays, and a sample of $\approx$600 thousand $Z$ bosons produced with longitudinally polarized electron beams was analyzed by SLD.

Defining the electroweak mixing angle $\theta_W$ via the vector boson masses:

$$\frac{m_W^2}{m_Z^2} = 1 - \sin^2 \theta_W, \tag{3}$$

the $W$ boson mass can be expressed as [70]:

$$m_W^2 = \frac{\pi \alpha}{\sqrt{2} G_F} \cdot \frac{1}{\sin^2 \theta_W (1 - \Delta r)}, \tag{4}$$

where the radiative correction $\Delta r$ is a directly observable quantum effect of electroweak theory that depends on $\alpha, m_W, m_Z, m_H$ and $m_t$. The contributions from single-loop insertions containing the top quark and the Higgs boson, as depicted in Fig. 2, are [86]:

$$\Delta r^{\text{top}} = -\frac{3\sqrt{2} G_F \cot^2 \theta_W}{16\pi^2} \cdot m_t^2 \qquad (\text{for } m_t \gg m_b) \tag{5}$$

$$\Delta r^{\text{Higgs}} = \frac{3\sqrt{2} G_F m_W^2}{16\pi^2} \cdot \left( \ln \frac{m_H^2}{m_W^2} - \frac{5}{6} \right) \qquad (\text{for } m_H \gg m_W). \tag{6}$$

Thus, a precise measurement of $W$ and $Z$ boson masses provides access to the mass of the top quark and the Higgs boson. The top quark contribution to radiative corrections is large, primarily because of the large mass difference relative to its weak isospin partner, the $b$ quark. While the leading top quark contribution to $\Delta r$ is quadratic, it is only logarithmic in mass for the Higgs boson. Consequently, the constraints that can be derived on the mass of the top quark are much stronger than for the Higgs boson mass.

In 1994, the most stringent constraints on $m_t$ were based on preliminary LEP and SLD data, combined with measurements of $m_W$ in proton-antiproton experiments,
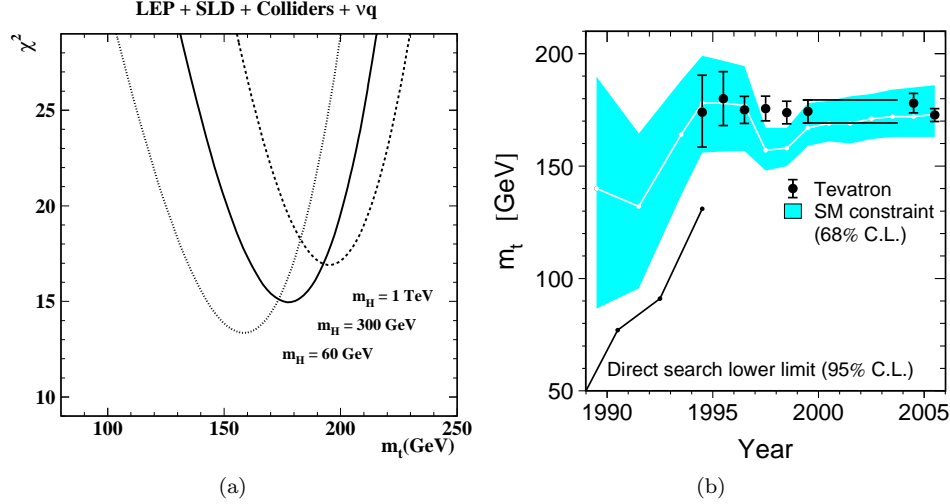
Fig. 3: (a) $\chi^2$ distributions of the standard model fit to precision electroweak data versus top quark mass for various Higgs boson masses [3]. (b) Comparison of the indirect top quark mass measurements via radiative corrections (shaded area) with the direct measurements from the Tevatron (points) versus time [68].

and neutral to charged-current ratios obtained from neutrino experiments, yielding $178 \pm 11 \, ^{+18}_{-19}$ GeV/c$^2$ [3]. As illustrated in Fig. 3(a), the central value and the first set of uncertainties are from a $\chi^2$ fit of the SM to precision electroweak data, assuming $m_H = 300$ GeV/c$^2$. The second set of uncertainties stems from the impact of varying $m_H$ between 60 and 1000 GeV/c$^2$.

The good agreement between predicted and observed values of $m_t$, shown in Fig. 3(b) as a function of time [68], is one of the great successes of the SM. The latest prediction from precision electroweak data yields $m_t = 179^{+12}_{-9}$ GeV/c$^2$ without imposing constraints on $m_H$ [14], and is in excellent agreement with the current world average of $m_t = 172.4 \pm 1.2$ GeV/c$^2$ [12].

This success of the SM also gives greater confidence in the predictions for $m_H$. Since the precision of the prediction depends crucially on the accuracy of $m_W$ and $m_t$, it provides a strong motivation for improving the corresponding measurements. The current constraints on the mass of the Higgs boson will be discussed in Section 7.3.4.

More details on precision electroweak measurements can be found in topical reviews such as given in Refs. [86, 87].

## 3. Production and Decay of Top Quarks

The production of top quarks is only possible at highest center of mass energies $\sqrt{s}$, set by the scale of $m_t$. The energies needed for production of top quarks in the SM are currently (and will be at least for the next decade) only accessible at

hadron colliders. The Tevatron proton-antiproton collider started operation at $\sqrt{s} = 1.8$ TeV in 1987 for a first period of data taking ("Run 0") that lasted until 1989, with the CDF experiment recording about 4 pb$^{-1}$ of integrated luminosity. The next data taking period from 1992 until 1996 at $\sqrt{s} = 1.8$ TeV (the so-called Run I) was utilized by both the CDF and D0 experiments and facilitated the discovery of the top quark. For the currently ongoing data taking that started in 2001 (Run II), the center of mass energy has increased to $\sqrt{s} = 1.96$ TeV. The Tevatron will lose its monopoly for top quark production only with the turning-on of the Large Hadron Collider (LHC) that will provide proton-proton collisions at $\sqrt{s} = 14$ TeV.

In the framework of the standard model, top quarks can be produced in pairs ($t\bar{t}$) predominantly via the strong interaction and singly via the electroweak interaction.

### 3.1. *Top quark pair production*

While hadron colliders provide the highest center of mass energies, the collision of hadrons complicates the theoretical description and prediction for processes such as $t\bar{t}$ production because of the composite nature of the colliding particles. These difficulties can be handled through the QCD factorization theorem [88,89] that provides a way to separate hadron collisions into universal long-distance (small momentum transfer) phenomena and perturbatively calculable short-distance phenomena. The latter processes involve therefore large square of momentum transfers $Q^2$, and consequently the production of particles with large transverse momenta or large mass. The two components are set apart by introducing a factorization scale $\mu_F^2$ in the calculation.

Using this approach, the proton can be described by a collection of partons (quarks, antiquarks, gluons) that interact at a low energy scale $\Lambda_{QCD} < 1$ GeV, whereas the elementary collisions between partons of the proton (or antiproton) occur on a "hard" energy scale characterized by large transverse momenta $\geq \mathcal{O}(100$ GeV).

Consequently, the partons participating in any hard process $(a, b)$ can be considered quasi-free, and the partonic cross section of interest $\hat{\sigma}_{a+b \to X}(\hat{s}, \alpha_s(\mu_R^2), \mu_R^2)$ can be calculated using perturbative QCD, independent of the type of hadrons containing the partons. (The hatted variables denote parton quantities.) The regularization of divergences in higher order calculations (such as ultraviolet divergences from loop insertions, where the infinite range of four-momentum in the loop causes infinities in the integration from high momentum contributions) requires the introduction of a renormalization scale $\mu_R^2$, along with the corresponding running coupling constant $\alpha_s(\mu_R^2)$. The leading order Feynman diagrams for $t\bar{t}$ production are shown in Fig. 4.

The partons within the incoming proton (or antiproton) cannot be described by perturbative QCD, as the soft energy scale corresponding to small inherent momentum transfers implies large $\alpha_s(Q^2)$ couplings. The distribution of the longitudinal momentum of the hadron among the partons is described by Parton Distribution
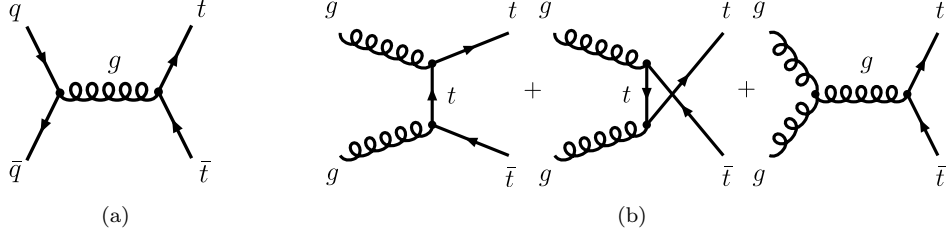
Fig. 4: Leading order Feynman diagrams for top quark pair production: (a) quark-antiquark annihilation and (b) gluon-gluon fusion.

Functions (PDFs): $f_{a/A}(x, \mu_F^2)$, corresponding to the probability to find a given parton $a$ inside hadron $A$ with momentum fraction $x$ when probed at an energy scale $\mu_F^2$. Collinear and soft (infrared) singularities that arise in the perturbative calculation of the partonic cross section discussed above are absorbed in these PDFs.

The factorization theorem is used to describe the $t\bar{t}$ production cross section via an integral over the corresponding hard scattering parton cross section, folded with the parton distribution functions of the incident hadrons as follows:

$$\sigma_{A+B \to t\bar{t}}(\sqrt{s}, m_t) = \sum_{a,b=g,q,\bar{q}} \int \hat{\sigma}_{a+b \to t\bar{t}}(\hat{s}, \alpha_s(\mu_R^2), \mu_R^2, \mu_F^2, m_t)$$
$$\times f_{a/A}(x_a, \mu_F^2) f_{b/B}(x_b, \mu_F^2) dx_a dx_b. \quad (7)$$

The hadrons $A$ and $B$ correspond to proton and antiproton in case of the Tevatron and to protons in case of the LHC.

The physical cross section $\sigma_{A+B \to t\bar{t}}(\sqrt{s}, m_t)$ that would emerge from the evaluation of the full perturbation series does not depend on either of the two arbitrary scales for factorization and renormalization $\mu_F^2, \mu_R^2$ that had to be introduced for the calculation. However, the parton distribution functions and the partonic cross section do depend on these scales, and hence the result of any finite order calculation will as well. This dependence gets weaker with the inclusion of higher order terms in the calculation. In practical application, both scales are usually set to the typical momentum scale $Q^2$ of the hard scattering process, such as the transverse momenta of the produced particles or the mass of the produced particle, so that for $t\bar{t}$ production, typically $\mu_F = \mu_R = \mu = m_t$. The scale dependence of the result is then usually tested by varying the central scale by a factor of two; the resulting variations are interpreted as systematic uncertainties that should not be mistaken as Gaussian in nature.

The PDFs have to be determined experimentally, for example via deeply inelastic lepton scattering on nucleons, so that they can be extracted from the measured cross sections using perturbative calculations of the (hard) partonic cross sections. Once the parton densities $f_{a/A}(x_a, Q^2)$ have been measured as a function of momentum fraction $x_a$ at a scale $Q^2$, their value at a different scale can be predicted
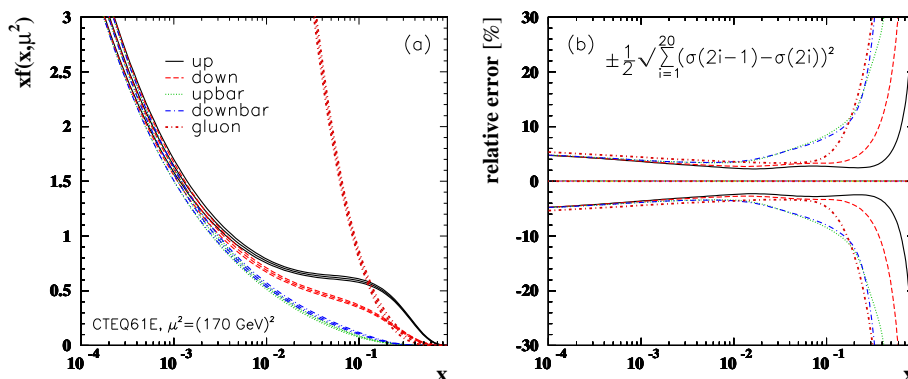
Fig. 5: (a) CTEQ61 [93] parton distribution functions with their uncertainty bands, for the $m_t$ mass scale ($Q^2 = (170 \text{ GeV})^2$) for (anti-) up quarks, (anti-) down quarks and gluons in the proton. (b) Relative uncertainties on the PDFs shown in (a).

perturbatively using the DGLAP evolution equation [90–92]. Since PDFs are universal and do not depend on the process they were derived from, they can be used to predict cross sections in other hard scattering processes. For consistent application, it is important that the PDFs are derived to same perturbative order and with the same renormalization scheme as the calculation of any prediction.

The PDFs are extracted from global fits to the available data, as is done, for example, by the CTEQ [94], MRST [95], GRV [96], Alekhin [97], H1 [98] and ZEUS [99] groups. Different PDFs are based on different data, different orders of perturbation theory, renormalization schemes and fitting techniques – see, for example, the overview given in Ref. [100]. One commonly used set of PDFs derived at NLO, using the $\overline{MS}$ renormalization scheme [101], is CTEQ61 [93], which incorporates the Tevatron Run I data on jet production, especially important for the gluon distribution. CTEQ61 also includes an error analysis based on different sets of PDFs that describe the behavior of a global $\chi^2$ function for the fit around its minimum. The resulting error on the PDF ($\Delta f$) can be obtained by summing over the variations $f_i^{\pm}$ along/against each PDF "eigenvector" for every free parameter in the global fit: $\Delta f = \pm\frac{1}{2}(\Sigma_{i=1}^{N_{par}}(f_i^+ - f_i^-)^2)^{\frac{1}{2}}$.

Figure 5 shows the most important parton distributions within protons for $t\bar{t}$ production at the Tevatron or LHC, and their corresponding uncertainties. (For antiprotons, quarks and antiquarks have to be interchanged in Fig. 5.) All PDFs vanish at large momentum fractions $x$, and the gluon density starts to dominate over the valence-quark densities near $x = 0.13$. There is no flavor symmetry between the up and down quark distributions, neither on the valence nor the sea quark level (the latter is best seen at low $Q^2$). At $x$-values below 0.1, typical relative uncertain-

ties on the PDFs of valence quarks and gluons are $\approx 5\%$. At larger $x$-values, these uncertainties increase drastically, especially for gluons.

To produce a top quark pair, the squared center of mass energy at the parton level $\hat{s} = x_a x_b s$ must at least equal $(2m_t)^2$. Assuming $x_a \approx x_b = x$ yields as threshold for $t\bar{t}$ production:

$$\langle x \rangle = \sqrt{\frac{\hat{s}}{s}} = \frac{2m_t}{\sqrt{s}} \approx \begin{cases} 0.192 \text{ @ Tevatron Run I, } \sqrt{s} = 1.8 \text{ TeV} \\ 0.176 \text{ @ Tevatron Run II, } \sqrt{s} = 1.96 \text{ TeV} \\ 0.025 \text{ @ LHC, } \sqrt{s} = 14 \text{ TeV} \end{cases} \quad (8)$$

Since large momentum fractions are required for $t\bar{t}$ production at the Tevatron, the process is dominated by quark-antiquark annihilation (Fig. 4 (a)) of the valence quarks. For Run I energies, quark-antiquark annihilation contributes roughly 90% of the total $t\bar{t}$ production rate, and for Run II energies this fraction is $\approx 85\%$ [25].

At the LHC, gluon-gluon fusion dominates (Fig. 4 (b)) with a contribution of about 90% [102], because a small momentum fraction suffices for $t\bar{t}$ production. This means that proton-proton collisions at the LHC have production cross sections comparable to $p\bar{p}$ rates, thereby obviating the need for the major technical challenge of producing an intense antiproton beam.

The increase in the center of mass energy by $\approx 10\%$ between Run I and Run II at the Tevatron and the correspondingly smaller minimum momentum fraction provide an increase in the $t\bar{t}$ production rate of 30%. At the LHC, the rate increases by roughly a factor of 100 compared to that of the Tevatron.

The highest-order complete perturbative calculations for heavy quark pair production have been available at next-to-leading order (NLO) – to order $\alpha_s^3$ – since the late 1980s from Nason *et al.* [103] and Beenakker *et al.* [104, 105]. These calculations can be refined by the inclusion of large logarithmic corrections [106–108] from soft-gluon emission that are particularly important for the production of heavy quarks close to the kinematic threshold ($\hat{s} \approx 4m^2$, $x \rightarrow 1$). The contributions of these logarithms are positive at all orders when evaluated at the heavy quark mass scale and their inclusion therefore increases the production cross section above the NLO level.

The impact of soft-gluon resummation on the $t\bar{t}$ production cross section has been studied by Berger and Contopanagos [109–111], Laenen, Smith and van Neerven [112, 113] and Catani, Mangano, Nason and Trentadue [114, 115] at the leading logarithmic (LL) level. Studies including even higher level corrections as carried out by Cacciari *et al.* [116], based on work by Bonciani *et al.* (BCMN) [117], and Kidonakis and Vogt [118, 119] are summarized in Table 3.

In the case of $t\bar{t}$ production at the Tevatron, the inclusion of leading and next-to-leading logarithmic (NLL) soft-gluon resummation affects the cross sections only mildly by $\mathcal{O}(5\%)$ (indicating production occurs not too close to the threshold), while significantly reducing the scale dependence of the predictions by roughly a factor of two to a level of $\approx 5\%$ [117]. At the LHC, $t\bar{t}$ production takes place even further away from the kinematic threshold, but since gluon fusion dominates there,

Table 3: NLO cross section predictions including soft-gluon resummations beyond LL for $t\bar{t}$ production at the Tevatron and the LHC for a top quark mass of 175 GeV/c$^2$. For the different sources of the quoted uncertainties please refer to the text.

| Hadron Collider | Processes | $\sigma_{t\bar{t}}$ [pb] | Group |
|---|---|---|---|
| Tevatron Run I | 90% $q\bar{q} \rightarrow t\bar{t}$ | $5.19^{+0.52}_{-0.68}$ | Cacciari *et al.* [116] |
| ($p\bar{p}$, $\sqrt{s} = 1.8$ TeV) | 10% $gg \rightarrow t\bar{t}$ | $5.24 \pm 0.31$ | Kidonakis *et al.* [119] |
| Tevatron Run II | 85% $q\bar{q} \rightarrow t\bar{t}$ | $6.70^{+0.71}_{-0.88}$ | Cacciari *et al.* [116] |
| ($p\bar{p}$, $\sqrt{s} = 1.96$ TeV) | 15% $gg \rightarrow t\bar{t}$ | $6.77 \pm 0.42$ | Kidonakis *et al.* [119] |
| LHC | 10% $q\bar{q} \rightarrow t\bar{t}$ | $833^{+52}_{-39}$ | Bonciani *et al.* [117] |
| ($pp$, $\sqrt{s} = 14$ TeV) | 90% $gg \rightarrow t\bar{t}$ | $873^{+2}_{-28}$ | Kidonakis *et al.* [118] |

the enhancement of the total production rate from soft-gluon resummation and the reduction of scale dependence stay at the same level as at the Tevatron.

The results of Cacciari *et al.* [116] for the Tevatron use the NLO calculation with LL and NLL resummation at all orders of perturbation theory as carried out by Bonciani *et al.* (BCMN) [117], but are based on the more recent PDF sets with error analysis CTEQ6 [94] and MRST2001E [95] and also MRST2001 [120], which includes varied $\alpha_s$ values in the PDF fit. The updated PDFs cause an increase in the central values of about 3% relative to Ref. [117]. While the central values are very similar for the MRST2001E and CTEQ6 PDFs, the uncertainties for CTEQ6 are almost twice as large as for MRST2001E, unless the variations in $\alpha_s$ in MRST2001 are also included. For the determination of the uncertainty on the cross section, Cacciari *et al.* combine linearly the uncertainty due to scale variation by a factor of two with the PDF uncertainty evaluated at that scale. As central values, the CTEQ6M results are chosen, and the maximum lower (upper) uncertainties given stem from the CTEQ6 PDF variation (the $\alpha_s$ variation in MRST2001). The PDF uncertainties and $\alpha_s$ variation contribute about 45% and 80% respectively to the total quoted uncertainty, including the scale variations, which emphasizes the importance of considering $\alpha_s$ uncertainties in PDF fits. The PDF uncertainties are in turn dominated by the uncertainty of the gluon PDF at large $x$ values, causing, for example, the gluon fusion contribution to the total production rate to fluctuate between 11% and 21% for $\sqrt{s} = 1.96$ TeV. Despite the large uncertainties on the $t\bar{t}$ production rate, the ratio of production cross sections for the two center of mass energies at the Tevatron is very stable and predicted with high precision: $\sigma(1.96 \text{ TeV})/\sigma(1.8 \text{ TeV}) = 1.295 \pm 0.015$ for top quark masses between 170 and 180 GeV/c$^2$ [116].

A prediction for the $t\bar{t}$ production rate at the LHC applying the same level of soft-gluon resummation is given by Bonciani *et al.* [117] using the MRS(R$_2$)

PDF [121]. Since no PDF uncertainties were available for Ref. [117], the quoted uncertainty in Table 3 comes from changing the scale by factors of two alone. Since gluon fusion is the dominant contribution to the total rate, uncertainties on the gluon PDFs alone lead to an uncertainty of $\approx 10\%$ on the total production cross section [122].

The studies performed by Kidonakis and Vogt [118, 119] consider soft-gluon corrections up to next-to-next-to-next-to leading logarithmic (NNNLL) terms at NNLO in a truncated resummation, resulting in a reduced sensitivity of $\approx 3\%$ to scale variations. For the Tevatron, the $t\bar{t}$ production cross section is evaluated using MRST2002 NNLO [95] and CTEQ6M NLO [94] parton densities. Two different parton-level conditions are considered for the scattering process: (i) one-particle inclusive (1PI) and (ii) pair-invariant mass (PIM) kinematics [102]. While both sets of PDFs give very similar results, the variations from the difference in kinematics are significant. Consequently, the average of 1PI and PIM kinematics for both PDFs is used as the central value in Table 3, while the separate averages over the PDFs for 1PI and PIM are quoted as uncertainties. For the predicted LHC rate, which is dominated by gluon fusion, the 1PI kinematics is considered more appropriate, and the value in Table 3 gives the corresponding result based on MRST2002 NNLO PDFs, using scale changes by factors of two for estimating the uncertainties.

All results in Table 3 are evaluated for a top quark mass of 175 GeV/c$^2$, and the Run II values serve as the main predictions for CDF and D0. To improve comparability of the uncertainties on the different predictions, the calculation by Kidonakis and Vogt has an additional uncertainty obtained from the maximum simultaneous changes in scale and PDFs[a] added in quadrature with the uncertainty due to the dependence on kinematics [123].

In spring 2008, Cacciari *et al.* [124] and Kidonakis *et al.* [125] updated their predictions using more recent PDFs such as CTEQ6.6M [126], which had only little impact on the results. In addition, Moch and Uwer [127] have now performed a complete NNLL soft-gluon resummation and provide an approximation of the NNLO cross section also based on CTEQ6.6M. To illustrate the dependence of the predictions on the top quark mass, Fig. 6 shows the central values and uncertainties from References [124, 125, 127] for Tevatron Run II versus $m_t$. An exponential form, as suggested in Ref. [114], is applied in a fit to the central values and uncertainties for Kidonakis *et al.*, while third-order polynomials, as provided by the authors, are used for the other references. The total uncertainties are obtained by linearly combining the provided uncertainties.

For the current world-averaged top quark mass of $172.4 \pm 1.2$ GeV/c$^2$ [12], the predicted $t\bar{t}$ production cross section is $7.2^{+0.8}_{-0.9}$ pb for Cacciari *et al.*, $7.3^{+0.8}_{-0.9}$ pb for Kidonakis *et al.*, and $7.5^{+0.5}_{-0.7}$ pb for Moch *et al.*. An additional uncertainty of $\pm 0.3$ pb arises from the uncertainty on the top quark mass for all three predictions. It should be noted that these predictions based on MRST 2006 NNLO PDFs [128]

---

[a]The PDF uncertainties in this case stem from CTEQ6 sets "129" and "130" alone.
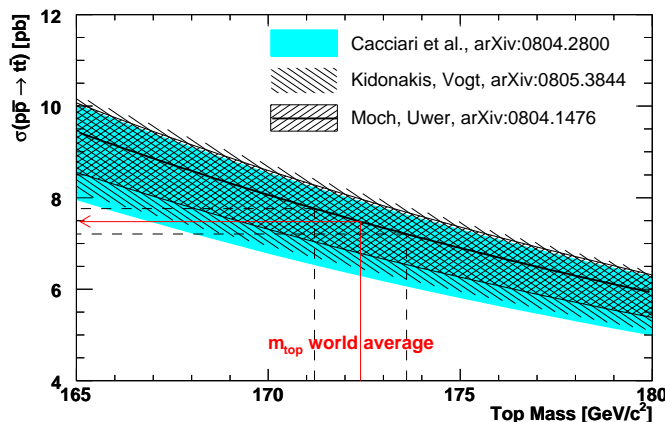
Fig. 6: Dependence of the $t\bar{t}$ production cross section on $m_t$ in Run II of the Tevatron. The current world-averaged top quark mass and the resulting expected $t\bar{t}$ production cross section are indicated by the vertical and horizontal lines, respectively. The predictions are based on the CTEQ6.6M PDFs [126].

yield about 6% higher central values and exhibit smaller uncertainties from PDFs.

A precise measurement of the $t\bar{t}$ production cross section provides a test of the predictions for physics beyond the SM. Together with a precise mass measurement, the self-consistency of the predictions can also be examined. Because $t\bar{t}$ production is a major source of background for single top production (to be discussed in the next section), standard model Higgs boson production and many other phenomena beyond the SM, its accurate understanding is crucial for such studies.

Figure 7 illustrates the production rates of various processes versus center of mass energy for proton-antiproton collisions below $\sqrt{s} = 4$ TeV and for proton-proton collisions above $\sqrt{s} = 4$ TeV. As can be appreciated from the plot, $t\bar{t}$ production is suppressed by ten orders of magnitude relative to the total interaction rate at the Tevatron and eight orders of magnitude at the LHC. While the LHC is often referred to as a "top-factory" because of the increased production cross section by two orders of magnitude, extraction of the signal from the large background is a challenge at both hadron colliders, requiring efficient triggers and selection methods. The $t\bar{t}$ cross section measurements performed in Run II of the Tevatron will be described in Section 5.1.

### 3.2. *Single top quark production*

In addition to the strong pair production discussed in the previous section, top quarks can also be produced singly via the electroweak interaction through a $Wtb$ vertex (see Fig. 8). $Wts$ and $Wtd$ vertices are strongly CKM suppressed (see Sec-
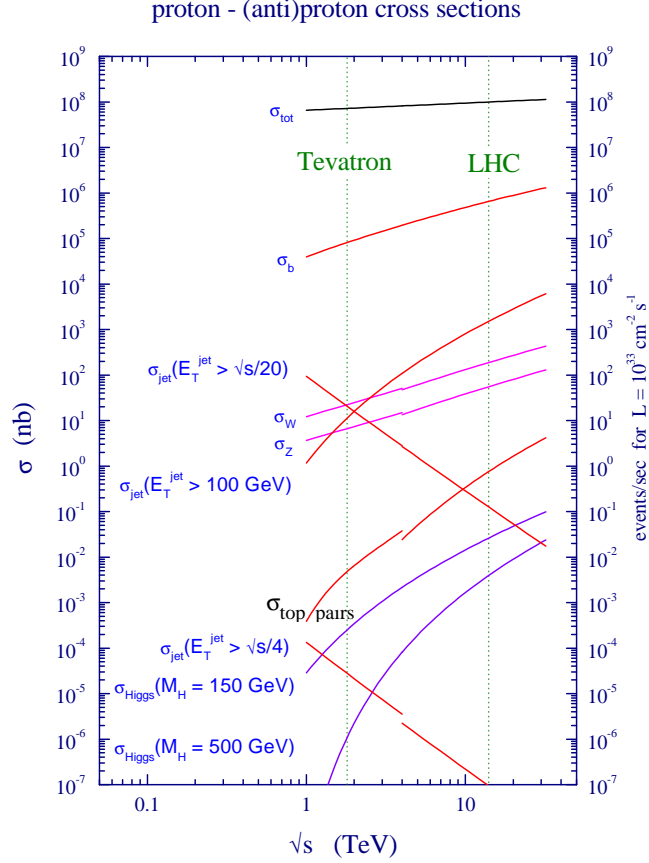
Fig. 7: Cross sections for various processes at hadron colliders as a function of center of mass energy [122]. $\sigma_{\mathrm{toppairs}}$ denotes the $t\bar{t}$ production cross section.

tion 3.3.1). There are three different production modes, classified via the virtuality (negative of the square of the four-momentum $q$) of the participating $W$ boson ($Q_W^2 = -q^2$):

- The Drell-Yan-like *s-channel* production proceeds via quark-antiquark annihilation into a time-like virtual $W$ boson ($q^2 \geq (m_t + m_b)^2 > 0$), as illustrated in Fig. 8(a): $q\bar{q}' \to t\bar{b}$ [129, 130].
- In the *t-channel* "flavor excitation" process, a space-like virtual $W$ boson ($q^2 < 0$) couples to a $b$ quark from the nucleon's sea to produce a top quark, as shown in Fig. 8(b) for $qb \to q't$. A higher order contribution of $\mathcal{O}(\alpha_s)$ comes from gluon splitting, as depicted in Fig. 8(c), which is also referred to as W-gluon fusion for $qg \to tq'\bar{b}$ [131–134].
- In *associated production*, an on-shell $W$ boson ($q^2 = m_W^2$) is produced together
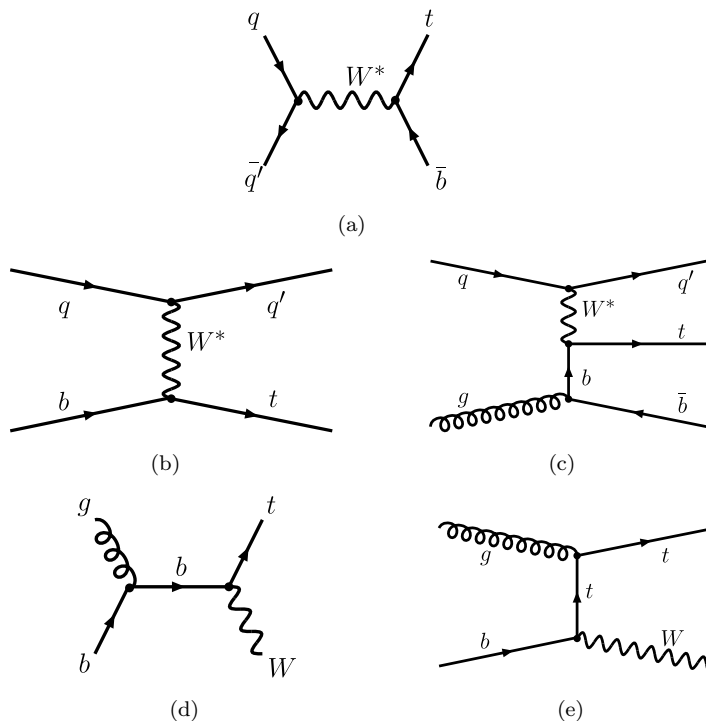
Fig. 8: Representative Feynman diagrams for electroweak single top quark production: (a) *s*-channel, (b,c) *t*-channel and (d,e) associated production.

with a top quark from a *b* quark and a gluon, as illustrated in Figs. 8(d) and 8(e) for $gb \rightarrow tW$ [135–140].

In the above discussion, charge conjugate processes are implied for each production mode, and *q* represents a light-flavor quark. All three modes differ in both their initial and final states, and the processes are simply denoted as *s*-channel (*tb*), *t*-channel (*tq*, *tqb*) and associated (*tW*) production. The corresponding signatures can be used to discriminate between the production modes: The *s*-channel is characterized by an additional *b* quark accompanying the top quark, the *t*-channel by a forward light quark, and associated production by the decay products of the *W* boson in addition to those of the top quark. Due to the incoming *b* quark and gluon, the *t*-channel and *tW*-channel rates are especially sensitive to the corresponding PDFs, which are known with less precision than the PDFs for the valence quarks of the proton. The measured cross sections will therefore provide further constraints on the *b* quark and gluon PDFs.

The cross sections for all three modes have been evaluated at NLO, including radiative corrections of $\mathcal{O}(\alpha_s)$: s-channel [141–143], t-channel [143–145], and *tW*-channel [146, 147]. (The most recent references provide differential distributions.)

Table 4: Cross sections for *s*-channel (*tb*), *t*-channel (*tq*) and associated (*tW*) single-top production at NLO (Sullivan), and NLO, including soft-gluon resummations (Kidonakis), expected at the Tevatron and at the LHC, for a top quark mass of 175 GeV/c$^2$. (For sources of the quoted uncertainties see the text.)

| Hadron Collider | $t/\bar{t}$ | $\sigma_{tb}$ [pb] | $\sigma_{tq}$ [pb] | $\sigma_{tW}$ [pb] | Group |
|---|---|---|---|---|---|
| Tevatron Run I $(p\bar{p},\ \sqrt{s} = 1.8\text{ TeV})$ | $t, \bar{t}$ | $0.75^{+0.10}_{-0.09}$ | $1.46^{+0.20}_{-0.16}$ | — | Sullivan [156] |
| Tevatron Run II $(p\bar{p},\ \sqrt{s} = 1.96\text{ TeV})$ | $t, \bar{t}$ | $0.88^{+0.12}_{-0.11}$ | $1.98^{+0.28}_{-0.22}$ | — | Sullivan [156] |
| | | $0.98 \pm 0.04$ | $2.16 \pm 0.12$ | $0.26 \pm 0.06$ | Kidonakis [153] |
| LHC $(pp,\ \sqrt{s} = 14\text{ TeV})$ | $t$ | $6.56^{+0.69}_{-0.63}$ | $155.9^{+7.5}_{-7.7}$ | — | Sullivan [156] |
| | $\bar{t}$ | $4.09^{+0.43}_{-0.39}$ | $90.7^{+4.3}_{-4.5}$ | — | |
| | $t$ | $7.2^{+0.6}_{-0.5}$ | $146 \pm 5$ | $41 \pm 4$ | Kidonakis [153] |
| | $\bar{t}$ | $4.0 \pm 0.2$ | $89 \pm 4$ | $41 \pm 4$ | |

Subsequent calculations also include top quark decay at NLO for s-channel [148–150], *t*-channel [148, 150, 151], and *tW*-channel [152], and latest NLO calculations include higher-order soft-gluon corrections up to NNNLO at NLL accuracy [153–155].

Table 4 summarizes the expected single-top production cross sections at the Tevatron and the LHC for the NLO calculations by Sullivan [156] (based on the work of Harris *et al.* in [143]) and NLO results including soft-gluon resummations by Kidonakis [153] (based on his work in Refs. [154, 155] and matching to the exact NLO results of Harris *et al.* [143] and Zhu [146, 147]). Both results use current PDFs and include corresponding uncertainties.

While top and antitop production are identical at the Tevatron for all production modes, at the LHC this is only the case for associated production. Consequently, the results given for the Tevatron include both top and antitop production but are given separately for the LHC.

The NLO results of Sullivan are based on CTEQ5M1 PDFs [157] for their central values. The uncertainties for PDFs are derived from CTEQ6M [94], and added in quadrature with uncertainties from changes in scale by the usual factors of two, changes in top quark mass by 4.3 GeV/c$^2$ (using an older world-averaged $m_t = 178 \pm 4.3$ GeV/c$^2$ [158]), and uncertainties in *b* quark mass and $\alpha_s$, the latter two being negligible. The rate dependence on the top quark mass is approximated as linear and is especially important for the *s*-channel, since a change from 175 GeV/c$^2$ to the current world-averaged $m_t = 172.4$ GeV/c$^2$ raises the rates at the Tevatron by 7% for the *s*-channel and 5% for the *t*-channel. The observed uncertainties in scale are reduced relative to LO results, and amount to 4-6% at the Tevatron and 2-3% at the LHC.

The NLO calculations of Kidonakis that include higher order soft-gluon corrections provide single-top production cross sections based on MRST2004 NNLO PDFs [159]. The quoted values are obtained by matching the NLO cross section to the results of Harris *et al.* [143] and Zhu [146, 147], and including the additional soft-gluon corrections up to NNNLO. Exceptions are the $tW$ rate at the Tevatron, where no corresponding NLO result is available, and the given value is therefore not matched, and the $t$-channel rate at the LHC, where no soft-gluon corrections are considered and an updated NLO result with the quoted PDFs is given instead. The uncertainties given are derived from varying the scale by a factor of two, and adding in quadrature PDF uncertainties derived using the MRST2001E NLO PDFs [95]. No uncertainty in $m_t$ is included. At the Tevatron, the $t$-channel uncertainty is dominated by the uncertainty in PDFs, and corrections from soft-gluon resummations relative to LO are small ($\approx 5\%$). In contrast, the soft-gluon corrections have a large effect ($> 60\%$) for the $s$-channel at the Tevatron and scale uncertainties dominate over those from PDFs.

At the Tevatron, $t$-channel production dominates the total rate of single top quark production with a contribution of $\approx 65\%$, followed by $s$-channel production at $\approx 30\%$. Associated ($tW$) production at the Tevatron contributes only $\approx 5\%$ to the total rate, and is usually neglected. At the LHC, $t$-channel production again dominates at $\approx 74\%$, followed now by associated production at $\approx 23\%$, while $s$-channel production contributes only $\approx 3\%$ because of the missing contribution from valence antiquarks in the collisions, which will make it difficult to discriminate this channel from background. Despite being an electroweak process, single top production has a cross section of the same order of magnitude as $t\bar{t}$ production (of $\mathcal{O}(40\%)$ of the $t\bar{t}$ rate at both the Tevatron and the LHC). With only one heavy top quark to be produced, single top production is accessible at smaller and therefore better-populated momentum fractions of the partons. Furthermore, no color matching is required for the production. The fact that the observed yields of single-top and $t\bar{t}$-pairs are consistent with theory is a major triumph of the SM.

The measurement of single top production offers a check of the top quark's weak interaction, and direct access to the CKM matrix element $|V_{tb}|$, as the cross sections in all three production modes are proportional to $|V_{tb}|^2$. The polarization of the top quark at production is preserved due to its short lifetime and provides a test of the $V - A$ structure of the weak interaction via angular correlations among the decay products [160–163]. All three production modes provide different sensitivity to various aspects of physics beyond the standard model (BSM) [164], which makes their independent reconstruction a desirable goal. The $s$-channel is sensitive to the existence of new charged bosons (such as $W'$ or charged Higgs) that couple to the top-bottom weak-isospin doublet, an effect that could be detectable through an enhancement of the observed cross section. Such effects would not be observed in the $tW$ mode, where the $W$ boson is on-shell, or in the t-channel, where the virtual $W$ boson is space-like and cannot go on-shell as in the $s$-channel. The $t$-channel production rate could be enhanced via FCNC processes involving new couplings

between the up-type quarks and a boson (Higgs, gluon, photon, $Z$). This would be hard to observe in the $s$-channel, since there is no $b$ quark in the final state, which is essential for discrimination of the signal in that production mode. Finally, the $tW$ channel is the only mode that provides a more direct test of the $Wtb$ vertex since the $W$ boson appears in the final state.

A thorough understanding of single top quark production will also facilitate the study of processes exhibiting a similar signature such as SM $W$-Higgs production or BSM signals to which single top production is a background process. Despite a production rate similar to that of $t\bar{t}$, the signature for single top quark production is much harder to separate from background, which has delayed first measurements until very recently. The current analyses at the Tevatron provide first evidence for production of single top quarks, and this will be described in Section 5.8.

### 3.3. *Top quark decay*

3.3.1. *Top quark CKM matrix elements*

Since the mass of the top quark is larger than that of the $W$ boson, decays $t \rightarrow Wq$, with $q$ being one of the down-type quarks $d, s, b$, are dominant. The contribution of each quark flavor to the total decay width is proportional to the square of the respective CKM matrix element $V_{tq}$. Utilizing the unitarity of the CKM matrix and assuming three quark generations, the corresponding matrix elements can be constrained indirectly at 90% confidence level to [165]:

$$|V_{td}| = 0.0048 - 0.014 \tag{9}$$

$$|V_{ts}| = 0.037 - 0.043 \tag{10}$$

$$|V_{tb}| = 0.9990 - 0.9992. \tag{11}$$

Consequently, the decay $t \rightarrow Wb$ is absolutely dominant and will be considered exclusively throughout this article, unless noted to the contrary. Potential deviations from the SM decay will be discussed in Section 6.

It should be noted that the above constraints on the CKM matrix elements would change dramatically (especially $V_{tb}$) if there were more than three quark generations. Assuming the unitarity of the expanded matrix, the limits become [165]:

$$|V_{td}| = 0 - 0.08 \tag{12}$$

$$|V_{ts}| = 0 - 0.11 \tag{13}$$

$$|V_{tb}| = 0.07 - 0.9993. \tag{14}$$

It is therefore important to constrain these matrix elements through direct measurements, as outlined below.

The $V_{td}$ and $V_{ts}$ matrix elements cannot be extracted from lowest-order (tree level) top decays in the framework of the standard model, but can be inferred from B-meson mixing, as shown in Fig. 9. While all up-type quarks can contribute in the depicted box diagrams, the contribution from the top quark is dominant [166]. The
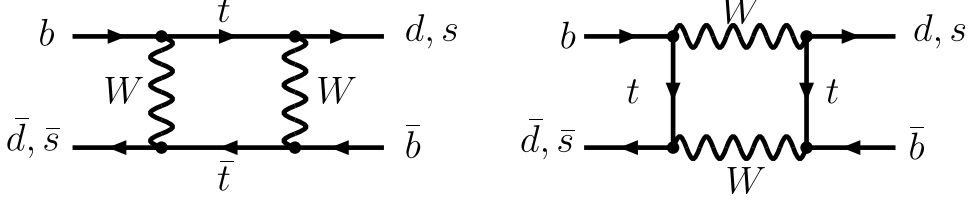
Fig. 9: Feynman "box" diagrams for $B_d^0 - \overline{B_d^0}$ and $B_s^0 - \overline{B_s^0}$ mixing.

oscillation frequency given by the mass difference between heavy and light mass eigenstates, $\Delta m_d$ for $B_d^0 - \overline{B_d^0}$ and $\Delta m_s$ for $B_s^0 - \overline{B_s^0}$ oscillations, is proportional to the combination of CKM matrix elements $|V_{tb}^* V_{td}|^2$ and $|V_{tb}^* V_{ts}|^2$, respectively. The mass difference for the $B_d^0 - \overline{B_d^0}$ system is $\Delta m_d = 0.507 \pm 0.004$ ps$^{-1}$ [167]. Using CKM unitarity and assuming three generations, yielding $|V_{tb}| \approx 1$, translates into $V_{td} = (7.4 \pm 0.8) \cdot 10^{-3}$ [168], where the uncertainty arises primarily from the theoretical uncertainty on the hadronic matrix element, which is obtained from lattice QCD calculations. To reduce these theoretical uncertainties, a measurement of the ratio, in which some uncertainties cancel, is more desirable ($\Delta m_d / \Delta m_s \propto |V_{td}|^2 / |V_{ts}|^2$). With the recent first measurement of $\Delta m_s$ in $B_s^0$-oscillations by D0 and CDF at the Tevatron [169,170], yielding 17 ps$^{-1} < \Delta m_s < 21$ ps$^{-1}$ at 90% C.L. and $\Delta m_s = (17.31_{-0.18}^{+0.33}(\text{stat.}) \pm 0.07(\text{syst.}))$ ps$^{-1}$, this ratio has now been measured for the first time as $|V_{td}/V_{ts}| = 0.208_{-0.002}^{+0.001}(\text{expt.})_{-0.006}^{+0.008}(\text{theor.})$. These results are in good agreement with SM expectations.

The direct measurement of the $V_{tb}$ matrix element without assuming three quark generations and unitarity of the CKM matrix is only possible via single top quark production (described in Section 3.2), because the production rate in each channel is proportional to $|V_{tb}|^2$. One way to assess the *relative* size of $|V_{tb}|$ compared to $|V_{td}|$ and $|V_{ts}|$ is to measure the ratio $R$ of the top quark branching fractions, which can be expressed via CKM matrix elements as

$$R = \frac{\mathcal{B}(t \to Wb)}{\mathcal{B}(t \to Wq)} = \frac{|V_{tb}|^2}{|V_{tb}|^2 + |V_{ts}|^2 + |V_{td}|^2} \ . \tag{15}$$

Assuming three generation unitarity, the denominator in the above expression equals one, and constraints on $|V_{tb}|$ can be inferred. The current status of these measurements is discussed in Section 6.2.

The most precise extraction of the top quark CKM matrix elements proceeds via global fits to all available measurements, imposing the SM constraints of three generation unitarity, as done by the CKMfitter [171] or UTfit [172] groups. The CKMfitter update for summer 2008 yields [171]:

$$|V_{td}| = 0.00853_{-0.00027}^{+0.00034} \tag{16}$$

$$|V_{ts}| = 0.04043_{-0.00116}^{+0.00038} \tag{17}$$

$$|V_{tb}| = 0.999146_{-0.000016}^{+0.000047}. \tag{18}$$

3.3.2. *Decay width of the top quark*

The decay width of the top quark in the SM, including first-order QCD corrections, can be expressed as follows [173, 174]:

$$\Gamma_t = |V_{tb}|^2 \frac{G_F\, m_t^3}{8\pi\sqrt{2}} \left(1 - \frac{m_W^2}{m_t^2}\right)^2 \left(1 + 2\frac{m_W^2}{m_t^2}\right) \left[1 - \frac{2\alpha_s}{3\pi}\left(\frac{2\pi^2}{3} - \frac{5}{2}\right)\right], \qquad (19)$$

where the above formula assumes $m_b^2/m_t^2 \to 0$, $m_t^2 \gg m_W^2$ and ignores corrections of $\mathcal{O}(\frac{\alpha_s}{\pi}\frac{m_W^2}{m_t^2})$ and $\mathcal{O}(\alpha_s^2)$. While the above QCD corrections lower the width by $\approx 10\%$, first-order electroweak corrections increase the width by 1.7% [175, 176]. However, the electroweak correction is almost cancelled when the finite width of the $W$ boson is taken into account, thereby decreasing the width again by 1.5% [177, 178]. Corrections to the top quark width of $\mathcal{O}(\alpha_s^2)$ have also been evaluated [179, 180] and reduce the width by 2%. Including all these effects, the decay width is predicted to a precision of $\approx 1\%$. The other SM decays, $t \to Wd$ and $t \to Ws$, contribute negligibly to the total decay width $\Gamma_t = \Sigma_q \Gamma_{tq}$ because of proportionality to $|V_{td}|^2$ and $|V_{ts}|^2$.

Equation 19 yields the top width to better than 2% accuracy, and the width increases with $m_t$. For $\alpha_s(m_Z) = 0.1176$ and $G_F = 1.16637 \cdot 10^{-5}(\text{GeV}/\text{c}^2)^{-2}$ [47], $\Gamma_t$ is 1.02/1.26/1.54 GeV for top quark masses of 160/170/180 GeV/c$^2$.

The resulting lifetime of the top quark $\tau_t = \hbar\Gamma_t^{-1} \approx \hbar(1.3\text{ GeV})^{-1}$ is approximately $5 \cdot 10^{-25}$ s, and significantly shorter than the hadronization time $\tau_{\text{had}} \approx \hbar\Lambda_{\text{QCD}}^{-1} \approx \hbar(0.2\text{ GeV})^{-1} \approx 3 \cdot 10^{-24}$ s. As a consequence, the top quark decays before it can form hadrons, and in particular there can be no $t\bar{t}$ bound states (toponium), as was already pointed out in the 1980s [13, 181, 182]. Nevertheless, although the top quark can generally be considered as a free quark, residual non-perturbative effects associated with hadronization should still be present in top quark events, and the fragmentation and hadronization processes will be influenced by the color structure of the hard interaction.

In electron-positron annihilation, top quark pairs are produced in color singlet states, so that hadronization before decay depends mainly on the mass of the top quark and collision energy. In hadronic $t\bar{t}$ production, $t$ and $\bar{t}$ are usually produced in color octet states and form color singlets with the proton and antiproton remnants. The energy in the color field (or in the string when using the picture of string fragmentation) is proportional to the distance between top quark and the remnant. If a characteristic length of about 1 fm is reached before the top quark decays, light hadrons can materialize out of the string's energy. The possibility for such string fragmentation depends strongly on the center of mass energy in the hadron collisions. For Tevatron energies, this can be neglected [183], while it may be more important at LHC energies, where top quarks are produced with sizeable Lorentz boosts. Since heavy quarks have hard fragmentation functions and the fractional energy loss of the top quarks is therefore expected to be small, it will be difficult to experimentally establish these effects directly, even at the LHC. In case no string
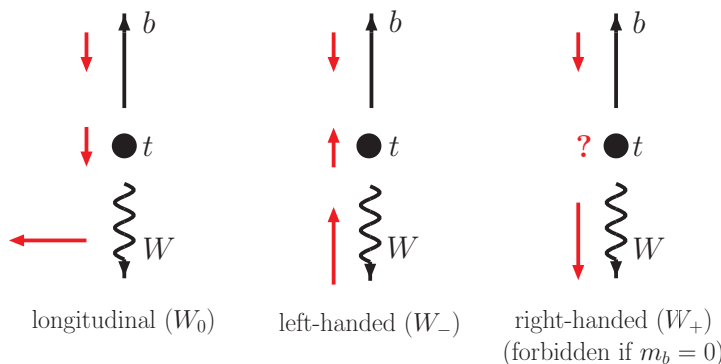
longitudinal ($W_0$)    left-handed ($W_-$)    right-handed ($W_+$)
(forbidden if $m_b = 0$)

Fig. 10: Angular momentum conservation in top quark decay does not allow right-handed $W$ bosons when $b$ quarks are assumed massless.

fragmentation takes place before the top quark decays, long-distance QCD effects will still connect the decay products of the top quark.

With top quark mass measurements aiming at uncertainties of $\leq 1$ GeV/c$^2$, it becomes more and more important to assess the impact of such non-perturbative effects on the measurements. One example that may play an important role in this context is the possibility of color reconnections before hadronization, and the corresponding modeling of the underlying event (beam-remnant interactions) [184, 185].

### 3.3.3. *Helicity of the W boson*

Top quark decay in the framework of the standard model proceeds via the left-handed charged current weak interaction, exhibiting a vector minus axial vector $(V - A)$ structure. This is reflected in the observed helicity states of the $W$ boson, which can be exploited to examine the couplings at the $Wtb$ vertex [186–188].

The emitted $b$ quark can be regarded as massless compared to the top quark, and hence expected to be predominantly of negative helicity (left-handed), meaning that its spin points opposite to its line of flight. The emitted $W$ boson, being a massive spin-1 particle, can assume any of three helicities: one longitudinal ($W_0$) and two transverse states ($W_-$, left-handed and $W_+$, right-handed). To conserve angular momentum in the $t \rightarrow Wb$ decay, the spin projection of the $W$ boson onto its momentum must vanish if the $b$ quark's spin points along the spin of the top quark, while a left-handed $W$ boson is needed if the $b$ quark's spin points opposite to the spin of the top quark. In the limit of a massless $b$ quark, a right-handed $W$ boson cannot contribute to the decay, as illustrated in Fig. 10. For the decay of an antitop quark, a left-handed $W$ boson is forbidden.

At lowest "Born"-level, the expected fractions of decays with different $W$ boson

helicities, taking the finite $b$ quark mass into account, are given by [189]:

$$f_0 = \Gamma_0/\Gamma_t = \frac{(1 - y^2)^2 - x^2(1 + y^2)}{(1 - y^2)^2 + x^2(1 - 2x^2 + y^2)} \approx \frac{1}{1 + 2x^2} \tag{20}$$

$$f_- = \Gamma_-/\Gamma_t = \frac{x^2(1 - x^2 + y^2 + \sqrt{\lambda})}{(1 - y^2)^2 + x^2(1 - 2x^2 + y^2)} \approx \frac{2x^2}{1 + 2x^2} \tag{21}$$

$$f_+ = \Gamma_+/\Gamma_t = \frac{x^2(1 - x^2 + y^2 - \sqrt{\lambda})}{(1 - y^2)^2 + x^2(1 - 2x^2 + y^2)} \approx y^2 \frac{2x^2}{(1 - x^2)^2(1 + 2x^2)} \tag{22}$$

where the scaled masses $x = m_W/m_t$, $y = m_b/m_t$ and the "Källén"-type function $\lambda = 1 + x^4 + y^4 - 2x^2y^2 - 2x^2 - 2y^2$ were used. Inserting $m_t = 175$ GeV/c$^2$, $m_W = 80.419$ GeV/c$^2$, and a pole mass of $m_b = 4.8$ GeV/c$^2$, the partial helicity rates are found to be [189]:

$$f_0 = 0.703, \; f_- = 0.297, \; f_+ = 0.00036. \tag{23}$$

$m_b \neq 0$ results in a reduction of $f_0$ and $f_-$ at the per mill level. Including one-loop QCD corrections [189], electroweak one-loop corrections and finite width corrections [190] leads basically to a cancellation of the last two corrections, as was already mentioned in Section 3.3.2, and a change in partial helicity rates $f_0$ and $f_-$ at the 1-2% level. The right-handed helicity fraction $f_+$ remains at the per mill level with these corrections included. Consequently, any observation of $f_+$ at the percent level would signal the presence of physics beyond the standard model.

Using a more general extension to the standard model $Wtb$ interaction Lagrangian, assuming that both the $W$ boson and $b$ quark are on-shell, leads to [186]:

$$\mathcal{L} = \frac{g}{\sqrt{2}} \left[ W_\mu^- \bar{b} \gamma^\mu \left( f_1^L P_L + f_1^R P_R \right) t - \frac{1}{m_W} \partial_\nu W_\mu^- \bar{b} \sigma^{\mu\nu} \left( f_2^L P_L + f_2^R P_R \right) t \right] + h.c. \tag{24}$$

where $P_{R(L)}$ are the right- and left-handed chiral projectors $P_{R(L)} = \frac{1}{2}(1 \pm \gamma^5)$ and $i\sigma^{\mu\nu} = -\frac{1}{2}[\gamma^\mu, \gamma^\nu]$. This model-independent extension has four form factors $f_{1/2}^{R/L}$, and includes the standard model as a special case, with $f_1^L = 1$ (left-handed vector coupling) and the other form factors (right-handed vector, and left- and right-handed tensor couplings) vanishing. These four general couplings for the $Wtb$ vertex can be determined by measuring four observables sensitive to this interaction: the $W$ helicity fractions $f_0$ and $f_+$ in $t\bar{t}$ events, and the single-top production cross sections in the $s$- and $t$-channel. This model-independent determination of the parameters of the $Wtb$ vertex can in turn be used to distinguish between different models proposed for EWSB [191].

## 4. Experimental Setup

This section describes the experimental ingredients that are needed to study top quarks. Since this review focusses mainly on results obtained at Run II of the Tevatron, only the corresponding accelerator and detector setups are discussed. The experimental setup for Run I can be found, for example, in Ref. [192].
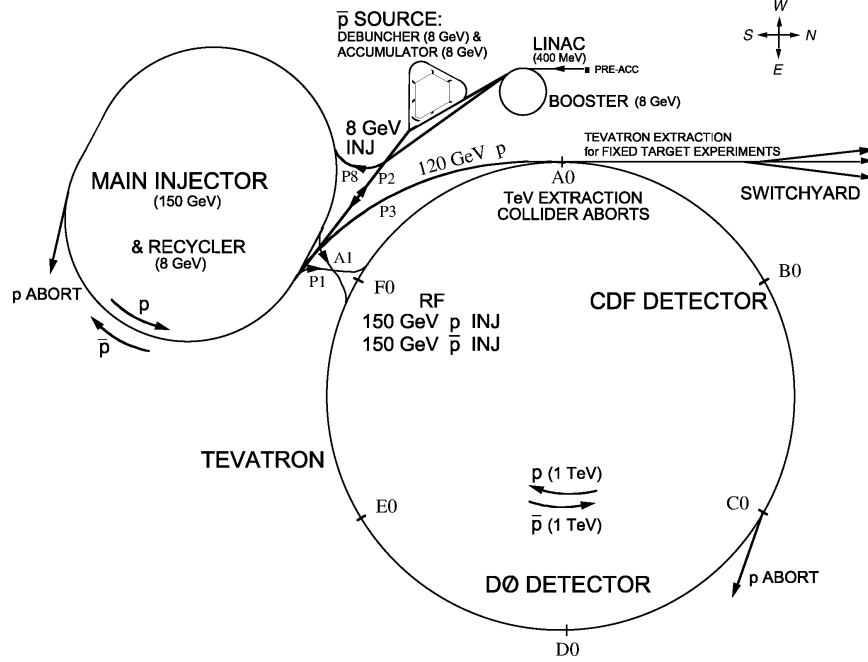
Fig. 11: The Fermilab Run II accelerator complex consisting of the Tevatron $p\bar{p}$ collider and its pre-accelerators [193, 196].

The Tevatron collider is discussed in the first part of this chapter, followed by a description of the two general-purpose detectors CDF and D0 surrounding the two interaction points where protons and antiprotons are brought to collision. Subsequently, the reconstruction and identification of particles produced in the collisions are briefly reviewed before the resulting experimental signatures of top quark events are described. Finally, the Monte Carlo (MC) simulation tools needed to model interactions in the detectors are considered.

### 4.1. *The Tevatron collider*

The Tevatron collider is part of the Fermi National Accelerator Laboratory (Fermilab, FNAL) in Batavia, Illinois, close to Chicago. Until the Large Hadron Collider at CERN starts operation, the Tevatron remains the particle accelerator with the highest center of mass energy worldwide. Here, 36 bunches of protons and antiprotons with a spacing of 396 ns are brought to collision at $\sqrt{s} = 1.96$ TeV at the two interaction points where the multi-purpose detectors CDF and D0 reside. As illustrated in Fig. 11, the Tevatron is the final stage in a chain of eight pre-accelerators and storage rings [193–196].

Beam protons are generated using a magnetron surface plasma source that produces $H^-$ ions from hydrogen gas [197]. The $H^-$ ions are then accelerated to 750 keV

in a Cockcroft-Walton electrostatic accelerator, followed by a linear accelerator, bringing the ions to 400 MeV. Using a carbon stripping foil, both electrons are removed from the $H^-$ ions, and the resulting protons are then accelerated to 8 GeV within 33 ms in the first of five synchrotrons, called the "Booster", which has a ring circumference of 475 m. All these components are often referred to as the "Proton Source".

Acceleration continues in the oval Main Injector synchrotron that has a circumference of 3.3 km. Depending on their ultimate use, protons are either brought from 8 GeV to 120 GeV within 2 s for fixed-target operation (including the production of antiprotons) or to 150 GeV within 3 s for injection into the Tevatron. With a ring radius of 1 km, the Tevatron is the final and largest synchrotron at Fermilab. It accelerates protons and antiprotons in a single beam pipe from 150 GeV to 980 GeV in about 85 s.

For the production of antiprotons, 120 GeV protons from the Main Injector are directed every two seconds at a Nickel target, producing one 8 GeV antiproton for every $\mathcal{O}(50,000)$ incident protons, in total $\mathcal{O}(10^8)$ per pulse. These antiprotons are focused into a beamline using a Lithium lens and separated from the other produced particles with a pulsed dipole magnet used as a charge-mass spectrometer. Once transferred to the "Debuncher" ring, the large momentum spread of the antiprotons is reduced using radio-frequency bunch rotation [198] and stochastic cooling [199], before the beam is passed to the "Accumulator" ring, where the antiprotons are collected ("stacked") and cooled further. For collider operation, approximately 30,000 such cycles are needed. The Debuncher and Accumulator are both 8 GeV rounded, triangle-shaped, concentric synchrotrons with circumferences of 505 m and 474 m, respectively, and together with the target station are referred to as the "Antiproton Source".

To operate at optimal stacking rates, antiprotons are transferred every few hours from the Accumulator to the "Recycler" (an 8 GeV storage ring housed in the Main Injector tunnel), providing both stochastic and electron cooling [200] and thereby improved beam quality. As the name implies, the Recycler was originally planned to reuse antiprotons from the Tevatron, but this was abandoned in favor of large stashes ($6 \cdot 10^{12}$) of antiprotons of high beam quality [201]. The 8 GeV antiprotons from either Accumulator or Recycler are accelerated in the Main Injector to 150 GeV for injection into the Tevatron, where they together with the protons are ramped up to 980 GeV for collisions. The bunch spacing of 396 ns corresponds to a collision rate of 2.5 MHz. With 36 out of 53 bunches being filled, the average rate is reduced to 1.7 MHz.

A typical store at the Tevatron contains about $9 \cdot 10^{10}$ antiprotons and $26 \cdot 10^{10}$ protons per bunch. Characteristic r.m.s. bunch dimensions are 45 cm (50 cm) in the longitudinal and 16 $\mu$m (28 $\mu$m) in the transverse direction for antiprotons (protons) [29], respectively. A store lasts typically 16 to 24 hours for data taking (governed by the remaining instantaneous luminosity versus the one achievable with a new store) before the beam is dumped and the Tevatron refilled (within two
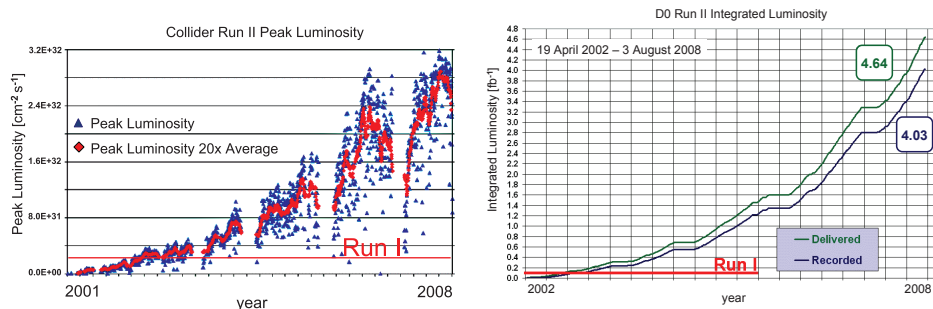
Fig. 12: Left: Peak luminosities achieved at Run II Tevatron versus time [202]. Right: Integrated luminosity delivered by the Tevatron and recorded by the D0 experiment in Run II versus time [203].

to three hours). The increased antiproton stacking rates achieved recently provide shorter overall turnaround times and store durations while raising initial luminosities, thereby enabling the maximization of the delivered luminosity per time period.

The Tevatron is performing well and keeps setting new world records on peak luminosity at a hadron collider. As of July 2008, the record is $3.2 \cdot 10^{32}$ cm$^{-2}$s$^{-1}$ [196]. For comparison, during Run I, from 1992 to 1996 at a center of mass energy of 1.8 TeV, the record peak luminosity was $0.2 \cdot 10^{32}$ cm$^{-2}$s$^{-1}$, and both experiments recorded an integrated luminosity of $\approx$0.1 fb$^{-1}$, respectively. As illustrated in Fig. 12, since the beginning of Run II in 2001, each experiment has recorded more than 4 fb$^{-1}$, and up to half of the total Run I luminosity is now collected by the experiments in one single week. The analyses discussed in this review utilize datasets up to an integrated luminosity of 2.8 fb$^{-1}$.

Until the currently scheduled end of Run II in October 2009, the Tevatron is expected to deliver more than 6 fb$^{-1}$ to each experiment, with possible improvements on that value crucially dependent on the achievable antiproton stacking rates [195]. An extension of Tevatron running into 2010 is currently being discussed and could increase the integrated luminosity by an additional 2 fb$^{-1}$.

### 4.2. *The collider experiments*

Both general-purpose detectors CDF and D0 follow the generic layout of a collider detector in having their subdetectors arranged symmetrically in layers around the interaction point and beam pipe (see Fig. 13). The inner detectors are arranged in concentric cylindrical layers, with charged-particle tracking systems of low mass surrounded by solenoidal magnets defining the core. These are enclosed by electromagnetic and hadronic calorimeters that provide energy measurements and identification of electrons, photons and hadrons. The outer systems are dedicated to muon detection, relying on the penetration capabilities of muons past all inner detectors.

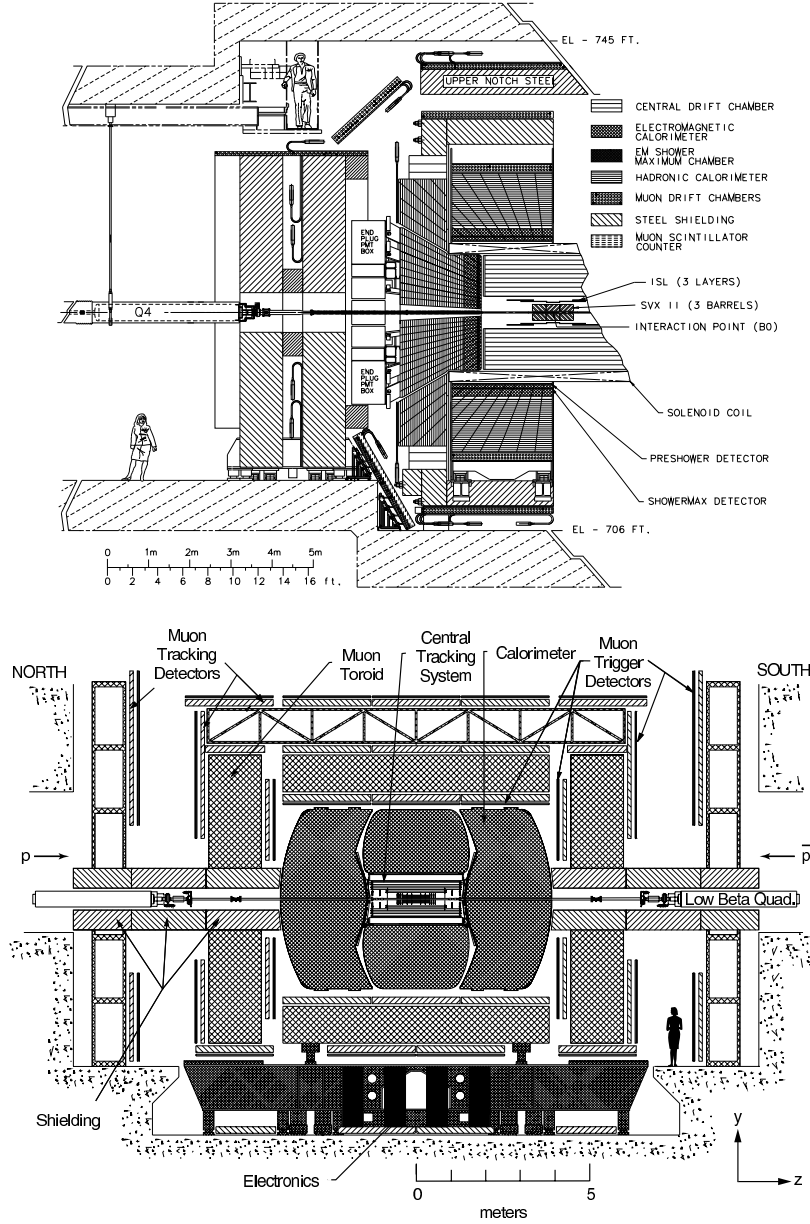Both detectors use a right-handed coordinate system with the origin at the center

Fig. 13: Cross section views of the CDF detector (top, [204]) and the D0 detector (bottom, [205]).

of the detector and the $z$-axis pointing along the direction of the proton beam. The transverse plane is spanned by the $y$-axis, which points vertically upwards, and the $x$-axis that points away from the center of the Tevatron. Positions in the

transverse plane are frequently described using the azimuthal angle $\phi$ with respect to the $x$-axis, $\phi = \arctan\frac{y}{x}$, and radius $r = \sqrt{x^2 + y^2}$. Based on the polar angle $\theta$ relative to the $z$-axis, the pseudo-rapidity $\eta$ is defined as $\eta = -\ln(\tan\frac{\theta}{2})$. For massless particles (or in the ultra-relativistic case where masses can be neglected), the pseudo-rapidity is equivalent to the rapidity $y = \frac{1}{2}\ln[(E + p_z)/(E - p_z)]$, which is additive under parallel Lorentz transformations, resulting in Lorentz-invariant rapidity differences $\Delta y$. The distance of two objects in the $\eta - \phi$ plane is usually denoted as $\Delta R = \sqrt{\Delta\eta^2 + \Delta\phi^2}$. To differentiate between variables calculated with respect to $p\bar{p}$ collision point and the center of the detector, the latter is often denoted with a subscript "det" to indicate origin of the detector coordinate system. In this review, unless indicated to the contrary, $\eta$ is used to refer to $\eta_{\mathrm{det}}$.

Enclosing the luminous region which exhibits a Gaussian width of approximately 25 cm, both CDF and D0 have their innermost silicon microstrip trackers. These provide vertexing and tracking capabilities extending to pseudo-rapidities of $|\eta| \leq 2$ and $|\eta| \leq 3$ for CDF and D0, respectively. CDF complements its tracking system with a cylindrical open-cell drift chamber that provides 96 track measurements for $|\eta| \leq 1$, while D0 utilizes a scintillating-fiber tracker consisting of eight cylindrical layers with two overlapping 835 $\mu$m diameter fiber doublets each, providing coverage for $|\eta| \lesssim 1.7$. Both tracking systems are enclosed by superconducting solenoidal magnets that provide magnetic fields of 1.4 T (CDF) and 1.9 T (D0) along the beamline for measuring transverse momenta ($p_T$) of charged particles.

Supplemental particle identification systems are placed inside and also outside of the magnet for the CDF and D0 detectors. Within the magnet, CDF employs a Time-of-Flight detector based on plastic scintillator panels covering $|\eta| \lesssim 1$, mainly to discriminate low-energetic ($p < 1.6$ GeV/c) charged pions from kaons (for tagging heavy-flavor). Outside of the magnet, CDF uses scintillator tiles for early sampling of electromagnetic showers to improve electron and photon identification in the central detector. D0 uses central ($|\eta| \leq 1.3$) and forward ($1.5 \leq |\eta| \leq 2.5$) preshower detectors consisting of several layers of plastic scintillator strips to enhance electron and photon identification.

Sampling calorimeters with an inner electromagnetic and an outer hadronic section enclose all inner subdetectors, providing energy measurement and identification capabilities for photons, charged leptons and hadrons. CDF uses lead/iron-scintillator sampling devices covering pseudo-rapidities $|\eta| \lesssim 3.6$, while D0 uses mainly depleted uranium ($U^{238}$) as absorber material and liquid argon as active medium for nearly compensating calorimetry within $|\eta| \lesssim 4.2$. Between the central and endcap calorimeter-cryostats ($1.1 \leq |\eta| \leq 1.4$), layers of scintillating tiles provide additional sampling of showers for D0.

The outermost subdetectors serve to identify muons. These devices are based on the fact that muons rarely interact or radiate, but rather traverse the calorimeter as minimum ionizing particles that rarely generate electromagnetic or hadronic showers. CDF and D0 employ scintillators and drift tubes for muon detection within $|\eta| \leq 1.5$ and $|\eta| \leq 2$, respectively. D0 has in addition 1.8 T solid-iron toroidal

magnets between the detection layers to provide stand-alone measurements of muon momentum that are independent of the central tracking system.

The luminosity for CDF and D0 is measured, respectively, using Cherenkov and plastic scintillation counters covering $3.6 \leq |\eta| \leq 4.6$ and $2.7 \leq |\eta| \leq 4.4$, respectively. To select events of interest from the effective 1.7 MHz bunch-crossing rate, both experiments employ three-level trigger systems of dedicated hardware at the initial levels and commercial processor farms at the later (higher) levels. Based on information from tracking, calorimetry and muon systems, events are recorded at a rate of approximately 100 Hz for storage and further processing.

More detailed descriptions of the CDF and D0 detectors can be found in Refs. [204, 206, 207] and [205], respectively.

### 4.3.  *Object reconstruction*

To analyze top quark events and to study properties of the top quark, the fundamental objects resulting from top quark decays must first be reconstructed. This section gives a brief overview of the objects to be considered, and how they can be reconstructed in the detectors. More information on such reconstruction, specific to the CDF and D0 experiments, can be found, for example, in Refs. [22, 208]. As will become clear, analyses of the top quark utilize all detector components and therefore need a thorough understanding of their performance and calibration.

#### 4.3.1.  *Primary vertices*

The point of the primary hard scatter is referred to as the primary vertex and is determined through a fit of well-measured emerging tracks and beamline constraints to a common origin. With increasing luminosity, the average number of interactions per bunch crossing increases as well, leading to the reconstruction of multiple primary-vertex candidates, only one of which will generally be compatible with the hard interaction of interest. The selection of the primary vertex can be based, for example, on the presence of an energetic lepton, the (maximal) scalar sum of $p_T$ of associated tracks, or the (lowest) compatibility with being a "minimum-bias" interaction, based on track $p_T$ templates [22, 207].

The primary vertex is the origin of all objects produced in the interaction, including those from top quark and their subsequent $W$ boson decays, both of which cannot be separated from the primary vertex within the detector resolution due to the extremely short lifetimes (see also Section 7.2). The primary vertex is also used as the origin of coordinates for evaluating kinematic variables of the $p\bar{p}$ collision.

#### 4.3.2.  *Charged leptons*

Leptonically decaying $W$ bosons are a source of isolated energetic charged leptons that can be measured well with the tracking, calorimeter and muon systems de-

scribed in the previous section. Such leptons are part of the event signatures for several top quark decay modes (see Section 4.4) and key in selecting these events at the trigger stage. However, $\tau$ leptons play a special role due to their decay characteristics. They decay leptonically 35% of the time, yielding electrons or muons (and two neutrinos) that on average have far lower momenta than $e$ or $\mu$ from direct $W \to \ell\nu$ decay, but are otherwise hard to distinguish due to the relatively short $\tau$ lifetime. Consequently, such decays are usually included in the event selections for electrons and muons which are then referred to as "leptonic" final states of the $W$ boson. Decays of $\tau$ into hadrons (and a neutrino) are treated separately and are discussed further below.

In the context of this review, the term "leptons" refers only to electrons and muons, unless specified to the contrary. Their reconstruction proceeds as follows:

- **Electrons** leave a track in the inner tracking system and form showers, mainly in the electromagnetic part of the calorimeter. These are reconstructed as clusters of energy deposition in the electromagnetic calorimeter and matched to reconstructed tracks. Further requirements include selections based on the fraction of energy deposited in the electromagnetic calorimeter, isolation from other energy depositions in a cone defined by the electron candidate, the transverse and longitudinal distribution of the shower, and the $E/p$ ratio of cluster energy and the reconstructed track momentum.
- **Muons** are identified via their characteristic penetration and minimum ionization along their path in the calorimeter. They are reconstructed by matching central tracks to track segments in the outer muon system and must be consistent with originating from a primary vertex. Cosmic-ray muons are suppressed via timing requirements. Isolation of muon trajectories can be imposed both on the charged-track candidate and within the calorimeter.

The misidentification of isolated leptons has different origins for electrons and muons. Assuming contributions from hadrons "punching through" the calorimeter are negligible, false isolated muons arise mainly from muons emitted in semileptonic decays of heavy quarks where an associated jet (see below) is not reconstructed or the muon emerges outside of the cone of the jet. While such semileptonic heavy-flavor decays also contribute false isolated electrons, significant contributions arise here as well, for example, from jets with large electromagnetic fractions that can mimic electrons, photon conversions to $e^+e^-$, or photons that overlap a random track. Such instrumental background processes are usually estimated from data, as realistic simulation of these effects is quite difficult.

The energy scale and resolution for leptons can be assessed by studying the reconstructed mass of the $Z$ boson in $Z \to \ell\ell$ events. $Z$ boson decays are also useful for studying lepton identification efficiencies with the "tag and probe" method in which one lepton is required to be well-identified (the "tag"), thereby providing a reasonably pure sample of $Z$ bosons, while the second lepton serves as a probe for the efficiency being studied.
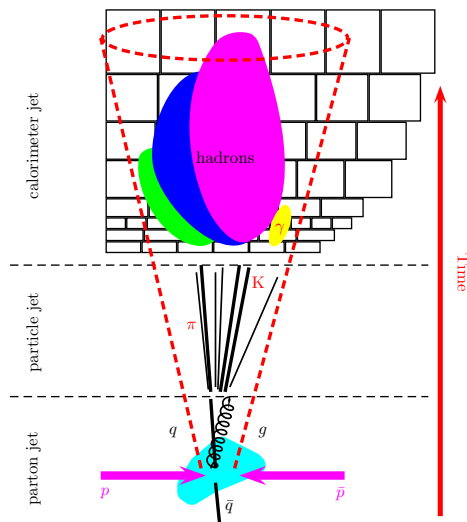
Fig. 14: Illustration of the evolution of a calorimeter jet from an initial parton [209].
The dashed lines represent the jet cone.

### 4.3.3. *Quark and gluon jets*

The hadronization of quarks and gluons leads to collimated showers of hadrons,
referred to as "jets". The jet axis is highly correlated with the original parton's
direction. While it is not possible to differentiate between quark and gluon jets on
a per-object basis, they can be distinguished on a statistical basis because of small
differences in shower shape (gluon jets tend to be wider and contain more "soft"
particles).

Jets are reconstructed from their energy depositions in the cells of the calorimeter
using cone algorithms [210, 211] that combine cell energies within a cone of fixed
radius $\Delta R$ (see Fig. 14). The size of the cone radius is a compromise between
collecting a high fraction of the original parton's energy and resolving the energy
depositions of close-by partons, especially in busy $t\bar{t}$ events. D0 uses a cone size of
$\Delta R = 0.5$, while CDF uses $\Delta R = 0.4$.

The measured jet energies are converted into particle-level energies through jet
energy scale (JES) corrections [212, 213] that take into account effects such as the
presence of energy depositions not originating from the hard scattering process
(noise in the calorimeter, multiple interactions, . . . ), particles within the jet cone
that deposit energy in the calorimeter but outside of the cone or vice versa, due to
their curved trajectories in magnetic fields and showering effects, and the calorimeter
response accounting, for example, for nonlinearities or energy loss in uninstrumented
regions of the detector.

The electromagnetic calorimeter scale determined from resonances such as $Z \rightarrow$
$ee$, as described above, can be transferred to the full calorimeter by requiring a

balance in $p_T$ in photon + jet events. The intercalibration of the calorimeter is then complemented with dijet events. A precise JES calibration is a challenging task involving highly complex procedures to ensure understanding of all contributions and their systematic uncertainties. D0 has achieved a JES precision at the 1-2% level over a wide kinematic range [213]. For this level of precision, strictly speaking, the JES is only applicable to photon + jet samples, and additional uncertainties need to be taken into account when transferring the JES, for example, to top quark samples [214]. The first direct measurement of the JES for $b$ quarks at the Tevatron based on $Z \rightarrow bb$ events has recently been performed by CDF, reaching a precision of better than 2% [215].

### 4.3.4. *τ jets*

$\tau$ leptons decay into hadrons (and a neutrino) 65% of the time, with $\approx$77.5% of these decays yielding a single charged particle ("1-prong decays") and $\approx$22.5% three charged particles ("3-prong decays") [29]. These "hadronic" $\tau$ decays are reconstructed as jets (that often also contain $\pi^0$ mesons) and can be discriminated statistically from quark and gluon jets via their narrow shower shape and low track multiplicity within the jet cone [216, 217].

### 4.3.5. *b jets*

The identification ("tagging") of $b$ jets is a very powerful tool for separating the top quark signal from its background processes, which typically exhibit little heavy-flavor content. Also, the combinatorics for reconstructing top quark events from their final-state objects can be reduced using this additional information. There are in general two different approaches to identifying $B$ hadrons formed from $b$ quarks:

- **Lifetime Tagging:** Due to their lifetime of about 1.5 ps and the boost from top quark decay, B hadrons can travel several millimeters before they decay. The resulting charged particle tracks therefore originate from (point to) a vertex different than the primary one. This can be exploited by searching for secondary vertices significantly displaced relative to the primary event vertex (*secondary-vertex tagging*) or by requiring significant impact parameters relative to the primary vertex for tracks, without reconstructing a secondary vertex (*impact-parameter tagging*). A probability can also be calculated for a jet to come from the primary vertex based on the impact parameters of all its associated tracks (*jet-probability tagging*), or a combination of all information from the above tagging algorithms into a neural network response can be used (*NN tagging*). The two latter methods yield continuous output variables that can be used as input for further multivariate analysis or for selecting analysis-specific values as compromises between $b$-tagging efficiency and the fraction of light-quark jets that are misidentified as $b$ jets.

- **Soft-Lepton Tagging:** This tagging is based on semileptonic decays of $b$ and $c$ hadrons with branching fractions of $\approx 11\%$ and $10\%$, respectively. With two $b$ quarks and two $W$ bosons per $t\bar{t}$ decay, and the fact that about one third of the $W$ boson decays yield charm quarks ($c\bar{s}$), the fraction of events containing a soft (low $p_T$) lepton in a jet is about $40\%$ per lepton flavor ($e, \mu$). The isolation criteria used for leptonic $W$ boson decays do not work for these leptons, and their reconstruction within jets is quite challenging, especially for electrons.

Although the mistag rate for lifetime-tagging is usually very small for light-quark ($u, d, s$) and gluon jets, this is not the case for charm jets. For example, a typical operating point for D0's NN tagger yields a $b$-tag efficiency of $\approx 50\%$ and a mistag rate for light jets of $\approx 0.5\%$, while it is $\approx 10\%$ for $c$ jets [214]. More information on $b$-tagging algorithms and their application in top quark analyses, including the performance for $b$ jets, $c$ jets and light-quark or gluon jets, can be found in Refs. [207, 208, 218] for CDF and [22, 214, 219] for D0.

### 4.3.6. *Neutrinos*

Neutrinos are not detected directly because of their negligible interaction cross section. Since the energy component along the beam axis at a hadron collider is unknown, only the transverse momentum carried away by neutrinos (or any other "invisible" particles) can be inferred from momentum conservation in the transverse plane. This "missing" transverse momentum ($\not{p}_T$) is calculated from the vector sum of transverse energy depositions in the calorimeter, corrected for the energy scale of reconstructed electrons and jets and for the momenta of reconstructed muons (corrected for energy loss in the calorimeter). The $\not{p}_T$ resolution therefore depends strongly on the other objects present in the event. Taking this into account, for example, through selections on the significance of $\not{p}_T$ rather than its absolute value, improves performance.

### 4.4. *Top quark event signatures in the standard model*

Having discussed the reconstruction of the fundamental objects from the initially occurring particles, the experimental signatures of top quark events can be examined. As noted in Section 3.3.1, in the framework of the standard model the top quark decays dominantly into a $W$ boson and a $b$ quark. Consequently, the observed final states are defined by the decay modes of the $W$ boson.

W bosons decay into two fermions, either leptons (a charged lepton-neutrino pair $\ell\bar{\nu}_\ell, \ell = e, \mu, \tau$), with equal probability per lepton flavor at lowest order in perturbation theory, or into quark-antiquark pairs $q\bar{q}'$ with $q = u, c$ and $\bar{q}' = \bar{d}, \bar{s}, \bar{b}$. At Born level, the "hadronic" decay widths are enhanced over the leptonic modes by a color factor of three (taking the three possible quark colors into account), and scaled by the appropriate squared CKM matrix element $|V_{qq'}|^2$. Similar to top quark decay, the off-diagonal CKM matrix elements are greatly suppressed,
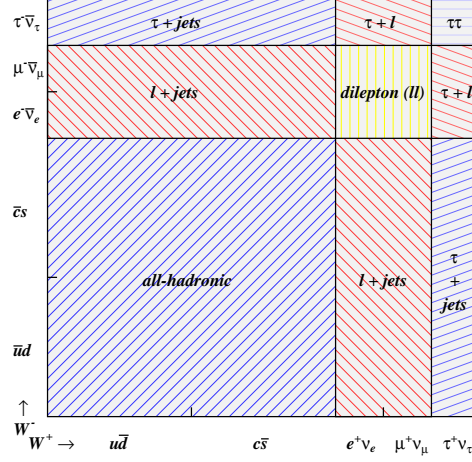
Fig. 15: Illustration of the SM $t\bar{t}$ decay modes and their branching fractions via the possible $W$ boson decays. For each decay mode, a $b\bar{b}$ quark pair from $t\bar{t}$ decay is also present.

and therefore only the $u\bar{d}$ and $c\bar{s}$ decay modes are considered in the following, contributing approximately 95% of the hadronic decay width [29].

In summary, $W$ bosons decay leptonically with a branching fraction of $\approx$1/9 per lepton flavor and $\approx$1/3 for each of the hadronic decays ($u\bar{d}$ and $c\bar{s}$). The resulting possibilities for $t\bar{t}$ decays are illustrated in Fig. 15, where also the nomenclature for the different decay modes is introduced. These branching fractions do not yet take account of the leptonic decays of $\tau$ leptons and their contributions to final states involving electrons and muons, as discussed in Section 4.3. This is considered in the following description of the four basic $t\bar{t}$ event classes:

(i) **Dilepton channels:** Both $W$ bosons decay leptonically ($\ell\bar{\nu}_\ell, \ell = e, \mu$), resulting in a final state comprised of two isolated high-$p_T$ leptons, $\not{p}_T$ corresponding to the two neutrinos, and two $b$ jets. Including leptonic $\tau$ decays, this channel has a branching fraction of approximately 6.5%, shared $\approx$1:1:2 by the $ee$, $\mu\mu$ and $e\mu$ final states. While these channels give samples of highest $t\bar{t}$ signal purity, they suffer from limited statistics due to the small branching fractions.

(ii) **Lepton + jets channels:** One $W$ boson decays leptonically and the other one hadronically, yielding a final state containing one isolated high-$p_T$ lepton, $\not{p}_T$, and four jets. Including leptonic $\tau$ decays, these channels exhibit a branching fraction of approximately 34.3%, shared about equally by the $e$ + jets and $\mu$ + jets final states. These channels represent the best compromise between purity of sample and available statistics.

(iii) **All-hadronic channel:** Both $W$ bosons decay to $q\bar{q}'$ pairs, resulting in a six-jet final state. With a branching fraction of $\approx$45.7%, this channel yields the highest statistics of $t\bar{t}$ events but also suffers from large background from multijet

production.

(iv) **Hadronic $\tau$ channels:** Final states where at least one $W$ boson yields a charged $\tau$ lepton that in turn decays into hadrons (and a neutrino) are called hadronic $\tau$ channels, and together comprise a branching fraction of $\approx$13.5%. The nature of the decay of the second $W$ boson is used to differentiate between the $\tau$ + jets, $\tau$ + lepton, and $\tau\tau$ final states, which contribute with 9.5%, 3.6% and 0.5% branching fractions, respectively. The corresponding experimental signature has four/two/two jets, $\not{p}_T$, one/one/two hadronic $\tau$ final states, and no/one/no isolated high-$p_T$ lepton. The identification of $\tau \rightarrow$ hadrons makes these final states especially challenging to reconstruct. More inclusive sample selections, requiring, for example, leptons and isolated tracks or $\not{p}_T$ and ($b$-tagged) jets provide significant fractions of $\tau \rightarrow$ hadrons events, without their explicit reconstruction.

In all of the above final states, two of the jets are $b$ jets from $t\bar{t}$ decay. The $\tau\tau$ final state of $t\bar{t}$ production remains the only channel that has not yet been explicitly analyzed. All others are discussed in Section 5.1. Properties of top quarks have been extracted mainly from the first three of the above channels, and especially from the lepton + jets channel.

Full kinematic reconstruction of $t\bar{t}$ events is possible in the all-hadronic final state since there are no high-$p_T$ neutrinos present. In the lepton + jets channel, a twofold ambiguity arises from the determination of the neutrino $p_z$ when constraining the invariant mass of the lepton and missing neutrino to $m_W$, while the dilepton channel is kinematically underconstrained because two neutrinos contribute to $\not{p}_T$. The unknown assignment between partons and reconstructed objects in $t\bar{t}$ events leads to various possible combinations. The combinatorics can be reduced through identification of $b$ jets. In particular, when both $b$ jets are identified, only four combinations remain to be considered in the lepton + jets channel (including the neutrino $p_z$ ambiguity), and six combinations in the all-hadronic channel.

The experimental signature for single top quark production is based on the top quark decay mode and the production channel: in the $s$- ($tb$-) channel, the top quark is produced with an additional $b$ jet, while in the $t$- ($tqb$-) channel a forward light-quark jet accompanies top quark production, sometimes along with another $b$ jet from the gluon splitting into $b\bar{b}$ (see Fig. 8). The $W$ boson from top quark decay is usually required to decay leptonically ($\ell\bar{\nu}_\ell, \ell = e, \mu$) so as to suppress multijet background. Consequently, the final state signature of single top quark production contains an energetic isolated electron or muon, $\not{p}_T$ and at least two jets, with at least one of them being a $b$ jet.

The large mass of the top quark makes it less likely that it is produced with large kinetic energy at the Tevatron. Its decay products therefore tend to be emitted at central rapidities, non-planar with good angular separation, and are characterized by a large sum of transverse energies $H_T$. Event selections usually require the channel-characteristic objects (leptons, $\not{p}_T$, and ($b$ tagged) jets) to be present

with energies typically greater than 15 to 20 GeV. Apart from selections on data quality to ensure a well-performing detector and specific trigger selections, a well-reconstructed primary vertex in the central detector region is also required. Variations in observed jet multiplicities are possible as well due to, for example, jet reconstruction thresholds, jet splitting and merging during reconstruction, and additional gluon jets (from initial- and final-state radiation).

More details on event selection, contributions from background, and sample compositions in different analyses (including those concerned with non-standard-model signatures), are given in the following chapters.

### 4.5. *Monte Carlo generation*

A reliable and well-understood Monte Carlo (MC) simulation of signal and background processes is a crucial ingredient for any top quark analysis. MC samples are needed to understand detector response and acceptance, selection efficiencies and kinematic distributions of physical variables and their normalizations. This requires both good modeling of the production process from the parton to the hadron level, and an accurate simulation of detector response to signatures of interest.

MC simulations of hadron interactions are based on the factorization theorem discussed in Section 3.1, splitting up hadron collisions into universal long distance (small $Q^2$) phenomena and perturbatively calculable short distance phenomena. A generic example of steps in the simulation of a hadron collision is illustrated in Fig. 16, and described below.

The non-perturbative Parton Distribution Functions (PDFs) describe the distribution of the proton (or antiproton) momentum among its partons. The interaction of the incoming partons in the hard process of interest is then evaluated based on fixed-order (usually LO) matrix elements, yielding the outgoing partons and their characteristics, such as their momenta and colors. The ensuing parton showering adds higher-order effects through parton splitting into pairs of softer partons (gluon radiation, gluon-splitting, photon radiation,...), until non-perturbative hadronization sets in at low $Q^2$, forming color-neutral hadrons from the colored partons, which is based on phenomenological models. Unstable particles and resonances are then made to decay into the final remnants.

The colored beam-remnants of the proton and antiproton, other soft multi-parton interactions, and color connections to the hard process are added, and all form the "underlying event". Additional soft proton-antiproton collisions from the same colliding bunch (minimum-bias events) have to be superimposed in the MC, and depend on the instantaneous luminosity. Finally, any overlapping interactions from consecutive bunch crossings "leaking" into the current event (pile up) must also be considered.

In principle, different programs and models can be used for every stage in the above process, and the best choice may depend on the process to be studied, which illustrates the complexity of these MC simulations. Also, the parameters in some
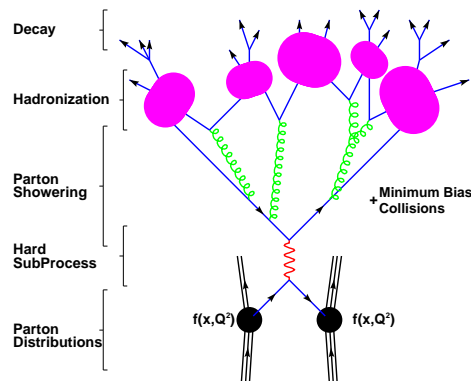
Fig. 16: Illustration of a hadron collision [220], indicating some of the steps involved in MC simulation.

models have to be tuned to distributions in data before they can provide adequate descriptions of interactions [221]. General purpose, complete event generators such as HERWIG [222] and PYTHIA [223] include LO matrix elements for a variety of processes, as well as models for showering and hadronization of partons. They are widely used, either stand-alone or in combination with other generators that simulate the hard process and pass on the information to implement showering and hadronization. An introduction and overview of available MC generators can be found in Ref. [224], and specific simulation tools for top quark production and decay are reviewed in Ref. [225].

CDF and D0 have implemented different simulation chains for their top quark analyses, and certain analyses use variants on what is described here. CDF uses CTEQ5L [157] PDFs for its generators, while D0 employs CTEQ6L1 [94] PDFs. The $t\bar{t}$ signal is generated either with PYTHIA v6.2 [226] (CDF) or ALPGEN v2.1 [227] interfaced with PYTHIA v6.3 [228] for parton showering (D0). The latter employs a jet-parton matching algorithm to avoid double counting of final states that could otherwise be populated from both the hard process and parton showering [229,230]. CDF also uses HERWIG v6.4 [231] for systematic cross checks of modeling of signal. For single top MC, D0 uses SINGLETOP [232] based on COMPHEP [233], interfaced with PYTHIA, while CDF utilizes MADEVENT [234] and MADGRAPH [235], also interfaced with PYTHIA. Both experiments approximate $t$-channel production at NLO through a combination of contributing $2 \rightarrow 2$ and $2 \rightarrow 3$ processes. Any signal cross sections obtained at LO are scaled up to match higher-order theoretical prescriptions (see Sections 3.1 and 3.2). Most analyses use a top quark mass of 175 GeV/c$^2$.

For simulation of $W$+jets and $Z$+jets background processes, both collaborations utilize ALPGEN, interfaced with HERWIG (CDF) or PYTHIA (D0) for parton showering, and both apply the above-mentioned jet-parton matching technique.

ALPGEN generates higher final-state parton multiplicities from $2 \rightarrow n$ processes, and therefore large jet multiplicities, based on exact LO matrix elements, including the production of heavy-flavors, which is especially important for analyses using $b$ tagging. For the decays of $\tau$ leptons, both collaborations use TAUOLA [236, 237]. For $b$ and $c$ hadron decays EvtGen [238] and QQ [239] are used, the latter only by CDF. Effects of additional minimum-bias events and pile up are based on PYTHIA at CDF, and D0 uses zero-bias collider data taken by randomly sampling filled bunch crossings, overlaid with the simulated events.

The generated events are propagated through detector simulation based on GEANT [240], which contains a full description of positions, geometrical shapes, and types and amounts of material comprising the detectors. The particles in an event are tracked through the detector volume, where they encounter energy loss and multiple scattering that depend on particle type, the traversed material and the particle momenta, and undergo decay corresponding to their lifetimes. The response of the detector's readout electronics to these interactions, including noise and inefficiencies, is then obtained in a digitization step that yields initial simulated event characteristics that are processed with the same reconstruction chain as collider data.

It is not easy to obtain good agreement between any simulation and experimental data. For example, object reconstruction, identification and selection efficiencies tend to be higher in MC compared to data, and must be corrected via scale factors. Such scale factors are usually derived from comparison of efficiencies in control samples of simulations and data in final states such as $Z \rightarrow \ell\ell$ for leptons, and $\gamma$+jets for jets. Scale factors can be parametrized in terms of variables sensitive to these corrections. Also, energy scales and resolutions for reconstructed objects must generally be adjusted. Certain effects are hard to simulate, so that at times only data can be used to provide rates for, e.g. jets to mimic lepton signatures.

Before searching for any signal, the background model must be verified using data in control samples that are sufficiently depleted from possible signal, as, for example, by requiring a reduced jet multiplicity or no $b$ jets to be present. Sometimes the shape or normalization of differential distributions has to be corrected, which usually reflects not optimally tuned MC or insufficient precision in the model.

With increasing Tevatron luminosity, data-based constraints can improve the understanding of dominant background processes such as vector boson + (heavy-flavor) jet production, both in terms of shapes and normalization. This can benefit MC simulations and the precision of measurements. For example, the production of $W$ bosons has been investigated in terms of associated jet production [241] and compared with LO and NLO predictions, or associated heavy-flavor production was compared with standard model expectations and found to be in agreement [242, 243]. Nevertheless, dedicated studies of $W$ boson + $c$ [244, 245] or $b$ jet [246, 247] production have been performed as well, with the most recent results indicating that the production rates for these processes are currently underestimated by ALPGEN.

A more detailed overview of MC simulations used in top quark analyses at the

Tevatron, both for signal and background processes, and the remaining challenges can be found in Refs. [248, 249].

## 5. Measurements of Top Quark Production

In this chapter, measurements of top quark production both via the strong and electroweak interactions are described. Observed rates and mechanisms of production are compared with the standard model expectations and used to derive constraints on specific extensions of the standard model impacting the properties under consideration.

### 5.1. *Top quark pair production cross section*

Measurements of the $t\bar{t}$ production cross section are important for several reasons. They provide a powerful test of the predictions of perturbative QCD calculations at high transverse momenta. As shown in Section 3.1, the uncertainties on the $t\bar{t}$ rate predictions have reached the level of $\approx 10\%$, a precision which has already been matched by the measurements performed at the Tevatron.

Deviations from the standard model prediction could arise, for example, from novel production mechanisms such as a new resonant production mode in addition to the standard model one as discussed in Section 5.7. New physics contributing to the electroweak symmetry breaking will probably couple to particles proportional to their mass, making the top quark and its strong coupling reflected in its production rate a highly interesting probe for such effects. Different top quark decay modes, such as the decay via a charged Higgs boson competing with SM decay, as examined in Section 6.5, could cause apparent different production rates amongst the various decay channels via modified branching fractions. Contributions of new physics to the background samples in the various channels could have similar effects. Analyzing different decay channels consequently helps not only to improve statistics and studies of properties of top events, but is also a sensitive probe for physics beyond the standard model.

To extract a cross section requires good understanding of the reconstruction and identification of the involved objects and of the modeling of the contributing background processes. By providing selections for samples enriched in top quark signal and of well characterized composition, cross section analyses form the foundation of all further top quark property analyses.

Top quark pair production has been studied by now in all possible decay modes – the dilepton, lepton + jets, all-hadronic and hadronic $\tau$ channels as defined in Section 4.4, with the $\tau\tau$ decay mode being the only exception due to marginal branching fraction and challenging separation from background processes. As mentioned before, in the context of this review the term leptons refers to electrons and muons alone unless indicated to the contrary.

The event selections usually require the presence of characteristic objects from the top quark decay, namely, leptons, $\not{p}_T$, (heavy-flavor) jets, or hadronically decay-

ing $\tau$, with energies typically exceeding 15 to 20 GeV. Further kinematic characteristics can be exploited to separate the top quark signal from the various background processes. Due to the large mass of the top quark, its decay products tend to be very energetic, emitted at central rapidities and non-planar with good angular separation. In contrast to this, the jet energy spectrum for background processes with jets from gluon radiation is steeply falling. The observed objects are emitted less isotropically but more back to back, and mismeasured objects giving rise to $\not{p}_T$ tend to exhibit characteristic angular correlations with the reconstructed $\not{p}_T$.

Consequently, additional variables available for top quark signal selection are based on the energy present in the event, such as the sum of transverse energies $(H_T)$, or the invariant mass of a combination of reconstructed objects. Event shape variables such as sphericity and aplanarity, derived from the eigenvalues of the normalized momentum tensor of the objects considered [250], or centrality, defined as the ratio of $H_T$ and the sum of the objects' energies, provide additional discrimination. Furthermore, angular relations between reconstructed objects (for example $\Delta\phi(\not{E}_T, \ell)$) and single-object kinematic quantities (such as the jet of highest (leading) transverse momentum) are frequently used as well.

Depending on the $t\bar{t}$ decay mode considered, the use of $b$ tagging in its different forms (see Section 4.3) is optional for the event selection. In the dilepton and lepton + jets channels selections based purely on topological and kinematic characteristics suffice for a good signal to background ratio (S/B). Adding $b$ tagging improves sample purities but also implies a stronger model dependence by relying on $b$ quarks to be present in the final state. The actual extraction of the signal fraction proceeds either in a counting experiment or via template fits using the full shape information of the sensitive variable under consideration. While the latter is usually more sensitive, it also exhibits a stronger dependence on the MC modeling. Using different methods with different systematic uncertainties to measure the same quantity provides a way to assess the model assumptions from different perspectives and to check internal consistency, and is beneficial for combinations of increased precision. Non-overlapping (orthogonal) sample selections facilitate later combinations of results as independent measurements by removing the need to evaluate the correlation amongst the measurements from ensemble tests.

Once the sample composition is measured, the $t\bar{t}$ production cross section is calculated as follows:

$$\sigma_{t\bar{t}} = \frac{N_{\text{observed}} - N_{\text{background}}}{\varepsilon \; \mathcal{B} \; \int \mathcal{L}dt}, \tag{25}$$

where $N_{\text{observed}}$ ($N_{\text{background}}$) is the total (background) number of events, $\varepsilon$ is the $t\bar{t}$ selection efficiency, including detector acceptance, $\mathcal{B}$ is the branching fraction for the $t\bar{t}$ decay mode in question and $\int \mathcal{L}dt$ is the integrated luminosity of the used dataset.

As illustrated in Section 3.1, the $t\bar{t}$ cross section depends on the top quark mass, decreasing by about 0.2 pb for each GeV/c$^2$ increase in the $m_t$ mass range

from 170 GeV/c$^2$ to 180 GeV/c$^2$. The $t\bar{t}$ cross section results given in the following sections generally refer to a top quark mass of 175 GeV/c$^2$; the few cases where a top quark mass of 178 GeV/c$^2$ was assumed will be pointed out explicitly. Especially for the recent measurements, a parametrization of the obtained result versus top quark mass is provided to allow easy projection to the current world-averaged top quark mass. The cross section dependence on the mass can also be turned around to provide a measurement of the top quark mass from the cross section, which will be discussed further in Section 7.3.4.

In the following subsections the published and latest preliminary Run II results will be referenced for the different $t\bar{t}$ decay modes. Some analyses will be highlighted in more detail. The agreement with theoretical predictions is illustrated in the summary section, where results of combinations across channels are also given.

### 5.1.1. *Dilepton final state*

A typical $t\bar{t}$ dilepton event selection requires two isolated high-$p_T$ leptons of opposite charge, $\not{p}_T$ and at least two central energetic jets. The dominant physics background processes exhibiting both real leptons and $\not{p}_T$ arise from diboson ($WW, ZZ, WZ$) production and from $Z/\gamma^*$+jets processes, with $Z/\gamma^* \to \tau^+\tau^-, \tau \to e, \mu$. Misreconstructed $\not{p}_T$ caused by experimental resolution in $Z/\gamma^*$+jets events (with $Z/\gamma^* \to e^+e^-/\mu^+\mu^-$) contributes to the instrumental background, as does $W$+jets and multijet production (often called QCD), where one or more jets mimic the isolated-lepton signature. The physics background processes are usually modeled using Monte Carlo simulation, while instrumental background processes (especially those involving false isolated-lepton signatures) typically are estimated from data. The signal purities of the resulting samples are usually quite good, with a signal to background ratio (S/B) typically better than two.

The sample purity can be further enhanced by means of additional kinematic requirements such as $H_T$ to be above a certain threshold, or by selecting events with at least one identified $b$ jet. However, this reduces the already limited statistics in this channel. To increase the signal acceptance, the reconstruction and isolation requirements on the second lepton can be relaxed. If the second lepton is only required to be reconstructed as an isolated track (termed lepton + track selection), especially 1-prong hadronic $\tau$ decays can then also contribute to the signal.

In a recent preliminary analysis, CDF determines the $t\bar{t}$ cross section from a 2.8 fb$^{-1}$ dataset by requiring two oppositely charged reconstructed isolated leptons with $E_T \geq 20$ GeV, $\not{p}_T \geq 25$ GeV and at least two jets within $|\eta| < 2.5$ and $E_T \geq 15$ GeV, with the leading jet fulfilling $E_T \geq 30$ GeV. The $t\bar{t}$ cross section is extracted from the resulting sample once without any additional cuts and once after increasing the purity by requiring at least one of the jets to be $b$ tagged. The background from $Z/\gamma^*$ and diboson $WW, ZZ, WZ$ events is derived from MC, while false isolated-lepton signatures are estimated from a dilepton dataset where both leptons have the same charge (same sign, "SS"), assuming their contribution
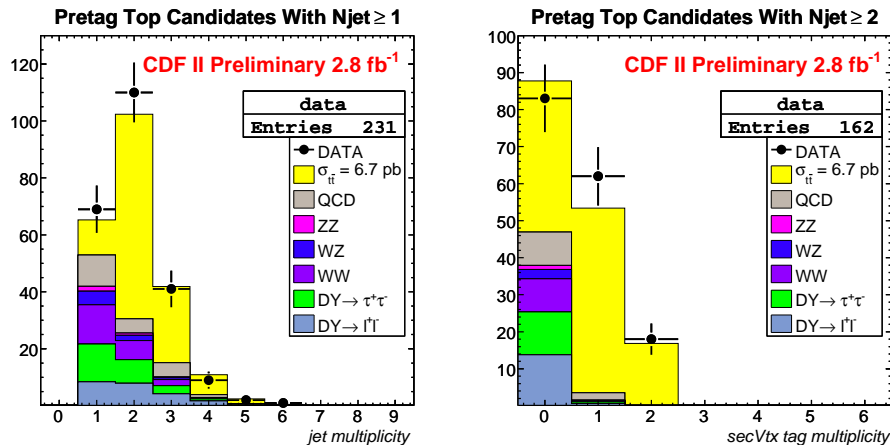
Fig. 17: Distributions in jet multiplicity (left) and number of $b$ tags (right) in $t\bar{t}$ dilepton candidate events, respectively, for $\geq 1$ and $\geq 2$ jets in 2.8 fb$^{-1}$ of data analyzed by CDF [251].

is identical in the opposite sign ("OS") signal selection [251].

The untagged sample yields 162 events with a total background contribution of $51.9 \pm 4.5$, where the dominant uncertainties arise from the estimate of false leptons and the uncertainty on the jet multiplicity correction factors applied in the MC. Requiring at least one $b$ tagged jet, 80 events remain, with an expected total background of $4.0 \pm 1.7$, with the dominant uncertainties arising again from the estimates of false leptons and also from uncertainties on the $b$ tag modeling. The sample composition is illustrated in Fig. 17, and detailed in Table 5. The extracted cross sections are given in Table 6, together with the other dilepton channel results obtained thus far in Run II.

### 5.1.2. *Lepton + jets final state*

A typical $t\bar{t}$ lepton + jets event selection requires exactly one isolated high-$p_T$ lepton, $\not{p}_T$ and at least three central energetic jets, allowing both lepton + jets and lepton + hadronic $\tau$ signatures to contribute. The dominant physics background in this final state arises from $W$ boson + jets production, and the main instrumental background comes from QCD multijet production with a jet mimicking the isolated-lepton signature. Additional smaller background contributions arise from $Z/\gamma^*$ + jets, diboson and single top production. While for these smaller background processes shape and normalization are determined commonly from simulation and NLO cross sections, $W$ + jets events are usually normalized to data, and their differential distributions derived from Monte Carlo. The QCD multijet background's shape and normalization are typically derived from data, using, for example, datasets fulfilling

Table 5: Event yields and sample composition after $t\bar{t}$ preselections in CDF's 2.8 fb$^{-1}$ dilepton dataset before and after requiring at least one $b$ tagged jet [251].

| Process | before tagging | | | | $b$ tagged |
|---|---|---|---|---|---|
| | $e^+e^-$ | $\mu^+\mu^-$ | $e^\pm\mu^\mp$ | $\ell^+\ell^-$ | $\ell^+\ell^-$ |
| $t\bar{t}$, $\sigma = 6.7$ pb | 29.2 | 21.5 | 59.9 | 110.6 | 65.2 |
| $Z/\gamma^* \to \ell^+\ell^-$ | 9.25 | 4.79 | 0.52 | 14.6 | 0.78 |
| $Z/\gamma^* \to \tau^+\tau^-$ | 2.84 | 2.55 | 6.62 | 12.0 | 0.60 |
| $WW \to \ell^+\ell^-$ | 3.05 | 2.03 | 5.07 | 10.2 | 0.44 |
| $WZ \to \ell^+\ell^-$ | 1.52 | 0.72 | 0.67 | 2.91 | 0.09 |
| $ZZ \to \ell^+\ell^-$ | 0.80 | 0.40 | 0.26 | 1.46 | 0.10 |
| Totals (MC) | 46.7 | 32.0 | 73.0 | 151.7 | 67.2 |
| $\pm\pm$ (SS) Data | 3.81 | 0.00 | 6.96 | 10.8 | 2.00 |
| Sum Expected | $50.5 \pm 1.7$ | $32.0 \pm 1.3$ | $80.0 \pm 2.5$ | $162.5 \pm 4.5$ | $69.2 \pm 1.7$ |
| $+-$ (OS) Data | 54 | 33 | 75 | 162 | 80 |

Table 6: $t\bar{t}$ cross section measurements in dilepton final states performed thus far at the Run II Tevatron with their integrated luminosities, data selections ($\ell\ell$ = dilepton, $\ell$+trk = lepton + track) and analysis methods used. The first three results have been published; the others are preliminary. The measurement marked with an asterisk refers to $m_t$ of 178 GeV/c$^2$ rather than 175 GeV/c$^2$, and, unlike the other results, incorporates the luminosity uncertainty within the first given uncertainty.

| $\int \mathcal{L}dt$ [fb$^{-1}$] | Sel. | $b$ tag | $\sigma_{t\bar{t}}\pm$(stat.)$\pm$(syst.)$\pm$(lumi.) [pb] | Ref. |
|---|---|---|---|---|
| 0.2 | $\ell\ell,\ell$+trk | no | $7.0^{+2.4}_{-2.1}{}^{+1.6}_{-1.1} \pm 0.4$ | [252] |
| 0.2 | $\ell\ell$ | no | $8.6^{+3.2}_{-2.7} \pm 1.1 \pm 0.6$ | [253] |
| 0.4 | $\ell\ell,\ell$+trk | no,yes | $7.4 \pm 1.4 \pm 0.9 \pm 0.5$ | [254] |
| 0.4 | $\ell\ell$ | no | $8.5^{+2.6}_{-2.2}{}^{+0.7}_{-0.3}$ $(*)$ | [255] |
| 1.0 | $\ell\ell$ | no | $6.8^{+1.2}_{-1.1}{}^{+0.9}_{-0.8} \pm 0.4$ | [256] |
| 1.0 | $\ell\ell$ | no | $7.0^{+1.1}_{-1.0}{}^{+0.8}_{-0.6} \pm 0.4$ | [257] |
| 1.0 | $\ell$+trk | yes | $5.0^{+1.6}_{-1.4}{}^{+0.9}_{-0.8} \pm 0.3$ | [258] |
| 1.0 | $\ell\ell,\ell$+trk | no,yes | $6.2 \pm 0.9^{+0.8}_{-0.7} \pm 0.4$ | [259] |
| 1.0 | $\ell$+trk | yes | $10.1 \pm 1.8 \pm 1.1 \pm 0.6$ | [260] |
| 1.1 | $\ell$+trk | no | $8.3 \pm 1.3 \pm 0.7 \pm 0.5$ | [261] |
| 2.8 | $\ell\ell$ | yes | $7.8 \pm 0.9 \pm 0.7 \pm 0.4$ | [251] |
| 2.8 | $\ell\ell$ | no | $6.7 \pm 0.8 \pm 0.4 \pm 0.4$ | [251] |

the complete event selection, except the tight lepton isolation, for the background shape, and the rate for jets to mimic leptons is derived from data for the normalization.

Samples selected with such a basic preselection exhibit S/B ratios below unity, around 1/4. Signal purity can be improved significantly via additional topological selections or by using $b$ tagging. When no $b$ tagging is used in an analysis, then multiple topological and kinematic event properties are usually combined in a multivariate discriminant to yield good signal to background separation without relying on the presence of $b$ jets in the events, therefore being less model dependent. The sample composition can then be determined from a template fit in that sensitive variable, providing a higher sensitivity than a plain cut.

Requiring identified $b$ jets to be present in an event is a powerful tool to reject the background processes which exhibit little heavy-flavor content. $b$ tagging algorithms based on the long lifetime of $B$ hadrons or reconstruction of soft leptons within jets that originate from semileptonic $B$ decays, as discussed in Section 4.3, have been deployed for that purpose. Using $b$ tagging, very pure $t\bar{t}$ samples can be selected that have S/B > 10, if at least four jets and at least two identified $b$ jets are required in each event.

The most precise $t\bar{t}$ cross section measurement published thus far has been performed by D0 on a 0.9 fb$^{-1}$ lepton + jets dataset [262]. Events are selected by requiring exactly one isolated electron or muon with $E_T > 20$ GeV, $\not{p}_T > 20$ GeV for $e +$ jets and $> 25$ GeV for $\mu +$ jets, at least three jets with $|\eta| < 2.5$ and $E_T > 20$ GeV, and leading-jet $E_T > 40$ GeV. Cuts on the azimuthal separation between lepton and $\not{p}_T$ are applied to suppress background from misreconstructed objects. After these selections, the $t\bar{t}$ signal contributes only about 20% of the total sample. The $t\bar{t}$ cross section is measured using two complementary analyses.

One approach is based on lifetime $b$ tagging, requiring at least one jet in the event to be tagged and determining the $t\bar{t}$ production rate through a maximum likelihood fit to the observed event yields in the different subchannels defined by lepton flavor, jet multiplicity and $b$ tag multiplicity. The dominant systematic uncertainties arise from uncertainties on tagging efficiencies for $b, c, q$ and gluon jets and the jet energy calibration. The second analysis utilizes topological likelihood discriminants for the different subchannels based on lepton flavor and jet multiplicity. After applying an additional cut on jets of $H_T > 120$ GeV for three-jet events, five or six different variables such as angular object separation, sphericity and aplanarity (which provide good discrimination power and are well modeled in MC) are combined into discriminants for each subchannel. The sample composition is then determined in a maximum likelihood fit of templates of signal and background contributions to the observed discriminant distributions. The dominant systematic uncertainties in this method arise from uncertainties on the selection efficiencies and the likelihood fit uncertainty derived using statistical fluctuations in the likelihood discriminant template shapes. The sample compositions for both analyses are illustrated in Fig. 18, and detailed in Table 7.
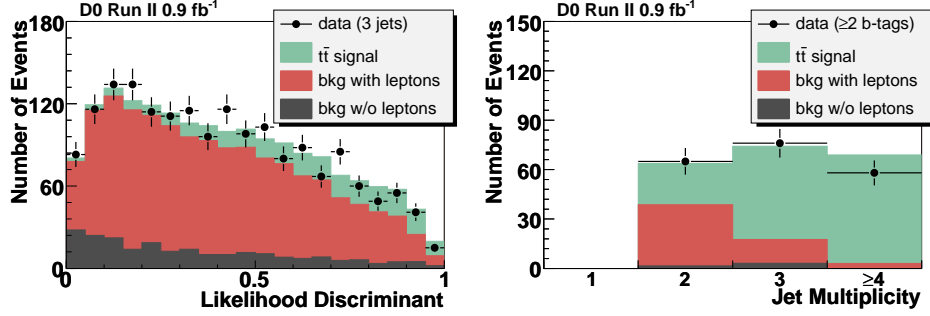
Fig. 18: Topological likelihood distribution for $\ell + $ jets $t\bar{t}$ candidate events when three jets are required (left), and jet multiplicity distribution when at least two $b$ tagged jets are required (right) in D0's 0.9 fb$^{-1}$ lepton + jets dataset [262].

Table 7: Event yields and sample composition in D0's 0.9 fb$^{-1}$ lepton + jets dataset for both the topological and the $b$ tagging analysis. The $t\bar{t}$ contribution is based on the measured cross section in the respective analysis [262].

| | 3 jets, 1 tag | 3 jets, $\geq$2 tags | $\geq$4 jets, 1 tag | $\geq$4 jets, $\geq$2 tags | 3 jets, topo | $\geq$4 jets, topo |
|---|---|---|---|---|---|---|
| $N_{t\bar{t}}$ | 147 $\pm$12 | 57 $\pm$6 | 130 $\pm$10 | 66 $\pm$7 | 245 $\pm$20 | 233 $\pm$19 |
| $N_{W+\text{jets}}$ | 105 $\pm$5 | 10 $\pm$1 | 16 $\pm$2 | 2 $\pm$1 | 1294 $\pm$48 | 321 $\pm$30 |
| $N_{\text{other}}$ | 27 $\pm$2 | 5 $\pm$1 | 8 $\pm$1 | 2 $\pm$1 | | |
| $N_{\text{multijet}}$ | 27 $\pm$6 | 3 $\pm$2 | 6 $\pm$3 | 0 $\pm$2 | 227 $\pm$28 | 70 $\pm$12 |
| total | 306 $\pm$14 | 74 $\pm$6 | 159 $\pm$11 | 69 $\pm$7 | 1766 $\pm$59 | 624 $\pm$37 |
| $N_{\text{data}}$ | 294 | 76 | 179 | 58 | 1760 | 626 |

Both analyses exhibit a statistical correlation of 0.31, as determined from ensemble studies and are combined using the best linear unbiased estimate (BLUE) approach [276, 277]. The resulting cross section is given in Table 8, together with the other lepton + jets channel results obtained thus far in Run II.

### 5.1.3. All-hadronic final state

To select all-hadronic $t\bar{t}$ decays typically requires at least six central energetic jets per event, and no isolated energetic leptons or significant $\not{p}_T$ to be present. The overwhelming background process here is QCD multijet production, dominating over the signal by three orders of magnitude after online selection of events using triggers on multiple jets and $H_T$ in the event above a certain threshold. This background is usually modeled from the data, as the theoretical description of final states with such high jet multiplicities has large uncertainties and datasets even more depleted from signal can be easily obtained, for example, by selecting a lower

Table 8: $t\bar{t}$ lepton + jets cross section measurements performed thus far at the Run II Tevatron with their integrated luminosities, data selections and analysis methods used. The first eleven results have been published; the others are preliminary. The measurements marked with asterisks (∗) refer to $m_t$ of 178 GeV/c$^2$ rather than the standard 175 GeV/c$^2$. Measurements marked with a double cross (‡) include the luminosity uncertainty in the systematic uncertainty, while measurements marked with a cross (†) have the first uncertainty represent the statistical and systematic uncertainties combined in quadrature and the second representing the luminosity.

| $\int \mathcal{L}dt$ [fb$^{-1}$] | Sel. | $b$ tag | $\sigma_{t\bar{t}}\pm$(stat.)$\pm$(syst.)$\pm$(lumi.) [pb] | Ref. |
|---|---|---|---|---|
| 0.2 | $\ell$+jets | yes | $5.6^{+1.2}_{-1.1}{}^{+0.9}_{-0.6}$ (‡) | [207] |
| 0.2 | $\ell$+jets | yes | $6.0^{+1.5}_{-1.6}{}^{+1.2}_{-1.3}$ (‡) | [263] |
| 0.2 | $\ell$+jets | yes, soft-$\mu$ | $5.3 \pm 3.3^{+1.3}_{-1.0}$ (‡) | [264] |
| 0.2 | $\ell$+jets | no | $6.6 \pm 1.1 \pm 1.5$ (‡) | [265] |
| 0.2 | $\ell$+jets | no | $6.7^{+1.4}_{-1.3}{}^{+1.6}_{-1.1} \pm 0.4$ | [266] |
| 0.2 | $\ell$+jets | yes | $8.6^{+1.6}_{-1.5} \pm 0.6$ (†) | [267] |
| 0.3 | $\ell$+jets | yes | $8.7 \pm 0.9^{+1.1}_{-0.9}$ (∗,‡) | [268] |
| 0.3 | $\ell$+jets | yes | $8.9 \pm 1.0^{+1.1}_{-1.0}$ (∗,‡) | [208] |
| 0.4 | $\ell$+jets | yes | $6.6 \pm 0.9 \pm 0.4$ (†) | [219] |
| 0.4 | $\ell$+jets | no | $6.4^{+1.3}_{-1.2} \pm 0.7 \pm 0.4$ | [269] |
| 0.9 | $\ell$+jets | no, yes | $7.4 \pm 0.5 \pm 0.5 \pm 0.5$ | [262] |
| 0.4 | $\ell$+jets | yes, soft-$\mu$ | $7.3^{+2.0}_{-1.8} \pm 0.4$ (†) | [270] |
| 0.7 | $\ell$+jets | yes | $8.5 \pm 0.6 \pm 1.0$ (‡) | [271] |
| 1.0 | $\ell$+jets | yes | $8.2 \pm 0.5^{+0.8}_{-0.7} \pm 0.5$ | [257] |
| 1.7 | $\ell$+jets | yes, soft-$e$ | $7.8 \pm 2.4 \pm 1.5 \pm 0.5$ | [272] |
| 2.0 | $\ell$+jets | yes, soft-$\mu$ | $8.7 \pm 1.1^{+0.9}_{-0.8} \pm 0.6$ | [273] |
| 2.7 | $\ell$+jets | yes | $7.2 \pm 0.4 \pm 0.5 \pm 0.4$ | [274] |
| 2.8 | $\ell$+jets | no | $6.8 \pm 0.4 \pm 0.6 \pm 0.4$ | [275] |

jet multiplicity.

After preselection, signal and background are separated further by applying $b$ jet identification and using multivariate discriminants based on topological and kinematic event properties.

CDF has published the most precise cross section analysis in the all-hadronic final state to date, based on 1 fb$^{-1}$ of data [278]. Events are required to have at least six and at most eight jets with $E_T \geq 15$ GeV, $\Delta R \geq 0.5$ from each other and $|\eta| \leq 2$, no isolated energetic electrons or muons as used in the leptonic $t\bar{t}$ analyses,
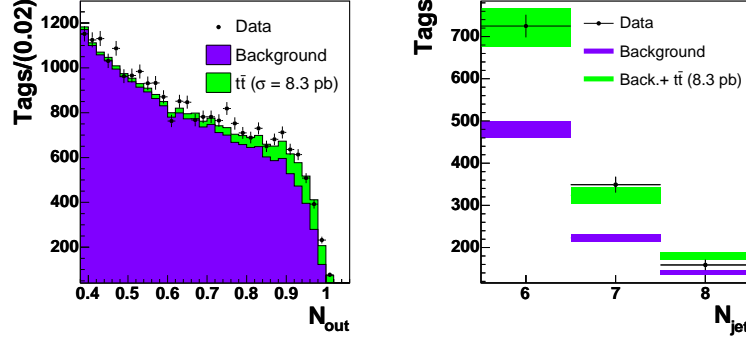
Fig. 19: Left: Number of $b$ tags in 1 fb$^{-1}$ of all-hadronic candidate events selected by CDF versus neural network discriminant ($N_{out}$). Right: Number of tags versus jet multiplicity after requiring $N_{out} > 0.94$. The $t\bar{t}$ contributions are normalized to the measured cross section of 8.3 pb [278].

and $\not{p}_T$ divided by $\sqrt{H_T}$ of the selected jets has to be $< 3\ \sqrt{\text{GeV}}$. This yields S/B of $\approx 1/370$. The signal purity is then increased using a neural network discriminant based on variables such as $H_T$, centrality, aplanarity and minimal/maximal invariant dijet or trijet mass values of all jet permutations. The signal is modeled using MC, and the selected data are used directly for the background, as the expected signal contribution in these events is very small.

At least one of the jets in each event is required to be $b$ tagged, and the sample composition is then determined in terms of the number of tags rather than events. The average number of tags per signal event for a given neural network cut is determined from MC, and is used to derive the $t\bar{t}$ cross section from the observed excess in $b$ tags beyond the background expectation obtained from data. The tagging efficiencies of the simulation are corrected for differences relative to data. The cut on the neural network discriminant ($N_{out}$) is optimized for the highest expected signal significance after $b$ tagging, taking both statistical and systematical uncertainties of signal and background into account, yielding $N_{out} > 0.94$. This cut yields S/B of $\approx 1/12$ before $b$ tagging, and $1/2$ after tagging.

The dominant systematical uncertainty in the measurement arises from the uncertainty in jet energy scale, strongly impacting both the preselection of events and the input variables for the further neural network selection. The sample composition of candidate tags in data is illustrated in Fig. 19, and is detailed in Table 9. The resulting cross section is given in Table 10, together with the other all-hadronic channel results obtained thus far in Run II.

Table 9: Expected and observed yields of tags after requiring $N_{\text{out}} > 0.94$, with uncertainties corresponding to statistical and systematic contributions added in quadrature. The corrected background (BG) contribution accounts for the signal contamination in the dataset used for its estimate. After tagging, 1020 events remain in the signal sample with 1233 tags and an expected background of $846 \pm 37$ tags. The average number of tags in $t\bar{t}$ events is $0.95 \pm 0.07$ [278].

|  | 4 jets | 5 jets | 6 jets | 7 jets | 8 jets |
|---|---|---|---|---|---|
| BG | $16060 \pm 575$ | $2750 \pm 92$ | $536 \pm 17$ | $255 \pm 8$ | $146 \pm 5$ |
| BG (corrected) | $15961 \pm 677$ | $2653 \pm 112$ | $481 \pm 20$ | $223 \pm 10$ | $142 \pm 7$ |
| $t\bar{t}$ ($\sigma_{t\bar{t}} = 8.3$ pb) | $120 \pm 20$ | $266 \pm 45$ | $242 \pm 41$ | $101 \pm 17$ | $38 \pm 7$ |
| BG + $t\bar{t}$ | $16081 \pm 677$ | $2919 \pm 121$ | $723 \pm 46$ | $324 \pm 20$ | $180 \pm 10$ |
| Data | 16555 | 3139 | 725 | 349 | 159 |

Table 10: $t\bar{t}$ all-hadronic cross section measurements performed thus far at the Run II Tevatron with their integrated luminosities, data selections and analysis methods used. All three results have been published. The measurement marked with an asterisk refers to $m_t$ of 178 GeV/c$^2$ rather than the standard 175 GeV/c$^2$.

| $\int \mathcal{L}dt$ [fb$^{-1}$] | Sel. | $b$ tag | $\sigma_{t\bar{t}} \pm$(stat.)$\pm$(syst.)$\pm$(lumi.) [pb] | Ref. |
|---|---|---|---|---|
| 0.3 | jets only | yes | $7.5 \pm 2.1^{+3.3}_{-2.2}{}^{+0.5}_{-0.4}$ ($*$) | [279] |
| 0.4 | jets only | yes | $4.5^{+2.0}_{-1.9}{}^{+1.4}_{-1.1} \pm 0.3$ | [280] |
| 1.0 | jets only | yes | $8.3 \pm 1.0^{+2.0}_{-1.5} \pm 0.5$ | [278] |

5.1.4. *Hadronic $\tau$ channels*

By choosing a more inclusive $t\bar{t}$ event selection, hadronic $\tau$ decays can be included as already mentioned in the discussion of lepton + jets and dilepton channels for the $\tau$ + lepton case. A first measurement without any explicit lepton identification has been published by CDF, selecting events with at least four jets, with at least one being $b$ tagged, and significant $\not{p}_T$ not aligned with any jet. Since events with isolated energetic electrons or muons are rejected, the resulting sample is enriched in $\tau$ + jets events [281].

Explicit reconstruction of hadronic $\tau$ decays is far more demanding and usually relies on multivariate discriminants. Based on the decay mode (1-prong or 3-prong, with or without associated electromagnetic subclusters from neutral pions), different discriminants can be deployed, exploiting differences between hadronic $\tau$ decays and jets. For example, isolation in the tracking system and calorimetry, shower shape, track multiplicity or correlations between tracks and clusters in the calorimeter can be applied. Using such discriminants, the $\tau$ + jets and $\tau$ + lepton $t\bar{t}$ decay modes
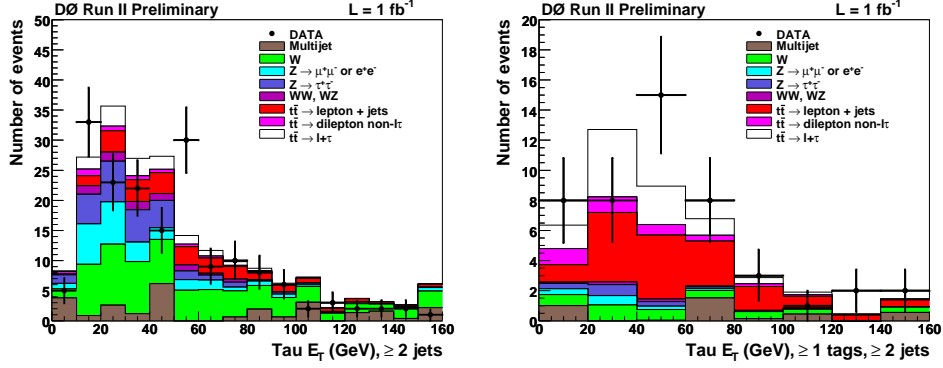
Fig. 20: Hadronic-$\tau$ $E_T$ spectrum before (left) and after (right) $b$ tagging is applied in the preselected 1 fb$^{-1}$ $\ell + \tau$ sample analyzed by D0. The $t\bar{t}$ signal is normalized to the SM expectation. The highest $E_T$ bin contains all overflows [283].

have been studied based on their experimental signature of $\not{p}_T$, at least one hadronic $\tau$ candidate, and at least four or two jets, and no or one isolated energetic electron or muon for the two channels, respectively. $b$ jet identification is crucial to improve sample purity in such analyses.

A first $\tau$ + jets cross section analysis has been performed by D0 on 0.3 fb$^{-1}$ of data, deploying a preselection and $\tau$ identification as outlined above. $b$ jet identification and neural networks based on event topology and kinematics provide further separation of $t\bar{t}$ signal and background that is mainly due to QCD multijet production, where jets mimic $\tau$ decays [282]. While the measurement suffers from large statistical uncertainties, it is a proof of principle that will benefit greatly from the tenfold increased dataset already in hand.

D0 has also performed a first measurement of the $t\bar{t}$ production rate in the $\tau$ + lepton final state based on 1 fb$^{-1}$ of data [283]. Events are required to have exactly one isolated electron or muon with $E_T > 15$ GeV and $|\eta| < 1.1$ or $E_T > 20$ GeV and $|\eta| < 2$, respectively, at least one $\tau$ candidate of opposite charge within $|\eta| < 1$, $\not{p}_T$ between 15 and 200 GeV, at least two jets within $|\eta| < 2.5$ with $E_T > 20$ GeV and the leading jet above 30 GeV, and at least one of these jets identified as $b$ jet. Additional channel-specific background rejection is achieved by vetoing events collected in the $\mu\tau$ analysis with invariant mass of the isolated muon and a second non-isolated muon between 70 and 100 GeV/c$^2$. In the $e\tau$ channel, events are rejected where electron and $\not{p}_T$ are aligned in azimuthal angle $\phi$ by requiring $\cos(\Delta\phi(e, \not{E}_T)) < 0.9$. The resulting sample composition is illustrated in Fig. 20, and detailed in Table 11 – there are significant contributions to signal from the lepton + jets and dilepton channels.

Background contributions arise from $W$ boson + jets production, $Z/\gamma^*$ + jets events with $Z/\gamma^* \rightarrow \ell^+\ell^-/\tau^+\tau^-$, and diboson production, as described by MC.

Table 11: Event yields and sample composition before and after $b$ tagging in the preselected 1 fb$^{-1}$ $\ell + \tau$ sample analyzed by D0. The $t\bar{t}$ signal is normalized to the SM expectation. The uncertainties are purely statistical [283].

| | before $b$ tagging | | after $b$ tagging | |
|---|---|---|---|---|
| | $\mu\tau$ | $e\tau$ | $\mu\tau$ | $e\tau$ |
| $W$+jets | $38.0 \pm 1.7$ | $34.1 \pm 3.5$ | $2.31 \pm 0.22$ | $2.13 \pm 0.27$ |
| $Z/\gamma^* \to ee, \mu\mu$ | $20.7 \pm 1.1$ | $5.8 \pm 0.6$ | $1.09 \pm 0.11$ | $0.38 \pm 0.05$ |
| $Z/\gamma^* \to \tau\tau$ | $19.6 \pm 1.2$ | $7.5 \pm 0.6$ | $1.02 \pm 0.10$ | $0.54 \pm 0.06$ |
| Diboson | $2.8 \pm 0.1$ | $5.1 \pm 0.6$ | $0.21 \pm 0.01$ | $0.34 \pm 0.07$ |
| Multijet | $10.6 \pm 6.3$ | $12.7 \pm 6.6$ | $4.52 \pm 3.01$ | $-1.27 \pm 1.77$ |
| $t\bar{t} \to \ell + \tau$ | $7.8 \pm 0.1$ | $6.67 \pm 0.1$ | $5.64 \pm 0.04$ | $4.70 \pm 0.05$ |
| $t\bar{t} \to \ell\ell$ | $4.3 \pm 0.1$ | $0.73 \pm 0.1$ | $3.14 \pm 0.03$ | $0.47 \pm 0.07$ |
| $t\bar{t} \to \ell+$ jets | $12.7 \pm 0.1$ | $12.41 \pm 0.2$ | $8.40 \pm 0.11$ | $7.88 \pm 0.12$ |
| Total Expected | $116.6 \pm 6.8$ | $85.0 \pm 7.7$ | $26.33 \pm 3.02$ | $15.17 \pm 1.97$ |
| Data | 104 | 69 | 29 | 18 |

Table 12: $t\bar{t}$ cross section measurements using hadronic $\tau$ decays performed thus far at the Run II Tevatron, with their integrated luminosities, data selections and analysis methods used. The first two results have been published; the others are preliminary. The measurement marked with a double cross (‡) includes the luminosity uncertainty in the systematic uncertainty.

| $\int \mathcal{L}dt$ [fb$^{-1}$] | Sel. | $b$ tag | $\sigma_{t\bar{t}} \pm$(stat.)$\pm$(syst.)$\pm$(lumi.) [pb] | Ref. |
|---|---|---|---|---|
| 0.2 | $\ell + \tau$ | no | $< 5.2 \cdot \sigma_{\text{SM}}$ (95% C.L.) | [216] |
| 0.3 | $\not{p}_T +$ jets | yes | $6.0 \pm 1.2^{+0.9}_{-0.7}$ (‡) | [281] |
| 0.3 | $\tau$+jets | yes | $5.1^{+4.3}_{-3.5} \pm 0.7 \pm 0.3$ | [282] |
| 0.4 | $\ell + \tau$ | no | significance at $\approx 1$ sd | [284] |
| 1.0 | $\ell + \tau$ | yes | $8.3^{+2.0}_{-1.8}{}^{+1.4}_{-1.2} \pm 0.5$ | [283] |
| 1.2 | $\ell + \tau$ | yes | $6.4^{+1.8}_{-1.6}{}^{+1.4}_{-1.3} \pm 0.4$ | [285] |
| 2.2 | $\ell + \tau$ | yes | $7.3^{+1.3}_{-1.2}{}^{+1.2}_{-1.1} \pm 0.5$ | [285] |

The $W$ boson + jets contribution is normalized to data. Background from QCD multijet production is estimated from data where the lepton and $\tau$ are of same charge, corrected for significant contributions from $W$ boson + jets and $t\bar{t}$ production. The dominant systematic uncertainties in this analysis arise from limited background/MC statistics, the rate for jets or leptons to mimic $\tau$ decays, modeling of $b$ tagging uncertainties, and jet energy calibration.

The corresponding cross section is given in Table 12, together with an update from an additional 1.2 fb$^{-1}$ of D0 data, as well as other results involving hadronic $\tau$ final states obtained thus far in Run II.

### 5.1.5. *Summary*

An overview of the current status of $t\bar{t}$ cross section measurements performed in different decay channels is given in Fig. 21 for CDF and D0, showing good agreement among channels, analysis methods and experiments. The theoretical predictions discussed in Section 3.1 are also shown for comparison as shaded/hatched bands, and also show very good agreement with the measurements.

CDF combines the results obtained in the lepton + jets and dilepton channels using $1.7 - 2.8$ fb$^{-1}$ samples of data, achieving a relative uncertainty on the result of 9% [286]. The most precise single measurement is obtained in the lepton + jets channel using secondary-vertex $b$ tagging on 2.7 fb$^{-1}$ of data, yielding a relative uncertainty of about 10% [274]. D0 combines the results from lepton + jets, dilepton and $\tau$ + lepton channels obtained from approximately 1.0 fb$^{-1}$ of data, yielding a relative uncertainty of about 11% [257]. The most precise single D0 measurement, with a precision of 11%, has been published in the lepton + jets channel, using both secondary-vertex $b$ tagging and kinematic information in 0.9 fb$^{-1}$ of data in a combined result [262]. For comparison, the final Run I combined cross section from CDF [287, 288] and D0 [289] had a precision of $\approx$25%. Unfortunately, no combined cross section measurement from both experiments exists to date, unlike for top quark mass measurements (see Section 7.3.4). However, such combination for the $t\bar{t}$ production rate is planned in the future.

With increasing integrated luminosity, the statistical uncertainties are becoming less important and precision is starting to be limited by systematic uncertainties, which in turn can also be further constrained with more data. One of the main challenges for future measurements will be to study systematic uncertainties in greater detail rather than use "conservative" estimates. The most precise single $t\bar{t}$ production cross section measurement at the Run II Tevatron with the anticipated total of 8 fb$^{-1}$ of data can be expected in the lepton + jets channel – probably using both kinematical and $b$ tagging information – at a relative precision of $\approx$8%. This will be dominated by uncertainties on luminosity and systematic effects. For combination of results, the precision may ultimately be driven by the current luminosity uncertainty of 6% for both experiments. The luminosity uncertainty could be avoided by measuring cross section ratios, for example, relative to $Z$ boson production[b]. Also, with large datasets, a ratio of $t\bar{t}$ cross sections measured in different channels (such as the lepton + jets and the dilepton channels) could be obtained with good statistical precision while benefiting from cancellations of common systematic uncertainties.

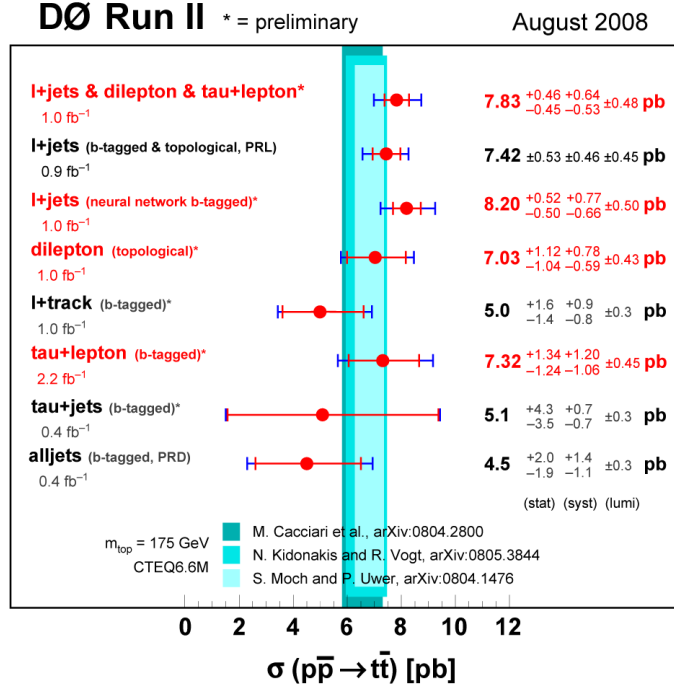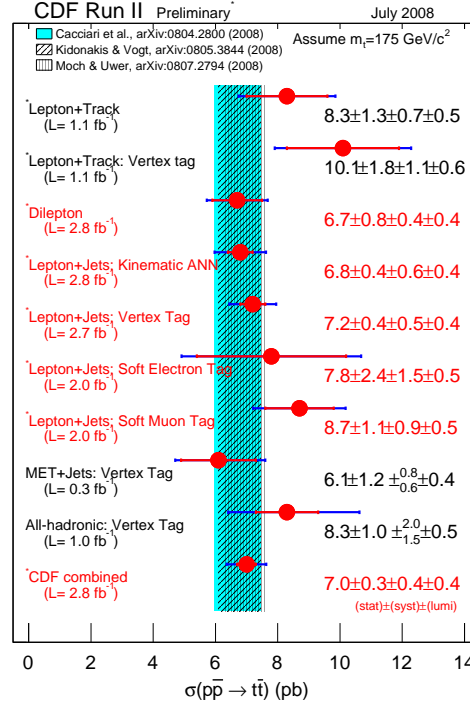[b]After completion of this review, first such measurements became available from CDF [292, 293].

Fig. 21: Current status of the $t\bar{t}$ production cross section measurements by CDF (top, [290]) and D0 (bottom, [291]) compared with SM predictions (shown as shaded/hatched bands). The channels contributing to the combined results are highlighted [257, 286].

The precision of the measured $t\bar{t}$ cross section now matches that of the theoretical predictions, which provides stringent tests of perturbative QCD calculations. This furthers our understanding of the standard model, which still provides an excellent description of all current measurements. Based on the observed production rate alone, severe constraints on phenomena beyond the SM become feasible [294]. More detailed tests of the standard model predictions for $t\bar{t}$ production will be described in the following sections. Via its mass dependence, the $t\bar{t}$ production rate can also be used to test consistency of the SM with the top quark mass measurements performed at the Tevatron (with the benefit of easier theoretical interpretation of the mass parameter as discussed in Section 7.3.4). Studying and comparing all available $t\bar{t}$ final states, including those with hadronic $\tau$ decays, provides a probe for novel contributions that can affect the observed final states in different ways. For example, searches for charged Higgs bosons in top quark decays are discussed in Section 6.5.

## 5.2. *Top quark pair production mechanism*

Top quark pair production at the Tevatron proceeds predominantly via $q\bar{q}$ annihilation, as described in Section 3.1. The remaining fraction from gluon-gluon fusion ($f_{gg}$) is $15 \pm 5\%$, with the uncertainty mainly reflecting that of the corresponding PDFs [116].

While the total $t\bar{t}$ production rate has been studied extensively (see Section 5.1) and has been found to be in agreement with the SM expectation, the production mechanism has not yet been subject to such scrutiny. A measurement of the fraction of $t\bar{t}$ events produced via gluon-gluon fusion $f_{gg} = \sigma(gg \to t\bar{t})/\sigma(p\bar{p} \to t\bar{t})$ provides a test of QCD, and can contribute to a reduction in the uncertainties of the corresponding PDFs. In addition, contributions from extensions of the SM to $t\bar{t}$ production could be unveiled [295], some of which may have remained undetected because of the presence of new compensating decay mechanisms [296].

CDF performs a first measurement of $f_{gg}$ in a 1 fb$^{-1}$ $b$ tagged lepton + jets dataset [297]. The analysis is based on the fact that soft gluons are emitted with a higher probability from gluons than from quarks [90–92, 298], and the average number of charged particles (tracks) with low transverse momentum should therefore be higher in $gg \to t\bar{t}$ events than in $q\bar{q} \to t\bar{t}$ events.

To avoid the large theoretical uncertainties on soft-gluon radiation in the Monte Carlo modeling of the multiplicity of soft tracks, $W$ + jets and dijet collider data, with well understood production mechanisms, are used to relate the observed soft-track multiplicity to the gluon content of a sample (see Fig. 22). Templates for the soft-track multiplicity distribution in gluon-poor and gluon-enriched events are obtained, respectively, from $W$ boson events without jets and dijet events with a leading-jet $E_T$ of $80-100$ GeV. The observed soft-track multiplicity distribution in $t\bar{t}$ candidate events is fitted with these templates. From the fit result, $f_{gg}$ is extracted and found to be $7 \pm 14\%$(stat.) $\pm 7\%$(syst.), corresponding to a 95% C.L.
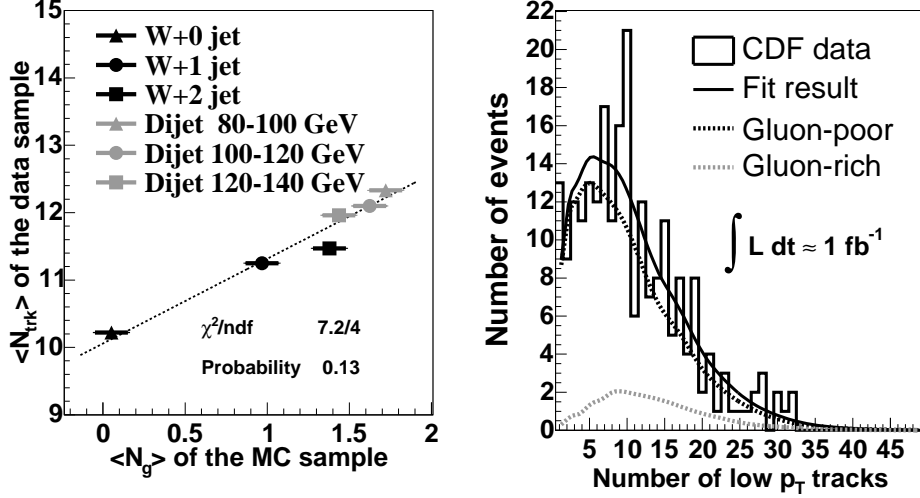
Fig. 22: Left: Correlation between the soft-track multiplicity observed in collider data and the average number of gluons in the corresponding Monte Carlo samples. Right: Fit result of the soft-track multiplicity distribution observed in $b$-tagged lepton $+\geq 4$ jets $t\bar{t}$ candidate events with a gluon-poor and a gluon-rich template [297].

upper limit of 33%.

CDF uses a complementary second method to extract $f_{gg}$ from the same dataset, based on templates from a neural network using kinematic event properties to separate $gg \to t\bar{t}$, $q\bar{q} \to t\bar{t}$ and the dominant $W$ + jets background [299], yielding a 95% C.L. upper limit for $f_{gg}$ of 61%. Combining both results yields $f_{gg} = 7^{+15}_{-\ 7}\%$(stat. + syst.), in good agreement with the SM expectation.

CDF has also performed a first measurement of $f_{gg}$ in 2 fb$^{-1}$ of dilepton data, based on the variation of the azimuthal correlation of the charged leptons for the different $t\bar{t}$ production modes [300]. This difference arises from the fact that, close to threshold, top quark pairs are produced in a $^3S_1$ state via $q\bar{q}$ annihilation and in a $^1S_0$ state via gluon-gluon fusion (see Section 5.5). Consequently, the top quark spins tend to be antiparallel for $t\bar{t}$ production via gluon-gluon fusion and aligned for production via $q\bar{q}$ annihilation, which is reflected in the azimuthal correlation of the charged leptons. The relative fraction of $t\bar{t}$ production via gluon fusion is determined in a fit of the observed $\Delta\phi$ distribution in data, with templates for $gg \to t\bar{t}$, $q\bar{q} \to t\bar{t}$ and background arising from diboson, $Z/\gamma^*$ + jets and $W$ boson + jets production, yielding $f_{gg} = 53^{+35}_{-37}\%$(stat.)$^{+7}_{-8}\%$(syst.), consistent with the SM.

### 5.3. *Top quark charge asymmetry*

The strong production of top quark pairs is symmetric under charge conjugation at leading order, implying it does not discriminate between top and antitop quarks.

Considering that the initial proton-antiproton state at the Tevatron is not an eigen-state of charge conjugation, this symmetry is a coincidence. At higher orders, a charge asymmetry arises from interference between amplitudes that are symmetric and antisymmetric under the exchange of top and antitop quarks [301, 302], leading to an excess of top over antitop quarks in specific kinematic regions. One resultant observable is the integrated forward-backward production asymmetry for inclusive $t\bar{t}$ production at the Tevatron. This is predicted to be $5 - 10\%$ at NLO [301–305], implying that top quarks are preferentially emitted in the direction of the incoming protons. The asymmetry depends strongly on the region of phase space being probed, and particularly on the production of additional jets: While the asymmetry for exclusive $t\bar{t}$ production without additional jets is predicted to be $6.4\%$ [303], the inclusive $t\bar{t}$ production with one additional jet exhibits an asymmetry of about $-7\%$ at LO [303, 306], which is reduced drastically to $(-1.5 \pm 1.5)\%$ at NLO [306].

The size of higher order corrections for the $t\bar{t} + $ jet subprocess illustrates that higher-order evaluations of the whole process are still necessary for the total asymmetry prediction to converge and correctly describe the partial cancellations of the various interference contributions. It should also be noted that in the above theoretical predictions, the top quark decay and possible effects on the asymmetry from reconstruction of the final-state objects are not considered. The top quark charge asymmetry is also sensitive to extensions of the standard model in $t\bar{t}$ production involving, e.g., axigluons [304], technicolor [307] or additional neutral $Z'$ gauge bosons [308]. Consequently, a measurement of the asymmetry can be used to set limits on such processes, particularly for extending the sensitivity of searches for $t\bar{t}$ production via heavy resonances (see Section 5.7.1) to include not only those of narrow width but also wide resonances.

D0 has published the first measurement of the integrated forward-backward charge asymmetry in $t\bar{t}$ production, based on a 0.9 fb$^{-1}$ $b$ tagged lepton + jets dataset [309]. The $t\bar{t}$ system is reconstructed using a constrained kinematic fit, where the charged lepton is used to differentiate between the top and the antitop quark. The signed rapidity difference of the top and the antitop quark $\Delta y = y_t - y_{\bar{t}}$ is used as an observable from which the charge asymmetry is obtained as $A_{fb} = (N_f - N_b)/(N_f + N_b)$, with $N_f$ ($N_b$) being the event yields with positive (negative) $\Delta y$. The sample composition is determined in a template fit based on a multivariate kinematic likelihood discriminant for both signs of the reconstructed $\Delta y$ simultaneously as shown in Fig. 23.

The resulting measurement is not corrected for reconstruction and acceptance due to the limited theoretical knowledge of the shape of the asymmetry. Instead, a prescription is provided to model the detector acceptance at the particle level, for ease of comparison of any model with the measurement. For comparison with the standard model, a slightly more detailed prescription than the one provided in Ref. [309] is applied to the prediction from the MC@NLO [310, 311] generator, and found to be in agreement with the measurement for different jet multiplicities, including a change in the sign of the asymmetry, as shown in Table 13. The domi-
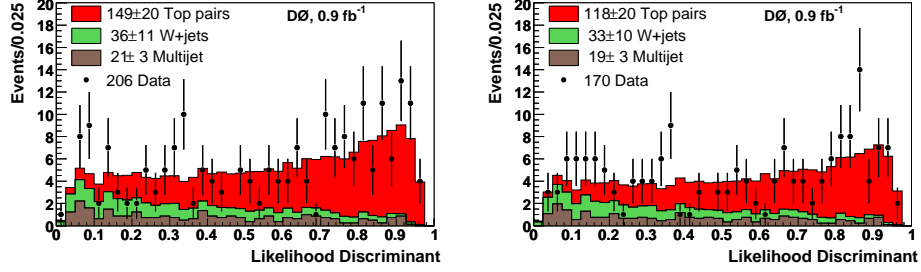
Fig. 23: Likelihood-discriminant output distribution for data with ≥4 jets, overlaid with the result of a template fit determining the sample composition for events with $\Delta y > 0$ (left) and $\Delta y < 0$ (right) [309].

Table 13: $A_{\text{fb}}^{\text{pred}}$: MC@NLO SM prediction for the observed $t\bar{t}$ charge asymmetry in the D0 detector, including uncertainties from acceptance and dilution (misreconstruction of sign in $\Delta y$). $A_{\text{fb}}^{\text{obs}}$: Uncorrected $t\bar{t}$ charge asymmetry observed by D0 [309].

| $N_{jet}$ | $A_{\text{fb}}^{\text{pred}}$ [%] | $A_{\text{fb}}^{\text{obs}}$ [%] |
|---|---|---|
| ≥ 4 | $0.8 \pm 0.2(\text{stat.}) \pm 1.0(\text{acc.}) \pm 0.0(\text{dil.})$ | $12 \pm 8 \,(\text{stat.}) \pm 1 \,(\text{syst.})$ |
| = 4 | $2.3 \pm 0.2(\text{stat.}) \pm 1.0(\text{acc.}) \pm 0.1(\text{dil.})$ | $19 \pm 9 \,(\text{stat.}) \pm 2 \,(\text{syst.})$ |
| ≥ 5 | $-4.9 \pm 0.4(\text{stat.}) \pm 1.0(\text{acc.}) \pm 0.2(\text{dil.})$ | $-16^{+15}_{-17} \,(\text{stat.}) \pm 3 \,(\text{syst.})$ |

nant systematic uncertainty for the ≥4 jet sample arises from the relative jet energy calibration between simulation and data, and for its subsamples from event migration between the subsamples when splitting the sample up into one with exactly four and one with at least five jets. However, these systematics are negligible compared to the statistical uncertainties. The measurement is also used to derive 95% C.L. limits on the fraction of $t\bar{t}$ events that are produced via a specific $Z'$ resonance model [307, 312] with parity-violating couplings as a function of the resonance mass.

CDF has obtained two measurements of $A_{\text{fb}}$ based on 1.9 fb$^{-1}$ $b$-tagged lepton + jets data, using different observables after reconstruction of the $t\bar{t}$ kinematics in a constrained fit [313–315]. CDF chooses a different approach for the measurements than D0 by providing results both before and after background subtraction *and* correction for acceptance and reconstruction effects.

The first analysis uses as observable the rapidity difference between the hadronically and semileptonically decaying (anti-) top quark multiplied by the lepton charge [313, 315]. This is equivalent to $\Delta y$ in the measurement reported by D0. After background subtraction, asymmetries of 0.119±0.064, 0.132±0.075 and 0.079±0.123 are observed for jet multiplicities ≥ 4, = 4 and ≥ 5, respectively, which is consistent

with the measurement by D0, and which correspond to MC@NLO predictions of $0.017 \pm 0.007, 0.038 \pm 0.008$ and $-0.033 \pm 0.012$ (errors are statistical). The result for the inclusive sample with at least four jets is then corrected for reconstruction and acceptance effects, yielding $A_{\mathrm{fb}}^{\mathrm{corr}} = 24 \pm 13\,(\mathrm{stat.}) \pm 4\,(\mathrm{syst.})\%$. The dominant systematic uncertainty comes from the shape uncertainty of the $\Delta y$-distribution. The result is bigger than expected from NLO predictions, but consistent within errors.

The second analysis measures the charge asymmetry using the product of inverse lepton charge and $\cos\theta_{t_{\mathrm{had}}}$ as observable, where $\theta_{t_{\mathrm{had}}}$ is the angle of the top quark with the hadronic decay chain relative to the proton beam [314, 315]. Since this measurement is performed in the laboratory frame rather than the parton rest frame, the asymmetry is reduced by about 30% [304]. For $\geq 4$ jets, the corrected asymmetry is $A_{\mathrm{fb}}^{\mathrm{corr}} = 17 \pm 7\,(\mathrm{stat.}) \pm 4\,(\mathrm{syst.})\%$, with the dominant systematic uncertainty arising from background shape and its normalization. This result is consistent with the theoretical prediction at the level of two standard deviations (sd) for a Gaussian distribution.

It should be noted that the forward-backward asymmetry in the laboratory frame vanishes at the LHC due to the symmetric initial state, in contrast to the Tevatron $p\bar{p}$ collider. The dominance of $t\bar{t}$ production via the charge symmetric gluon fusion reaction at $\sqrt{s} = 14$ TeV reduces the observable charge asymmetry at the LHC.

### 5.4. *Top quark pair production kinematics*

New contributions to $t\bar{t}$ production can alter the observed event kinematics, which can be exploited in searches for such processes, as described in Section 5.7. The basic kinematic properties of leptons, jets, $\not{p}_T$ and corresponding angular distributions are continuously compared to the SM expectation, both in signal-enriched datasets and signal-depleted control samples exhibiting features similar to the signal, in all studies of top quark properties and especially in the cross section analyses. Thus far, no significant deviation from the SM expectation has been found that would be indicative of new physics contributions to top quark samples.

In Run I, CDF and D0 observed a slight excess of the $t\bar{t}$ production rate over the SM prediction in the dilepton channel, especially in the $e\mu$ final state [316, 317]. Since some of these events had rather large $\not{p}_T$ and lepton-$p_T$, their consistency with the SM was questioned and, for example, the kinematic compatibility of these events with cascade decays of heavy supersymmetric quarks was pointed out [318]. Triggered by this, CDF performed a search for anomalous $t\bar{t}$ kinematics in Run II, based on $0.2$ fb$^{-1}$ dilepton data yielding 13 candidate events [319].

A priori four kinematic event variables, including $\not{p}_T$ and leading-lepton $p_T$, were chosen to quantify any possible deviations of the observed distributions from SM predictions. Using a shape comparison based on the Kolmogorov-Smirnov statistic, no significant discrepancy was found, and the probability of observing a sample less

consistent with the SM was determined to be 1.6%. Including systematic uncertainties, the $p$-value was 1.0-4.5%, where the lowest value was obtained by lowering the background expectation by one standard deviation. Consequently, presence of processes beyond the SM, with high $\not{p}_T$ and high lepton-$p_T$, are not favored by these data.

It is also of great interest to study the kinematic properties of the top quark itself and to compare these with the SM expectation. In Run I, D0 performed such an analysis and found good agreement with the SM [320, 321], which was then also confirmed through a dedicated study of the $p_T$ spectrum of the top quark by CDF [322]. A corresponding analysis has not yet been published in Run II. However, a measurement of the differential $t\bar{t}$ production cross section $d\sigma/dM_{t\bar{t}}$ has been performed by CDF using 1.9 fb$^{-1}$ of Run II data, as described in Section 5.7.3, and also shows good agreement with the SM [323].

### 5.5. *Spin correlations in $t\bar{t}$ production*

Top quark pairs are expected to be produced essentially unpolarized in hadron collisions when the incident particles are unpolarized. A small polarization at the percent level is induced by QCD processes [324–326], and is perpendicular to the production plane, as strong interactions conserve parity. A measurement of this effect will be very difficult both at the Tevatron and the LHC, which in return suggests to use a corresponding analysis to probe for non-standard contributions in $t\bar{t}$ production [327]. An even smaller additional polarization in the production plane arises from mixed strong and weak contributions to $t\bar{t}$ production at order $\alpha_s^2\alpha$ [328].

While no observable spin polarization in $t\bar{t}$ production is predicted in the framework of the standard model, the spins of the top and the antitop quark are expected to be correlated [329]. This correlation depends both on the production mode of the $t\bar{t}$ pair and the production energy. Close to threshold, the top quark pair is produced in a $^3S_1$ state via $q\bar{q}$ annihilation and in a $^1S_0$ state via gluon-gluon fusion [330,331]. Consequently, the top quark spins are (anti-) parallel and the top quarks have opposite (same) helicities for $t\bar{t}$ production via $q\bar{q}$ annihilation (gluon-gluon fusion). Above threshold, this simple picture becomes more complicated, as effects of orbital angular momentum must be taken into account. In the high-energy limit, where the top quark mass can be neglected, the conservation of chirality dictates that top and antitop quarks be produced with opposite helicities. Since $t\bar{t}$ production at the Tevatron proceeds mainly via $q\bar{q}$ annihilation, as opposed to the LHC where the main contribution comes from gluon-gluon fusion, the observable correlation will have opposite signs at the two colliders [332].

The short lifetime of the top quark (see Section 3.3.2) assures that its spin information is passed on to its decay products, and is reflected in their corresponding angular distributions. This provides experimental access to spin correlations, and a way to check whether the top quark can indeed be considered as a free quark.

The resulting indirect limits on the top quark lifetime (see Section 7.2) can provide limits on the CKM matrix element $|V_{tb}|$, free from the assumption of three quark families [333] together with the measurement of the top quark branching fractions (Section 6.2). In addition, spin correlations probe the dynamics of top quark production and decay for possible contributions from physics beyond the SM.

The down-type ($T_3 = -\frac{1}{2}$) decay products of the $W$ boson from top quark decay are most sensitive to the original top quark spin. Their angular distribution in the top-quark rest frame is described by $1 + \cos\theta$, with $\theta$ being the angle between the line of flight of the down-type fermion and the top spin direction. The experimental difficulties of distinguishing between jets from up-type and down-type quarks (charm tagging would help only in 50% of the cases) can be avoided by focusing on the dilepton final state, where the charged (down-type) leptons are clearly identified.

At the Tevatron, an optimal spin-quantization basis is provided by the "off-diagonal" basis [334, 335], where the spins of top and antitop quarks produced by $q\bar{q}$ annihilation are fully aligned for all energies, and only the contribution of top quark pairs from gluon-gluon fusion leads to a reduction of the correlation. The off-diagonal basis is defined via the top quark's velocity $\beta^*$ and scattering angle $\theta^*$ in the collision rest frame of the incoming partons. The quantization axis then forms an angle $\psi$ with the proton-antiproton beam axis, defined by $\tan\psi = \beta^{*2}\sin\theta^*\cos\theta^*/(1 - \beta^{*2}\sin^2\theta^*)$. Consequently, in the limit of $\beta^* \to 0$ (top quark production at rest), the spins of top and antitop quarks point along the beam axis in the same direction. At very high energies, the spins are aligned with respect to the direction of the $t\bar{t}$ momenta.

Using as observables the angles $\theta_+$ and $\theta_-$ of the down-type fermions relative to the quantization axis in the rest frame of their respective parent (anti-) top quark, the spin correlation is given by [336]:

$$\frac{1}{\sigma}\frac{d^2\sigma}{d(\cos\theta_+)d(\cos\theta_-)} = \frac{1 + \kappa\cdot\cos\theta_+\cdot\cos\theta_-}{4}, \qquad (26)$$

where the correlation coefficient $\kappa$ is predicted to be $+0.88$ at Run I of the Tevatron when using the off-diagonal basis. Since the distribution is symmetric under exchange of the two angles, an electric charge measurement of the top decay products is not necessary.

D0 performed a first search for evidence of spin correlations in $t\bar{t}$ production in Run I, using a 0.1 fb$^{-1}$ dilepton data sample containing six candidate events [337]. From the dependence of a likelihood function on $\kappa$, at 68% C.L. a lower limit on $\kappa$ of $-0.25$ was extracted. This is in agreement with the standard model expectation and disfavors anti-correlation of spins ($\kappa = -1$) that would arise from $t\bar{t}$ production via a scalar particle. While this limit is rather weak, it is a proof of principle that the analysis can be performed. Unfortunately, there has been no result as yet from Run II, although it would greatly benefit from the increase in data already available.
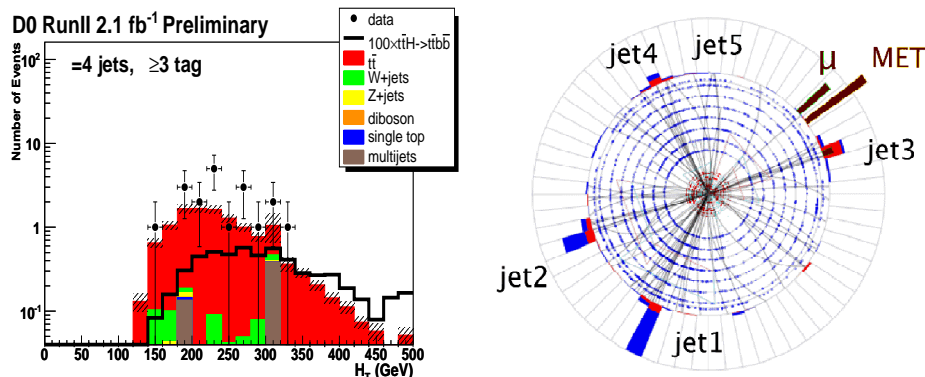
Fig. 24: Left: $H_T$ distribution observed in D0's 2.1 fb$^{-1}$ lepton + jets data with four jets and at least three $b$ tags, compared with expected standard model background processes and $t\bar{t}H$ signal scaled up by a factor of 100. Right: Event display ($xy$-view along the proton beam direction) for the triple $b$ tagged event of highest $H_T$ (444 GeV). The first three jets have $b$ tags [338].

### 5.6. *Search for associated Higgs boson production*

D0 performs a first search for associated $t\bar{t}$ and standard model Higgs boson production in the $t\bar{t}b\bar{b}$ final state in 2.1 fb$^{-1}$ of $b$ tagged lepton + jet data [338]. While the observation of a significant signal in this channel is beyond the reach of the Tevatron, this analysis can nevertheless contribute to future combinations of the Tevatron searches for Higgs bosons at low masses, as favored by the standard model (see Section 7.3.4). The investigated events exhibit high jet and $b$ tag multiplicities that were not studied separately before. It is therefore interesting to search for deviations from the SM predictions that could arise, e.g., from anomalous top-Higgs couplings [339] or from a new quark singlet of charge $\frac{2}{3}e$ [340].

The signal signature has the $t\bar{t}$ lepton + jets event characteristics, but with two additional $b$ jets from the Higgs boson decay. The main background arises from $t\bar{t}$ with additional heavy-flavor jet production, but also $W$ boson + jets and QCD multijet production contribute to the background. For signal discrimination, the shape of the $H_T$ distribution of the selected jets is used in events with four or at least five jets and one, two or at least three $b$ tags. The observed events in all these distributions are consistent with background expectation, which is especially interesting for the events with at least three $b$ tags that were studied separately for the first time. Figure 24 shows the observed $H_T$ distribution for events with four jets and at least three $b$ tags, and an event display for the triple $b$ tagged event of highest $H_T$.

Since no signal is observed, 95% C.L. limits on $t\bar{t}H$ production multiplied by $\mathcal{B}(H \to b\bar{b})$ are derived for Higgs boson masses between 105 and 155 GeV/c$^2$. For

a Higgs boson mass of 115 GeV/c$^2$, the expected limit is a factor of 45 larger than the SM production rate, while the observed limit is a factor of 64 above the SM expectation. Optimization of the preselection (currently corresponding to the standard $t\bar{t}$ selection) for the $t\bar{t}H$ signal, and of the signal discrimination using additional kinematic variables, is underway.

## 5.7. *Search for top quark pair production beyond the standard model*

### 5.7.1. *Search for a narrow-width resonance decaying into $t\bar{t}$*

The existence of yet undiscovered heavy resonances could be revealed through their decays into top quark pairs, which would add a resonant contribution to the standard model process. Theories beyond the standard model predict the existence of massive $Z$-like bosons, for example, such as Kaluza-Klein excitations of the gluon [341] or of $\gamma$ and $Z$ bosons [342], extended gauge theories [343, 344], massive axigluons with axial vector couplings [345] or topcolor [346, 347].

The wealth of such models demonstrates the importance of model-independent searches. One general way an additional production mode can be observed – provided the resonance $X$ decaying to $t\bar{t}$ is sufficiently heavy and narrow – is to analyze the $t\bar{t}$ invariant mass distribution for an excess over expectation. In the corresponding analyses performed at the Tevatron, no significant deviations from the SM expectation have thus far been observed, resulting in 95% C.L. upper limits on $\sigma_X \cdot \mathcal{B}(X \to t\bar{t})$ as a function of resonance mass $M_X$.

These results can be used to set lower mass limits for specific benchmark models that provide easy comparison. For example, topcolor [346, 347] provides a dynamic electroweak symmetry breaking mechanism via a top quark pair condensate [348] $Z'$, formed by a new strong gauge force, that couples preferentially to the third fermion generation. Particularly, a topcolor-assisted technicolor model [307, 312] predicts this $Z'$ boson to couple strongly only to the first and third generation of quarks, while exhibiting no significant coupling to leptons. This leptophobic and topophyllic $Z'$ boson has a significant cross section $\sigma(p\bar{p} \to Z' \to t\bar{t})$ that is observable at the Tevatron for a variety of masses and widths, and is used as a reference model.

CDF and D0 performed model-independent searches for narrow massive vector bosons decaying into $t\bar{t}$ already in Run I in lepton + jets datasets of 106 pb$^{-1}$ and 130 pb$^{-1}$, respectively. Using the best kinematic fit to the $t\bar{t}$ hypothesis in each event, the $t\bar{t}$ invariant mass distribution was reconstructed and no excess observed above expectation. The resulting upper limits on $\sigma_X \cdot \mathcal{B}(X \to t\bar{t})$ are turned into 95% C.L. mass limits of $M_{Z'} > 480$ GeV/c$^2$ for CDF [349] and $M_{Z'} > 560$ GeV/c$^2$ for D0 [350]. For these results, a width of the $Z'$ (or $X$) of 1.2% of its mass is assumed, which is well below the detector mass resolutions for $t\bar{t}$ systems. Consequently, the results are dominated by detector resolution and independent of $\Gamma_{Z'}$ for values below the mass resolution of a few percent ($\approx 0.04 M_{Z'}$ for D0 in Run I [351]). This kind of resonance width is also used in the Run II measurements described below.
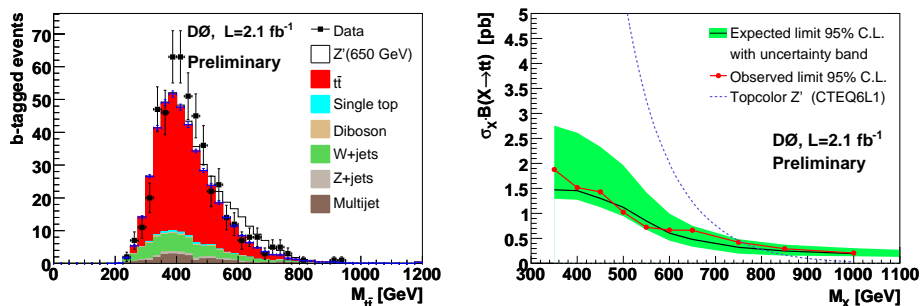
Fig. 25: Left: Expected and observed $t\bar{t}$ invariant mass distribution in lepton + jets events with four or more jets. Right: Expected and observed 95% C.L. upper limits on $\sigma_X \cdot \mathcal{B}(X \to t\bar{t})$ [352].

In Run II, both CDF and D0 search for a generic heavy resonance $X$ of narrow width ($\Gamma_X = 0.012 M_X$) compared to the detector mass resolution in $b$ tagged lepton + jets datasets. The $t\bar{t}$ invariant mass spectrum is reconstructed using either the best kinematic fit to the $t\bar{t}$ production hypothesis (CDF) or directly from the four-momenta of the up to four leading jets, the lepton and the neutrino momentum (D0). The latter approach was shown to provide greater sensitivity for large resonance masses than the previously used constrained kinematic fit, and also allows for the inclusion of data with fewer than four jets in case jets merged. As both experiments observe no significant deviation from SM expectation, 95% C.L. upper limits on $\sigma_X \cdot \mathcal{B}(X \to t\bar{t})$ are given for values of $M_X$ between 450 and 900 GeV/c$^2$ (CDF) and $M_X$ between 350 and 1000 GeV/c$^2$ (D0, see Fig. 25) in increments of 50 GeV/c$^2$.

Both experiments provide 95% C.L. mass limits for the leptophobic topcolor-assisted technicolor $Z'$ boson as a benchmark model. With 1 fb$^{-1}$, CDF finds $M_{Z'} > 720$ GeV/c$^2$ (expected limit = 710 GeV/c$^2$) [353], while D0 finds $M_{Z'} > 760$ GeV/c$^2$ (expected limit = 795 GeV/c$^2$) [352] using 2.1 fb$^{-1}$ of data, which supersedes a previous result on 0.9 fb$^{-1}$ of data [354]. CDF also obtains a result on a subset of 0.7 fb$^{-1}$ of the data analyzed above, using an untagged lepton + jets sample where $b$ tag information only contributes as a way to reduce jet combinatorics in a standard model $t\bar{t}$ matrix element based reconstruction of $M_{t\bar{t}}$. This yields a slightly better limit than the analysis on the full 1 fb$^{-1}$ of $M_{Z'} > 725$ GeV/c$^2$ [355].

For future studies, it would be interesting to see how sensitive the observed limits are to the assumption of $Z$ boson-like couplings used in the analyses. The limits obtained apply to resonances of narrow width only. Wider resonances could be detected by studying the $t\bar{t}$ differential cross section (see Section 5.7.3) or the forward-backward charge asymmetry in $t\bar{t}$ production (see Section 5.3).
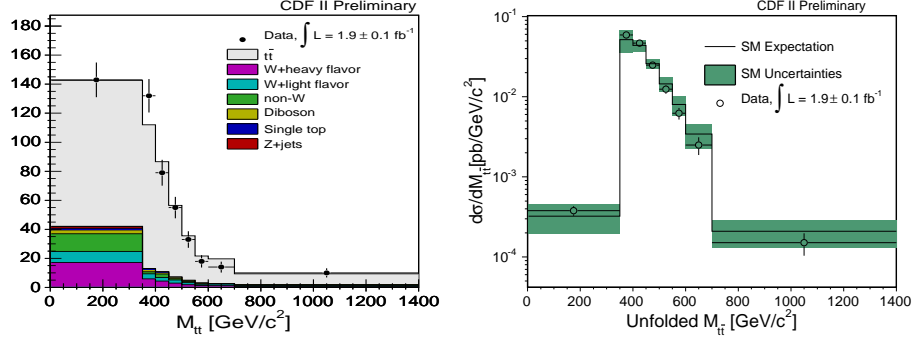
Fig. 26: Left: Expected and observed reconstructed $t\bar{t}$ invariant mass distribution in $b$ tagged lepton + jets events with at least four jets. Right: Corresponding $t\bar{t}$ differential cross section after background subtraction and unfolding, compared to the SM expectation [323].

### 5.7.2. *Search for $t\bar{t}$ production via a massive gluon*

Instead of a new color singlet particle decaying into $t\bar{t}$ , as described in the previous subsection, there could also be a new massive color octet particle $G$ contributing to $t\bar{t}$ production [347]. Such a "massive gluon" production mode would interfere with the corresponding standard model production process. Assuming SM top decay, CDF has performed a search for a corresponding contribution by comparing the $t\bar{t}$ invariant mass distribution in a 1.9 fb$^{-1}$ $b$ tagged lepton + jets dataset with the standard model expectation. As the largest discrepancy relative to the standard model is found to be 1.7 sd for masses and widths of 400 GeV/c$^2$ $\leq M_G \leq$ 800 GeV/c$^2$ and $0.05 \leq \Gamma_G/M_G \leq 0.5$, respectively, 95% C.L. upper and lower limits are extracted on the corresponding coupling strengths of such massive gluons [356].

### 5.7.3. *Measurement of the $t\bar{t}$ differential cross section $(d\sigma/dM_{t\bar{t}})$*

Since new production mechanisms for top quark pairs could manifest themselves in the $t\bar{t}$ invariant mass distribution as resonances of different widths or, more generally, as shape distortions [357], one approach for detecting such contributions is to compare the shape of the observed differential $t\bar{t}$ production cross section $d\sigma/dM_{t\bar{t}}$ with the SM expectation.

CDF reconstructs the $t\bar{t}$ invariant mass spectrum in a 1.9 fb$^{-1}$ $b$ tagged lepton + jets data sample (see Fig. 26) by combining the four-vectors of the four leading jets, lepton and $\not{p}_T$. After subtracting the background processes, the distortions in the reconstructed distribution due to detector effects, object resolutions and geometric/kinematic acceptance are corrected for through a regularized unfolding technique [358]. From the unfolded distribution, the $t\bar{t}$ differential cross section $d\sigma/dM_{t\bar{t}}$ is extracted and its shape compared with the SM expectation. The compar-

ison shows good agreement with the standard model, yielding an Anderson-Darling $p$-value of 0.45 [323].

### 5.7.4. *Search for new heavy top-like quark pair production*

The number of light neutrino species (for $m_\nu < m_Z/2$) has been determined to be $N_\nu = 2.9840 \pm 0.0082$ based on the invisible $Z$ boson decay width in precision electroweak measurements [68]. This rules out a fourth generation of fermions with a light neutrino $\nu_4$. However, the existence of a fourth generation is consistent with precision electroweak data for a fermion mass range $m_Z/2 \lesssim m_{f4} \lesssim \mathcal{O}(174 \text{ GeV/c}^2)$, even without introducing new physics [359,360]. Fourth-generation quark masses up to 400 GeV/c$^2$ are compatible with current measurements, and are constrained to exhibit small mass splitting, so that decays of an up-type fourth-generation quark into $Wq$ ($q = d, s, b$) are preferred [361]. Such an additional generation would have a drastic impact on the phenomenology of the Higgs boson, thereby relaxing the mass bounds obtained from the SM up to 750 GeV/c$^2$ at 95% C.L., and altering expected kinematics and production rates.

The existence of a fourth chiral-fermion generation is predicted by various extensions of the standard model, for example, in an SO(1,13) framework unifying charges and spins [362], or in models with flavor democracy [363, 364]. Other models that add more exotic additional heavy quarks that can decay via $Wq$ have been brought up as well [365]. For example, the "beautiful mirrors" model [366] introduces mirror quark-doublets with the same quantum numbers as their SM counterparts, but with vector couplings to the $W$ boson. This addition helps to improve the fit of electroweak observables by removing the observed discrepancy in the forward-backward asymmetry of the $b$ quark.

CDF performs a search for pair production of heavy top-like quarks ($t'\bar{t}'$) that do not necessarily exhibit SM-like up-type fourth-generation properties in terms of charge or spin. The analysis is based on the assumptions that the $t'$ is pair-produced via the strong interaction, has a mass larger than that of the top quark, and decays promptly into a $W$ boson and a down-type $d, s, b$ quark with 100% branching ratio. As a consequence, the $t'$ decay chain is identical to that of the top quark, and $t'\bar{t}'$ production can be sought in a lepton + jets sample selected solely based on event kinematics to not restrict the search to $Wb$ final states by using $b$ tagging.

The $t'$ signal can be distinguished from SM background using, e.g., the observed distributions of total transverse energy $H_T$ in the event based on lepton, jets and $\not{p}_T$, and the reconstructed $t'$ mass ($M_{\text{reco}}$) from the best kinematic fit to the $t'\bar{t}'$ hypothesis in each event (see Fig. 27). Superseding a previously published result based on 0.8 fb$^{-1}$ [368], CDF uses a two-dimensional binned likelihood fit in $H_T$ and $M_{\text{reco}}$ to separate SM background and $t'$ signal in 2.8 fb$^{-1}$ of data [367].

Since no evidence for $t'$ production is found, 95% C.L. upper limits on the $t'\bar{t}'$ production cross section (assuming $\mathcal{B}(t' \to Wq) = 100\%$) are derived for 180 GeV/c$^2$ $\leq m_{t'} \leq 500 \text{ GeV/c}^2$. Assuming SM couplings, a 95% C.L. lower limit on the fourth-
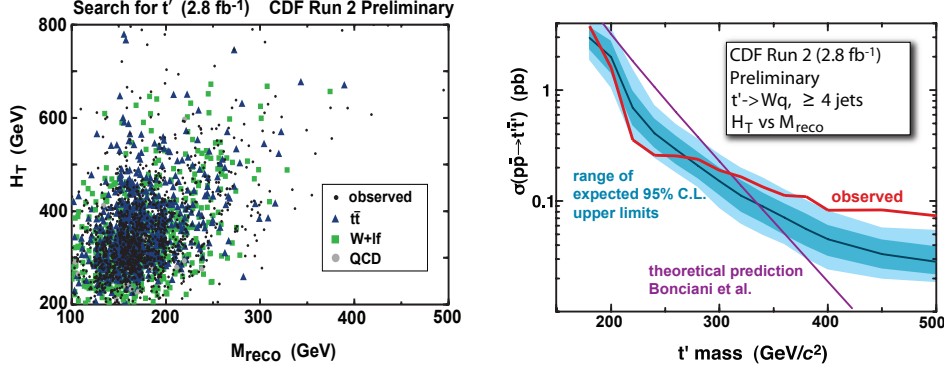
Fig. 27: Left: $H_T$ versus $M_{\mathrm{reco}}$ distribution observed in data (black points) overlaid with the fitted number of standard model background events from $t\bar{t}$, $W$+jets and QCD. Right: Expected and observed 95% C.L. upper limits on the $t'\bar{t}'$ production cross section, assuming 100% $\mathcal{B}(t' \to Wq)$. The dark/light regions represent the 1/2 sd bands on the expected limit [367].

generation $t'$ mass of 311 GeV/c$^2$, based on the calculations in Refs. [116, 117], is obtained, where the largest systematic uncertainty arises from the jet energy scale. The deviation of the observed limit from its expected value above $\approx$400 GeV/c$^2$ is being investigated. Using *a priori* defined groups of bins in $H_T$ and $M_{\mathrm{reco}}$, the $p$-values to observe at least the number of events found in data, given the SM expectation, are evaluated. With the smallest $p$-value being 0.01, the excess in the data tails is concluded to be not statistically significant.

### 5.7.5. *Search for scalar top quark production*

Many processes beyond the standard model exhibit signatures similar to $t\bar{t}$ events. Consequently, $t\bar{t}$ data samples can, in principle, contain admixtures of such contributions.

For example, the Minimal Supersymmetric Standard Model (MSSM) [369] predicts that supersymmetric partners of the top quarks, scalar top or "stop" quarks, are predominantly produced in pairs via the strong interaction just like SM top quarks. The stop-quark pair-production cross section has been calculated at NLO supersymmetric-QCD and depends mainly on the stop quark mass and very little on other supersymmetric parameters [370]. At a center of mass energy of 1.96 TeV, the pair production cross section for the lightest stop quarks ($\tilde{t}_1\bar{\tilde{t}}_1$) of 175 GeV/c$^2$ mass is 0.58 pb [371], or roughly 10% of the SM $t\bar{t}$ production rate (see Section 3.1). The observable final states from stop decays depend strongly on supersymmetric parameters, especially the masses of supersymmetric particles in the decay chain.
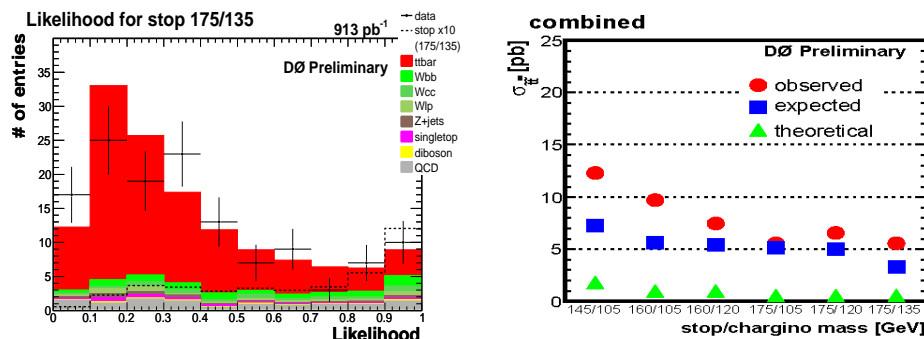
Fig. 28: Left: Multivariate kinematic discriminant distribution for electron $+\geq 4$ jets events in 0.9 fb$^{-1}$ of D0 data and simulated signal and background. The dashed black line shows the expected signal shape for a $\tilde{t}_1$ ($\tilde{\chi}_1^{\pm}$) mass of 175 (135) GeV/c$^2$, enhanced by a factor of ten. Right: Expected and observed 95% C.L. limits on the $\tilde{t}_1\bar{\tilde{t}}_1$ production cross section, together with the prediction for different stop and chargino mass combinations [376].

In Run II, the decay mode $\tilde{t}_1 \rightarrow b\ell^+\tilde{\nu}_\ell$ has been studied by D0 [372] in 0.4 fb$^{-1}$ of data. The decay channel $\tilde{t}_1 \rightarrow c\tilde{\chi}_1^0$, where the lightest neutralino $\tilde{\chi}_1^0$ is the lightest supersymmetric particle (LSP), was studied by CDF [373] in 0.3 fb$^{-1}$ and by D0 in 0.4 and 1 fb$^{-1}$ of data [374, 375]. 95% C.L. mass-exclusion limits on the involved supersymmetric particles were provided for both decay channels.

Another important decay mode for stop is $\tilde{t}_1 \rightarrow \tilde{\chi}_1^+ b$, where the lightest chargino $\tilde{\chi}_1^+$ decays to $W^+\tilde{\chi}_1^0$, resulting in final states identical to those from $t\bar{t}$ decays, but with two additional neutralinos (LSPs) that contribute to $\not{p}_T$. First limits for this channel were provided by CDF in Run I on 0.1 fb$^{-1}$ of lepton + jets data [377].

D0 performs the first study of this channel in Run II in 0.9 fb$^{-1}$ $b$ tagged lepton + jets data [376]$^c$, assuming a neutralino mass of 50 GeV/c$^2$ (slightly above the limit set by LEP [379]) while varying the stop and chargino masses between 145 and 175 GeV/c$^2$, and 105 and 135 GeV/c$^2$, respectively.

A possible stop admixture in the sample is searched for by employing a multivariate discriminant based on kinematic event properties (see Fig. 28), with the main challenge being to separate the topologically similar $t\bar{t}$ background from $\tilde{t}_1\bar{\tilde{t}}_1$ signal. Counterintuitively, the additional neutralinos do not provide large differences in $\not{p}_T$ that can be exploited, but the larger chargino mass compared to that of the $W$ boson reduces the phase space for $b$ jets in the event.

Since no significant signal admixture in the lepton + jets dataset is observed, 95% C.L. upper limits on the $\tilde{t}_1\bar{\tilde{t}}_1$ production rate are set that are a factor of $\approx 7-12$ above the prediction, as illustrated in Fig. 28. Consequently, the stop quark masses

---

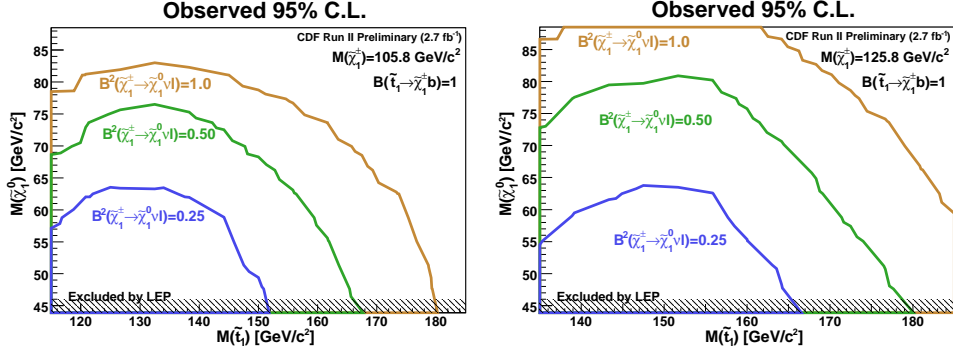$^c$An updated version of the result has been published after completion of this review, see Ref. [378].

Fig. 29: Excluded areas observed at 95% C.L. in the neutralino versus stop mass plane for various assumed dilepton branching fractions and two different chargino masses (left: 105.8 GeV/c$^2$, right: 125.8 GeV/c$^2$), obtained by CDF in 2.7 fb$^{-1}$ of dilepton data. The contributions of $e, \mu, \tau$ to the final state are assumed to be equal [380].

considered cannot yet be excluded, and this analysis should greatly benefit from the increased datasets already in hand. The weaker observed limits relative to their expected values are driven by the muon + jets channel. The corresponding excess in data was tested with pseudo-datasets to be statistically consistent with the standard model expectation.

CDF searches for a stop admixture in the $t\bar{t}$ dilepton channel using a 2.7 fb$^{-1}$ dilepton dataset of both $b$ tagged and untagged events [380]. Assuming $\tilde{\chi}_1^0$ to be the LSP, heavy sfermions, the stop mass below the top mass, and the chargino mass smaller than the mass difference between stop and $b$ quark, the decay $\tilde{t}_1 \to \tilde{\chi}_1^+ b$ obtains 100% branching fraction. The dilepton final state resulting from $\tilde{\chi}_1^\pm \to \tilde{\chi}_1^0 \ell^\pm \nu$ decays is then identical to the $t\bar{t}$ final state, but with two additional neutralinos contributing to $\not{p}_T$. It can be reached through a variety of chargino decay channels, resulting in variations of the branching fraction depending on SUSY parameters.

The stop quark signal is discriminated from standard model background using a single quantity, the reconstructed stop mass, in a fit to the observed data distribution. The mass is reconstructed from this underconstrained system by treating the neutralino and neutrino from each stop decay as one massive pseudo-particle, and then applying a standard top mass reconstruction technique in the dilepton channel, neutrino weighting (see Section 7.3.1). Since the observed distributions are consistent with standard model processes, 95% C.L. limits are extracted on the dilepton branching ratio in $\tilde{t}_1\bar{\tilde{t}}_1$ production for stop masses $115 - 185$ GeV/c$^2$, neutralino masses $43.9 - 88.5$ GeV/c$^2$, and chargino masses $105.8 - 125.8$ GeV/c$^2$, as illustrated in Fig. 29. A 100% branching fraction for $\tilde{t}_1 \to \tilde{\chi}_1^+ b$, and equal contributions from $e, \mu$ and $\tau$ to the final state are assumed throughout.

Model-independent searches for novel admixtures in top quark samples, via the

search for anomalous event kinematics, were discussed in Section 5.4.

## 5.8. *Single top quark production*

Electroweak production of top quarks without their antiparticles can provide a direct measure of the $|V_{tb}|$ CKM matrix element, test the $Wtb$ vertex structure, and probe for physics beyond the standard model, such as flavor changing neutral currents or new heavy gauge bosons $W'$ (see Section 3.2). A thorough understanding of single top quark production is also important for studies of processes with similar signatures, such as standard model $W$-Higgs associated production, for which this process constitutes a major background. While the single-top production rate is $\approx 40\%$ of the strong $t\bar{t}$ production, the signal extraction from background is very challenging because only one top quark signature is present in the final state. Simple kinematic selections are insufficient for such an analysis, and sophisticated multivariate techniques have to be deployed.

For single top quark production at the Tevatron, only $s$- and $t$-channel production are relevant, contributing, respectively, $0.88^{+0.12}_{-0.11}$ pb and $1.98^{+0.28}_{-0.22}$ pb to the total rate at NLO [156]. The experimental signature comprises a $b$ jet and the $W$ boson decay products from the top quark decay. In the $s$- ($tb$-) channel, one additional $b$ jet arises from the $b$ quark produced together with the top quark. In the $t$- ($tqb$-) channel, a forward light-quark jet accompanies the production of the top quark, sometimes along with another $b$ jet from the gluon splitting into $b\bar{b}$ (see Fig. 8). In order to suppress multijet background, the $W$ boson is usually required to decay leptonically into an electron or muon and corresponding neutrino. Consequently, the final state signature of single top quark production contains an energetic isolated electron or muon, $\not{p}_T$ and two or three jets, with at least one of them being a $b$ jet. As usual, additional jets can arise from initial- or final-state radiation.

### 5.8.1. *Production cross section and $V_{tb}$*

Searches for single top quark production were already performed in Run I using 0.1 fb$^{-1}$ of data by D0 [381, 382] and by CDF [383, 384], yielding upper limits on the production rate that were at least a factor of six larger than the SM expectation. In Run II, first results were published using 0.2 fb$^{-1}$ of data by CDF [385] and D0 [386, 387], where the best observed limit was less than a factor of three greater than the SM prediction. Finally, D0 published first evidence for single top quark production using 0.9 fb$^{-1}$ of data [21, 22], observing a signal of 3.6 standard deviations significance. Preliminary results from CDF based on 2.2 fb$^{-1}$ confirmed evidence for single top quark production [388–391] with an observed signal significance of 3.7 standard deviations obtained by combining three of these analyses [392][d].

The analyses yielding first evidence for electroweak top quark production apply event selections requiring one energetic isolated electron or muon and $\not{p}_T$. CDF uses

---

[d]A slightly updated version of the result was published by CDF [23] after completion of this review.

Table 14: Expected and observed event yields of the single top selections for $e$ and $\mu$, single and double $b$ tagged channels combined (left for D0 based on 0.9 fb$^{-1}$ [21], and right for CDF based on 2.2 fb$^{-1}$ [390]). For the D0 result, the overall $W$ + jets background includes $Z$ + jets and diboson events.

| Source | 2 jets | 3 jets | 4 jets |
|--------|--------|--------|--------|
| $tb$ | 16±3 | 8±2 | 2±1 |
| $tqb$ | 20±4 | 12±3 | 4±1 |
| $t\bar{t}$ | 59±10 | 135±26 | 154±33 |
| $Wb\bar{b}$ | 261±55 | 120±24 | 35±7 |
| $Wc\bar{c},Wcj$ | 151±31 | 85±17 | 23±5 |
| $Wjj$ | 119±25 | 43±9 | 12±2 |
| Multijets | 95±19 | 77±15 | 29±6 |
| BG Sum | 686±41 | 460±39 | 253±38 |
| Data | 697 | 455 | 246 |

| Source | 2 jets | 3 jets |
|--------|--------|--------|
| $tb$ | 41.2±5.9 | 13.5±1.9 |
| $tqb$ | 62.1±9.1 | 18.3±2.7 |
| $t\bar{t}$ | 146.0±20.9 | 338.7±48.2 |
| $Wb\bar{b}$ | 461.6±139.7 | 141.1±42.6 |
| $Wc\bar{c},Wcj$ | 395.0±121.8 | 108.8±33.5 |
| $Wjj$ | 339.8±56.1 | 101.8±16.9 |
| Multijets | 59.5±23.8 | 21.3±8.5 |
| Dibosons | 63.2±6.3 | 21.5±2.2 |
| $Z$+jets | 26.7±3.9 | 11.0±1.6 |
| BG Sum | 1491.8±268.6 | 754.8±91.3 |
| Data | 1535 | 712 |

events with two or three jets and one or two $b$ tags, while D0 includes additionally events with four jets, where the extra jet arises from initial- or final-state radiation. The signal acceptances for the $s$- and $t$-channel are 2.8% and 1.8% (CDF), and 3.2% and 2.1% (D0). The expected and observed event yields are shown in Table 14. The dominant background contributions come from $W$+jets production, $t\bar{t}$ production in the lepton + jets or dilepton final states, where one jet or lepton is not reconstructed, and from multijet production. The main sources of systematic uncertainty are background normalization, jet energy scale, and the modeling of the $b$ tagging and triggers. As can be appreciated from the table, the uncertainty on the background is larger than the expected signal, which makes advanced analysis techniques necessary.

D0 applies three different multivariate analysis techniques to the preselected data sample: boosted decision trees (BDT), Bayesian neural networks (BNN) and matrix elements (ME), where the latter two reflect reoptimized studies [22] of previous work [21]. Being based on leading-order matrix elements for the description of signal and background processes, the ME analysis does not use four-jet events. For each analysis, the combined $s$- and $t$-channel cross sections are extracted from the peak of the Bayesian posterior probability density derived from a binned likelihood of the respective discriminants. The results are then combined, yielding:

$$\begin{aligned}
\sigma^{\text{obs}}(p\bar{p} \to tb + X,\ tqb + X) &= 4.9^{+1.4}_{-1.4} \text{ pb (BDT,} \quad 3.4 \text{ sd)} \\
&= 4.4^{+1.6}_{-1.4} \text{ pb (BNN,} \quad 3.1 \text{ sd)} \\
&= 4.8^{+1.6}_{-1.4} \text{ pb (ME,} \quad 3.2 \text{ sd)} \\
&= 4.7^{+1.3}_{-1.3} \text{ pb (Combined, 3.6 sd)},
\end{aligned} \tag{27}$$

where the uncertainties correspond to the combination of statistical and systematic

sources. The observed production rates are in agreement with SM expectation and with each other. The significances in the parentheses are obtained from studies of large ensembles of pseudo-experiments. The expected sensitivity of the combined result is 2.3 standard deviations, indicating that the measurement benefited from a statistical upward fluctuation. Separate measurements of the $s$- and $t$-channel cross sections are also performed with the BDT analysis. The results are $\sigma_s = 1.0 \pm 0.9$ pb and $\sigma_t = 4.2^{+1.8}_{-1.4}$ pb, where the other channel (not measured) is set to its SM expectation ($\sigma_s = 0.88^{+0.12}_{-0.11}$ pb and $\sigma_t = 1.98^{+0.28}_{-0.22}$ pb [156]). The observed enhancement in the $t$-channel with respect to the standard model prediction is not statistically significant.

CDF uses the following multivariate analysis techniques on their preselected dataset: neural networks (NN [388]), a likelihood function (LHF [389]), a matrix element discriminant (ME [390]) and boosted decision trees (BDT [391]). The results are:

$$
\begin{aligned}
\sigma^{\mathrm{obs}}(p\bar{p} \to tb + X, \ tqb + X) &= 2.0^{+0.9}_{-0.8} \text{ pb (NN,} \qquad 3.2 \text{ sd)} \\
&= 1.8^{+0.9}_{-0.8} \text{ pb (LHF,} \qquad 2.0 \text{ sd)} \\
&= 2.2^{+0.8}_{-0.7} \text{ pb (ME,} \qquad 3.4 \text{ sd)} \\
&= 2.2^{+0.7}_{-0.7} \text{ pb (Combined, } 3.7 \text{ sd)} \\
&= 1.9^{+0.8}_{-0.7} \text{ pb (BDT,} \qquad 2.8 \text{ sd),}
\end{aligned}
\tag{28}
$$

where the uncertainties given are both statistical and systematic. The BDT analysis became available after the combination of results [392], and was therefore not included in that compilation. The observed results agree with each other and with the standard model. The expected sensitivity of the combination is 5.1 standard deviations, pointing to a statistical downward fluctuation in the data.

Figure 30 shows the discriminant outputs of the two most significant single measurements from CDF (ME) and D0 (BDT). A graphical summary of the measurements and a comparison with the standard model expectation is given in Fig. 31. All analyses assume a top quark mass of 175 GeV/c$^2$, $\mathcal{B}(t \to Wb) = 100\%$, and the SM ratio for $s$- to $t$-channel cross sections.

In a recent update, CDF has added 0.5 fb$^{-1}$ of data to its single top sample, and thereby increased the observed significance for all previous analysis techniques. The matrix element analysis yields again the most significant single result, exceeding four standard deviations. A combination of the measurements has not yet become available. The results for 2.7 fb$^{-1}$, with combined statistical and systematic uncertainties, are [393–396]:

$$
\begin{aligned}
\sigma^{\mathrm{obs}}(p\bar{p} \to tb + X, \ tqb + X) &= 2.1^{+0.7}_{-0.6} \text{ pb (NN, } 3.7 \text{ sd)} \\
&= 2.0^{+0.9}_{-0.8} \text{ pb (LHF, } 2.6 \text{ sd)} \\
&= 2.7^{+0.8}_{-0.7} \text{ pb (ME, } 4.2 \text{ sd)} \\
&= 2.4^{+0.8}_{-0.7} \text{ pb (BDT, } 3.6 \text{ sd).}
\end{aligned}
\tag{29}
$$

Since the single top quark production rate is proportional to $|V_{tb}|^2$, the observed cross sections can be turned into measurements of $|V_{tb}|$ under the following
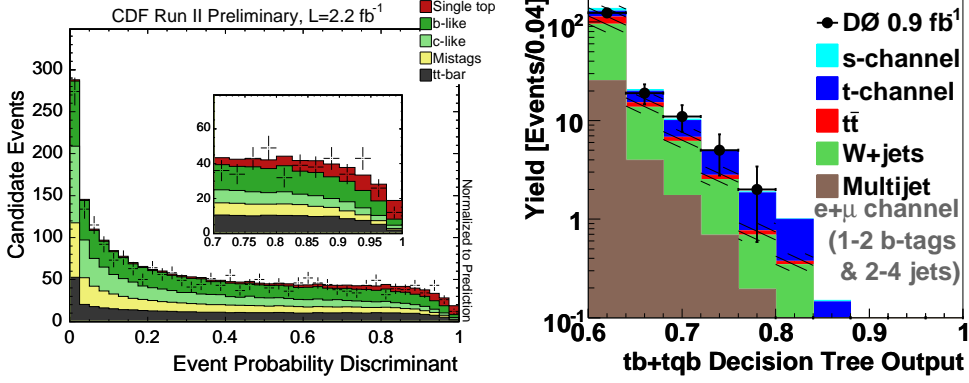
Fig. 30: Multivariate discriminant outputs observed in single-top candidate events compared to contributions from signal and background processes. Left: CDF matrix element discriminant, with yields normalized to their SM predictions [390]. Right: D0 BDT output in the single-top signal region, with signal normalized to the measured cross section [21].

assumptions: (i) there are no single top quark production modes beyond the SM, (ii) single top quark production and decay are dominated by the $Wtb$ interaction ($|V_{tb}| \gg |V_{td}|, |V_{ts}|$, as indicated by measurements of $R$ described in Section 6.2), and (iii) the $Wtb$ interaction exhibits a $V - A$ structure and is CP conserving. The latter premise allows for anomalous left-handed vector couplings $f_1^L$ (see Section 3.3.3), but not for right-handed vector or tensor couplings. Anomalous $f_1^L$ values ($\neq 1$) do not affect the $t\bar{t}$ production rate or kinematics, nor $tb$ or $tqb$ kinematics, but simply rescale the single-top production rate. Consequently, $|V_{tb}f_1^L|$ extracted from single-top production can be $> 1$, and constraining the measurement to lie between $0 - 1$ implies that $f_1^L = 1$, as predicted by the standard model. The measurements of $|V_{tb}f_1^L|$ and $|V_{tb}|$ are independent from the number of fermion generations and unitarity of the CKM matrix.

Using the result of the BDT analysis and a positive flat prior for $|V_{tb}|^2$, D0 obtains $|V_{tb}f_1^L| = 1.31^{+0.25}_{-0.21}$. Restricting the prior to $[0, 1]$ yields $|V_{tb}| = 1.00^{+0.00}_{-0.12}$, with a corresponding 95% C.L. lower limit of $|V_{tb}| > 0.68$ [22]. CDF uses its combined measurement in the same way to obtain a 95% C.L. lower limit of $|V_{tb}| > 0.66$ [392]. The matrix element analysis based on 2.7 fb$^{-1}$ yields $|V_{tb}| > 0.71$ [395].

With most of the current measurements giving evidence of $> 3$ sd for single top quark production, the observation at the five standard deviation level seems imminent at the Run II Tevatron. Extrapolating from the 2.2 fb$^{-1}$ result, as illustrated in Fig. 32, CDF estimates that a $> 5$ sd significance should be reached by adding one more fb$^{-1}$ of data to the analyses. D0 could reach that level in the 2.3 fb$^{-1}$
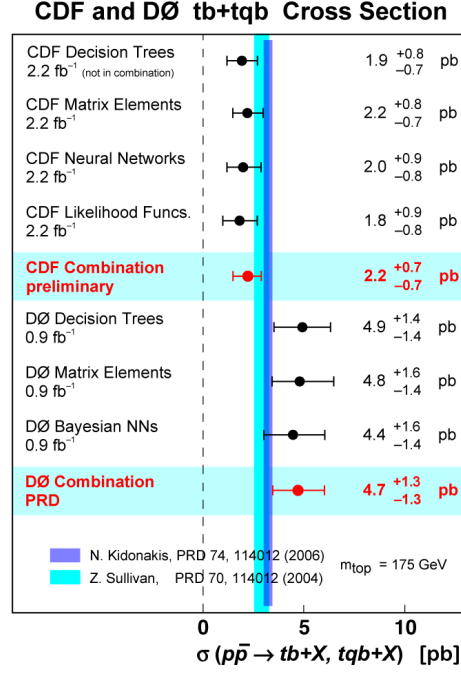
Fig. 31: Cross section measurements of first evidence for single top production, and the combined results from CDF and D0 compared to the SM prediction.

dataset that is currently being analyzed[e].

As discussed in Section 3.2, $s$- and $t$-channel production exhibit different sensitivity to physics beyond the standard model. Measuring both rates separately provides a valuable tool to check for various exotic model contributions to single top quark production. Figure 32 shows D0's expected sensitivity to physics beyond the standard model [164] for the already analyzed data and for the anticipated accumulation of 6.8 fb$^{-1}$ of Run II data. With this increase in integrated luminosity, the exclusion of certain models at 95% C.L. should be feasible. With more than 6 fb$^{-1}$, a measurement of $|V_{tb}|$ with an absolute uncertainty below 0.07 per experiment should be achievable as well. In addition, further refinements of the analysis techniques should facilitate improvements in precision beyond that expected just from the accumulation of more data.

[e]After submission of this review, both collaborations announced 5 sd observations of single top quark production, see Refs. [397, 398].
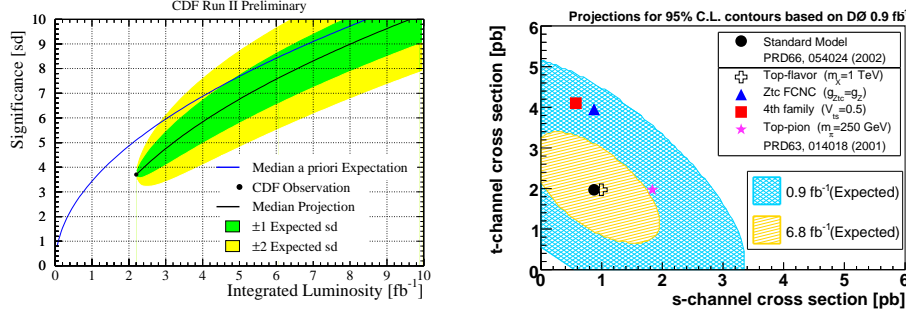
Fig. 32: Left: Extrapolation of the single-top signal significance as a function of integrated luminosity from the 2.2 fb$^{-1}$ CDF analysis result. Right: Expected 95% C.L. contours for a simultaneous measurement of the *s*- and *t*-channel single-top production rate by D0 for different integrated luminosities. The standard model expectation is shown together with various other models.

### 5.8.2. *Polarization of the spin of the top quark*

As opposed to top quark pair production via the strong interaction, where the top quarks are produced essentially unpolarized (see Section 5.5), top quarks produced singly via the electroweak interaction are expected to be highly left-handedly polarized [160]. The polarization of the top quark is reflected in the kinematic distributions of its decay products, providing a test of the $V - A$ structure of the $Wtb$ coupling [137, 399]. An observation of this polarization would also provide limits on the top-quark decay width and $|V_{tb}|$, since this would confirm that top quarks decay before depolarizing through QCD interactions.

Both relevant single top quark production mechanisms at the Tevatron (*s*- and *t*-channel) exhibit up-type–down-type and $tb$ quark lines interconnected by a $W$ boson. Since the $W$ boson couples solely to fermions of left-handed chirality, in their rest frame single top quarks are highly polarized along the direction of the down-type quark [161, 400, 401]. (For the contributing $2 \rightarrow 2$ processes this polarization is 100%. These diagrams are related to the top decay with hadronic $W$ boson decay via crossing symmetry, where the down-type decay products of the $W$ boson exhibit optimal analyzing power.) The optimal spin basis for studying the single-top spin polarization therefore will use the direction of the down-type quark.

For *s*-channel production, predominantly proceeding via $u\bar{d} \rightarrow t\bar{b}$, the antiproton beam is expected to provide the down-type quark most of the time. Indeed, measuring the top quark spin along the direction of the antiproton beam ("antiproton basis") results in 98% of the top quark spins aligned in that direction. For the *t*-channel, the situation is slightly more complicated, since the down-type quark is contained in either the spectator jet or in one of the beams. With the largest contribution to the total production rate arising from $ug \rightarrow t\bar{b}d$, where the down-type

quark produces the (light quark) spectator jet, a reasonable choice for the spin basis is the spectator jet direction ("spectator basis"). Since the spectator jet is emitted in the forward direction, this basis is also still compatible with the cases where the down-type quark is in the initial state, resulting in 96% of the top quarks having their spins polarized along the light-quark jet direction.

With the top quark decaying before it hadronizes, its spin information is passed on to its decay products. A straightforward observable is the angular distribution of the top quark decay product $i$ in the top quark rest-frame:

$$\frac{1}{\Gamma}\frac{d\,\Gamma}{d\cos\theta_i^t} = \frac{1}{2}\Big(1 + \mathcal{A}_{\uparrow\downarrow}\alpha_i\cos\theta_i^t\Big), \tag{30}$$

where $\theta_i^t$ is the angle between the decay product and spin-quantization axis, $\alpha_i$ is the analyzing power describing the correlation between top quark spin and decay product and $\mathcal{A}_{\uparrow\downarrow} = (N_\uparrow - N_\downarrow)/(N_\uparrow + N_\downarrow)$ is the spin asymmetry determining the magnitude of the observable angular correlations. The analyzing power is maximal $(+1)$ for the down-type $(T_3 = -\frac{1}{2})$ decay products of the $W$ boson (charged lepton, $d$- or $s$-quark), making the charged lepton the most sensitive and easily accessible spin analyzer. Using the spin quantization axes described above, the expected spin asymmetry is 0.96 for the $s$-channel and 0.93 for the $t$-channel [161, 400, 401].

To perform a spin polarization measurement at the Tevatron, single top quark production in the $t$-channel is most promising due to its higher rate relative to the $s$-channel. The required integrated luminosity to observe spin polarization in the $t$-channel at the Tevatron was determined in a study, including effects of jet resolution and acceptance [162]. To establish the polarization at a level of five sd, $\approx$5 fb$^{-1}$ of data will be needed, which should be available very soon.

At the LHC, measurements of single-top spin polarization will benefit from the expected high-statistics single-top datasets, and optimal spin bases have already been explored for the two dominant production modes ($t$-channel [163], associated $tW$ production [402]). Already with the first 2 fb$^{-1}$, a polarization measurement with an uncertainty of 4% should be achievable based on the $t$-channel production alone [403].

### 5.8.3. *Search for $W'$ bosons*

Electrically charged gauge bosons that are not part of the standard model are usually denoted as $W'$. Such bosons are predicted in a variety of extensions of the standard model, incorporating larger gauge groups that reduce to the standard model at sufficiently low energies [164, 404].

The most stringent limit to date in a direct search on the mass of such a $W'$ boson has been set by D0 in the leptonic final state ($W' \to \ell\nu$) using 1 fb$^{-1}$ of Run II data [405]. Assuming the $W'$ boson exhibits standard model $W$ boson couplings to fermions, this search excludes the mass range below 1 TeV/c$^2$ at 95% C.L. by studying the tail of the transverse mass [406] spectrum calculated from

lepton transverse energy and $\not{p}_T$. Indirect $W'$ mass constraints are strongly model-dependent and range between lower limits of 549 GeV/c$^2$ and 23 TeV/c$^2$, being derived from (semi-) leptonic processes as well as from astrophysical and cosmological constraints [47].

A direct search for $W'$ bosons in the hadronic final state ($W' \rightarrow q\bar{q}'$) provides a less model-dependent measurement since both left-handed and right-handed $W'$ bosons can be observed in this final state, independent of any assumption about the mass of a right-handed neutrino $m_{\nu_R}$ in the latter case. In contrast to this, the leptonic final state is only accessible for a right-handed $W'$ boson if the corresponding right-handed neutrino is not too massive ($m_{\nu_R} < m_{W'}$). Searches for $W'$ bosons as resonant structures in the dijet invariant mass spectrum have been carried out by UA2 [407] and at the Run I Tevatron by CDF [408] and D0 [409].

Focusing on "hadronic" $W'$ searches using third generation quarks in the final state, reduces the QCD multijet background compared to the (light) dijet final state searches. Such measurements are only sensitive to $W'$ bosons with masses above the $tb$ threshold of $\approx$200 GeV/c$^2$, but the low-mass range is excluded already by the current limits on single top quark production [410]. A $W'$ signal would be observed as peak in the invariant mass distribution of its $tb$ decay products (as usual, $tb$ includes both $t\bar{b}$ and its charge-conjugate $\bar{t}b$).

Since the $W' \rightarrow tb$ decay mode contributes to $s$-channel single top production (see Section 3.2), these searches are based on the single-top production cross section analyses (see Section 5.8.1). For left-handed $W'$ bosons, interference occurs with SM single top production, which is not the case for right-handed $W'$ bosons due to the different (right-handed) final state particles. Considering a right-handed $W'$ boson, the decay width depends on the mass of the right-handed accompanying neutrino in leptonic decays. If $m_{\nu_R} > m_{W'}$, only $q\bar{q}'$ final states are accessible, resulting in a width reduced by about 25%. This scenario generally results in a more stringent mass limit due to the enhanced $tb$ branching fraction. A contribution of the $W'$ boson to top quark decay is usually not considered due to its large mass.

A first search for $W' \rightarrow tb$ was performed by CDF in Run I, based on 0.1 fb$^{-1}$ of lepton + jets data. At 95% C.L., lower limits on the mass of a right-handed $W'$ boson were obtained, yielding 536 GeV/c$^2$ for $m_{\nu_R} \ll m_{W'}$ and 566 GeV/c$^2$ for $m_{\nu_R} > m_{W'}$ [411].

D0 published a first search for $W' \rightarrow tb$ in Run II, based on 0.2 fb$^{-1}$ of lepton + jets data and the corresponding single top cross section result [386]. For a right-handed $W'$ boson with CKM mixing equal to that of the SM, 95% C.L. lower mass limits of 630 GeV/c$^2$ (670 GeV/c$^2$) are obtained for $m_{\nu_R} < m_{W'}$ ($m_{\nu_R} > m_{W'}$). In addition, a first corresponding lower mass limit for a left-handed $W'$ boson is derived, taking the interference with SM production into account, yielding 610 GeV/c$^2$ [410].

Based on the 0.9 fb$^{-1}$ lepton + jets dataset and the analysis from which the first evidence for single top production was obtained [21,22], D0 obtains further improved
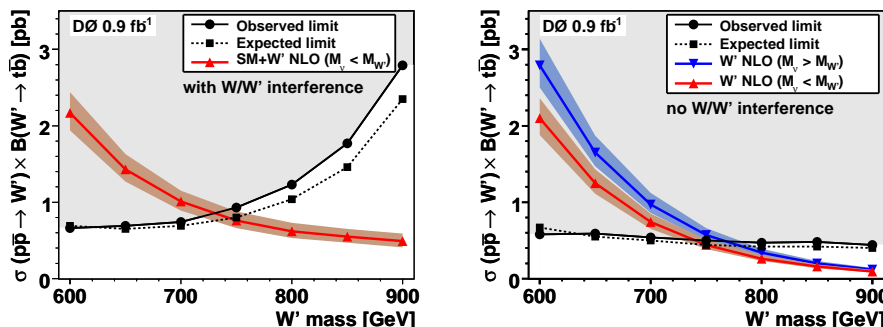
Fig. 33: Theoretical prediction at NLO and 95% C.L. limits for $\sigma(p\bar{p} \rightarrow W') \times \mathcal{B}(W' \rightarrow tb)$ versus mass of the $W'$ boson. Left: Left-handed $W'$ boson. Right: Right-handed $W'$ boson [412]. Results are from the D0 experiment.

$W'$ mass limits [412]. Using the invariant mass of charged lepton, leading two jets and neutrino as a sensitive variable for separating signal and background, the 95% C.L. lower mass limit for a left-handed $W'$ boson interfering with SM single-top production increases to 731 GeV/c$^2$. For a right-handed $W'$ boson, the 95% C.L. lower mass limits are 739 GeV/c$^2$ (768 GeV/c$^2$) for $m_{\nu_R} < m_{W'}$ ($m_{\nu_R} > m_{W'}$), as illustrated in Fig. 33. The latter two cross section limits correspond to upper limits on the $W'$ gauge coupling in units of the SM weak coupling of 0.72 (0.68) for a $W'$ boson mass of 600 GeV/c$^2$. The dominant systematic uncertainties included in these limits are the theoretical cross sections (affecting the background normalization) and uncertainties on jet energy calibration and $b$ jet simulation (affecting background normalization and distribution in the sensitive variable).

CDF has obtained a preliminary result for their $W' \rightarrow tb$ search, based on 1.9 fb$^{-1}$ lepton + jets Run II data, using the invariant mass of the reconstructed $W$ boson and the two leading jets as sensitive variable. 95% C.L. lower limits on the mass of a right-handed $W'$ boson are found to be 800 GeV/c$^2$ for $m_{\nu_R} < m_{W'}$ and 825 GeV/c$^2$ for $m_{\nu_R} > m_{W'}$. Neglecting interference effects the former limit is considered to apply for a left-handed $W'$ boson as well. The corresponding $W'$ gauge coupling in units of the SM weak coupling is found to be <0.68 and <0.63, respectively, for a $W'$ boson mass of 600 GeV/c$^2$ [413].

The more general case of a $W'$ boson with an admixture of left- and right-handed couplings to SM fermions has not been studied thus far.

### 5.8.4. *Search for single top production via charged Higgs bosons*

The standard model Higgs sector, with its single Higgs doublet of complex scalar fields to break electroweak symmetry and generate masses of weak gauge bosons and fermions (see Section 2.1) can be easily extended to include a second Higgs doublet,
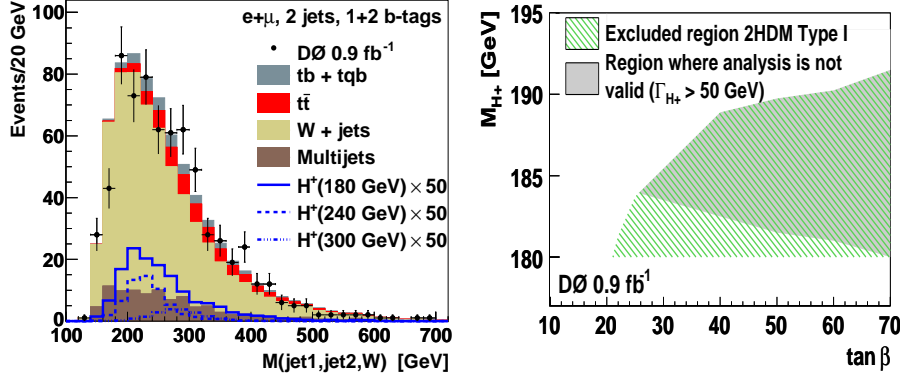
Fig. 34: Left: Distribution of the invariant mass of reconstructed $W$ boson and two jets in 0.9 fb$^{-1}$ lepton + jets data, SM background processes, and charged Higgs boson signal in a Type-III THDM for several $m_{H^\pm}$, with the expected rate enhanced by a factor of 50. Right: 95% C.L. exclusion region in the $(m_{H^\pm}, \tan\beta)$ plane for a Type-I THDM. If $\Gamma_{H^\pm}$ exceeds 50 GeV/c$^2$, the analysis is no longer valid, and no limits can be derived as illustrated by the darker area [417].

resulting in "Two Higgs Doublet Models" (THDM or 2HDM) [414,415]. In contrast to the single neutral scalar CP-even Higgs boson predicted by the SM, THDM give rise to five physical scalar Higgs bosons after electroweak symmetry breaking. Two of these are charged bosons ($H^\pm$), providing a unique signature for physics beyond the standard model. Three different Higgs-fermion couplings are discerned in THDM. Type-I models provide coupling of only one of the Higgs doublets to fermions. In Type-II models, each of the doublets couples solely to up-type fermions and down-type fermions, respectively, while in Type-III models general couplings of both Higgs doublets to fermions are allowed. In the latter case, Higgs-mediated flavor-changing neutral currents at tree level must be sufficiently suppressed to be compatible with experimental limits. This can be achieved through an appropriate choice of the Higgs parameters [416].

If the charged Higgs boson is heavier than the top quark ($m_{H^\pm} > m_t$), its production via quark fusion can contribute to single top quark production through the decay into third-generation quarks: $q\bar{q}' \to H^\pm \to tb$. Due to mass dependent couplings of the charged Higgs boson, this decay is dominant in many models. The signature of this process is identical to that of $s$-channel single top-quark production, and the search for charged Higgs bosons can be performed similar to that for $W'$ bosons, with the simplification that interference with the SM production process can be neglected.

D0 performs a first direct search for the process $q\bar{q}' \to H^\pm \to tb \to \ell\nu b\bar{b}$ [417], based on the analysis providing first evidence for single top production [21,22] in a 0.9 fb$^{-1}$ lepton + jets dataset. Restricting the jet multiplicity in the events to

exactly two jets, corresponding to the $s$-channel final state, charged Higgs bosons are sought in the mass range 180 GeV/c$^2$ $\leq m_{H^\pm} \leq$ 300 GeV/c$^2$ for all three types of THDM. The sensitive variable used to discriminate the charged Higgs boson signal from SM background processes is the invariant mass of the reconstructed $W$ boson and the two jets, as illustrated in Fig. 34. Since no evidence for signal is observed in the data, 95% C.L. upper limits on the charged Higgs boson production cross section multiplied by branching fraction into third generation quarks are provided for all three types of THDM. The dominant systematic uncertainties result from the jet energy scale calibration, modeling of the $b$ jet identification and theoretical uncertainties in modeling and normalizing the signal. For the Type-I THDM, the limits are translated into a 95% C.L. exclusion region in $(m_{H^\pm}, \tan \beta)$ parameter space (see Fig. 34), where $\tan \beta$ is the ratio of the vacuum expectation values for the two Higgs doublets.

More searches for charged Higgs bosons, especially those in top quark decays (for $m_{H^\pm} < m_t$), are described in Section 6.5.

### 5.8.5. *Search for single top production through neutral currents*

Single top quark production via flavor changing neutral interactions of light $u, c$ quarks and the $Z, \gamma, g$ gauge bosons is possible in the standard model through higher-order radiative corrections, but so strongly suppressed that it cannot be observed. Consequently, searches for these production mechanisms at tree level probe for corresponding anomalous coupling strengths $\kappa$ [164, 418] that are predicted by various extensions of the standard model [419].

The processes involving photon or $Z$ boson exchange have been extensively studied at LEP and HERA. At both accelerators top quarks can only be produced singly at the available center of mass energies due to the large top quark mass.

At LEP, single top quark production proceeds via the SM process $e^+ e^- \rightarrow e^- \bar{\nu}_e t \bar{b}$, which can be ignored in the available datasets due to its tiny production rate. All four LEP experiments searched for single top production via $e^+ e^- \rightarrow t\bar{c}/t\bar{u}$ in both hadronic and semileptonic final states, resulting from the different $W$ boson decay modes from the top quark decay. While only the SM decay $t \rightarrow Wb$ is considered, a possible reduction of its branching ratio due to possible FCNC decays is accounted for when deriving the results. Since no evidence for single top quark production is observed, 95% C.L. upper limits on the cross section are extracted, and corresponding model-dependent upper limits on the anomalous coupling parameters $\kappa_\gamma$ and $\kappa_Z$ are determined [420–423].

Single top quark production at HERA is possible via the charged current SM process $ep \rightarrow \nu t \bar{b} X$ that has a negligible production rate here as well. Both H1 and ZEUS have searched for the inclusive neutral current production of top quarks in $ep \rightarrow etX$. Because of the large $Z$ boson mass, this reaction is most sensitive to couplings involving photons. Due to the large proton momentum fractions needed for single top production, the $u$ quark contribution will dominate over that from
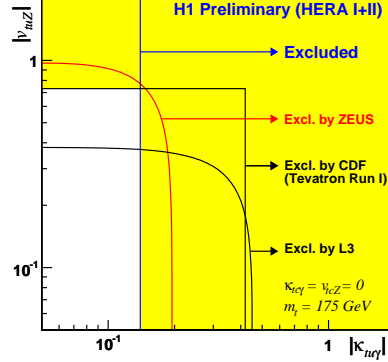
Fig. 35: 95% C.L. upper limits on the top quark anomalous couplings to photons and $Z$ bosons $\kappa_{tu\gamma}$ and $v_{tuZ}$ [424]. Depicted are the limits from CDF [425, 426], L3 [422], H1 [424] and ZEUS [427].

the $c$ quark (see Fig. 5), resulting therefore in highest sensitivity to $tu\gamma$ couplings at HERA.

Using 0.1 fb$^{-1}$ of integrated luminosity, and assuming the SM top quark decay $t \to Wb$, H1 and ZEUS search for single top production both in the leptonic and hadronic $W$ boson decay channel. ZEUS observes good agreement with the SM prediction, and sets 95% C.L. upper limits on single-top production rate and on the FCNC magnetic coupling $\kappa_{tu\gamma}$ and vector coupling $v_{tuZ}$, neglecting charm contributions [427]. H1 observes five events in the leptonic channel, with an expected SM background contribution of $1.31 \pm 0.22$ events, while the hadronic channel exhibits no excess over the standard model prediction. These two channels are compatible at the 1.1 sd level, and both a combined single-top cross section with about 2 sd significance and 95% C.L. upper limits on the cross section and on $\kappa_{tu\gamma}$ (assuming a statistical fluctuation in the data) are provided [428]. In a recent preliminary update of the measurement in the leptonic channel by H1, using an integrated luminosity of 0.5 fb$^{-1}$, good agreement with the standard model expectation is observed and improved limits on the single-top cross section and $\kappa_{tu\gamma}$ are obtained [424].

Further limits on the anomalous couplings $\kappa_\gamma$ and $\kappa_Z$ (inclusive for $u, c$ contributions) have been measured at the Tevatron by CDF via a search for neutral-current top quark decays $t \to \gamma q$ and $t \to Zq$ as will be discussed in Section 6.3. The most stringent results on anomalous top quark couplings involving photons and $Z$ bosons obtained at LEP, HERA and the Tevatron are summarized in Fig. 35, with the exception of the latest CDF limit on $t \to Zq$ decays [429] that constrains $\kappa_Z$ better than the limit from L3.

Flavor changing neutral-current (FCNC) couplings of top quarks and gluons have not been studied as extensively. A constraint on the anomalous gluon coupling
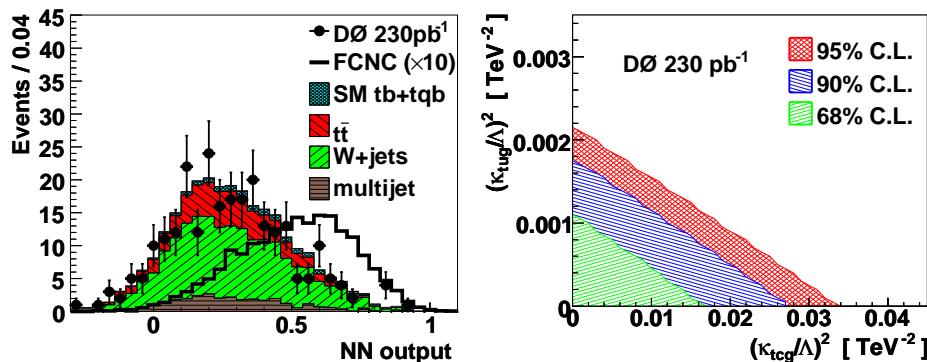
Fig. 36: Left: Neural Network (NN) discriminant distribution in 0.2 fb$^{-1}$ lepton + jets data, with simulated FCNC signal increased by a factor of ten, and SM background. The signal distribution represents the sum of *tug* and *tcg* processes, evaluated for $\kappa_{tqg}/\Lambda = 0.03$ TeV$^{-1}$. Right: Exclusion contours for anomalous top-gluon couplings for different levels of confidence [432].

$\kappa_{tqg}/\Lambda$ of $< 0.52$ TeV$^{-1}$, where $\Lambda$ gives the scale for new physics, was extracted from the observed $t\bar{t}$ pair production cross section at the Run I Tevatron and a possible new physics contribution that could be still accommodated within two sd of combined experimental and theoretical uncertainties [430]. Another limit on the anomalous gluon coupling was obtained using the single-top production cross section limit measured by ZEUS [427]. Neglecting any effects that arise from the different final states obtained in the gluon channel compared to the original search (one additional light jet is present in the gluon case), at 95% C.L. $\kappa_{tqg}/\Lambda < 0.4$ TeV$^{-1}$ is obtained [431].

D0 has performed a first search for single top production via flavor changing neutral-current couplings to gluons at a hadron collider, using 0.2 fb$^{-1}$ lepton + jets data [432]. The analysis is based on the corresponding search for SM single-top production [386, 387], but is restricted to events with only one $b$ tagged jet, and treats $s$- and $t$-channel SM single-top production as background. Since the neutral current decays $t \rightarrow gu/gc$ exhibit a negligible branching fraction for $\kappa_{tqg}/\Lambda \lesssim 0.2$ TeV$^{-1}$ [433], exclusively the standard model top quark decay can be considered.

To separate the FCNC signal from the overwhelming SM background, a neural network is deployed, with ten input variables based on global event kinematics, angular correlations and kinematics of the individual reconstructed objects. The resulting data distribution is shown in Fig. 36, and exhibits good agreement with the SM prediction, which provides limits on the FCNC couplings $\kappa_{tug}/\Lambda$ and $\kappa_{tcg}/\Lambda$.

Systematic uncertainties affecting either the normalization or both normalization and shape of the distributions are taken into account when calculating the two-dimensional Bayesian posterior probability density, resulting in the exclusion contours for the two couplings for different confidence levels shown in Fig. 36. The
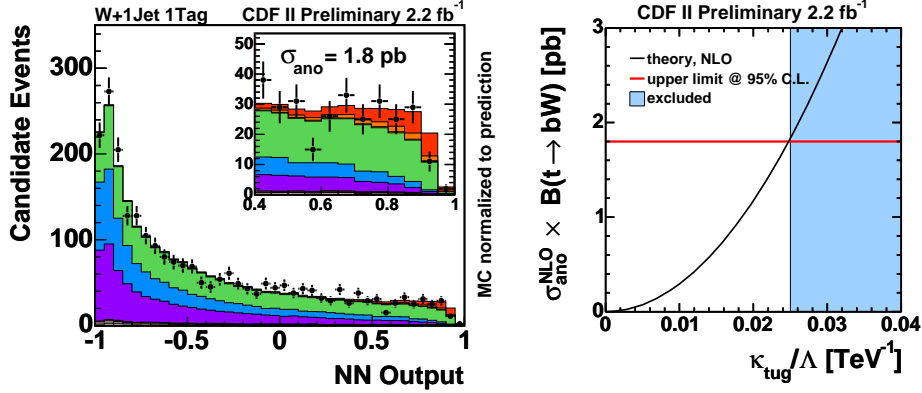
Fig. 37: Left: Neural network discriminant output in $W +$ one $b$ jet events observed in 2.2 fb$^{-1}$ of CDF data (black points) and standard model background processes. A FCNC single top signal with the observed 95% C.L. *excluded* production rate is added in red. Right: Extraction of the $\kappa_{tug}/\Lambda$ limit from the intersection of the observed cross section limit and theoretical rate prediction, assuming $\kappa_{tcg} = 0$ [434].

largest normalization uncertainties arise from the background cross section uncertainties, which includes the uncertainty on the top quark mass for $t\bar{t}$ and single top samples. The largest uncertainties affecting the shape as well arise from jet energy scale calibration and $b$ tag modeling. 95% C.L. upper limits on $\kappa_{tug}/\Lambda$ and $\kappa_{tcg}/\Lambda$ are obtained by integrating over the other variable, and yield 0.037 TeV$^{-1}$ and 0.15 TeV$^{-1}$ for *tug* and *tcg* couplings, respectively. These limits represent a significant improvement over previous values by up to an order of magnitude.

CDF also reports a recent preliminary search for FCNC single top production, based on 2.2 fb$^{-1}$ of data [434][f]. In distinction to the D0 analysis, where $2 \to 2$ *tcg* and *tug* signal processes are considered, CDF investigates the $2 \to 1$ processes $u(c) + g \to t$. Since also in this analysis only SM top quark decay is considered, events with one isolated energetic lepton, $\not{p}_T$ and one $b$ tagged jet are selected.

Signal and SM background processes are separated using a Bayesian neural network based on 14 input variables containing information from the reconstructed objects and event kinematics. In a template fit to the observed distribution in data good agreement is found with the SM background, as illustrated in Fig. 37, and a 95% C.L. upper limit on FCNC single top production via $u(c) + g \to t$ of 1.8 pb is obtained in accordance with the expected sensitivity.

Based on LO predictions for the FCNC signal process from TOPREX [436], and using NLO $k$-factors [437–439], the obtained cross section limit can be converted into limits on anomalous gluon couplings. No two-dimensional information is used in this

---

[f]An updated version of the result has been published after completion of this review, see Ref. [435].

analysis for contributions of $tcg$ relative to $tug$ signal processes, and one coupling is assumed to vanish in deriving the limit for the other coupling. The resulting 95% C.L. upper limits are $\kappa_{tug}/\Lambda < 0.025 \text{ TeV}^{-1}$ (see Fig. 37) and $\kappa_{tcg}/\Lambda < 0.105 \text{ TeV}^{-1}$ (not shown).

### 5.8.6. *Anomalous Wtb couplings in single top production*

The couplings between quarks and electroweak gauge bosons were directly scrutinized at LEP [440], with the exception of the top quark. At the Tevatron, the couplings of the top quark and the $W$ boson can be studied in measurements of top quark decay properties in $t\bar{t}$ production (see for example Section 6.1) and via single top quark production. Physics beyond the standard model could modify the Lorentz structure of the $Wtb$ vertex. Considering a more general extension of the standard model $Wtb$ interaction Lagrangian, as discussed in Section 3.3.3, new physics could introduce contributions from right-handed vector $(f_1^R)$ and left- and right-handed tensor couplings $(f_2^L, f_2^R)$, in addition to the pure left-handed vector coupling $(f_1^L)$ of the standard model.

D0 has published constraints on such extended $Wtb$ interactions, including the first direct limits on the left- and right-handed tensor couplings [441], based on the analysis that provided first evidence for single top production in 0.9 fb$^{-1}$ of lepton + jets data [21, 22]. In the analysis, single top quark production and decay are considered to take place only via $W$ bosons, with the dominant contribution arising from the $Wtb$ interaction, which is assumed to be $CP$ conserving. Anomalous couplings at the $Wtb$ vertex can modify both the total single-top production rate and the observed kinematics in the events relative to SM expectation [137, 442–444]. The latter effect is illustrated in Fig. 38 for the charged-lepton transverse momentum distribution.

Since a simultaneous fit of all four couplings to data is not feasible with the available statistics, the SM coupling and one additional anomalous coupling contribution at a time is considered in varying proportions (with the remaining two other anomalous couplings set to zero). The resulting scenarios are denoted as $(L_1, R_1)$, $(L_1, R_2)$ and $(L_1, L_2)$. Non-negligible interference effects in the last case are also taken into account. For signal discrimination from SM background, boosted decision trees are used that are based on the same variables as used in Refs. [21, 22], but with the lepton $p_T$ distribution added. One example distribution for the $(L_1, R_2)$ case is shown in Fig. 38.

The decision tree output in data is compared with the various single-top signal models in the twelve subchannels defined by lepton flavor $(e, \mu)$, jet multiplicity (two, three, four) and $b$ tag multiplicity (one, two). This yields a two-dimensional Bayesian posterior probability density, depending on $|f_1^L|^2$ and the anomalous coupling $|f_{\text{ano}}|^2$ considered in the respective scenarios. Systematic uncertainties are taken into account, with dominant contributions arising from background normalization, modeling of $b$ tagging and jet energy scale calibration. The latter two affect
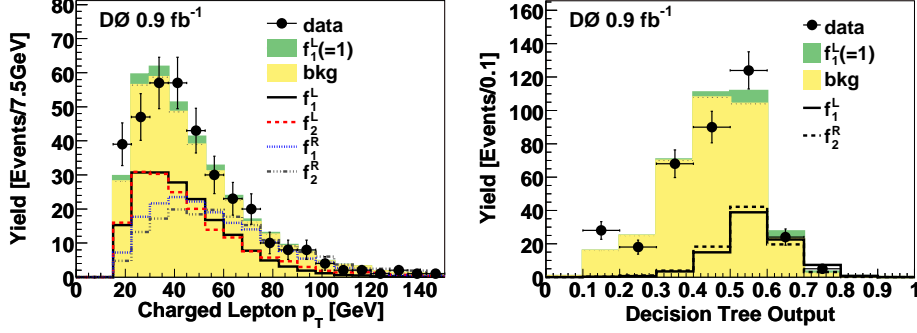
Fig. 38: Left: Charged-lepton $p_T$ distribution in 0.9 fb$^{-1}$ lepton + jets data (two jets and one $b$ tag) and the corresponding SM single-top signal and background contributions. The effect of each of the four different $Wtb$ couplings on the signal is also shown (calculated with the other couplings set to zero), with the normalization enhanced by a factor of ten. Right: Boosted decision tree output for the same data, signal and background contributions, with the $(L_1, R_2)$ scenario couplings overlaid (normalization increased by a factor of five) [441].

Table 15: Total single-top production rates obtained in three anomalous coupling scenarios, together with the corresponding one-dimensional measurements and limits for the selected couplings [441].

| Scenario | Cross Section $(tb + tqb)$ | Considered Couplings |
|----------|----------------------------|----------------------|
| $(L_1, R_1)$ | $5.2^{+2.6}_{-3.5}$ pb | $|f_1^L|^2 = 1.8^{+1.0}_{-1.3}$ <br> $|f_1^R|^2 < 2.5$ (95% C.L.) |
| $(L_1, R_2)$ | $4.5^{+2.2}_{-2.2}$ pb | $|f_1^L|^2 = 1.4^{+0.9}_{-0.8}$ <br> $|f_2^R|^2 < 0.3$ (95% C.L.) |
| $(L_1, L_2)$ | $4.4^{+2.3}_{-2.5}$ pb | $|f_1^L|^2 = 1.4^{+0.6}_{-0.5}$ <br> $|f_2^L|^2 < 0.5$ (95% C.L.) |

both normalization and shape of the simulated spectra. The maxima of the likelihoods in all three considered scenarios yield zero for $|f_{\mathrm{ano}}|^2$, and 95% C.L. upper limits on these anomalous couplings are provided from the one-dimensional likelihood projections. These results are summarized together with the measured single-top production rates and $|f_1^L|^2$ values obtained from one-dimensional likelihood projections in Table 15. The SM $Wtb$ interaction is favored over any anomalous alternative studied. This analysis will greatly benefit from the increased statistics already in hand and from more expected until the end of Run II.

## 6. Decay Properties of the Top Quark

The previous chapter demonstrated that no significant deviations from the standard model expectations for top quark production via the strong or electroweak interaction have thus far been observed. In this chapter, decay properties of the top quark will be investigated based on $t\bar{t}$ data, generally assuming that top quark production proceeds according to the standard model.

### 6.1. *Measurement of the* W *boson helicity in* $t\bar{t}$ *decays*

The helicity of the $W$ boson in top quark decays can be used to test the $V-A$ Lorentz structure of the $Wtb$ interaction (see Section 3.3.3). According to the expectation from the standard model, $W$ bosons from top quark decays should be longitudinally polarized with a fraction $f_0 \approx 70\%$ and left-handed with a fraction $f_- \approx 30\%$. The right-handed fraction $f_+$ is strongly suppressed, and below the per mill level [189]. For the decay of antitop quarks, the $CP$ conjugate statement is implied, resulting in $W^-$ bosons from $\bar{t}$ decays with either longitudinal or right-handed polarization.

A pure $V + A$ structure of the $Wtb$ interaction would result in an observation of a right-handed fraction $f_+ = 30\%$, with negligible left-handed contribution. Small $V + A$ admixtures to the SM left-handed charged-current weak interaction are predicted, for instance, within $SU(2)_R \times SU(2)_L \times U(1)_Y$ extensions of the SM [445–448]. Such contributions would result in an enhancement of $f_+$ while not significantly affecting $f_0$. Since the decay amplitude for longitudinally polarized $W$ bosons is proportional to the top quark's Yukawa coupling [174], $f_0$ is sensitive to the mechanism of EWSB, and would be altered, for example, in topcolor-assisted technicolor models [191, 449].

The radiative decay rate $b \rightarrow s\gamma$ can be used to set indirect limits on the $V + A$ admixture in top quark decays to below a few percent [450–453], assuming there are no contributions from gluonic penguin diagrams in addition to the electroweak ones. This section will discuss the direct measurements of the $W$ boson helicity performed at the Tevatron using lepton + jets and dilepton datasets.

Thus far, four analysis techniques have been deployed to extract the $W$ boson helicity fractions, based on:

(i) *helicity angle (*$\cos\theta^*$*)*: The helicity of the $W$ boson is reflected in the angular distribution $\cos\theta^*$ of its decay products, with $\theta^*$ being the angle of the down-type $(T_3 = -\frac{1}{2})$ decay products of the $W$ boson (charged lepton, $d$ or $s$ quark) in the $W$ boson rest frame relative to the top quark direction [186–189]:

$$\frac{dN}{d\cos\theta^*} = f_- \cdot \frac{3}{8}(1 - \cos\theta^*)^2 + f_0 \cdot \frac{3}{4}(1 - \cos^2\theta^*) + f_+ \cdot \frac{3}{8}(1 + \cos\theta^*)^2, \quad (31)$$

where $f_-$ can be replaced by $(1 - f_+ - f_0)$. The resulting distributions for each helicity fraction and the superposition expected from the standard model are shown in Fig. 39. A measurement of $\cos\theta^*$ provides the most direct measurement of the $W$ boson helicity, but it requires the reconstruction of the momenta
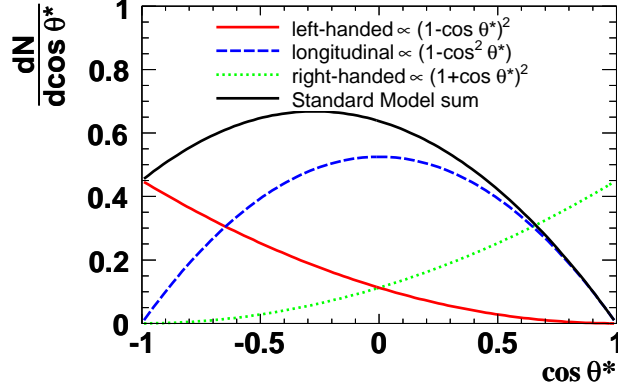
Fig. 39: Helicity angle $\cos \theta^*$ distributions for left-handed, longitudinal and right-handed $W$ bosons. The superposition expected from the standard model is shown as well.

of the top quark and $W$ boson, which is challenging and involves using $\not{p}_T$, which has a rather poor resolution.

(ii) *charged-lepton $p_T$ spectrum ($p_T^\ell$)*: The helicity of the $W$ boson is correlated with the charged-lepton momentum distribution: Since the $\nu_\ell$ from $W^+$ decays are left-handed, while the $\ell^+$ are right-handed, in case of a left-handed $W^+$ decay the $\ell^+$ are preferentially emitted opposite to the momentum vector of the $W^+$. This leads to a softer $p_T^\ell$ spectrum in the laboratory frame. Conversely, the $\ell^+$ are preferentially emitted along the direction of the $W^+$ momentum in case of a right-handed $W^+$ decay, leading to a harder $p_T^\ell$ spectrum. The $\ell^+$ from longitudinal $W^+$ decay represent an intermediate case (see Fig. 40).

(iii) *squared invariant mass of b quark and charged lepton ($M_{\ell b}^2$)*: In the limit of $m_b = 0$, the helicity angle distribution $\cos \theta^*$ can be approximated using the squared invariant mass of the system composed of the $b$ quark and the charged lepton $M_{\ell b}^2$:

$$\cos \theta^* = \frac{p_\ell \cdot p_b - E_\ell E_b}{|\mathbf{p}_\ell||\mathbf{p}_b|} \simeq \frac{2M_{\ell b}^2}{m_t^2 - M_W^2} - 1. \tag{32}$$

This way one avoids the challenge of kinematic reconstruction of the top quark and the application of $\not{p}_T$ by using only momenta measured in the laboratory frame.

(iv) *Matrix Element method (ME)*: The Matrix Element method was originally developed by D0 [454], yielding a very precise mass measurement given the limited Run I data sample (see also Section 7.3.2). Using all the available kinematic information in each event, a probability for the event to correspond to a $t\bar{t}$ final state as a function of the helicity of the $W$ boson can be calculated, based on
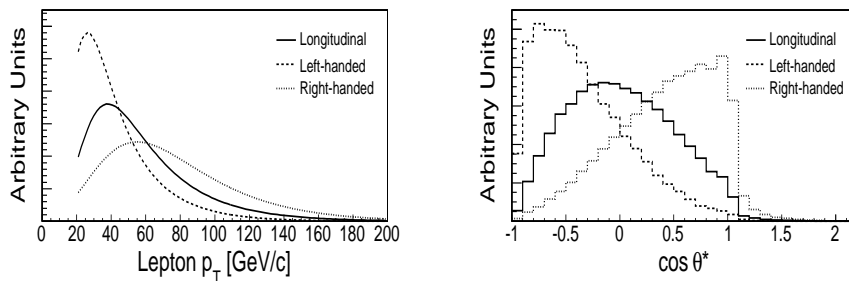
Fig. 40: Distributions of reconstructed charged-lepton $p_T$ and $\cos\theta^*$ (based on Eq. 32) for top quark decays involving left-handed, right-handed and longitudinally polarized $W$ bosons [455].

the LO matrix element.

The following subsections will give brief examples for each method, followed by a summary of the current status of the measurements.

### 6.1.1. $p_T^\ell$ and $M_{\ell b}^2$

CDF has measured the $W$ boson helicity in a 0.2 fb$^{-1}$ Run II dataset using the charged-lepton $p_T$ ($p_T^\ell$) and the squared invariant mass of the $b$ quark and charged lepton ($M_{\ell b}^2$) to approximate $\cos\theta^*$ [455]. The dependence of these observables on the $W$ boson helicity for a top quark mass of 175 GeV/c$^2$ after event selection and reconstruction is shown in Fig. 40. Since the world-averaged top and $W$ boson masses are used for calculating $\cos\theta^*$, rather than the corresponding event-by-event reconstructed masses that would smear out the distribution due to the larger inherent uncertainties, values are observed outside of the physical range $-1 \leq \cos\theta^* \leq 1$.

For the $p_T^\ell$ analysis, a $b$ tagged lepton + jets sample is used requiring at least three jets, and yielding 57 events of which approximately 2/3 are $t\bar{t}$ signal. In addition a dilepton sample, with a minimum value for the scalar sum of the transverse energy of jets, leptons and $\not{p}_T$ is analyzed, yielding 13 events with a signal fraction of ≈0.79. The analysis based on $M_{\ell b}^2$ uses the lepton + jets sample alone, requiring a fourth jet and a good kinematic fit to the $t\bar{t}$ hypothesis for a top mass of 175 GeV/c$^2$. This provides the lepton and appropriate jet to form $M_{\ell b}^2$, and leaves 31 events for this analysis with a signal fraction of ≈0.78.

For both analyses, the data distributions are fitted separately to $p_T^\ell$ and $\cos\theta^*$ templates of signal with the different $W$ boson helicities and background. Because of limited statistics, the helicity fractions $f_0$ and $f_+$ cannot be fitted simultaneously. Consequently, $f_0$ or $f_+$ are constrained to their standard model values when fitting for $f_+$ or $f_0$, respectively. Both analyses are finally combined, taking statistical and systematic correlations into account, and yield results consistent with

Table 16: Results of individual and combined measurements of $f_0$ and $f_+$ using $M_{\ell b}^2$ and $p_T^\ell$. $N$ indicates the number of events or leptons used. If two uncertainties are given, the first is statistical and the second systematic. For the combined results, the statistical and systematic combined uncertainty is given. For the $p_T^\ell(\ell\ell)$ result, an observation of $\leq -0.54$ is expected 0.5% of the time for the SM $f_0$ value of 0.7 [455].

| Analysis | $N$ | $f_0$ | $f_+$ |
|----------|-----|-------|-------|
| $M_{\ell b}^2$ | 31 | $0.99^{+0.29}_{-0.35} \pm 0.19$ | $0.23 \pm 0.16 \pm 0.08$ |
| $p_T^\ell(\ell\ell)$ | 26 | $-0.54^{+0.35}_{-0.25} \pm 0.16$ | $-0.47 \pm 0.10 \pm 0.09$ |
| $p_T^\ell(\ell j)$ | 57 | $0.95^{+0.35}_{-0.42} \pm 0.17$ | $0.11^{+0.21}_{-0.19} \pm 0.10$ |
| $p_T^\ell(\ell\ell, \ell j)$ | 83 | $0.31^{+0.37}_{-0.23} \pm 0.17$ | $-0.18^{+0.14}_{-0.12} \pm 0.12$ |
| Combined | | $0.74^{+0.22}_{-0.34}$ | $0.00^{+0.20}_{-0.19}$ |
| 95% C.L. limit | | $< 0.95, > 0.18$ | $< 0.27$ |

the standard model expectation, as shown in Table 16. The dominant systematic uncertainties come from uncertainties on the top quark mass, background shape and normalization, effects of initial- and final-state radiation (ISR/FSR) and the PDFs.

CDF has also measured the fraction of right-handed $W$ bosons assuming $f_0$ to be 0.7, using the $M_{\ell b}^2$ method on a 0.7 fb$^{-1}$ Run II dataset [456]. Using a single and double $b$ tagged lepton + jets in addition to a dilepton dataset, $f_+$ is extracted via maximum likelihood fits of the $M_{\ell b}^2$ distributions in data to $V+A$ and $V-A$ $t\bar{t}$ signal Monte Carlo and background contributions. Including uncertainties on the $t\bar{t}$ signal and background cross sections, the lepton + jets sample yields $f_+ = 0.06 \pm 0.08$, while the dilepton sample gives $f_+ = -0.19 \pm 0.11$, corresponding to a compatibility of the measurements at the level of 2.3 sd. A combination of these measurements, including all systematic uncertainties, yields $f_+ = -0.02 \pm 0.07(\text{stat} + \text{syst})$, corresponding to $f_+ < 0.09$ at 95% C.L. The main contributions to the systematic uncertainty come from the jet energy scale, background shape and normalization and limited Monte Carlo statistics.

### 6.1.2. *Matrix element method*

D0 has used the matrix element method that was originally employed to measure the top quark mass [454] to extract the longitudinal $W$ boson helicity fraction from 0.1 fb$^{-1}$ of Run I data [457]. The selected lepton + jets event sample corresponds to that of the preceding mass analysis [320] and comprises both soft muon $b$ tagged events and untagged events, which have additional kinematic requirements, yielding a total of 91 events.

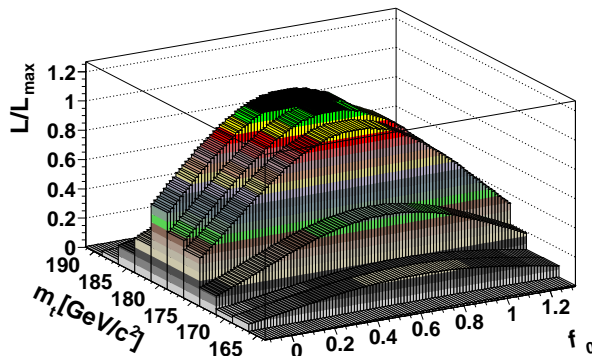By comparing the measured set of four-vectors in each event with the differential

Fig. 41: Two-dimensional probability density observed in $0.1$ fb$^{-1}$ lepton $+$ jets Run I data as a function of $f_0$ and top quark mass $m_t$ [457].

cross section for $t\bar{t}$ signal and the dominant $W$+jets background, $f_0$ can be extracted by fixing $f_+$ to its SM value, allowing the ratio $f_0/f_-$ to vary. The use of both $W$ boson decays per signal event increases the statistical sensitivity of the method. Since the calculation of signal and background probabilities is based on leading-order matrix elements, only events with exactly four jets are accepted, reducing the sample to 71 events. In order to increase signal purity, a cut on the background probability is applied, leaving 22 events to be analyzed (as in the corresponding matrix-element mass analysis [454]), with a signal to background ratio of 12/10.

To take the dependence of the $f_0$ measurement on the top quark mass into account, a two-dimensional likelihood, depending on $f_0$ and $m_t$, is calculated and corrected for response deviations from unity for different $f_0$ input values (see Fig. 41). Since statistics are insufficient, a simultaneous optimization for both observables is not feasible; instead $f_0$ is evaluated by integrating over the top quark mass, for a range between 165 and 190 GeV/$c^2$. The maximum in the probability yields the central value of the measurement, with the 1 sd uncertainty band corresponding to a convolution of statistical and top quark mass uncertainties. Other systematic uncertainties from acceptance and linearity of response or jet energy scale are small compared to this, yielding the final result:

$$f_0 = 0.56 \pm 0.31(\text{stat} \oplus \text{m}_\text{t}) \pm 0.07(\text{syst}). \tag{33}$$

CDF has obtained a preliminary result for $f_0$ using the same method on $1.9$ fb$^{-1}$ of Run II data, assuming a fixed top quark mass of 175 GeV/c$^2$ [458]. 468 events are selected in a $b$ tagged lepton $+$ jets sample with at least four jets (only the leading four are used in the analysis) and a minimum value for $H_T$, yielding a signal fraction of about 0.84. Fixing $f_+$ to its SM value, the longitudinal $W$ boson helicity fraction

is found to be $f_0 = 0.64 \pm 0.08(\text{stat.}) \pm 0.07(\text{syst.})$, with the dominant systematic uncertainty coming from the Monte Carlo generator used (PYTHIA versus HERWIG) for the calibration of the measurement. $f_0$ is found to change by $\mp 0.035$ for a $\pm 2.5$ GeV/c$^2$ variation in the top quark mass. Thus far, the analysis has not yet been extended to measure $f_0$ and $f_+$ or $f_0$ and $m_t$ simultaneously.

### 6.1.3. *Helicity angle* $\cos\theta^*$

D0 has published a first model-independent measurement of the $W$ boson helicity fractions by comparing the $\cos\theta^*$ distribution in data to templates of background and right-handed, left-handed or longitudinal $W$ bosons in $t\bar{t}$ signal, using $f_+$ and $f_0$ as freely floating parameters and $f_- = 1 - f_+ - f_0$ [459]. In a 1 fb$^{-1}$ dataset, lepton $+ \geq 4$ jets and dilepton events are selected. The signal purity is increased in each subsample by a cut on an individually optimized multivariate likelihood discriminant based on event kinematics and the output of a neural network $b$-tagging discriminant. The cut values are chosen in each subsample to yield the best expected precision for the helicity measurement.

The statistical sensitivity of the analysis is further improved by about 20% by including the $W \to q\bar{q}'$ decays in the lepton $+$ jets sample in the measurement. This is accomplished through picking one of the $W$ boson daughter jets at random for the calculation of $\cos\theta^*$, which introduces a sign ambiguity. Consequently, only $|\cos\theta^*|$ is considered which does not permit to discriminate left- from right-handed $W$ bosons, but still adds information on $f_0$.

The four-momenta of the top quarks and $W$ bosons in the lepton $+$ jets sample are reconstructed based on the best kinematic fit to a top quark event hypothesis for $m_t = 172.5$ GeV/c$^2$, using the leading four jets to obtain $\cos\theta^*$ and $|\cos\theta^*|$. For the kinematically less constrained dilepton events, a top quark mass of $m_t = 172.5$ GeV/c$^2$ is assumed and the kinematics solved up to a four-fold ambiguity in addition to the two-fold ambiguity from the lepton-jet pairing (only the leading two jets are used). Jet and lepton energies in each event are smeared within their resolutions to explore the phase space consistent with the observed values. The average of the obtained $\cos\theta^*$ values is then used for each charged lepton, providing two measurements per event. The resulting distributions are shown in Fig. 42. Note that due to reconstruction effects the shape of the standard model expectation differs from the theoretical prediction in Fig. 39.

A template fit of these distributions yields $f_0 = 0.425 \pm 0.166(\text{stat.}) \pm 0.102(\text{syst.})$ and $f_+ = 0.119 \pm 0.090(\text{stat.}) \pm 0.053(\text{syst.})$. The result is compatible with the standard model expectation at 30% C.L. It should be noted that the individual measurements in the lepton $+$ jets and dilepton channels differ by about 2.1 sd [460]. The major systematic uncertainties on the measurement are summarized in Table 17, with the largest uncertainty arising from $t\bar{t}$ signal modeling, evaluated through varying the Monte Carlo generators used (PYTHIA versus ALPGEN), from changing underlying event models to estimate the effects of gluon radiation, and
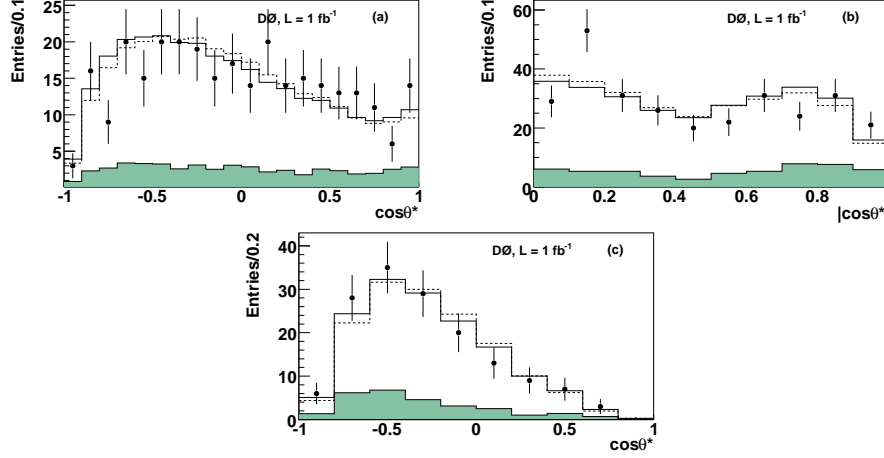
Fig. 42: Helicity angle distributions in lepton + jets (a,b) and dilepton events (c). Points with error bars represent 1 fb$^{-1}$ of D0 data. The solid open histograms show the result of the model independent fit described in the text, while the dashed open histograms show the standard model expectation. The filled histograms represent the background contribution [459].

Table 17: Major systematic uncertainties on the simultaneous measurement of $f_0$ and $f_+$ by D0 in 1 fb$^{-1}$ of data [459].

| Source | Uncertainty $(f_0)$ | Uncertainty $(f_+)$ |
|---|---|---|
| Top mass | 0.009 | 0.018 |
| Jet reconstruction eff. | 0.021 | 0.010 |
| Jet energy calibration | 0.012 | 0.019 |
| $b$ fragmentation | 0.016 | 0.010 |
| $t\bar{t}$ model | 0.068 | 0.032 |
| Background model | 0.049 | 0.016 |
| Template statistics | 0.049 | 0.025 |
| Total | 0.102 | 0.053 |

restricting the samples to contain only one primary vertex to study the sensitivity of the measurement to variations in instantaneous luminosity. Constraining $f_0$ or $f_+$ to their SM values, when fitting for $f_+$ or for $f_0$, respectively, yields $f_0 = 0.619 \pm 0.090(\text{stat.}) \pm 0.052(\text{syst.})$ and $f_+ = -0.002 \pm 0.047(\text{stat.}) \pm 0.047(\text{syst.})$, in agreement with expectations from the SM.

In a recent preliminary update, D0 has added 1.2 fb$^{-1}$ lepton + jets and 1.7 fb$^{-1}$ dilepton ($e\mu$ only) data [461] to the above analysis. The model-independent fit for the combined data yields $f_0 = 0.490 \pm 0.106(\text{stat.}) \pm 0.085(\text{syst.})$ and $f_+ =$
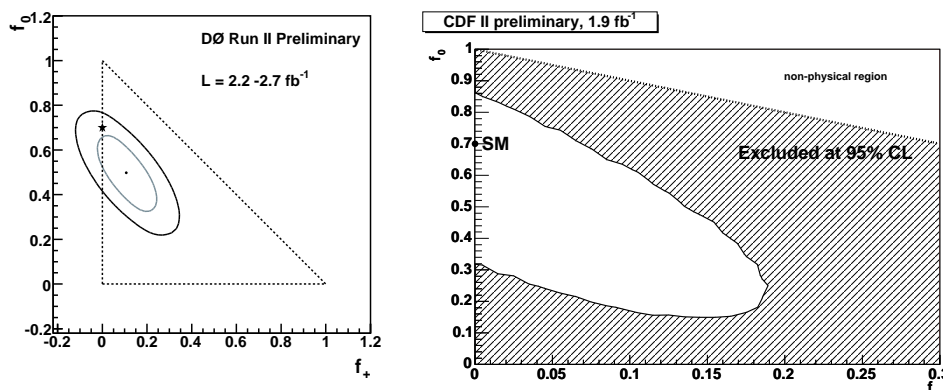
Fig. 43: Left: Result of the model-independent $W$ boson helicity fit by D0 [461]. The ellipses show the 68% and 95% C.L. contours around the measured data point. The star shows the SM expectation, and the triangle denotes the physically allowed region where $f_0$ and $f_+$ sum to $\leq 1$. Right: Two-dimensional 95% C.L. exclusion area in the $(f_+, f_0)$ plane measured by CDF [462].

$0.110 \pm 0.059$(stat.) $\pm 0.052$(syst.), consistent at 23% C.L. with the standard model (see Fig. 43). The results from the lepton + jets and dilepton channels remain marginally consistent with a $p$-value of 1.6%.

CDF has obtained two preliminary results for a model-independent extraction of $W$ boson helicity in 1.9 fb$^{-1}$ of data. These are based on using only the charged lepton in $b$ tagged lepton $+ \geq 4$ jets events to obtain $\cos\theta^*$ [462,463]. A combination of both results also has become available [464][g]. The measurements are compatible with the standard model expectation, with each other, and with the D0 measurements presented above and are summarized together with other results in Table 18. The two-dimensional 95% C.L. exclusion area in the $(f_+, f_0)$ plane measured by CDF [462] is shown in Fig. 43.

### 6.1.4. *Summary*

All available measurements of the $W$ boson helicity performed thus far in $t\bar{t}$ events at the Tevatron are compatible with the standard model expectation, and are summarized in Table 18.

The sensitivity of the measurements in Run I and initial studies in Run II only allowed model-dependent measurements of any single helicity fraction to be performed at a time, while fixing the other fraction to its standard model value. However, with the large amount of data available by now, a simultaneous extraction

---

[g]This result has been published after completion of this review, see Ref. [465].

Table 18: $W$ boson helicity measurements in $t\bar{t}$ events performed thus far at the Tevatron, with their integrated luminosities, data selections ($\ell j$ = lepton + jets, $\ell\ell$ = dilepton) and analysis methods used. Model independent results are indicated by a yes in the "Ind. fit" column. The three analyses using $0.1$ fb$^{-1}$ are from Run I; the analyses using more than 1 fb$^{-1}$ are preliminary. Ref. [464] provides a combination of the results from Refs. [462, 463].

| $\int \mathcal{L}dt$ [fb$^{-1}$] | Sel. | $f_0$ | $f_+$ | Ind. fit | $f_+ <$ (95% C.L.) | Method | Ref. |
|---|---|---|---|---|---|---|---|
| 0.1 | $\ell j, \ell\ell$ | $0.91 \pm 0.37 \pm 0.13$ | $0.11 \pm 0.15$ | no | 0.28 | $p_T^\ell$ | [466] |
| 0.1 | $\ell j, \ell\ell$ | — | $-0.02 \pm 0.11$ | no | 0.18 | $M_{\ell b}^2, p_T^\ell$ | [467] |
| 0.1 | $\ell j$ | $0.56 \pm 0.31$ | — | no | — | ME | [457] |
| 0.2 | $\ell j, \ell\ell$ | $0.74_{-0.34}^{+0.22}$ | $0.00_{-0.19}^{+0.20}$ | no | 0.27 | $M_{\ell b}^2, p_T^\ell$ | [455] |
| 0.2 | $\ell j$ | — | $0.00 \pm 0.13 \pm 0.07$ | no | 0.25 | $\cos \theta^*$ | [468] |
| 0.3 | $\ell j$ | $0.85_{-0.22}^{+0.15} \pm 0.06$ | $0.05_{-0.05}^{+0.11} \pm 0.03$ | no | 0.26 | $\cos \theta^*$ | [469] |
| 0.4 | $\ell j, \ell\ell$ | — | $0.06 \pm 0.08 \pm 0.06$ | no | 0.23 | $\cos \theta^*$ | [470] |
| 0.7 | $\ell j, \ell\ell$ | — | $-0.02 \pm 0.07$ | no | 0.09 | $M_{\ell b}^2$ | [456] |
| 1.0 | $\ell j, \ell\ell$ | $0.62 \pm 0.09 \pm 0.05$ | $0.00 \pm 0.05 \pm 0.05$ | no | — | $\cos \theta^*$ | [459] |
| | | $0.43 \pm 0.17 \pm 0.10$ | $0.12 \pm 0.09 \pm 0.05$ | yes | | | |
| 1.9 | $\ell j$ | $0.64 \pm 0.08 \pm 0.07$ | — | no | — | ME | [458] |
| 1.9 | $\ell j$ | $0.59 \pm 0.11 \pm 0.04$ | $-0.04 \pm 0.04 \pm 0.03$ | no | 0.07 | $\cos \theta^*$ | [462] |
| | | $0.65 \pm 0.19 \pm 0.03$ | $-0.03 \pm 0.07 \pm 0.03$ | yes | — | | |
| 1.9 | $\ell j$ | $0.66 \pm 0.10 \pm 0.06$ | $0.01 \pm 0.05 \pm 0.03$ | no | 0.12 | $\cos \theta^*$ | [463] |
| | | $0.38 \pm 0.21 \pm 0.07$ | $0.15 \pm 0.10 \pm 0.05$ | yes | — | | |
| 1.9 | $\ell j$ | $0.62 \pm 0.11$ | $-0.04 \pm 0.05$ | no | — | $\cos \theta^*$ | [464] |
| | | $0.66 \pm 0.16$ | $-0.03 \pm 0.07$ | yes | | | |
| 2.7 | $\ell j, \ell\ell$ | $0.49 \pm 0.11 \pm 0.09$ | $0.11 \pm 0.06 \pm 0.05$ | yes | — | $\cos \theta^*$ | [461] |

of $f_+$ and $f_0$ for $W$ bosons is possible without constraint, except for unitarity ($f_+ + f_0 + f_- = 1$). Such measurements will also clearly benefit from increased luminosity. A combination with the measurement of the single-top production cross section in the $s$- and $t$-channel will help to fully specify the $tWb$ coupling [191] (see Section 3.3.3)[h].

The model-dependent measurements, where one of the helicity fractions is fixed to its standard model value, have reached a considerable precision with statistical

[h]A first such measurement was published by D0 [471] after completion of this review.

approaching systematic uncertainties.

It is interesting to note that discrepancies of $> 2$ sd between results from the dilepton and lepton + jets samples have been observed both at CDF and D0 using different analysis techniques. This deserves further scrutiny in future analyses.

### 6.2. *Measurement of* $\mathcal{B}(t \to Wb)/\mathcal{B}(t \to Wq)$

As described in Section 3.3.1, in the standard model framework the top quark decays almost exclusively into a $W$ boson and a $b$ quark due to the dominant corresponding CKM matrix element $V_{tb}$. The ratio $R$ of the top quark branching fractions can be expressed via the CKM matrix elements as:

$$R = \frac{\mathcal{B}(t \to Wb)}{\displaystyle\sum_{q=d,s,b} \mathcal{B}(t \to Wq)} = \frac{\mid V_{tb} \mid^2}{\mid V_{tb} \mid^2 + \mid V_{ts} \mid^2 + \mid V_{td} \mid^2} \ . \tag{34}$$

Measuring $R$ provides therefore the relative size of $|V_{tb}|$ compared to $|V_{td}|$ and $|V_{ts}|$, with the current measurements indicating $|V_{tb}| \gg |V_{td}|, |V_{ts}|$. While a direct measurement of the $V_{tb}$ matrix element is only possible through single top quark production, as described in Section 3.2, model-dependent constraints on $V_{tb}$ can also be inferred from a measurement of $R$: Assuming the validity of the standard model, specifically the existence of three fermion generations, unitarity of the CKM matrix and insignificance of non-$W$ boson decays of the top quark (see Sections 6.3-6.5), the denominator in Eq. 34 equals one. $R$ then simplifies to $|V_{tb}|^2$, and is therefore strongly constrained to $0.9980 < R < 0.9984$ at 90% C.L. by global CKM fits [165].

Deviations of $R$ from unity could, for example, be caused by the existence of a fourth heavy quark generation, non standard model top quark decays, or non standard model background processes. Consequently, precise measurements of R probe for physics beyond the standard model, and provide a required ingredient for the model-independent direct determination of the $|V_{tq}|$ CKM matrix elements from electroweak single top production [472].

The most precise measurement of $R$ thus far has been performed by D0 in the lepton + jets channel using data corresponding to an integrated luminosity of 0.9 fb$^{-1}$ [473], superseding the previously published measurement based on 0.2 fb$^{-1}$ [474]. The $t\bar{t}$ signal sample composition depends on $R$ in terms of the number of $b$ jets present in the sample, as illustrated in Fig. 44. By comparing the event yields with zero, one and two or more $b$ tagged jets, and using a topological discriminant to separate $t\bar{t}$ signal from background in events without $b$ tags, $R$ can be extracted simultaneously with the $t\bar{t}$ production cross section $\sigma_{t\bar{t}}$. This approach yields a measurement of $\sigma_{t\bar{t}}$ without assuming $\mathcal{B}(t \to Wb) = 100\%$, and exploits the different sensitivity of the two measured quantities to systematic uncertainties, thereby improving overall precision.
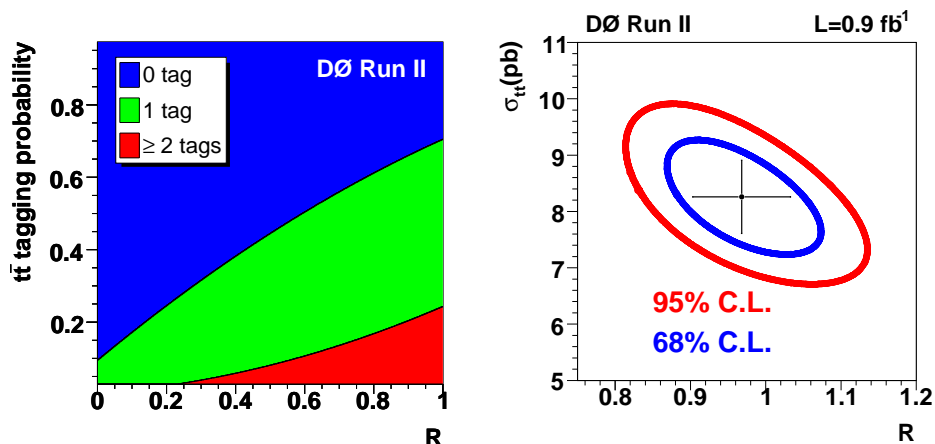
Fig. 44: Left: Fractions of events with 0, 1 and $\geq 2$ $b$ tags for $t\bar{t}$ events with $\geq 4$ jets as a function of $R$. Right: 68% and 95% C.L. statistical uncertainty contours in the R vs. $\sigma_{t\bar{t}}$ plane around the measured point in 0.9 fb$^{-1}$ of D0 data [473].

A maximum likelihood fit to the sample composition observed in data gives

$$R = 0.97^{+0.09}_{-0.08} \text{ (stat.} + \text{syst.) and} \tag{35}$$

$$\sigma_{t\bar{t}} = 8.18^{+0.90}_{-0.84} \text{ (stat.} + \text{syst.)} \pm 0.50 \text{ (lumi) pb} \tag{36}$$

(see Fig. 44) with a correlation of $-58\%$ for a top quark mass of 175 GeV/c$^2$, in agreement with the standard model prediction. From the measurement 95% C.L. limits are extracted, yielding $R > 0.79$ and $|V_{tb}| > 0.89$, the latter being model-dependent as mentioned above. $R$ exhibits no significant dependence on the top quark mass within $\pm 10$ GeV/c$^2$, while $\sigma_{t\bar{t}}$ varies by $\mp 0.09$ pb per $\pm 1$ GeV/c$^2$ in the same mass range. The total uncertainty on $R$ in this measurement is 9%, dominated by the statistical uncertainty of $^{+0.067}_{-0.065}$ and the largest systematic uncertainty from the $b$ tagging efficiency estimation of $^{+0.059}_{-0.047}$. The cross section measurement yields a result similar but not identical to the measurement on the same dataset [262], presented in Section 5.1.2. This is due to the assumption of $R = 1$, and slightly different event selection in the latter analysis.

CDF performed the first measurement of $R$ in Run I using both dilepton and lepton + jets events on 0.1 fb$^{-1}$ of data [475], and repeated the analysis in Run II on 0.2 fb$^{-1}$ of data [476], also finding good agreement with the standard model expectation.

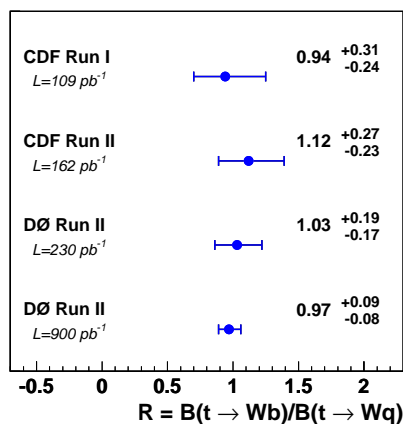All measurements of $R$ performed thus far at the Tevatron are summarized in Fig. 45.

Fig. 45: Summary of the branching ratio $R$ measurements and their total uncertainties obtained at the Tevatron by CDF [475, 476] and D0 [473, 474].

### 6.3. *Search for neutral-current top decays*

Flavor changing neutral interactions of the top quark with a light quark $q = u, c$ through gauge $(Z, \gamma, g)$ or Higgs $(H^0)$ bosons are forbidden at lowest order and are suppressed by the GIM mechanism [56] at higher orders in the standard model framework. Consequently, the corresponding FCNC top quark decays are expected to occur, at most, with branching ratios at $\mathcal{O}(10^{-12})$ [419], well out of reach of sensitivity of the Tevatron or the LHC. Any observation of such FCNC decays would therefore signal physics beyond the standard model.

Many extensions of the standard model predict the occurrence of FCNC interactions, affecting both electroweak single top production (see Section 5.8.5) and top quark decay. The branching fractions of FCNC top decays can increase by many orders of magnitude in such models, as for example in Supersymmetry [477–479], additional broken symmetries [480], dynamical EWSB [481, 482] including topcolor-assisted technicolor [483] or extended Higgs models such as Two Higgs Doublet Models [484–487]. Overviews of such models and their impact on top couplings are given in Refs. [419, 488–490].

A search for the top quark FCNC decay $t \rightarrow Zq$ at the Tevatron is considered especially interesting due the large top quark mass and very distinct experimental signature (see Fig. 46). It was already suggested in 1989 [491], well before the discovery of the top quark. The expected sensitivity for such a branching ratio measurement is $\mathcal{O}(10^{-2})$ at the Run II Tevatron and $\mathcal{O}(10^{-4})$ at the LHC [492], while the largest expected branching fractions from SM extensions reach up to $\mathcal{O}(10^{-2})$ [482] and $\mathcal{O}(10^{-4})$ [419], respectively. The best published limit before Run II on $\mathcal{B}(t \rightarrow Zq)$ was obtained at LEP by the L3 Collaboration via a search for single top quark pro-
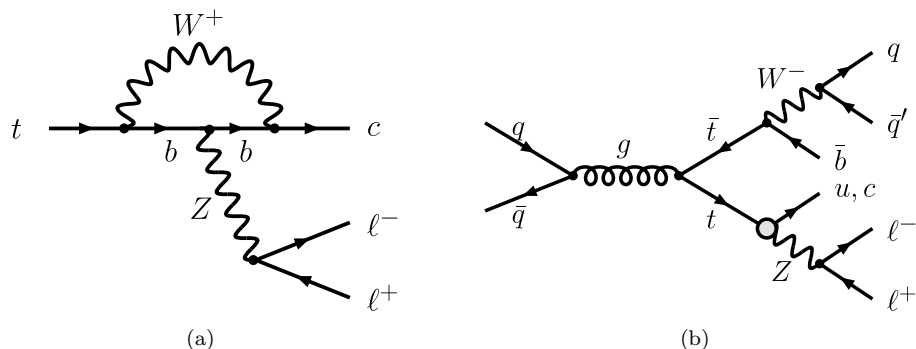
Fig. 46: (a) Feynman "penguin" diagram for the FCNC decay $t \to Zc$ with $Z \to \ell^+\ell^-$. Including the corresponding diagrams with a $d$ and $s$ quark in the loop, the process is nearly cancelled in the standard model. (b) Event signature for top quark pairs containing one FCNC $t \to Zq$ decay and one $W \to q\bar{q}'$ decay from $t \to Wb$, resulting in a final state that contains a $Z$ boson and four jets.

duction, where no significant deviation from the SM background expectation was observed, yielding $\mathcal{B}(t \to Zq) < 13.7\%$ at 95% C.L. [422].

In Run I, the CDF Collaboration performed a search for the FCNC decays $t \to Zq$ and $t \to \gamma q$ on a dataset with an integrated luminosity of 0.1 fb$^{-1}$ [425]. For the $t \to \gamma q$ search, a photon is reconstructed as an energy cluster in the electromagnetic calorimeter, either without an associated track or with a single soft track (presumably a random overlap) carrying less than 10% of the photon energy pointing to the cluster. Two event signatures are considered, where the $W$ boson from the standard-model-like second top decay branches either leptonically into $e\nu_e$ or $\mu\nu_\mu$, or hadronically into $\bar{q}q'$ quarks. Consequently, these samples are selected by requiring either a charged lepton ($e$ or $\mu$), $\not{p}_T$, at least two jets and a photon, or by requiring at least four jets and a photon. In both samples, a photon-jet combination must yield a mass between 140 and 210 GeV/c$^2$ and the SM-like top decay must contain one $b$ tag. 40% of the $t \to \gamma q$ acceptance comes from the photon + multijet selection, while the lepton + photon mode contributes 60%. After all selections, one event remains in the leptonic channel and none in the photon + multijet channel, with an expected background of about 0.5 events mainly from $W\gamma$ production with additional jets in each channel. This translates into a 95% C.L. upper limit on the branching fraction of $\mathcal{B}(t \to c\gamma) + \mathcal{B}(t \to u\gamma) < 3.2\%$.

In the $t \to Zq$ search, $W \to q\bar{q}'$ decays from the SM-like second top decay are considered together with a leptonically decaying $Z$ boson into $e^+e^-$ or $\mu^+\mu^-$. Using the leptonic $W$ boson decay as well does not substantially increase the acceptance and consequently does not improve the limit. The resulting event signature therefore contains four jets and two leptons with an invariant mass consistent with that of a $Z$ boson, as illustrated in Fig. 46. Since the branching ratio of $Z \to \ell^+\ell^-$ is
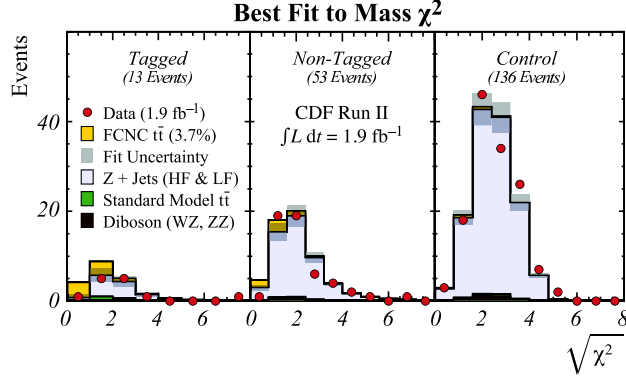
Fig. 47: Expected and observed mass $\chi^2$ distributions in $Z+ \geq 4$ jets events in signal samples with and without $b$ tags and in a background-enriched sample used to ascertain uncertainties in the background shape and normalization in 1.9 fb$^{-1}$ of CDF data [429]. The expected FCNC $t \to Zq$ signal with the observed 95% C.L. upper limit on the branching fraction is shown as well.

small, this search is less sensitive than the $t \to \gamma q$ one. One $Z \to \mu^+\mu^-$ event passes the selection, with an expected background of $\approx 0.6$ events from $Z+$ multijet and $t\bar{t}$ production. This corresponds to a 95% C.L. upper limit on the branching fraction of $\mathcal{B}(t \to cZ) + \mathcal{B}(t \to uZ) < 33\%$. These measurements can be translated into limits on the FCNC couplings $\kappa_\gamma$ and $\kappa_Z$ at 95% C.L. [426], which are $\kappa_\gamma^2 < 0.176$ and $\kappa_Z^2 < 0.533$ (see Section 5.8.5 and Fig. 35).

In Run II, the CDF Collaboration has performed a search for the FCNC decay $t \to Zq$ on a dataset with an integrated luminosity of 1.9 fb$^{-1}$ [429]. Events consistent with a leptonically decaying $Z$ boson to $e^+e^-$ or $\mu^+\mu^-$ are selected together with at least four jets, one of which can be $b$ tagged (see Fig. 46). The event selection was optimized in a preceding version of this analysis with 1.1 fb$^{-1}$ of data [493], which was a "blind" cut-based counting experiment. By requiring only one well-identified lepton for $Z$ reconstruction, while the second lepton can be formed from an isolated track, the acceptance is doubled compared to using only fully identified leptons. The sensitivity of the search is further increased by dividing the data into two subsamples, one $b$ tagged and one not tagged. The best discriminant found to separate signal from background is a mass $\chi^2$ variable that combines the kinematic constraints present in FCNC decays: Two jets in the event have to form a $W$ boson, and together with a third jet a top quark, while the $Z$ boson has to form a top quark with the fourth jet. Because the event signature does not contain neutrinos, the events can be fully reconstructed. The signal fraction in the selected dataset is determined via a template fit in signal samples with or without $b$ tags, and a background-enriched control sample is used to constrain uncertainties on the background shape and normalization (see Fig. 47).

Table 19: Relative signal acceptances and observed 95% C.L. upper limits on the branching fractions for several non-SM top quark decay modes as a function of assumed top quark mass in a 1.9 fb$^{-1}$ doubly $b$ tagged lepton + jets dataset [494].

| Decay | $\mathcal{R}_{\mathrm{WX/WW}}$ [%] | Limit [%] (175 GeV/c$^2$) | Limit [%] (172.5 GeV/c$^2$) | Limit [%] (170 GeV/c$^2$) |
|---|---|---|---|---|
| $\mathcal{B}(t \to Zc)$ | 32 | 13 | 15 | 18 |
| $\mathcal{B}(t \to gc)$ | 27 | 12 | 14 | 17 |
| $\mathcal{B}(t \to \gamma c)$ | 18 | 11 | 12 | 15 |
| $\mathcal{B}(t \to \text{invisible})$ | 0 | 9 | 10 | 12 |

Since the observed distributions are consistent with the standard model background processes, a 95% C.L. upper limit is extracted on the branching fraction $\mathcal{B}(t \to cZ) + \mathcal{B}(t \to uZ)$ of $< 3.7\%$. The expected limit in absence of signal is 5%. This is the best limit on $\mathcal{B}(t \to Zq)$ to date, starting to constrain predictions from a dynamic EWSB model [482].

## 6.4. *Search for invisible top decays*

Apart from the direct search for $t \to (Z/\gamma)\, q$ decays, as described in the previous section, one can also perform an indirect search for "invisible" top quark decays by comparing the predicted $t\bar{t}$ production cross section with the observed yield in data. In order to be sensitive to novel top decay modes with this method, these decays must exhibit a significantly different acceptance from the standard model top quark decay.

Based on a 1.9 fb$^{-1}$ doubly $b$ tagged lepton + jets dataset, CDF searches for deviations of the observed $t\bar{t}$ production rate from the theoretical prediction [124] due to the decays $t \to Zc$, $t \to gc$, $t \to \gamma c$ and $t \to$ "invisible" states [494]. These decays exhibit a relative acceptance $\mathcal{R}_{\mathrm{WX/WW}}$, where one novel and one SM top quark decay occur, normalized to the standard model $t\bar{t}$ decay acceptance, from 32% down to no acceptance (for decays to invisible states).

With an observed $t\bar{t}$ production cross section of 8.8 pb, and a prediction of 6.7 pb for a top quark mass of 175 GeV/c$^2$, the obtained limits on the novel top quark decay modes are all lower than expected, but statistically consistent with expectation. The results are summarized in Table 19 for top quark masses of 170, 172.5 and 175 GeV/c$^2$.

## 6.5. *Search for top decays to charged Higgs bosons*

As indicated previously, the standard model incorporates one Higgs doublet of complex scalar fields to break electroweak symmetry and to generate masses of weak gauge bosons and fermions (see Section 2.1). As a consequence, one obtains a single neutral scalar CP-even particle that still remains to be discovered, the Higgs

boson $H$. An extension of the standard model Higgs sector introduces a second Higgs doublet, referred to in Section 5.8.4 as Two Higgs Doublet Models (THDM or 2HDM) [414, 415]. These models provide five physical scalar Higgs bosons after electroweak symmetry breaking, namely two neutral CP-even Higgs bosons $H^0$ and $h^0$, one neutral pseudoscalar CP-odd Higgs particle $A^0$, and two charged Higgs bosons $H^{\pm}$. The observation of charged Higgs bosons would therefore offer clear evidence for physics beyond the standard model.

Three choices of Higgs-fermion couplings are differentiated in THDM. In Type-I models only one of the two Higgs doublets couples to fermions, while in Type-II models one doublet couples to up-type fermions and the other doublet to down-type fermions. Type-III models have general Higgs-fermion Yukawa couplings of both Higgs doublets, leading to Higgs-mediated FCNC at tree level, which requires tuning of the Higgs parameters to ensure sufficient suppression of FCNC to be compatible with current experimental limits. One example of a Type-II THDM is the Minimal Supersymmetric Standard Model (MSSM) [369] which is frequently used as reference in the analyses described below. The relevant model parameters in searches for charged Higgs bosons are the ratio of the vacuum expectation values of the two Higgs doublets ($\tan\beta$) and the mass of the charged Higgs boson $m_{H^{\pm}}$.

The inclusive single charged Higgs boson production rate $\sigma(p\bar{p} \to tH^-X)$ reaches a maximum of $\mathcal{O}(1\text{ pb})$ at the Tevatron where the charged Higgs boson can be produced via the decay of a top quark. The corresponding inclusive cross section for pair production of charged Higgs bosons $\sigma(p\bar{p} \to H^+H^-X)$ is below $\mathcal{O}(0.1\text{ pb})$ [495, 496].

The decay mode $t \to Hb$ is kinematically accessible if the mass of the charged Higgs boson is less than the difference between top and $b$ quark masses $m_{H^{\pm}} < (m_t - m_b)$, and will then compete with the standard model decay $t \to Wb$. The distinct top quark decay signature provides an additional handle for background suppression compared to direct production of charged Higgs bosons. The branching fraction of $t \to Hb$ depends on $\tan\beta$ and $m_{H^{\pm}}$. As illustrated in Fig. 48 for the MSSM, the branching ratio of $t \to Hb$ increases significantly both for small $\tan\beta \lesssim 1$ and large $\tan\beta \gtrsim 40$, for a given $m_{H^{\pm}}$. The standard model decay is assumed to account for the difference of $\mathcal{B}(t \to Hb)$ from unity. For a given $\tan\beta$, the branching ratio of $t \to Hb$ decreases with increasing $m_{H^{\pm}}$. The decay of $H^{\pm}$ is dominated by $H^{\pm} \to \tau\nu$ for large $\tan\beta$, independent of $m_{H^{\pm}}$, which would result in an excess of $t\bar{t}$ events in the $\tau$ decay channel relative to standard model expectation. At small $\tan\beta$, the decay $H^{\pm} \to cs$ is enhanced for small $m_{H^{\pm}}$, while $H^{\pm} \to t^*b$ dominates for $m_{H^{\pm}}$ close to the top quark mass. Consequently, searches for charged Higgs bosons focus on these three fermionic decay modes.

In the early 1990s (before the discovery of the top quark) first searches for $t \to Hb$ in the $H^{\pm} \to \tau\nu$ decay mode assuming specific branching fractions were performed, and limits derived in the $m_t$ versus $m_{H^{\pm}}$ parameter space by the UA1 and UA2 experiments [498, 499] at the CERN $Sp\bar{p}S$ collider, and by CDF at the Run I Tevatron [500, 501]. All four LEP experiments searched for pair-production of
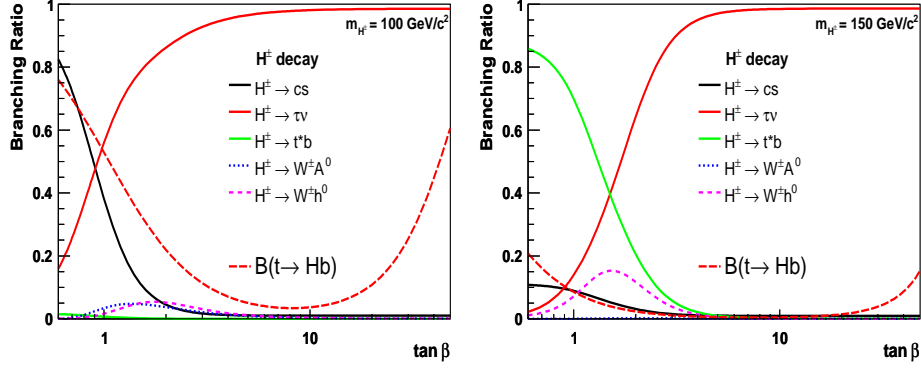
Fig. 48: Branching ratios for top quark and charged Higgs boson decays versus $\tan\beta$ in the MSSM framework as simulated with CPSUPERH [497] for $m_{H^\pm} = 100$ GeV/c$^2$ (left) and $m_{H^\pm} = 150$ GeV/c$^2$ (right).

charged Higgs bosons in $e^+e^- \to H^+H^-$, assuming that only the decays $H^\pm \to \tau\nu$ and $H^\pm \to cs$ can occur [502–505], as favored by Type-II THDM. The dominant background in the resulting three decay modes is pair production of $W$ bosons, yielding similar final states. 95% C.L. lower mass limits, independent of the $H^\pm$ decay mode, yielded $m_{H^\pm} > 78.6$ GeV/c$^2$ in a preliminary combination of all four experiments [506]. This was superseded by a more stringent limit obtained by ALEPH of 79.3 GeV/c$^2$ [502].

Indirect limits on the mass of the charged Higgs boson can be obtained from measurements of the $b \to s\gamma$ FCNC process at $B$ factories, since the involved loop diagrams are sensitive to contributions from new particles such as $H^\pm$. For a Type-II THDM scenario, a 95% C.L. lower limit of $m_{H^\pm} > 295$ GeV/c$^2$ can be derived [507] if the used theoretical description is assumed to be complete. Direct searches are less model dependent, and therefore serve as important tools to scan for new physics beyond the regions of parameter space excluded by the corresponding direct analyses described above. The direct searches for $t \to Hb$ performed at the Tevatron are based on Type-II THDM scenarios.

After the discovery of the top quark, the first searches for $H^\pm$ in top decays $t\bar{t} \to H^\pm W^\mp b\bar{b}, H^\pm H^\mp b\bar{b}$ focused on the decay $H^\pm \to \tau\nu$, which corresponds to large $\tan\beta$. CDF published an analysis superseding and extending a previous result [508], requiring inclusive final states with $\not{p}_T$, a hadronically decaying tau lepton ($\tau_h$), and (i) two jets and at least one additional either lepton or jet, or (ii) a second energetic $\tau_h$ [509]. Another search investigated the dilepton channels $e\tau_h, \mu\tau_h$, with accompanying $\not{p}_T$ and at least two jets [510]. D0 performed a first $H^\pm$ analysis in Run I based on a "disappearance" search in the lepton + jets channel, sensitive to $H^\pm$ fermionic decay modes, by looking for a discrepancy in the event yields relative to the standard model predictions [511]. This analysis was complemented through a

direct search for $H^{\pm} \to \tau\nu$ with a hadronically decaying $\tau$ reconstructed as narrow jet in a dataset with events containing $\not{p}_T$ and at least four, but no more than eight, jets [512]. All analyses observe good agreement with SM expectation, and provide limits in the $\tan\beta, m_{H^{\pm}}$ plane.

It should be noted that the above limits are based on tree level MSSM calculations of branching fractions depending on $\tan\beta$. By now, it has become clear that higher-order radiative corrections, which strongly depend on model parameters, modify these predictions significantly [513,514]. Also, non-fermionic (bosonic) $H^{\pm}$ decay modes can have non-negligible contributions at small $\tan\beta$, as illustrated in Fig. 48, affecting the limits derived in that area without taking this into account. Independent of these issues, one can still provide upper limits on $\mathcal{B}(t \to Hb)$ based on the observed production rate for any specified $H^{\pm}$ branching ratio. For example, for a purely tauonically decaying charged Higgs boson, 95% C.L. upper limits on $\mathcal{B}(t \to Hb)$ are found by CDF to lie between 0.5 and 0.6 for 60 GeV/c$^2 \leq m_{H^{\pm}} \leq$ 160 GeV/c$^2$ [510]. The combined D0 result corresponds to $\mathcal{B}(t \to Hb) < 0.36$ at 95% C.L. for $m_{H^{\pm}} < 160$ GeV/c$^2$ and $0.3 < \tan\beta < 150$, which is the full range where the leading-order MSSM calculation is valid [512].

CDF published a first search for $t \to Hb$ in Run II using 0.2 fb$^{-1}$ of integrated luminosity [515]. The search is based on the corresponding $t\bar{t}$ cross section analyses [207, 216, 252] in the topology $\not{p}_T$ + jets + $\ell$ + X, where $\ell$ corresponds to an electron or muon and X to either $\ell$ (dilepton channel), $\tau_h$ (lepton + $\tau$ channel) or one or more $b$ tagged jets (lepton + jets channels). Dropping the assumption of $\mathcal{B}(t \to Hb) = 0$, and avoiding overlaps of the channels, the observed yields can be compared with the expected deficits or excesses in the channels relative to the standard model prediction, depending on the top quark and $H^{\pm}$ branching fractions. Apart from the standard model top quark decays, $t \to Hb$ is considered with $H^{\pm}$ decaying to $\tau\nu$, $cs$, $t^*b$ or $Wh^0$, with $h^0 \to b\bar{b}$. The $t\bar{t}$ production rate is assumed to be not affected by the extension of the Higgs sector. Since no $H^{\pm}$ signal is observed, 95% C.L. upper limits on $\mathcal{B}(t \to Hb)$ are obtained, for example, for a tauonic Higgs model ($\mathcal{B}(H^{\pm} \to \tau\nu) = 1$) to be 0.4 for 80 GeV/c$^2 \leq m_{H^{\pm}} \leq 160$ GeV/c$^2$. 95% C.L. limits are also obtained in the $(m_{H^{\pm}}, \tan\beta)$ parameter space in the framework of the MSSM for certain benchmark settings of parameters [515], taking radiative corrections into account. While the excluded area for large $\tan\beta$ strongly depends on the different benchmarks investigated, this is not the case for small $\tan\beta$. An example result is shown in Fig. 49.

D0 performs a similar analysis based on the same $t\bar{t}$ final states in 1 fb$^{-1}$ of integrated luminosity [257]. Two models for the decay mode of the charged Higgs boson are studied: (i) a "tauonic" Higgs model with $\mathcal{B}(H^{\pm} \to \tau\nu) = 1$ that would give an enhancement of the lepton + $\tau$ channels and a deficit in the lepton + jets and dilepton channels, and (ii) a "leptophobic" model with $\mathcal{B}(H^{\pm} \to cs) = 1$ that would yield an enhancement of the all-hadronic channel and a deficit in all channels considered in this analysis. For both model assumptions, good agreement with the
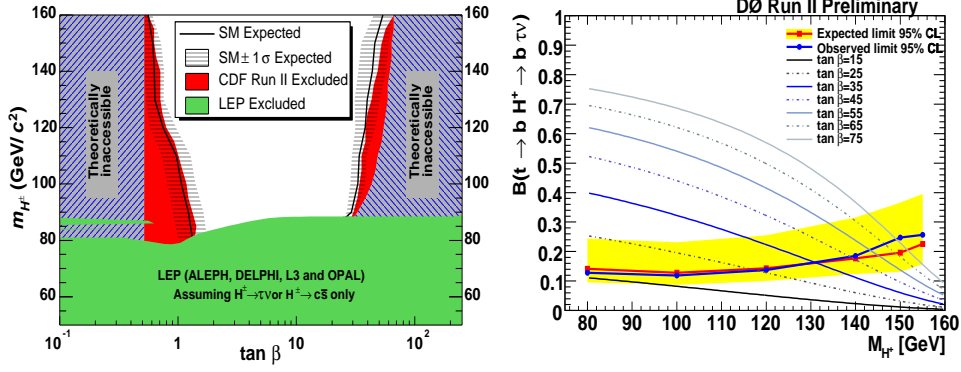
Fig. 49: Left: Expected and observed 95% C.L. exclusion limits for charged Higgs bosons in the $(m_{H^\pm}, \tan\beta)$ plane obtained by CDF for the MSSM benchmark scenario discussed in Ref. [515]. Right: Expected and observed 95% C.L. limits on $\mathcal{B}(t \to Hb)$ versus $m_{H^\pm}$ found by D0 for a tauonic charged Higgs model using a simultaneous fit of $\mathcal{B}(t \to Hb)$ and the $t\bar{t}$ production cross section [257]. MSSM tree-level predictions for several $\tan\beta$ values are shown as well.

standard model prediction is observed, and 95% C.L. upper limits on $\mathcal{B}(t \to Hb)$ are provided for 80 GeV/c$^2$ $\leq m_{H^\pm} \leq$ 155 GeV/c$^2$, yielding 0.16 - 0.20 for the tauonic and 0.2 for the leptophobic model. The dominant systematic uncertainties arise here from uncertainties on the $t\bar{t}$ cross section and the luminosity.

For the tauonic model, an improvement of the obtained limits by about 30% in the low $m_{H^\pm}$ range ($\lesssim$ 100 GeV/c$^2$) is possible when the $t\bar{t}$ cross section is allowed to float in the fit rather than be fixed to the SM value. The resulting limits are displayed in Fig. 49, and range from 0.12 to 0.26 in the indicated $m_{H^\pm}$ range. Assuming the standard model scenario of $\mathcal{B}(t \to Hb) = 0$, a combination of the $t\bar{t}$ cross sections from the analyzed final states is also obtained, as was discussed in Section 5.1.5.

As illustrated in Fig. 49, the results obtained in Ref. [515] leave room for improvement, particularly close to $\tan\beta \approx 1$ and $m_{H^\pm}$ above the $W$ boson mass. For this range of parameters, the MSSM predicts a significant branching fraction for the decay $H^\pm \to cs$. CDF has searched for $t \to Hb$ in this decay channel in 2.2 fb$^{-1}$ double $b$ tagged lepton + jets data [516]. Both standard model and exotic decay exhibit the same final state, but can be distinguished via the dijet invariant mass, where the two untagged leading jets are assigned to $W^\pm/H^\pm$ decay products. A binned likelihood fit using $W^\pm/H^\pm$ dijet mass templates yields no significant excess over the SM prediction, and 95% C.L. upper limits on $\mathcal{B}(t \to Hb)$ are provided for 90 GeV/c$^2$ $\leq m_{H^\pm} \leq$ 150 GeV/c$^2$, assuming a leptophobic Higgs model. The limits range from 8% for $m_{H^\pm} =$ 130 GeV/c$^2$ to 32% for $m_{H^\pm} =$ 90 GeV/c$^2$, complementing the analysis by D0 described above for the mass range above 100 GeV/c$^2$.

A first direct search for charged Higgs boson production in the mass range beyond $m_t$ via the process $q\bar{q}' \to H^\pm \to tb$ has been performed by D0, as was discussed previously in Section 5.8.4.

## 7. Top Quark Properties

In the past two chapters, it was demonstrated that both top quark production and decay thus far have been found to be consistent with the standard model expectations. No new particles or anomalous couplings have been observed yet. To actually confirm the top quark's standard model identity, its fundamental quantum numbers need to be measured and their self-consistency in the standard model framework needs to be confirmed as well.

In this chapter, measurements of the top quark's electric charge, lifetime and mass performed thus far at the Tevatron are described. Again, top quark pair events are used for this, because these events provide higher statistics and favorable sample purities compared to single top events. First direct measurements of the $V_{tb}$ matrix element in electroweak single top quark production have already been discussed in Section 5.8.1.

### 7.1. *Top quark electric charge*

The electric charge of quarks can be determined, for example, in electron-positron collisions via the ratio of the hadronic cross section to the muon cross section $R = \sigma(e^+e^- \to \text{hadrons})/\sigma(e^+e^- \to \mu^+\mu^-)$, which is proportional to the sum of the squared electric charges of the quark flavors accessible at the chosen center of mass energy. Due to the large top quark mass, such a direct measurement could not yet be performed at past and present electron-positron colliders. Also, a direct measurement of photon radiation in $t\bar{t}$ events at hadron colliders, which would give access to the top quark's charge and its electromagnetic coupling, is unrealistic due to limited statistics at the Tevatron [517]. Consequently, the top quark is the only quark whose fundamental quantum numbers of weak isospin and electric charge could thus far be determined only indirectly in the framework of the standard model from measurements of its weak isospin partner, the $b$ quark, to be $T_3 = +\frac{1}{2}$, $Q_t = +\frac{2}{3}e$ (see Section 2.2).

Information on the electric charge of the top quark can also be inferred from the electric charges of its decay products. However, there is an inherent ambiguity in $p\bar{p} \to t\bar{t} \to W^+W^-b\bar{b}$ events when pairing $W$ bosons and $b$ jets, resulting in possible charges of $|Q| = 2e/3$ or $4e/3$ for the top quark. An exotic quark with charge $-4e/3$ being the discovered particle at the Tevatron instead of the standard model top quark would be compatible with precision electroweak measurements if the right-handed $b$ quark were to mix with the $-1e/3$ charged exotic doublet partner of such an exotic top quark. The standard model top quark with charge $2e/3$ would yet have to be discovered in this scenario, due to its large mass of $271^{+33}_{-38}$ GeV/c$^2$ [366, 518, 519].
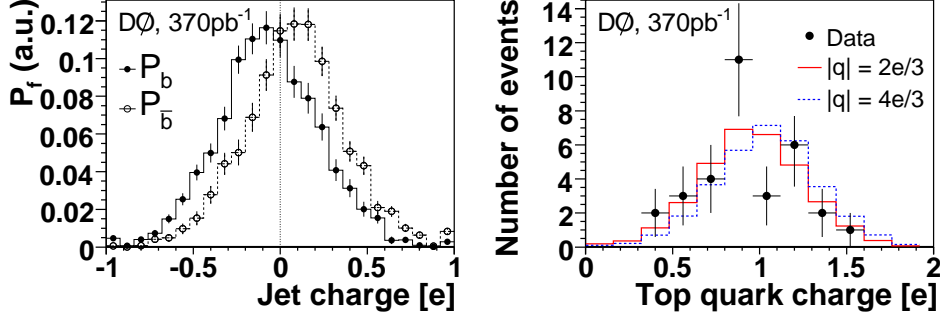
Fig. 50: Left: $b/\bar{b}$ jet charge distributions obtained in dijet data. Right: Distribution of the top quark charge obtained in data, overlaid with the expectations from standard model and exotic model [520].

D0 has published a first measurement discriminating between the $2e/3$ and $4e/3$ top quark charge scenarios in a 0.4 fb$^{-1}$ lepton + jets dataset with $\geq 2$ $b$ tagged jets [520]. The sample exhibits high signal purity, with the two dominant background processes of $Wb\bar{b}$ and single top production contributing only 5% and 1% to the selected events, respectively. Each $t\bar{t}$ event provides two measurements of the absolute value of the top quark charge, one from the leptonic and one from the hadronic decay of the $W$ boson in $t \to Wb$. The charge of the $W$ boson is determined from the (inverse) lepton charge for the leptonic (hadronic) $W$ boson decay. The $b$ jet charge, discriminating between $b$ and $\bar{b}$ jets, is determined using a jet charge algorithm, based on the $p_T$ weighted average of the charges of the tracks associated with the $b$ tagged jet. The corresponding distributions are derived from dijet collider data [520] (see Fig. 50). The top quark charge observable is then defined as the absolute value of the sum of the $W$ boson- and associated $b$ jet charge, where the right pairing is determined through a constrained kinematic fit. By comparing the distribution in data with the expected shape from the standard model and exotic model (see Fig. 50), respectively, D0 excludes the hypothesis of only exotic quarks of charge $|Q| = 4e/3$ being produced at up to 92% C.L. and limits an exotic quark admixture in the sample to at most 80% at the 90% C.L.

Using a similar analysis approach, CDF obtains a preliminary result on the top quark charge using double $b$ tagged lepton + jets and $b$ tagged dilepton events in a 1.5 fb$^{-1}$ dataset [521]. The observed $2\ln(\text{Bayes Factor})$ is 12, meaning that the data favor very strongly the SM top quark hypothesis over the exotic model.

While the results from CDF and D0 are not directly comparable because of different statistical approaches in the interpretation of their results, both agree to favor the SM top quark charge hypothesis. This is supported by the searches for new heavy top-like quark pair production (see Section 5.7.4), which are starting to exclude additional quark production in the mass range predicted by the alternative model. A top quark charge measurement determining the $b$ jet charge in soft-lepton

tagged events from the soft-lepton charge rather than the current track-based approach has not been performed yet.

The measurement of the top quark charge in $t\bar{t}\gamma$ events will be possible at the LHC because of the increased production rate and the reduction of irreducible background from photons radiated off the incoming quarks in $t\bar{t}$ production via $q\bar{q}$ annihilation. Consequently, top quark charge measurements via photon radiation in $t\bar{t}$ events are predicted to achieve a precision of 10% [517]. Using the top quark decay products to provide an additional charge measurement will help to disentangle the measurements of top quark electromagnetic coupling strength from the top quark charge in the $t\bar{t}\gamma$ events. This will help to rule out possible anomalous admixtures in the electromagnetic interaction of the top quark.

### 7.2. *Top quark lifetime*

The lifetime of the top quark $\tau_t = \hbar\Gamma_t^{-1} \approx \hbar(1.3\text{ GeV})^{-1}$ is approximately $5 \cdot 10^{-25}$ s in the framework of the standard model, as discussed in Section 3.3.2. Consequently, the production and decay vertices of the top quark are separated by $\mathcal{O}(10^{-16})$m, which is orders of magnitude below the spatial resolution of any detector. Also, the top quark width is narrower than the experimental resolution at both the Tevatron and the LHC. Consequently, a direct measurement of the top quark lifetime or its width will be limited by detector resolution. A measurement of the top quark lifetime is still useful to confirm the standard model nature of the top quark, and exclude new top quark production channels through long-lived particles. A measurable lifetime of the top quark itself would imply a correspondingly small $V_{tb}$ matrix element and render single top quark production at the Tevatron undetectable, in contradiction with the observed evidence described in Section 5.8.

CDF has set limits on the top quark lifetime and width using two approaches. One analysis uses a $b$ tagged lepton + jets dataset of 0.3 fb$^{-1}$ [522] to measure the impact parameter (smallest distance) between the top quark production vertex and the lepton track from the leptonic $W$ boson decay in the plane orthogonal to the beam direction. Fitting the obtained distribution with signal Monte Carlo templates for $c\tau_t$ between 0 and 500 $\mu$m and a background template, the template for 0 $\mu$m describes the data best, which translates into a 95% C.L. limit on $c\tau_t$ of < 52.5 $\mu$m.

The second analysis uses a $b$ tagged lepton + jets dataset of 1 fb$^{-1}$ [523] to reconstruct the top quark mass in each event using a kinematic fit. The observed distribution is compared in a fit to $t\bar{t}$ signal Monte Carlo templates of different widths for a top quark mass of 175 GeV/c$^2$ and background templates. From the fit result, at 95% C.L. the top quark width is found to be smaller than 13.1 GeV, corresponding to a lower limit on the top quark lifetime of $5 \cdot 10^{-26}$ s.

### 7.3. *Top quark mass*

The top quark is set apart from all other known fundamental particles by its large mass. Being the only particle with its Yukawa coupling close to unity also raises the

question whether it plays a special role in the process of mass generation. Since the lifetime of the top quark is so short (see Sections 3.3.2 and 7.2), unlike the other quarks, it does not hadronize and properties like its mass can be determined directly without the complication of having a quark embedded in a hadron. Being a sensitive probe for physics beyond the standard model, it is also important to measure its mass in different decay modes that could be affected differently by novel physics contributions.

In the framework of the standard model, the top quark mass is a free parameter. As discussed in Section 2.3, its precise determination together with a precise $W$ boson mass measurement provides a test of the self-consistency of the framework and constrains the mass of the yet undiscovered Higgs boson (or other new particles [524, 525]) via electroweak radiative corrections.

Measurements of the top quark mass have been performed thus far only in $t\bar{t}$ events, and mainly in the dilepton, lepton + jets and all-hadronic final states. A complete kinematic reconstruction of the $t\bar{t}$ pair from the observed objects in the event can be performed in the all-hadronic final state where no neutrinos are present. Assuming $\not{p}_T$ arises solely from the escaping neutrino in the lepton + jets channel, a kinematic fit can be performed here constraining the invariant mass of the charged lepton and neutrino to that of the $W$ boson, yielding a twofold ambiguity for the neutrino's longitudinal momentum solution. Because of the two neutrinos contributing to $\not{p}_T$ in the dilepton final state, a direct kinematic reconstruction of the $t\bar{t}$ event is not possible without adding more information or making other assumptions about the kinematics of the objects in the event.

Since the assignment of partons to reconstructed objects in an event is not definite, combinatorial ambiguities arise in all channels. Depending on the analysis technique, either all combinations are used to extract the top quark mass, or the best combinations are selected based on, for example, the lowest $\chi^2$ in a kinematic fit to the $t\bar{t}$ event hypothesis. Identification of $b$ jets can be used to reduce the number of combinations to consider in the lepton + jets and the all-hadronic channels. Even if both $b$ jets from the $t\bar{t}$ decay are identified, four combinations remain in the lepton + jets channel (including the neutrino $p_z$ ambiguity) and six in the all-hadronic channel. In these channels, usually at least one $b$ tagged jet is required to increase sample purity, or the data can be split on the basis of $b$ tag multiplicity, and therefore purity, to optimize overall sensitivity.

The techniques used in top quark mass analyses can be divided into three categories:

(i) **Template Method (TM):** Observables sensitive to the mass of the top quark such as the reconstructed top quark mass $m_{\text{reco}}$ or $H_T$ are evaluated in the dataset under consideration. The resulting distribution is then compared in a fit with expected contributions from $t\bar{t}$ signal (with varying top quark masses) and background processes.

(ii) **Matrix Element Method (ME):** Based on the leading-order matrix ele-

ments of contributing signal and background processes, the four-vectors of the reconstructed objects in each event define a probability density as a function of the top quark mass. The total likelihood for the event sample is given as the product of the individual event likelihoods. This method is also referred to as the Dynamical Likelihood Method (DLM).

(iii) **Ideogram Method (ID):** An event-by-event likelihood depending on the assumed top quark mass is formed based on a constrained fit of the event kinematics, taking all object permutations and possible background contributions into account. As mentioned above, this kind of constrained fit is only possible in the all-hadronic and lepton + jets channels.

Naturally, the analyses most sensitive to the top quark mass are also very sensitive to the jet energy scale (JES) calibration. The systematic uncertainty due to the external jet energy calibration (see Section 4.3.3) then is usually the dominant systematic uncertainty in such analyses. This can be reduced in decay channels where at least one $W$ boson decays "hadronically" by using the well-measured $W$ boson mass to constrain *in-situ* the jet energy calibration in top quark events [526, 527]. Determining such an overall scale factor for jet energies, absorbs a large part of this uncertainty into an uncertainty scaling with $t\overline{t}$ sample statistics, while residual uncertainties, for example, due to $\eta$ and $p_T$ dependence of JES corrections or differences between light-quark and $b$-quark JES still remain. By performing an analysis simultaneously in the dilepton and all-hadronic and/or lepton + jets channels, the *in-situ* JES calibration can also be transferred to the dilepton channel [528, 529].

Another approach to reduce the dependence of top quark mass measurements on JES is to utilize observables with minimal JES dependence that are still correlated with the top quark mass, such as the mean $p_T$ of the charged lepton from the $W$ boson decay ($p_T^\ell$) or the mean transverse decay length of $b$ jets $L_{xy}$ in $t\overline{t}$ events [530]. While such measurements are statistically limited at the Tevatron, their uncertainties are basically uncorrelated with those of other statistically more sensitive analyses. This helps to reduce the overall uncertainty on $m_t$ when all measurements are combined. Also, the observed signal event yield can provide an additional constraint on $m_t$ via the mass dependence of the $t\overline{t}$ production cross section [531].

Performance, calibration and statistical uncertainty derivation of each mass analysis are checked using sets of simulated pseudo-experiments (ensemble tests), based on mean and rms of the extracted mass and pull distributions.

Measurements of $m_t$ were pioneered in Run I, based on 0.1 fb$^{-1}$ of data in the dilepton [316, 532–535], lepton + jets [320, 321, 454, 536, 537] and all-hadronic [538, 539] channels. A combination of the Run I results yields $m_t = 178.0 \pm 2.7(\text{stat.}) \pm 3.3(\text{syst.})$ GeV/c$^2$ [158]. Also in Run II, results come mainly from the dilepton, lepton + jets and all-hadronic channels, with the most precise measurements being from lepton + jets samples. One analysis uses an inclusive $\not{p}_T$ + jets signature, vetoing energetic isolated leptons and thereby enhancing the $\tau$ + jets signal contribution to 44% [540]. This result is listed together with measurements in

the all-hadronic channel in Section 7.3.3, and is consistent with the world-averaged top quark mass. A top quark mass measurement with explicit hadronic $\tau$ reconstruction has not been performed thus far, but given the recent progress in the corresponding cross section analyses discussed in Section 5.1.4, this could still be feasible at the Tevatron.

In the following sections, the latest (final) Run I results are given, along with the current preliminary and published Run II top quark mass measurements using various analysis techniques for each of the three main decay channels. Some of the most precise analyses entering the world-averaged top quark mass will be highlighted. A more detailed review of top quark mass analysis techniques pursued at the Tevatron can be found in Ref. [541]. The final section presents the current world average and some of its implications.

### 7.3.1. *Dilepton final state*

Analyses in the dilepton final state are performed either based on the matrix element or the template method. For the template approach, additional assumptions on the kinematics of the involved objects are made in order to solve the otherwise underconstrained system kinematics. Assuming several top quark masses, the consistency of the observed event kinematics can be used to obtain weights for each event as a function of $m_t$, based on input parton distribution functions and the observed charged lepton energies ("matrix weighting" $\mathcal{M}$), or using simulated neutrino pseudo-rapidity or azimuthal angle ("neutrino weighting": $\nu_\eta$, $\nu_\phi$, or $t\bar{t}$ longitudinal momentum ($p_z^{t\bar{t}}$) distributions [534, 542]. Top quark mass estimators are derived from the obtained weight distributions, such as the peak mass position, or mean and rms of the distributions. These values are then used in a template fit to data to obtain the most likely $m_t$ from the sample.

The most precise top quark mass result in the dilepton channel entering the world average is from D0, and has a precision of 2.2% [543]. It combines results from neutrino weighting ($\nu_\eta$) obtained on 1 fb$^{-1}$ in the dielectron, dimuon and lepton + track channels [544] with a measurement in the $e\mu$ channel using 2.8 fb$^{-1}$ of data and the matrix element method [543].

The matrix element method evaluates the probability density for each event ($P_{\text{evt}}$) with measured object four-vectors $x$ to originate from $t\bar{t}$ production, depending on the top quark mass, or from the dominant background arising from $Z \to \tau\tau$ + jets production in the following linear combination, based on the known expected signal fraction in the sample $f$:

$$P_{\text{evt}}(x; m_t) = f \cdot P_{\text{sig}}(x; m_t) + (1 - f) \cdot P_{\text{bkg}}(x). \tag{37}$$

$P_{\text{sig}}$ and $P_{\text{bkg}}$ are the signal and background probability densities for $t\bar{t}$ and $Z \to \tau\tau$ + jets production, based on the leading order matrix element for $q\bar{q} \to t\bar{t}$ and the VECBOS [555] parametrization of the $Z$-production matrix element, respectively. The probability densities are calculated by integrating over all unknown quantities,

Table 20: Top quark mass measurements performed thus far at the Tevatron in the dilepton channel with their integrated luminosities, data selections ($\ell\ell$ = dilepton, $\ell$+trk = lepton + track, NN = neural network) and analysis methods used. The two analyses using 0.1 fb$^{-1}$ are from Run I, and the references marked with an asterisk correspond to preliminary results.

| $\int \mathcal{L}dt$ [fb$^{-1}$] | Selection | Method | $m_t \pm$ (stat.) $\pm$ (syst.) [GeV/c$^2$] | Ref. |
|---|---|---|---|---|
| 0.1 | $\ell\ell$ | TM:$\nu_\eta$ | $167.4 \pm 10.3 \pm 4.8$ | [532, 533] |
| 0.1 | $\ell\ell$ | TM:$\mathcal{M}, \nu_\eta$ | $168.4 \pm 12.3 \pm 3.7$ | [535] |
| 0.3 | $\ell\ell$ | ME | $165.2 \pm 6.1 \pm 3.4$ | [545, 546] |
| 0.4 | $\ell\ell,\ell$+trk | TM:$\nu_\eta, \nu_\phi, p_z^{t\bar{t}}$ | $170.1 \pm 6.0 \pm 4.1$ | [542] |
| 0.4 | $\ell\ell,\ell$+trk | TM:$\mathcal{M}, \nu_\eta$ | $178.1 \pm 6.7 \pm 4.8$ | [547] |
| 1.0 | $\ell\ell$ | ME | $164.5 \pm 3.9 \pm 3.9$ | [548] |
| 1.0 | $\ell\ell$ | TM:$\mathcal{M}$ | $175.2 \pm 6.1 \pm 3.4$ | [549]* |
| 1.0 | $\ell\ell,\ell$+trk | TM:$\nu_\eta$ | $176.0 \pm 5.3 \pm 2.0$ | [544]* |
| 1.2 | $\ell\ell$ | TM:$p_z^{t\bar{t}}$ | $169.7_{-4.9}^{+5.2} \pm 3.1$ | [531] |
| 1.2 | $\ell\ell$ | TM:$p_z^{t\bar{t}} \oplus \sigma_{t\bar{t}}$ | $170.7_{-3.9}^{+4.2} \pm 2.6 \pm 2.4$(th.) | [531] |
| 1.8 | $\ell\ell$ | TM:$p_T^\ell$ | $156_{-19}^{+22} \pm 4.6$ | [550]* |
| 1.8 | $\ell\ell$ | TM:$\nu_\eta$ | $172.0_{-4.9}^{+5.0} \pm 3.6$ | [551]* |
| 1.8 | $\ell\ell$ | ME | $170.4 \pm 3.1 \pm 3.0$ | [552]* |
| 2.0 | $\ell\ell \oplus$ NN | ME | $171.2 \pm 2.7 \pm 2.9$ | [553] |
| 2.8 | $\ell$+trk | TM:$\nu_\phi$ | $165.1_{-3.2}^{+3.3} \pm 3.1$ | [554]* |
| 2.8 | $e\mu$ | ME | $172.9 \pm 3.6 \pm 2.3$ | [543]* |
| 2.8 | $e\mu/\ell\ell,\ell$+trk | ME/TM:$\nu_\eta$ | $174.4 \pm 3.2 \pm 2.1$ | [543]* |

such as the unmeasured neutrino energies and all parton states that can lead to the $x$ objects observed in the detector:

$$P_{\text{sig}}(x; m_t) = 1/\sigma_{\text{obs}}(m_t) \int_{q_1,q_2,y} \sum_{\text{flavors}} dq_1 dq_2 f(q_1) f(q_2) \frac{(2\pi)^4 |\mathcal{M}|^2}{q_1 q_2 s} d\Phi_6 W(x,y),$$
(38)

where $q_1$ and $q_2$ are the momentum fractions of the colliding partons from the proton and antiproton, $f(q_i)$ the corresponding PDFs, $\mathcal{M}$ is the matrix element for the signal process yielding the partonic final state $y$, $s$ is the squared center-of-mass energy and $d\Phi_6$ a six-body phase space element. The transfer function $W(x,y)$, which incorporates the detector resolution, describes the probability for a final state $x$ in the detector to be reconstructed from the partonic state $y$. The two possible permutations from the unknown jet-parton assignment are summed

over, and the probability is normalized to the expected observable production rate $\sigma_{\mathrm{obs}}(m_t)$. The calculation of $P_{\mathrm{bkg}}(x)$ proceeds in an analogous way, except that there is no dependence on $m_t$.

The top quark mass of an event sample can be obtained by maximizing the total likelihood function, which is the product of the individual event probabilities, with respect to $m_t$. In this way, each event contributes according to its quality and inherent resolution. While the ME technique exploits the full kinematic information available, and usually yields the statistically most sensitive measurements, it is also computationally intensive because of the involved multidimensional integrations. The result of the 2.8 fb$^{-1}$ $e\mu$ analysis is given together with other mass measurements performed in the dilepton channel at the Tevatron in Table 20. The dominant systematic uncertainty in this analysis arises, as expected, from systematic uncertainties on the JES calibration, and response differences between light quarks and $b$ quarks.

### 7.3.2. *Lepton + jets final state*

The precision of the world-averaged top quark mass is driven by measurements in the lepton + jets channel that provides the best compromise between sample purity and signal statistics. In this channel, all three analysis methods (TM, ME, ID) have been deployed, with the most precise results consistently coming from matrix element analyses, starting with its first application at D0 in Run I [454].

For the current world-averaged mass, CDF and D0 contribute measurements in the lepton + jets channel based on the matrix element method, as discussed in the previous section, simultaneously fitting the top quark mass and an overall *in-situ* JES scale factor to the data. Events with one energetic isolated lepton, large $\not{p}_T$ and exactly four jets are selected so as to best comply with the leading order matrix element used in the calculations. Also, at least one of the jets is required to be $b$ tagged. Using datasets of 2.7 and 2.2 fb$^{-1}$, for CDF [556] and D0 [557], respectively, both measure the top quark mass with a precision of 1.0%, incidentally even yielding the same mass value of 172.2 GeV/c$^2$. A comparison of the invariant dijet and three-jet mass distributions based on the permutation of largest weight in data and simulation is shown in Fig. 51 for a 1 fb$^{-1}$ subset [558] of D0's 2.2 fb$^{-1}$ ME analysis.

The largest systematic uncertainties on the measurement by CDF arise from the $t\bar{t}$ MC generator used to calibrate the result (PYTHIA versus HERWIG) and the residual JES uncertainty. For D0, the dominant uncertainty comes from the $b$-jet over light-jet calorimeter-response ratio and the signal modeling uncertainty, taking the impact of extra jets into account based on the observed four to at least five jet event ratio in data. Both experiments are in the process of streamlining their methods used to assess systematic uncertainties as well as exploring new sources of uncertainties that start to become important at the current level of precision [567]. Examples for the latter are differences arising from using NLO rather than LO MC
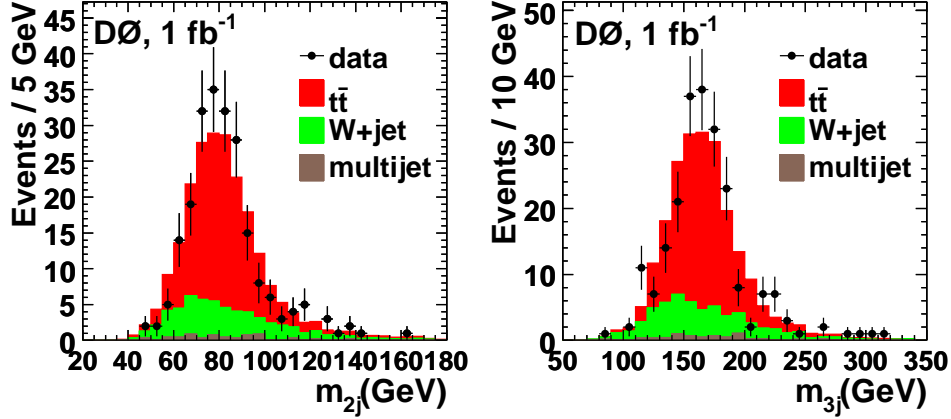
Fig. 51: Dijet (left) and three-jet (right) invariant mass distributions in 1 fb$^{-1}$ of D0 data compared with simulated $t\bar{t}$ signal (for $m_t = 170$ GeV/c$^2$) and background contributions [558]. The results are for jet permutations of largest weight using the ME method.

generators, or non-perturbative QCD effects such as color reconnection [184, 185].

Table 21 summarizes the latest (final) Run I results and the current preliminary or published Run II top quark mass measurements in the lepton + jets channel.

### 7.3.3. *All-hadronic final state*

Analyses in the all-hadronic channel have been performed so far using template and ideogram methods, and exhibit comparable sensitivity. The precision in this channel by now is similar to that in the dilepton final state, mainly as a result of using *in-situ* JES calibration, thereby reducing the otherwise overwhelming systematic uncertainty from the external JES.

CDF's best measurement in the all-hadronic channel entering the world average has been performed using a template method on 2.1 fb$^{-1}$ of data, yielding a precision of 2.4% [568]. Similar to the analysis [278] described in Section 5.1.3, events are required to have between six and eight energetic central jets, no isolated energetic lepton or significant $\not{p}_T$, and have to pass a selection based on the output of a neural network discriminant. The dataset is split into subsamples with exactly one and exactly two $b$ tagged jets.

The leading six jets in each event define the $t\bar{t}$ signal and multijet background templates for the reconstructed mass of the top quark and of the $W$ boson, with assignments based on a kinematic fit, where the permutation with lowest $\chi^2$ is selected for further study. While the signal templates depend on both $m_t$ and the JES scale factor, the background templates are assumed to not depend on the top quark mass, and no JES dependence is considered either. The measurement is then

Table 21: Top quark mass measurements performed thus far at the Tevatron in the lepton + jets channel with their integrated luminosities, data selections ($\ell$+jets = lepton + jets, $\ell\ell$ = dilepton) and analysis methods used. The two analyses using $0.1$ fb$^{-1}$ are from Run I, and the references marked with an asterisk correspond to preliminary results. Measurements marked with a cross contain the uncertainty from the *in-situ* JES calibration within the quoted statistical uncertainty.

| $\int \mathcal{L}dt$ [fb$^{-1}$] | Selection | Method | $m_t \pm$ (stat.) $\pm$ (syst.) [GeV/c$^2$] | Ref. |
|---|---|---|---|---|
| 0.1 | $\ell$+jets | TM:$m_{\mathrm{reco}}$ | $176.1 \pm 5.1 \pm 5.3$ | [537] |
| 0.1 | $\ell$+jets | ME | $180.1 \pm 3.6 \pm 3.9$ | [454] |
| 0.3 | $\ell$+jets | DLM | $173.2^{+2.6}_{-2.4} \pm 3.2$ | [526, 559] |
| 0.3 | $\ell$+jets | TM:$m_{\mathrm{reco}} \oplus$ JES | $173.5^{+3.7}_{-3.6} \pm 1.3^{\dagger}$ | [526, 527] |
| 0.4 | $\ell$+jets | ME $\oplus$ JES | $170.3^{+4.1}_{-4.5}\,^{+1.2}_{-1.8}\,^{\dagger}$ | [560] |
| 0.4 | $\ell$+jets | ME $\oplus$ JES | $169.2^{+5.0}_{-7.4}\,^{+1.5}_{-1.4}\,^{\dagger}$ | [560] |
| 0.4 | $\ell$+jets | ID $\oplus$ JES | $173.7 \pm 4.4^{+2.1}_{-2.0}\,^{\dagger}$ | [561] |
| 0.7 | $\ell$+jets | TM:$L_{xy}$ | $180.7^{+15.5}_{-13.4} \pm 8.6$ | [562] |
| 1.0 | $\ell$+jets | ME $\oplus$ JES | $171.5 \pm 1.8 \pm 1.1^{\dagger}$ | [558] |
| 1.0 | $\ell$+jets | ME $\oplus$ JES | $170.8 \pm 2.2 \pm 1.4^{\dagger}$ | [563] |
| 1.0 | $\ell$+jets | TM:$m_{\mathrm{reco}}$ | $168.9 \pm 2.2 \pm 4.2$ | [564]* |
| 1.2 | $\ell$+jets | ME $\oplus$ JES | $173.0 \pm 1.9 \pm 1.0^{\dagger}$ | [557]* |
| 1.7 | $\ell$+jets | DLM $\oplus$ JES | $171.6 \pm 2.0 \pm 1.3^{\dagger}$ | [565]* |
| 1.9 | $\ell$+jets | TM:$L_{xy}, p_T^{\ell}$ | $175.3 \pm 6.2 \pm 3.0$ | [530]* |
| 1.9 | $\ell$+jets $\ell\ell$ | TM:$m_{\mathrm{reco}} \oplus$ JES TM:$\nu_{\eta}, H_T$ | $171.9 \pm 1.7 \pm 1.1^{\dagger}$ | [528, 529] |
| 1.9 | $\ell$+jets | ME $\oplus$ JES | $172.7 \pm 1.8 \pm 1.2^{\dagger}$ | [566] |
| 2.2 | $\ell$+jets | ME $\oplus$ JES | $172.2 \pm 1.0 \pm 1.4$ | [557]* |
| 2.7 | $\ell$+jets | ME $\oplus$ JES | $172.2 \pm 1.3 \pm 1.0^{\dagger}$ | [556]* |

performed in a two-dimensional fit to $m_t$ and *in-situ* JES scale factor, using these templates and the observed distribution in data in both subsamples, and applying a Gaussian constraint from the external JES calibration. The reconstructed mass distributions obtained in data with two $b$ tags, overlaid with templates for expected background and $t\bar{t}$ signal (for $m_t = 177$ GeV/c$^2$ and unchanged JES with respect to the external calibration, as obtained from the fit) are shown in Fig. 52.

The result of this analysis is given in Table 22, together with other top quark mass measurements performed in the all-hadronic channel at the Tevatron. The dominant systematic uncertainties in this analysis arise from uncertainties on shape
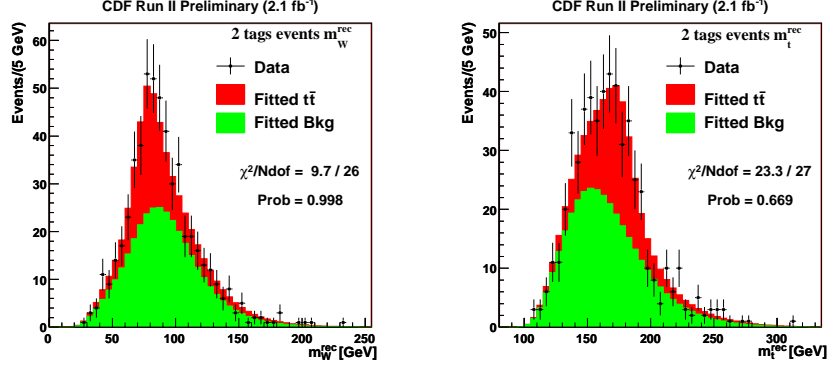
Fig. 52: Reconstructed mass of the $W$ boson (left) and top quark (right) obtained in 2.1 fb$^{-1}$ of double $b$ tagged CDF data compared to the expected contributions from multijet background and 177 GeV/c$^2$ $t\bar{t}$ signal, using the JES corresponding to the best fit [568].

Table 22: Top quark mass measurements performed thus far at the Tevatron in the all-hadronic channel with their integrated luminosities, data selections and analysis methods used. The two analyses using 0.1 fb$^{-1}$ are from Run I, and the references marked with an asterisk correspond to preliminary measurements. Results marked with a cross contain the uncertainty from the *in-situ* JES calibration within the quoted statistical uncertainty.

| $\int \mathcal{L} dt$ [fb$^{-1}$] | Selection | Method | $m_t \pm$ (stat.) $\pm$ (syst.) [GeV/c$^2$] | Ref. |
|---|---|---|---|---|
| 0.1 | jets only | TM:$m_{\mathrm{reco}}$ | $178.5 \pm 13.7 \pm 7.7$ | [539] |
| 0.1 | jets only | TM:$m_{\mathrm{reco}}$ | $186 \pm 10 \pm 5.7$ | [537, 538] |
| 0.3 | $\not{p}_T$+jets | TM:$H_T$ | $172.3^{+10.8}_{-9.6} \pm 10.8$ | [540] |
| 0.3 | jets only | ID | $177.1 \pm 4.9 \pm 4.7$ | [570] |
| 0.9 | jets only | TM:ME $\oplus$ JES | $171.1 \pm 3.7 \pm 2.1^{\dagger}$ | [571, 572] |
| 1.0 | jets only | TM:$m_{\mathrm{reco}}$ | $174.0 \pm 2.2 \pm 4.8$ | [278] |
| 1.9 | jets only | ID $\oplus$ JES | $165.2 \pm 4.4 \pm 1.9^{\dagger}$ | [569]* |
| 2.1 | jets only | TM:$m_{\mathrm{reco}} \oplus$ JES | $176.9 \pm 3.8 \pm 1.7^{\dagger}$ | [568]* |

and normalization of the background templates and residual JES uncertainties. The compatibility of this measurement with that using the ideogram method [569] on an overlapping dataset of almost the same size, which yields a central value $\approx$12 GeV/c$^2$ lower, is currently being investigated.

### 7.3.4. *World-averaged top quark mass*

The top quark mass has been measured at the Tevatron in the three main decay channels using various methods, as described in the past sections. In the lepton + jets channel, precisions of 1% are achieved in single measurements, while in the dilepton and all-hadronic channels the precision is ≈2%. The different methods assume standard model $t\bar{t}$ production and decay, but still exhibit differences in the strength of their model dependence. While ME methods provide the best sensitivity, they also are strongly model dependent through their implemented matrix elements. Template methods purely relying on the measured event kinematics are more robust with respect to possible deviations from the standard model, but in general exhibit lower sensitivity.

Pursuing mass measurements in all $t\bar{t}$ decay channels with different methods is a valuable test of the self-consistency of the standard model assumptions, and can also be used to probe for new phenomena [296]. While no top quark mass measurement has been performed thus far in $t\bar{t}$ decay modes involving hadronic $\tau$ decays, the progress in the corresponding cross section analyses discussed in Section 5.1.4 indicates this could still be possible at the Tevatron, completing the $t\bar{t}$ decay channels for measuring $m_t$.

CDF and D0 have combined their recent preliminary Run II results with their measurements obtained in Run I, respectively. Based on the results of highest sensitivity in the dilepton, lepton + jets and all-hadronic channels (CDF), and in the dilepton and lepton + jets channels (D0), both experiments attain a total precision of 0.9% on their combined measurements, respectively. Based on analyses using up to 2.7 fb$^{-1}$, CDF gets $172.4 \pm 1.0$(stat.)$\pm 1.3$(syst.) GeV/c$^2$ [573], while D0 obtains $172.8 \pm 0.9$(stat.)$\pm 1.3$(syst.) GeV/c$^2$ [574] using analyses on up to 2.8 fb$^{-1}$ of data.

The results of both experiments are in very good agreement, and their overall combination yields $172.4 \pm 0.7$(stat.) $\pm 1.0$(syst.) GeV/c$^2$ [12], corresponding to an overall precision of 0.7%, as illustrated in Fig. 53. Combining the separate results from the all-hadronic, the lepton + jets and the dilepton channels, yields $177.5 \pm 4.0$ GeV/c$^2$, $172.2 \pm 1.2$ GeV/c$^2$ and $171.5 \pm 2.6$ GeV/c$^2$, respectively. These results are consistent with each other, and have $\chi^2$ probabilities of at least 17% between any two of the channels.

All these combinations are calculated using the BLUE method [276, 277] and assume Gaussian systematic uncertainties, with their correlations properly accounted for. The different sources of systematic uncertainties are broken down into twelve orthogonal categories. Six of them deal with uncertainties related to the JES, while others address signal and background modeling, fitting procedures, specifics of MC generation and lepton energy scale. The main contributions to the 1.0 GeV/c$^2$ systematic error on the world average of $m_t$ are (in units of GeV/c$^2$): total JES ($\pm 0.8$), signal, background and MC model ($\pm 0.3$ each) and lepton scale and fitting procedure ($\pm 0.1$ each).

Having reached a precision of 0.7%, the world-averaged top quark mass is now
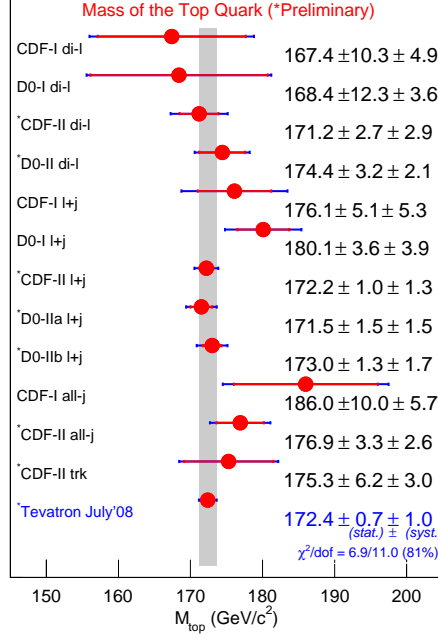
Fig. 53: Measurements of the mass of the top quark used as input to the current preliminary world average [12].

limited by the systematic uncertainties that in turn are dominated by JES-related uncertainties. Further improvements on the JES can be expected since the increasing integrated luminosity will help constrain the corresponding uncertainties better, especially the significant contribution from *in-situ* JES calibration. While a final absolute top quark mass uncertainty of $\Delta m_t \lesssim 1$ GeV/c$^2$ should be achievable by the end of Run II, it will still require a significant effort to determine the contributing systematic uncertainties consistently among the experiments, and evaluate any new contributions that should be considered at this level of precision.

This measurement marks the most precise determination of a quark mass and will certainly provide a legacy well into the LHC era, where it will serve as an important calibration signal until large datasets can produce more refined measurements. However, improving the precision by another order of magnitude can only be expected from a threshold scan of $t\bar{t}$ production at a future linear $e^+e^-$ collider [575–577].

Before the impact of the current top quark mass measurement is discussed, it should be noted that the value of this SM parameter depends on the defining convention. For instance, the $\overline{MS}$ calculation gives a value lower than the pole mass of the top quark propagator by $\approx$10 GeV/c$^2$ at $\mathcal{O}(\alpha_s^3)$. The pole mass itself exhibits an intrinsic ambiguity of $\mathcal{O}(\Lambda_{\mathrm{QCD}}) \approx 0.2$ GeV (see for example Ref. [578]
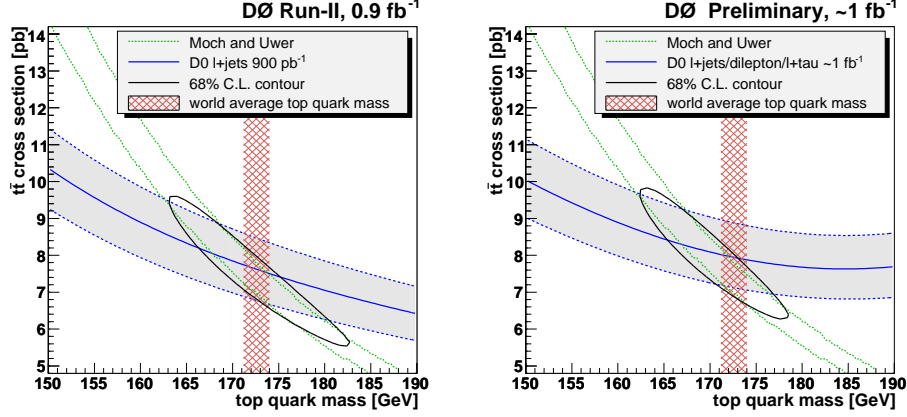
Fig. 54: Mass dependences of the $t\bar{t}$ production cross sections measured by D0 in the lepton + jets channel (left, [262]), and in a combination of lepton + jets, dilepton and $\tau$ + lepton channels (right, [257]), compared with the theoretical prediction by Moch and Uwer [127], based on CTEQ6.6M [126] PDFs. The previous world-averaged $m_t = 172.6\pm1.4\,\mathrm{GeV/c^2}$ [581], as well as the 68% C.L. contours of the joint likelihoods resulting from the convolutions of measurement and prediction [579], are also shown.

and references therein).

The top quark mass measurements described in this review are usually interpreted as representing the pole mass. However, they are calibrated using LO MC simulations with higher orders approximated by parton showers, where the top mass parameter does not follow a theoretically well-defined convention. Hence, calculations and predictions using the measured mass as the pole mass should be taken with a grain of salt.

D0 has conducted consistency checks of the compatibility of the direct top quark mass measurements at the Tevatron with the pole mass extracted from the $t\bar{t}$ production rate [262,579]. Comparing the measured $t\bar{t}$ production cross section with SM predictions derived at NLO, including soft-gluon resummations that are performed in a well-defined renormalization scheme using the top quark pole mass, constrains the mass of the top quark. The cross section measurements depend less on MC modeling of signal kinematics than direct mass measurements do. For cross sections, the MC is mainly needed for determining the signal acceptance, which is expected to be rather insensitive to higher order corrections: A comparison of NLO and LO predictions shows that higher order corrections affect more the normalization than the shape of the relevant kinematic distributions [580].

In a recent analysis, D0 uses two $t\bar{t}$ cross section measurements to extract constraints on the top quark mass by comparing measurement with theoretical predictions [579]. One result is obtained in the lepton + jets channel based on the

combination of a counting experiment using $b$ tagging and an analysis utilizing a topological multivariate discriminant for 0.9 fb$^{-1}$ of data [262], as discussed in Section 5.1.2. The second result combines measurements in the lepton + jets, dilepton and $\tau$ + lepton channels obtained from approximately 1.0 fb$^{-1}$ of data [257] (see Section 5.1.5). Being based on different analysis techniques and different final states, both results exhibit a different dependence on the top quark mass, as illustrated in Fig. 54.

One theoretical prediction used for the comparison is that of Moch and Uwer [127], and is based on CTEQ6.6M [126] PDFs (see Section 3.1). A joint likelihood depending on $m_t$ and $\sigma_{t\bar{t}}$ is obtained as the product of the likelihood functions of the measurement, including its total experimental uncertainty, and the theoretical prediction, including scale and PDF uncertainties. The contour of the joint likelihood's smallest region containing 68% of its integral is also shown in Fig. 54 for both measurements. By integrating over the $t\bar{t}$ production rate, the top quark mass can be extracted. For the lepton + jets channel measurement a top quark mass of $171.2^{+6.5}_{-6.2}$ GeV/c$^2$ is obtained. The combined lepton + jets, dilepton and $\tau$ + lepton measurement yields $169.6^{+5.4}_{-5.5}$ GeV/c$^2$, which includes an additional systematic uncertainty of 1 GeV/c$^2$ due to a smaller mass dependence range available from this measurement. Both results are in good agreement with the world-averaged $m_t$ obtained from the complementary direct measurements.

The current world-averaged $m_t$ of $172.4 \pm 1.2$ GeV/c$^2$ [12] is also in good agreement with its predicted value of $179^{+12}_{-9}$ GeV/c$^2$ [14] in the framework of the standard model, based on precision electroweak data, as discussed in Section 2.3. The top quark mass measurement together with that of the $W$ boson mass ($80.398 \pm 0.025$ GeV/c$^2$ [29]) can be used to obtain limits on the Higgs boson mass via the radiative corrections on the $W$ boson mass in a global electroweak fit. This yields $m_H = 84^{+34}_{-26}$ GeV/c$^2$ [14], as illustrated in Fig. 55, where the uncertainties are only from experiment. To demonstrate the impact of the improvements in precision for the measurements of both $m_t$ and $m_W$ since the beginning of Run II, the corresponding fit results in spring 2004 [582] are also shown in Fig. 55. The current resulting 95% C.L. upper limit on the Higgs boson mass is 154 GeV/c$^2$, which includes both experimental and theoretical uncertainties.

The direct searches for the standard model Higgs boson at LEP provide a 95% C.L. lower bound of 114.4 GeV/c$^2$ [583], as also illustrated in Fig. 55. CDF and D0 have recently excluded a SM Higgs boson of 170 GeV/c$^2$ mass at 95% C.L., and a mass range of about 165 to 175 GeV/c$^2$ at 90% C.L. [584] based on 3 fb$^{-1}$ of data. This is not reflected in Fig. 55.

## 8. Summary

More than thirteen years after its discovery, the properties of the top quark are being studied at the Tevatron with unprecedented precision by the CDF and D0 collaborations. The Tevatron is operating very smoothly, and has already delivered
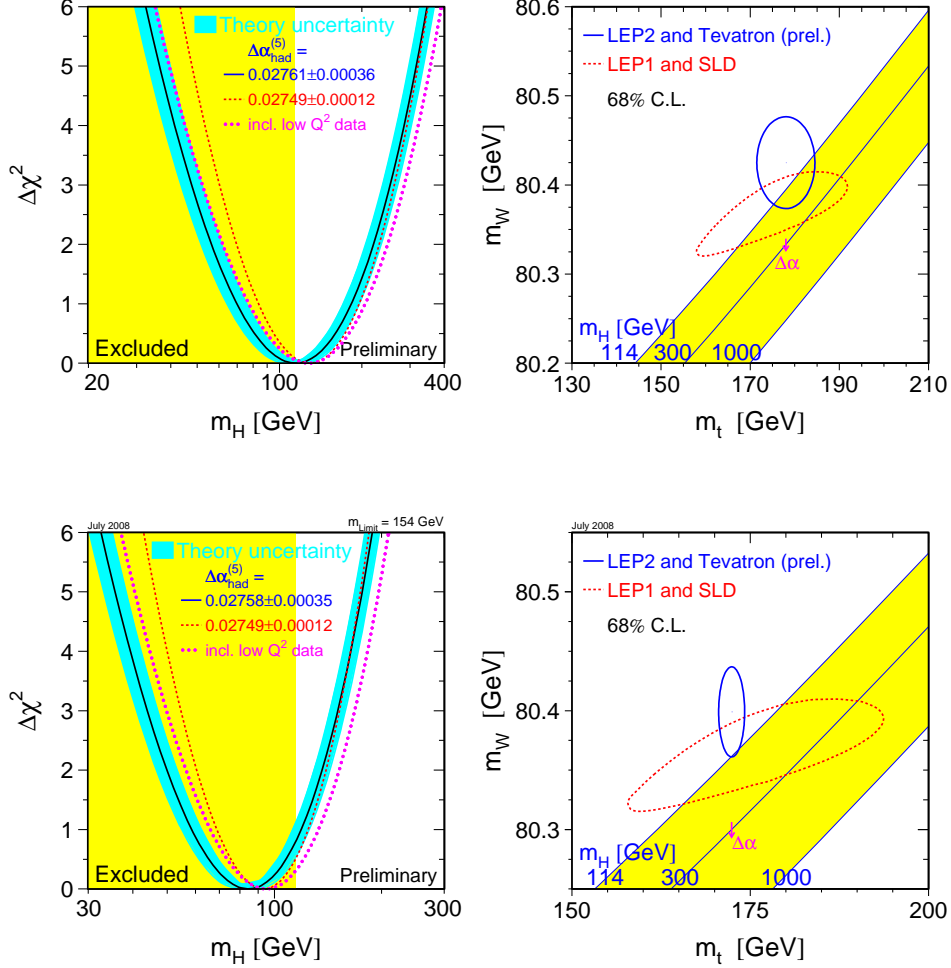
Fig. 55: Mass constraints on the Higgs boson in 2004 (top, [582]), using the Tevatron Run I mass combination of $m_t = 178.0 \pm 4.3$ GeV/c$^2$ [158], and now (bottom, [14]), using the current preliminary world-averaged result $m_t = 172.4 \pm 1.2$ GeV/c$^2$ [12].

more than 4 fb$^{-1}$ of integrated luminosity to each experiment. Before the end of Run II, it is expected to deliver 2 fb$^{-1}$ per year. CDF and D0 have exploited these increasing luminosities together with novel advanced analysis techniques to improve upon previous measurements, but also to explore top quark properties that were not accessible before such as its electroweak production, which provides first direct measurements of the $|V_{tb}|$ CKM matrix element. Thus far all results are consistent with standard model expectations and between the experiments, which

constrains specific extensions of the standard model impacting the properties under consideration.

Top quark pair production is well established in the lepton + jets, dilepton and all-hadronic final states, and these channels are also used to study further properties of the top quark, such as its mass. The top quark signal is also being established in final states involving hadronically decaying $\tau$ leptons. The observed production rates in all final states are consistent with each other and with the standard model expectation. No novel contributions to $t\bar{t}$ production and signal samples have yet been observed, and corresponding constraints are derived on $t\bar{t}$ production via resonances or massive gluons, and possible contributions of a fourth fermion generation or scalar top quarks to the selected signal samples. The kinematics of the observed events also agree with the SM prediction. Since contributions from physics beyond the standard model could affect the observed $t\bar{t}$ final states differently also via the top quark decay, for example, as a result of top quark decays into charged Higgs bosons, corresponding limits are derived as well.

The $t\bar{t}$ production cross section has been measured to be $\approx$7.3 pb for $m_t = 175$ GeV/c$^2$ with a precision of 10%, matching the uncertainties of the theoretical predictions. This provides stringent tests of the corresponding perturbative QCD calculations. Ultimately, the precision of the cross section at the Tevatron might reach the 6% level, dominated by the uncertainty on the integrated luminosity. First measurements have been performed to determine contributions of $q\bar{q}$ annihilation and gluon-gluon fusion to $t\bar{t}$ production, and are found to be consistent with QCD predictions. Also, higher order effects such as the top quark charge asymmetry, measured for the first time, agree with SM expectation within statistical precision.

First evidence for electroweak single top quark production has been found by both experiments, and observation at the five standard deviation level appears imminent. The observed production rates are consistent with the standard model expectation of $\approx$3 pb and provide first direct measurements of the CKM matrix element $|V_{tb}|$. The most stringent 95% C.L. lower limit is found to be $|V_{tb}| > 0.71$. Searches for contributions to single top production via mechanisms beyond the SM, e.g., mediated by $W'$ or charged Higgs bosons, or flavor changing neutral interactions with gluons, are also performed. The lack of any significant deviations from the standard model has been used to set corresponding stringent limits on such processes. Sensitivity of single top production to the $Wtb$ vertex structure has provided constraints on more general $Wtb$ interactions, including first limits on left- and right-handed tensor couplings.

The decay properties of top quarks have been studied using $t\bar{t}$ samples providing both sufficient statistics and sample purity. The $W$ boson helicity in $t\bar{t}$ decays can now be measured in a model independent way by extracting the fractions of left-handed and longitudinally polarized $W$ bosons simultaneously. This provides additional information about the $Wtb$ vertex structure that can be used together with constraints from single top quark production to fully specify $Wtb$ couplings. The $W$ boson helicity measurements are found to be consistent with SM expecta-

tion, and further studies in the lepton + jets and dilepton final states will scrutinize the observed > 2 sd discrepancies between the two channels. The ratio of decays of $t$ to $b$ quarks versus any quarks, i.e., $R = \mathcal{B}(t \to Wb)/\mathcal{B}(t \to Wq) = 0.97^{+0.09}_{-0.08}$, has reached a precision of 9%, confirming the expectation of dominant $t \to Wb$ decay assumed in most analyses. Top quark decays beyond the standard model, mediated through neutral currents, invisible decay modes, or decays to charged Higgs bosons have been sought, but have yielded only upper limits on such processes.

Measurements of fundamental top quark properties such as its charge, lifetime and mass based on $t\bar{t}$ final states thus far confirm the standard model nature of the top quark. First measurements of charge and lifetime are consistent with expectation, and help to constrain ideas beyond the SM. The top quark mass has been measured in lepton + jets, dilepton and all-hadronic final states, yielding consistent results among the channels and between the CDF and D0 experiments. Combining the results yields $m_t = 172.4 \pm 1.2 \text{ GeV/c}^2$, which marks the most precise measurement of the mass of any quark with a precision of 0.7%. By the end of Run II, a measurement with an absolute precision of $\lesssim 1 \text{ GeV/c}^2$ should be achievable. This result will provide an important calibration at the LHC, until there is sufficient luminosity for further refined measurements.

While these mass measurements are usually interpreted as representing the pole mass of the top quark, it should be recognized that their calibration through current Monte Carlo simulations raises certain ambiguities of interpretation. Nevertheless, indirect mass measurements utilizing the mass dependence of $t\bar{t}$ production based on the pole mass are consistent with the direct measurements.

Utilizing radiative corrections to the $W$ boson mass in a global electroweak fit to data that includes the world-averaged top quark and $W$ boson masses as inputs, the mass of the yet to be observed standard model Higgs boson can be constrained. This provides a 95% C.L. upper limit on the Higgs boson mass of 154 GeV/c$^2$.

The large mass of the top quark does not only render it an ideal window to new physics, but this most massive known fundamental object also has a lifetime that is short compared to hadronization times. Consequently, observables sensitive to the top quark spin can be accessed undisturbed by hadronization processes. Spin-related measurements have not as yet been performed in Run II, but it was shown in Run I that a measurement of $t\bar{t}$ spin correlations is feasible, and this measurement will greatly benefit from the increased statistics. The observation of single top quark production in addition should enable first studies of the polarization of top quarks when produced via the electroweak interaction.

For precision measurements such as those of top quark mass and pair production cross section, the study of systematic uncertainties (consistently across experiments) and evaluation of any possible new or smaller contributions not considered in the past become a high priority. Other measurements, particularly involving single top quark production, will remain statistically limited throughout Run II. The LHC will be a "top factory", producing millions of top quarks per year thanks to the two orders of magnitude increased production cross sections and enhanced luminosity

relative to the Tevatron. A broad top quark physics program is in preparation at the LHC [403, 578] that will complement and further expand that of the Tevatron.

A great many analyses are being pursued at the Tevatron, characterizing top quark data samples both as signal and as background contributions for other possible processes of similar signature that still remain to be studied. The top quark serves as a probe into new physics, both in production and decay, that could appear in the form of new particles or as modified couplings relative to the standard model. While thus far all measurements are in agreement with the standard model, there is still much room for new physics to be explored both at the Tevatron and the LHC.

## Acknowledgements

## References

1. M. L. Perl *et al.*, Phys. Rev. Lett. **35**, 1489 (1975).
2. S. W. Herb *et al.*, Phys. Rev. Lett. **39**, 252 (1977).
3. ALEPH, DELPHI, L3, OPAL, the LEP Electroweak Working Group, Contributed to the 27th International Conference on High- Energy Physics - ICHEP 94, Glasgow, Scotland, UK, 20 - 27 Jul 1994, CERN/PPE/94-187.
4. DØ, S. Abachi *et al.*, Phys. Rev. Lett. **72**, 2138 (1994).
5. CDF, F. Abe *et al.*, Phys. Rev. **D50**, 2966 (1994).
6. CDF, F. Abe *et al.*, Phys. Rev. Lett. **73**, 225 (1994), hep-ex/9405005.
7. DØ, S. Abachi *et al.*, Phys. Rev. Lett. **74**, 2422 (1995), hep-ex/9411001.
8. CDF, F. Abe *et al.*, Phys. Rev. **D51**, 4623 (1995), hep-ex/9412009.
9. DØ, S. Abachi *et al.*, Phys. Rev. **D52**, 4877 (1995).
10. CDF, F. Abe *et al.*, Phys. Rev. Lett. **74**, 2626 (1995), hep-ex/9503002.
11. DØ, S. Abachi *et al.*, Phys. Rev. Lett. **74**, 2632 (1995), hep-ex/9503003.
12. CDF, DØ, the Tevatron Electroweak Working Group, arXiv:0808.1089.

13. I. I. Y. Bigi, Y. L. Dokshitzer, V. A. Khoze, J. H. Kühn, and P. M. Zerwas, Phys. Lett. **B181**, 157 (1986).
14. ALEPH, CDF, DØ, DELPHI, L3, OPAL, SLD, the LEP, SLD and Tevatron Electroweak Working Groups, arXiv:0811.4682.
15. P. W. Higgs, Phys. Lett. **12**, 132 (1964).
16. P. W. Higgs, Phys. Rev. Lett. **13**, 508 (1964).
17. P. W. Higgs, Phys. Rev. **145**, 1156 (1966).
18. F. Englert and R. Brout, Phys. Rev. Lett. **13**, 321 (1964).
19. G. S. Guralnik, C. R. Hagen, and T. W. B. Kibble, Phys. Rev. Lett. **13**, 585 (1964).
20. T. W. B. Kibble, Phys. Rev. **155**, 1554 (1967).
21. DØ, V. M. Abazov *et al.*, Phys. Rev. Lett. **98**, 181802 (2007), arXiv:hep-ex/0612052.
22. DØ, V. M. Abazov *et al.*, Phys. Rev. **D78**, 012005 (2008), arXiv:0803.0739.
23. CDF, T. Aaltonen *et al.*, Phys. Rev. Lett. **101**, 252001 (2008), arXiv:0809.2581.
24. D. Chakraborty, J. Konigsberg, and D. L. Rainwater, Ann. Rev. Nucl. Part. Sci. **53**, 301 (2003), hep-ph/0303092.
25. M. Mangano and T. G. Trippe, Phys. Lett. **B592**, 482 (2004).
26. W. Wagner, Rept. Prog. Phys. **68**, 2409 (2005), hep-ph/0507207.
27. A. Quadt, Eur. Phys. J. **C48**, 835 (2006).
28. R. Kehoe, M. Narain, and A. Kumar, Int. J. Mod. Phys. **A23**, 353 (2008), arXiv:0712.2733.
29. Particle Data Group, C. Amsler *et al.*, Physics Letters **B667**, 1 (2008).
30. H. Fritzsch, M. Gell-Mann, and H. Leutwyler, Phys. Lett. **B47**, 365 (1973).
31. D. J. Gross and F. Wilczek, Phys. Rev. **D8**, 3633 (1973).
32. S. Weinberg, Phys. Rev. Lett. **31**, 494 (1973).
33. S. Weinberg, Phys. Rev. **D8**, 4482 (1973).
34. D. J. Gross and F. Wilczek, Phys. Rev. Lett. **30**, 1343 (1973).
35. H. D. Politzer, Phys. Rev. Lett. **30**, 1346 (1973).
36. S. L. Glashow, Nucl. Phys. **22**, 579 (1961).
37. A. Salam and J. C. Ward, Phys. Lett. **13**, 168 (1964).
38. S. Weinberg, Phys. Rev. Lett. **19**, 1264 (1967).
39. N. Cabibbo, Phys. Rev. Lett. **10**, 531 (1963).
40. M. Kobayashi and T. Maskawa, Prog. Theor. Phys. **49**, 652 (1973).
41. J. Davis, Raymond, D. S. Harmer, and K. C. Hoffman, Phys. Rev. Lett. **20**, 1205 (1968).
42. B. T. Cleveland *et al.*, Astrophys. J. **496**, 505 (1998).
43. Super-Kamiokande, Y. Fukuda *et al.*, Phys. Rev. Lett. **81**, 1562 (1998), hep-ex/9807003.
44. SNO, Q. R. Ahmad *et al.*, Phys. Rev. Lett. **87**, 071301 (2001), nucl-ex/0106015.
45. Super-Kamiokande, S. Fukuda *et al.*, Phys. Lett. **B539**, 179 (2002), hep-ex/0205075.
46. K2K, M. H. Ahn *et al.*, Phys. Rev. Lett. **90**, 041801 (2003), hep-ex/0212007.
47. Particle Data Group, W. M. Yao *et al.*, J. Phys. **G33**, 1 (2006).
48. B. Pontecorvo, Sov. Phys. JETP **26**, 984 (1968).
49. Z. Maki, M. Nakagawa, and S. Sakata, Prog. Theor. Phys. **28**, 870 (1962).
50. G. 't Hooft, Nucl. Phys. **B33**, 173 (1971).
51. G. 't Hooft, Nucl. Phys. **B35**, 167 (1971).
52. F. Halzen and A. D. Martin, "QUARKS AND LEPTONS: An Introductory Course in Modern Particle Physics". John Wiley & Sons, New York, USA (1984), 396p.
53. H.-K. Quang and X. Y. Pham, "Elementary Particles and Their Interactions". Springer, Berlin, Germany (1998), 661p.
54. M. Treichel, "Teilchenphysik und Kosmologie : Eine Einführung in Grundlagen und

Zusammenhänge". Springer, Berlin, Germany (2000), 389p.

55. A. Djouadi, Phys. Rept. **457**, 1 (2008), hep-ph/0503172.
56. S. L. Glashow, J. Iliopoulos, and L. Maiani, Phys. Rev. **D2**, 1285 (1970).
57. PLUTO, C. Berger *et al.*, Phys. Lett. **B76**, 243 (1978).
58. C. W. Darden *et al.*, Phys. Lett. **B76**, 246 (1978).
59. J. K. Bienlein *et al.*, Phys. Lett. **B78**, 360 (1978).
60. K. Gottfried, Invited paper presented at Int. Symp. on Lepton and Photon Interactions at High Energies, Hamburg, Germany, Aug 25-31, 1977.
61. J. L. Rosner, C. Quigg, and H. B. Thacker, Phys. Lett. **B74**, 350 (1978).
62. JADE, W. Bartel *et al.*, Phys. Lett. **B146**, 437 (1984).
63. BES, J. Z. Bai *et al.*, Phys. Rev. Lett. **88**, 101802 (2002), hep-ex/0102003.
64. CMD-2, R. R. Akhmetshin *et al.*, Phys. Lett. **B578**, 285 (2004), hep-ex/0308008.
65. KLOE, A. Aloisio *et al.*, Phys. Lett. **B606**, 12 (2005), hep-ex/0407048.
66. T. van Ritbergen and R. G. Stuart, Nucl. Phys. **B564**, 343 (2000), hep-ph/9904240.
67. FAST, A. Barczyk *et al.*, Phys. Lett. **B663**, 172 (2008), arXiv:0707.3904.
68. ALEPH, DELPHI, L3, OPAL, SLD, the LEP Electroweak Working Group, the SLD Electroweak and Heavy Flavour Groups, Phys. Rept. **427**, 257 (2006), hep-ex/0509008.
69. P. Langacker, Phys. Rev. Lett. **63**, 1920 (1989).
70. W. F. L. Hollik, Fortschr. Phys. **38**, 165 (1990).
71. G. Burgers and F. Jegerlehner, To appear in the Proceedings of the Workshop on Z Physics at LEP, Geneva, Switzerland, Feb 20, 1989 and edited by G. Altarelli, R. Kleiss and C. Verzegnassi.
72. S. Myers and E. Picasso, Contemp. Phys. **31**, 387 (1990).
73. D. Brandt, H. Burkhardt, M. Lamont, S. Myers, and J. Wenninger, Rept. Prog. Phys. **63**, 939 (2000).
74. ALEPH, D. Decamp *et al.*, Nucl. Instrum. Meth. **A294**, 121 (1990).
75. ALEPH, D. Buskulic *et al.*, Nucl. Instrum. Meth. **A360**, 481 (1995).
76. DELPHI, P. Aarnio *et al.*, Nucl. Instrum. Meth. **A303**, 233 (1991).
77. DELPHI, P. Abreu *et al.*, Nucl. Instrum. Meth. **A378**, 57 (1996).
78. L3, B. Adeva *et al.*, Nucl. Instrum. Meth. **A289**, 35 (1990).
79. L3 F/B Muon Group, A. Adam *et al.*, Nucl. Instrum. Meth. **A383**, 342 (1996).
80. OPAL, K. Ahmet *et al.*, Nucl. Instrum. Meth. **A305**, 275 (1991).
81. OPAL, P. P. Allport *et al.*, Nucl. Instrum. Meth. **A346**, 476 (1994).
82. Stanford Linear Accelerator Center, SLAC-R-0229.
83. B. Richter, Part. Accel. **26**, 33 (1990).
84. SLD, W. W. Ash *et al.*, SLAC-0273.
85. K. Abe *et al.*, Nucl. Instrum. Meth. **A400**, 287 (1997).
86. M. W. Grünewald, Phys. Rept. **322**, 125 (1999).
87. G. Quast, Prog. Part. Nucl. Phys. **43**, 87 (1999).
88. J. C. Collins, D. E. Soper, and G. Sterman, Nucl. Phys. **B263**, 37 (1986).
89. J. C. Collins and D. E. Soper, Ann. Rev. Nucl. Part. Sci. **37**, 383 (1987).
90. V. N. Gribov and L. N. Lipatov, Sov. J. Nucl. Phys. **15**, 438 (1972).
91. G. Altarelli and G. Parisi, Nucl. Phys. **B126**, 298 (1977).
92. Y. L. Dokshitzer, Sov. Phys. JETP **46**, 641 (1977).
93. D. Stump *et al.*, JHEP **10**, 046 (2003), hep-ph/0303013.
94. J. Pumplin *et al.*, JHEP **07**, 012 (2002), hep-ph/0201195.
95. A. D. Martin, R. G. Roberts, W. J. Stirling, and R. S. Thorne, Eur. Phys. J. **C28**, 455 (2003), hep-ph/0211080.
96. M. Glück, E. Reya, and A. Vogt, Eur. Phys. J. **C5**, 461 (1998), hep-ph/9806404.

97.  S. Alekhin, Phys. Rev. **D68**, 014002 (2003), hep-ph/0211096.
98.  H1, C. Adloff *et al.*, Eur. Phys. J. **C21**, 33 (2001), hep-ex/0012053.
99.  ZEUS, S. Chekanov *et al.*, Phys. Rev. **D67**, 012007 (2003), hep-ex/0208023.
100. R. S. Thorne, hep-ph/0606307.
101. W. A. Bardeen, A. J. Buras, D. W. Duke, and T. Muta, Phys. Rev. **D18**, 3998 (1978).
102. N. Kidonakis, E. Laenen, S. Moch, and R. Vogt, Phys. Rev. **D64**, 114001 (2001), hep-ph/0105041.
103. P. Nason, S. Dawson, and R. K. Ellis, Nucl. Phys. **B303**, 607 (1988).
104. W. Beenakker, H. Kuijf, W. L. van Neerven, and J. Smith, Phys. Rev. **D40**, 54 (1989).
105. W. Beenakker, W. L. van Neerven, R. Meng, G. A. Schuler, and J. Smith, Nucl. Phys. **B351**, 507 (1991).
106. G. Sterman, Nucl. Phys. **B281**, 310 (1987).
107. S. Catani and L. Trentadue, Nucl. Phys. **B327**, 323 (1989).
108. S. Catani and L. Trentadue, Nucl. Phys. **B353**, 183 (1991).
109. E. L. Berger and H. Contopanagos, Phys. Lett. **B361**, 115 (1995), hep-ph/9507363.
110. E. L. Berger and H. Contopanagos, Phys. Rev. **D54**, 3085 (1996), hep-ph/9603326.
111. E. L. Berger and H. Contopanagos, Phys. Rev. **D57**, 253 (1998), hep-ph/9706206.
112. E. Laenen, J. Smith, and W. L. van Neerven, Nucl. Phys. **B369**, 543 (1992).
113. E. Laenen, J. Smith, and W. L. van Neerven, Phys. Lett. **B321**, 254 (1994), hep-ph/9310233.
114. S. Catani, M. L. Mangano, P. Nason, and L. Trentadue, Phys. Lett. **B378**, 329 (1996), hep-ph/9602208.
115. S. Catani, M. L. Mangano, P. Nason, and L. Trentadue, Nucl. Phys. **B478**, 273 (1996), hep-ph/9604351.
116. M. Cacciari, S. Frixione, M. L. Mangano, P. Nason, and G. Ridolfi, JHEP **04**, 068 (2004), hep-ph/0303085.
117. R. Bonciani, S. Catani, M. L. Mangano, and P. Nason, Nucl. Phys. **B529**, 424 (1998), hep-ph/9801375.
118. N. Kidonakis and R. Vogt, Phys. Rev. **D68**, 114014 (2003), hep-ph/0308222.
119. N. Kidonakis and R. Vogt, Eur. Phys. J. **C33**, S466 (2004), hep-ph/0309045.
120. A. D. Martin, R. G. Roberts, W. J. Stirling, and R. S. Thorne, Eur. Phys. J. **C23**, 73 (2002), hep-ph/0110215.
121. A. D. Martin, R. G. Roberts, and W. J. Stirling, Phys. Lett. **B387**, 419 (1996), hep-ph/9606345.
122. S. Catani, hep-ph/0005233.
123. N. Kidonakis, Private communication (2006).
124. M. Cacciari, S. Frixione, M. M. Mangano, P. Nason, and G. Ridolfi, JHEP **09**, 127 (2008), arXiv:0804.2800.
125. N. Kidonakis and R. Vogt, Phys. Rev. **D78**, 074005 (2008), arXiv:0805.3844.
126. P. M. Nadolsky *et al.*, Phys. Rev. **D78**, 013004 (2008), arXiv:0802.0007.
127. S. Moch and P. Uwer, Phys. Rev. **D78**, 034003 (2008), arXiv:0804.1476, The CTEQ6.6 results were provided as private communication.
128. A. D. Martin, W. J. Stirling, R. S. Thorne, and G. Watt, Phys. Lett. **B652**, 292 (2007), arXiv:0706.0459.
129. S. Cortese and R. Petronzio, Phys. Lett. **B253**, 494 (1991).
130. T. Stelzer and S. Willenbrock, Phys. Lett. **B357**, 125 (1995), hep-ph/9505433.
131. S. Dawson, Nucl. Phys. **B249**, 42 (1985).
132. S. S. D. Willenbrock and D. A. Dicus, Phys. Rev. **D34**, 155 (1986).

133. C. P. Yuan, Phys. Rev. **D41**, 42 (1990).
134. R. K. Ellis and S. J. Parke, Phys. Rev. **D46**, 3785 (1992).
135. G. A. Ladinsky and C. P. Yuan, Phys. Rev. **D43**, 789 (1991).
136. S. Moretti, Phys. Rev. **D56**, 7427 (1997), hep-ph/9705388.
137. A. P. Heinson, A. S. Belyaev, and E. E. Boos, Phys. Rev. **D56**, 3114 (1997), hep-ph/9612424.
138. A. S. Belyaev, E. E. Boos, and L. V. Dudko, Phys. Rev. **D59**, 075001 (1999), hep-ph/9806332.
139. T. M. P. Tait, Phys. Rev. **D61**, 034001 (2000), hep-ph/9909352.
140. A. Belyaev and E. Boos, Phys. Rev. **D63**, 034012 (2001), hep-ph/0003260.
141. M. C. Smith and S. Willenbrock, Phys. Rev. **D54**, 6696 (1996), hep-ph/9604223.
142. S. Mrenna and C. P. Yuan, Phys. Lett. **B416**, 200 (1998), hep-ph/9703224.
143. B. W. Harris, E. Laenen, L. Phaf, Z. Sullivan, and S. Weinzierl, Phys. Rev. **D66**, 054024 (2002), hep-ph/0207055.
144. G. Bordes and B. van Eijk, Nucl. Phys. **B435**, 23 (1995).
145. T. Stelzer, Z. Sullivan, and S. Willenbrock, Phys. Rev. **D56**, 5919 (1997), hep-ph/9705398.
146. S. Zhu, Phys. Lett. **B524**, 283 (2002).
147. S. Zhu, Phys. Lett. **B537**, 351 (2002).
148. J. Campbell, R. K. Ellis, and F. Tramontano, Phys. Rev. **D70**, 094012 (2004), hep-ph/0408158.
149. Q.-H. Cao, R. Schwienhorst, and C. P. Yuan, Phys. Rev. **D71**, 054023 (2005), hep-ph/0409040.
150. Q.-H. Cao and C. P. Yuan, Phys. Rev. **D71**, 054022 (2005), hep-ph/0408180.
151. Q.-H. Cao, R. Schwienhorst, J. A. Benitez, R. Brock, and C. P. Yuan, Phys. Rev. **D72**, 094027 (2005), hep-ph/0504230.
152. J. Campbell and F. Tramontano, Nucl. Phys. **B726**, 109 (2005), hep-ph/0506289.
153. N. Kidonakis, arXiv:0705.2431.
154. N. Kidonakis, Phys. Rev. **D75**, 071501 (2007), hep-ph/0701080.
155. N. Kidonakis, Phys. Rev. **D74**, 114012 (2006), hep-ph/0609287.
156. Z. Sullivan, Phys. Rev. **D70**, 114012 (2004), hep-ph/0408049.
157. CTEQ, H. L. Lai *et al.*, Eur. Phys. J. **C12**, 375 (2000), hep-ph/9903282.
158. CDF, DØ, the Tevatron Electroweak Working Group, hep-ex/0404010.
159. A. D. Martin, R. G. Roberts, W. J. Stirling, and R. S. Thorne, Phys. Lett. **B604**, 61 (2004), hep-ph/0410230.
160. D. O. Carlson and C. P. Yuan, Phys. Lett. **B306**, 386 (1993).
161. G. Mahlon and S. J. Parke, Phys. Rev. **D55**, 7249 (1997), hep-ph/9611367.
162. T. Stelzer, Z. Sullivan, and S. Willenbrock, Phys. Rev. **D58**, 094021 (1998), hep-ph/9807340.
163. G. Mahlon and S. J. Parke, Phys. Lett. **B476**, 323 (2000), hep-ph/9912458.
164. T. Tait and C. P. Yuan, Phys. Rev. **D63**, 014018 (2001), hep-ph/0007298.
165. Particle Data Group, S. Eidelman *et al.*, Phys. Lett. **B592**, 1 (2004).
166. A. J. Buras, W. Slominski, and H. Steger, Nucl. Phys. **B245**, 369 (1984).
167. Heavy Flavor Averaging Group (HFAG), E. Barberio *et al.*, hep-ex/0603003.
168. M. Okamoto, PoS **LAT2005**, 013 (2006), hep-lat/0510113.
169. DØ, V. M. Abazov *et al.*, Phys. Rev. Lett. **97**, 021802 (2006), arXiv:hep-ex/0603029.
170. CDF, A. Abulencia *et al.*, Phys. Rev. Lett. **97**, 062003 (2006), hep-ex/0606027.
171. CKMfitter Group, J. Charles *et al.*, Eur. Phys. J. **C41**, 1 (2005), hep-ph/0406184, Updated results and plots available at: http://ckmfitter.in2p3.fr.
172. UTfit, M. Bona *et al.*, JHEP **10**, 081 (2006), hep-ph/0606167.

173. M. Jezabek and J. H. Kühn, Nucl. Phys. **B314**, 1 (1989).
174. J. H. Kühn, hep-ph/9707321.
175. A. Denner and T. Sack, Nucl. Phys. **B358**, 46 (1991).
176. G. Eilam, R. R. Mendel, R. Migneron, and A. Soni, Phys. Rev. Lett. **66**, 3105 (1991).
177. M. Jezabek and J. H. Kühn, Phys. Rev. **D48**, 1910 (1993), hep-ph/9302295.
178. M. Jezabek and J. H. Kühn, Phys. Rev. **D49**, 4970 (1994).
179. A. Czarnecki and K. Melnikov, Nucl. Phys. **B544**, 520 (1999), hep-ph/9806244.
180. K. G. Chetyrkin, R. Harlander, T. Seidensticker, and M. Steinhauser, Phys. Rev. **D60**, 114015 (1999), hep-ph/9906273.
181. J. H. Kühn, Acta Phys. Polon. **B12**, 347 (1981).
182. J. H. Kühn, Acta Phys. Austriaca Suppl. **24**, 203 (1982).
183. L. H. Orr, Phys. Rev. **D44**, 88 (1991).
184. P. Skands and D. Wicke, Eur. Phys. J. **C52**, 133 (2007), hep-ph/0703081.
185. D. Wicke and P. Z. Skands, arXiv:0807.3248.
186. G. L. Kane, G. A. Ladinsky, and C. P. Yuan, Phys. Rev. **D45**, 124 (1992).
187. R. H. Dalitz and G. R. Goldstein, Phys. Rev. **D45**, 1531 (1992).
188. C. A. Nelson, B. T. Kress, M. Lopes, and T. P. McCauley, Phys. Rev. **D56**, 5928 (1997), hep-ph/9707211.
189. M. Fischer, S. Groote, J. G. Körner, and M. C. Mauser, Phys. Rev. **D63**, 031501 (2001), hep-ph/0011075.
190. H. S. Do, S. Groote, J. G. Körner, and M. C. Mauser, Phys. Rev. **D67**, 091501 (2003), hep-ph/0209185.
191. C.-R. Chen, F. Larios, and C. P. Yuan, Phys. Lett. **B631**, 126 (2005), hep-ph/0503040.
192. P. C. Bhat, H. Prosper, and S. S. Snyder, Int. J. Mod. Phys. **A13**, 5113 (1998), hep-ex/9809011.
193. D. P. McGinnis, Prepared for Particle Accelerator Conference (PAC 05), Knoxville, Tennessee, 16-20 May 2005.
194. C. Y. Tan, Nucl. Instrum. Meth. **A557**, 615 (2006).
195. R. S. Moore, Nucl. Phys. Proc. Suppl. **177-178**, 5 (2008).
196. Fermilab Accelerator Division, http://www-bd.fnal.gov/.
197. Proton Driver, D. P. Moehs, J. Peters, and J. Sherman, IEEE Trans. Plasma Sci. **33**, 1786 (2005).
198. J. E. Griffin, J. Maclachlan, A. G. Ruggiero, and K. Takayama, IEEE Trans. Nucl. Sci. **30**, 2630 (1983).
199. D. Mohl, G. Petrucci, L. Thorndahl, and S. Van Der Meer, Phys. Rept. **58**, 73 (1980).
200. G. I. Budker, Sov. Atom. Energ. **22**, 438 (1967).
201. P. F. Derwent, Conf. Proc. **C07091010**, mom1i01 (2007), Presented at International Workshop On Beam Cooling And Related Topics (COOL07), Bad Kreuznach, Germany, 10-14 Sep 2007.
202. Fermilab Operations Department, http://www-bdnew.fnal.gov/operations/lum/lum.html.
203. D0 Run II Operations Group, http://d0server1.fnal.gov/Projects/Operations/D0RunII_DataTaking.htm.
204. CDF, A. Abulencia *et al.*, J. Phys. **G34**, 2457 (2007), hep-ex/0508029.
205. DØ, V. M. Abazov *et al.*, Nucl. Instrum. Meth. **A565**, 463 (2006), arXiv:physics/0507191.
206. CDF, R. Blair *et al.*, FERMILAB-PUB-96-390-E.
207. CDF, D. E. Acosta *et al.*, Phys. Rev. **D71**, 052003 (2005), hep-ex/0410041.
208. CDF, A. Abulencia *et al.*, Phys. Rev. **D74**, 072006 (2006), hep-ex/0607035.

209. DZero Final RunIIa Jet Energy Scale,
     http://www-d0.fnal.gov/phys_id/jes/public_RunIIa/.
210. CDF, F. Abe *et al.*, Phys. Rev. **D45**, 1448 (1992).
211. G. C. Blazey *et al.*, hep-ex/0005012.
212. A. Bhatti *et al.*, Nucl. Instrum. Meth. **A566**, 375 (2006), hep-ex/0510047.
213. DØ, J. Hegeman, J. Phys.: Conf. Ser. **160**, 012024 (2009).
214. DØ, A. Harel, arXiv:0807.3926, Presented at TOP2008: International Workshop on
     Top-Quark Physics, La Biodola, Isola d'Elba, Italy, 18-24 May 2008.
215. J. Donini *et al.*, Nucl. Instrum. Meth. **A596**, 354 (2008), arXiv:0801.3906.
216. CDF, A. Abulencia *et al.*, Phys. Lett. **B639**, 172 (2006), hep-ex/0510063.
217. DØ, V. M. Abazov *et al.*, DØ conference note **5484** (2007).
218. CDF, E. Palencia, CDF conference note **9371** (2008), Presented at TOP2008: In-
     ternational Workshop on Top-Quark Physics, La Biodola, Isola d'Elba, Italy, 18-24
     May 2008.
219. DØ, V. M. Abazov *et al.*, Phys. Rev. **D74**, 112004 (2006), arXiv:hep-ex/0611002.
220. M. Dobbs and J. B. Hansen, Comput. Phys. Commun. **134**, 41 (2001).
221. QCD Tools Working Group, R. K. Ellis *et al.*, hep-ph/0011122.
222. G. Marchesini *et al.*, Comput. Phys. Commun. **67**, 465 (1992).
223. T. Sjöstrand *et al.*, Comput. Phys. Commun. **135**, 238 (2001), hep-ph/0010017.
224. M. A. Dobbs *et al.*, hep-ph/0403045.
225. S. R. Slabospitsky, PoS **TOP2006**, 019 (2006), hep-ph/0603124.
226. T. Sjöstrand, L. Lonnblad, and S. Mrenna, hep-ph/0108264.
227. M. L. Mangano, M. Moretti, F. Piccinini, R. Pittau, and A. D. Polosa, JHEP **07**,
     001 (2003), hep-ph/0206293.
228. T. Sjöstrand, L. Lonnblad, S. Mrenna, and P. Skands, hep-ph/0308153.
229. S. Höche *et al.*, hep-ph/0602031.
230. M. L. Mangano, M. Moretti, F. Piccinini, and M. Treccani, JHEP **01**, 013 (2007),
     hep-ph/0611129.
231. G. Corcella *et al.*, JHEP **01**, 010 (2001), hep-ph/0011363.
232. E. E. Boos, V. E. Bunichev, L. V. Dudko, V. I. Savrin, and A. V. Sherstnev, Phys.
     Atom. Nucl. **69**, 1317 (2006).
233. CompHEP, E. Boos *et al.*, Nucl. Instrum. Meth. **A534**, 250 (2004), hep-ph/0403113.
234. F. Maltoni and T. Stelzer, JHEP **02**, 027 (2003), hep-ph/0208156.
235. T. Stelzer and W. F. Long, Comput. Phys. Commun. **81**, 357 (1994), hep-
     ph/9401258.
236. S. Jadach, J. H. Kühn, and Z. Was, Comput. Phys. Commun. **64**, 275 (1990).
237. Z. Was and P. Golonka, Nucl. Phys. Proc. Suppl. **144**, 88 (2005), hep-ph/0411377.
238. D. J. Lange, Nucl. Instrum. Meth. **A462**, 152 (2001).
239. P. Avery, K. Read, and G. Trahern, CLEO Report **CSN-212** (1985), Unpublished,
     see http://www.lepp.cornell.edu/public/CLEO/soft/QQ/.
240. R. Brun *et al.*, CERN Program Library Long Writeup **W5013** (1994).
241. CDF, T. Aaltonen *et al.*, Phys. Rev. **D77**, 011108 (2008), arXiv:0711.4044.
242. DØ, V. M. Abazov *et al.*, Phys. Rev. Lett. **94**, 152002 (2005), arXiv:hep-ex/0411084.
243. CDF, A. Abulencia *et al.*, Phys. Rev. **D73**, 051101 (2006), hep-ex/0512065.
244. CDF, T. Aaltonen *et al.*, Phys. Rev. Lett. **100**, 091803 (2008), arXiv:0711.2901.
245. DØ, V. M. Abazov *et al.*, Phys. Lett. **B666**, 23 (2008), arXiv:0803.2259.
246. DØ, V. M. Abazov *et al.*, Phys. Rev. Lett. **94**, 091802 (2005), hep-ex/0410062.
247. CDF, T. Aaltonen *et al.*, CDF conference note **9321** (2008).
248. CDF, DØ, U. Husemann, arXiv:0807.4589, Presented at TOP2008: International
     Workshop on Top-Quark Physics, La Biodola, Isola d'Elba, Italy, 18-24 May 2008.

249. CDF, DØ, A. Harel, arXiv:0807.4127, Presented at TOP2008: International Workshop on Top-Quark Physics, La Biodola, Isola d'Elba, Italy, 18-24 May 2008.
250. V. D. Barger, J. Ohnemus, and R. J. N. Phillips, Phys. Rev. **D48**, 3953 (1993), hep-ph/9308216.
251. CDF, T. Aaltonen *et al.*, CDF conference note **9399** (2008).
252. CDF, D. E. Acosta *et al.*, Phys. Rev. Lett. **93**, 142001 (2004), hep-ex/0404036.
253. DØ, V. M. Abazov *et al.*, Phys. Lett. **B626**, 55 (2005), arXiv:hep-ex/0505082.
254. DØ, V. M. Abazov *et al.*, Phys. Rev. **D76**, 052006 (2007), arXiv:0706.0458.
255. CDF, A. Abulencia *et al.*, Phys. Rev. **D78**, 012003 (2008), hep-ex/0612058.
256. DØ, V. M. Abazov *et al.*, DØ conference note **5371** (2007).
257. DØ, V. M. Abazov *et al.*, DØ conference note **5715** (2008).
258. DØ, V. M. Abazov *et al.*, DØ conference note **5465** (2007).
259. DØ, V. M. Abazov *et al.*, DØ conference note **5477** (2007).
260. CDF, T. Aaltonen *et al.*, CDF conference note **8912** (2007).
261. CDF, T. Aaltonen *et al.*, CDF conference note **8770** (2007).
262. DØ, V. M. Abazov *et al.*, Phys. Rev. Lett. **100**, 192004 (2008), arXiv:0803.2779.
263. CDF, D. E. Acosta *et al.*, Phys. Rev. **D71**, 072005 (2005), hep-ex/0409029.
264. CDF, D. E. Acosta *et al.*, Phys. Rev. **D72**, 032002 (2005), hep-ex/0506001.
265. CDF, D. E. Acosta *et al.*, Phys. Rev. **D72**, 052003 (2005), hep-ex/0504053.
266. DØ, V. M. Abazov *et al.*, Phys. Lett. **B626**, 45 (2005), arXiv:hep-ex/0504043.
267. DØ, V. M. Abazov *et al.*, Phys. Lett. **B626**, 35 (2005), arXiv:hep-ex/0504058.
268. CDF, A. Abulencia *et al.*, Phys. Rev. Lett. **97**, 082004 (2006), hep-ex/0606017.
269. DØ, V. M. Abazov *et al.*, Phys. Rev. **D76**, 092007 (2007), arXiv:0705.2788.
270. DØ, V. M. Abazov *et al.*, DØ conference note **5257** (2006).
271. CDF, T. Aaltonen *et al.*, CDF conference note **8272** (2006).
272. CDF, T. Aaltonen *et al.*, CDF conference note **9348** (2008).
273. CDF, T. Aaltonen *et al.*, CDF conference note **9304** (2008).
274. CDF, T. Aaltonen *et al.*, CDF conference note **9462** (2008).
275. CDF, T. Aaltonen *et al.*, CDF conference note **9474** (2008).
276. L. Lyons, D. Gibaut, and P. Clifford, Nucl. Instrum. Meth. **A270**, 110 (1988).
277. A. Valassi, Nucl. Instrum. Meth. **A500**, 391 (2003).
278. CDF, T. Aaltonen *et al.*, Phys. Rev. **D76**, 072009 (2007), arXiv:0706.3790.
279. CDF, A. Abulencia *et al.*, Phys. Rev. **D74**, 072005 (2006), hep-ex/0607095.
280. DØ, V. M. Abazov *et al.*, Phys. Rev. **D76**, 072007 (2007), arXiv:hep-ex/0612040.
281. CDF, A. Abulencia *et al.*, Phys. Rev. Lett. **96**, 202002 (2006), hep-ex/0603043.
282. DØ, V. M. Abazov *et al.*, DØ conference note **5234** (2006).
283. DØ, V. M. Abazov *et al.*, DØ conference note **5451** (2007).
284. CDF, T. Aaltonen *et al.*, CDF conference note **8376** (2008).
285. DØ, V. M. Abazov *et al.*, DØ conference note **5607** (2008).
286. CDF, T. Aaltonen *et al.*, CDF conference note **9448** (2008).
287. CDF, A. A. Affolder *et al.*, Phys. Rev. **D64**, 032002 (2001), hep-ex/0101036.
288. CDF, A. A. Affolder *et al.*, Phys. Rev. **D67**, 119901 (2003).
289. DØ, V. M. Abazov *et al.*, Phys. Rev. **D67**, 012004 (2003), hep-ex/0205019.
290. http://www-cdf.fnal.gov/physics/new/top/top.html.
291. http://www-d0.fnal.gov/Run2Physics/top/index.html.
292. CDF, T. Aaltonen *et al.*, CDF conference note **9474v2** (2008).
293. CDF, T. Aaltonen *et al.*, CDF conference note **9616** (2008).
294. M. Guchait, F. Mahmoudi, and K. Sridhar, JHEP **05**, 103 (2007), hep-ph/0703060.
295. L. Zhang, X.-L. Wang, Y.-P. Kuang, and H.-Y. Zhou, Phys. Rev. **D61**, 115007 (2000), hep-ph/9910265.

296. G. L. Kane and S. Mrenna, Phys. Rev. Lett. **77**, 3502 (1996), hep-ph/9605351.
297. CDF, T. Aaltonen *et al.*, arXiv:0712.3273.
298. L. N. Lipatov, Sov. J. Nucl. Phys. **20**, 94 (1975).
299. CDF, T. Aaltonen *et al.*, arXiv:0807.4262.
300. CDF, T. Aaltonen *et al.*, CDF conference note **9432** (2008).
301. J. H. Kühn and G. Rodrigo, Phys. Rev. Lett. **81**, 49 (1998), hep-ph/9802268.
302. J. H. Kühn and G. Rodrigo, Phys. Rev. **D59**, 054017 (1999), hep-ph/9807420.
303. M. T. Bowen, S. D. Ellis, and D. Rainwater, Phys. Rev. **D73**, 014008 (2006), hep-ph/0509267.
304. O. Antunano, J. H. Kühn, and G. Rodrigo, Phys. Rev. **D77**, 014003 (2008), arXiv:0709.1652.
305. L. G. Almeida, G. Sterman, and W. Vogelsang, Phys. Rev. **D78**, 014008 (2008), arXiv:0805.1885.
306. S. Dittmaier, P. Uwer, and S. Weinzierl, Phys. Rev. Lett. **98**, 262002 (2007), hep-ph/0703120.
307. C. T. Hill, Phys. Lett. **B345**, 483 (1995), hep-ph/9411426.
308. M. S. Carena, A. Daleo, B. A. Dobrescu, and T. M. P. Tait, Phys. Rev. **D70**, 093009 (2004), hep-ph/0408098.
309. DØ, V. M. Abazov *et al.*, Phys. Rev. Lett. **100**, 142002 (2008), arXiv:0712.0851.
310. S. Frixione and B. R. Webber, JHEP **06**, 029 (2002), hep-ph/0204244.
311. S. Frixione, P. Nason, and B. R. Webber, JHEP **08**, 007 (2003), hep-ph/0305252.
312. R. M. Harris, C. T. Hill, and S. J. Parke, hep-ph/9911288.
313. CDF, T. Aaltonen *et al.*, CDF conference note **9156** (2008).
314. CDF, T. Aaltonen *et al.*, CDF conference note **9169** (2008).
315. CDF, T. Aaltonen *et al.*, Phys. Rev. Lett. **101**, 202001 (2008), arXiv:0806.2472.
316. CDF, F. Abe *et al.*, Phys. Rev. Lett. **80**, 2779 (1998), hep-ex/9802017.
317. DØ, S. Abachi *et al.*, Phys. Rev. Lett. **79**, 1203 (1997), hep-ex/9704015.
318. R. M. Barnett and L. J. Hall, Phys. Rev. Lett. **77**, 3506 (1996), hep-ph/9607342.
319. CDF, D. E. Acosta *et al.*, Phys. Rev. Lett. **95**, 022001 (2005), hep-ex/0412042.
320. DØ, B. Abbott *et al.*, Phys. Rev. **D58**, 052001 (1998), hep-ex/9801025.
321. DØ, S. Abachi *et al.*, Phys. Rev. Lett. **79**, 1197 (1997), hep-ex/9703008.
322. CDF, A. A. Affolder *et al.*, Phys. Rev. Lett. **87**, 102001 (2001).
323. CDF, T. Aaltonen *et al.*, CDF conference note **9157** (2008).
324. W. G. D. Dharmaratna and G. R. Goldstein, Phys. Rev. **D41**, 1731 (1990).
325. W. Bernreuther, A. Brandenburg, and P. Uwer, Phys. Lett. **B368**, 153 (1996), hep-ph/9510300.
326. W. G. D. Dharmaratna and G. R. Goldstein, Phys. Rev. **D53**, 1073 (1996).
327. W. Bernreuther, A. Brandenburg, Z. G. Si, and P. Uwer, Acta Phys. Polon. **B34**, 4477 (2003), hep-ph/0304244.
328. W. Bernreuther, M. Fuecker, and Z. G. Si, Phys. Lett. **B633**, 54 (2006), hep-ph/0508091.
329. J. H. Kühn, Nucl. Phys. **B237**, 77 (1984).
330. Y. Hara, Prog. Theor. Phys. **86**, 779 (1991).
331. T. Arens and L. M. Sehgal, Phys. Lett. **B302**, 501 (1993).
332. W. Bernreuther, A. Brandenburg, Z. G. Si, and P. Uwer, Nucl. Phys. **B690**, 81 (2004), hep-ph/0403035.
333. T. Stelzer and S. Willenbrock, Phys. Lett. **B374**, 169 (1996), hep-ph/9512292.
334. S. J. Parke and Y. Shadmi, Phys. Lett. **B387**, 199 (1996), hep-ph/9606419.
335. G. Mahlon and S. J. Parke, Phys. Lett. **B411**, 173 (1997), hep-ph/9706304.
336. G. Mahlon and S. J. Parke, Phys. Rev. **D53**, 4886 (1996), hep-ph/9512264.

337. DØ, B. Abbott *et al.*, Phys. Rev. Lett. **85**, 256 (2000), hep-ex/0002058.
338. DØ, V. M. Abazov *et al.*, DØ conference note **5739** (2008).
339. T.-F. Feng, X.-Q. Li, and J. Maalampi, Phys. Rev. **D69**, 115007 (2004), hep-ph/0310247.
340. J. A. Aguilar-Saavedra, JHEP **12**, 033 (2006), hep-ph/0603200.
341. B. Lillie, L. Randall, and L.-T. Wang, JHEP **09**, 074 (2007), hep-ph/0701166.
342. T. G. Rizzo, Phys. Rev. **D61**, 055005 (2000), hep-ph/9909232.
343. J. L. Rosner, Phys. Lett. **B387**, 113 (1996), hep-ph/9607207.
344. A. Leike, Phys. Rept. **317**, 143 (1999), hep-ph/9805494.
345. L. M. Sehgal and M. Wanninger, Phys. Lett. **B200**, 211 (1988).
346. C. T. Hill, Phys. Lett. **B266**, 419 (1991).
347. C. T. Hill and S. J. Parke, Phys. Rev. **D49**, 4454 (1994), hep-ph/9312324.
348. G. Cvetic, Rev. Mod. Phys. **71**, 513 (1999), hep-ph/9702381.
349. CDF, A. A. Affolder *et al.*, Phys. Rev. Lett. **85**, 2062 (2000), hep-ex/0003005.
350. DØ, V. M. Abazov *et al.*, Phys. Rev. Lett. **92**, 221801 (2004), hep-ex/0307079.
351. S. Jain, FERMILAB-THESIS-2003-03.
352. DØ, V. M. Abazov *et al.*, DØ conference note **5600** (2008).
353. CDF, T. Aaltonen *et al.*, Phys. Rev. **D77**, 051102 (2008), arXiv:0710.5335.
354. DØ, V. M. Abazov *et al.*, Phys. Lett. **B668**, 98 (2008), arXiv:0804.3664.
355. CDF, T. Aaltonen *et al.*, Phys. Rev. Lett. **100**, 231801 (2008), arXiv:0709.0705.
356. CDF, T. Aaltonen *et al.*, CDF conference note **9164** (2008).
357. R. Frederix and F. Maltoni, JHEP **01**, 047 (2009), arXiv:0712.2355.
358. A. Höcker and V. Kartvelishvili, Nucl. Instrum. Meth. **A372**, 469 (1996), hep-ph/9509307.
359. H.-J. He, N. Polonsky, and S.-f. Su, Phys. Rev. **D64**, 053004 (2001), hep-ph/0102144.
360. V. A. Novikov, L. B. Okun, A. N. Rozanov, and M. I. Vysotsky, Phys. Lett. **B529**, 111 (2002), hep-ph/0111028.
361. G. D. Kribs, T. Plehn, M. Spannowsky, and T. M. P. Tait, Phys. Rev. **D76**, 075016 (2007), arXiv:0706.3718.
362. N. Borstnik *et al.*, hep-ph/0612250.
363. J. I. Silva-Marcos, JHEP **12**, 036 (2002), hep-ph/0204217.
364. E. Arik, O. Cakir, S. A. Cetin, and S. Sultansoy, Acta Phys. Polon. **B37**, 2839 (2006), hep-ph/0502050.
365. P. H. Frampton, P. Q. Hung, and M. Sher, Phys. Rept. **330**, 263 (2000), hep-ph/9903387.
366. D. Choudhury, T. M. P. Tait, and C. E. M. Wagner, Phys. Rev. **D65**, 053002 (2002), hep-ph/0109097.
367. CDF, T. Aaltonen *et al.*, CDF conference note **9446** (2008).
368. CDF, T. Aaltonen *et al.*, Phys. Rev. Lett. **100**, 161803 (2008), arXiv:0801.3877.
369. S. P. Martin, hep-ph/9709356.
370. W. Beenakker, M. Kramer, T. Plehn, M. Spira, and P. M. Zerwas, Nucl. Phys. **B515**, 3 (1998), hep-ph/9710451.
371. W. Beenakker, R. Hopker, and M. Spira, hep-ph/9611232, http://www.ph.ed.ac.uk/ tplehn/prospino/.
372. DØ, V. M. Abazov *et al.*, Phys. Lett. **B659**, 500 (2008), arXiv:0707.2864.
373. CDF, T. Aaltonen *et al.*, Phys. Rev. **D76**, 072010 (2007), arXiv:0707.2567.
374. DØ, V. M. Abazov *et al.*, Phys. Lett. **B645**, 119 (2007), arXiv:hep-ex/0611003.
375. DØ, V. M. Abazov *et al.*, Phys. Lett. **B665**, 1 (2008), arXiv:0803.2263.
376. DØ, V. M. Abazov *et al.*, DØ conference note **5438** (2007).
377. CDF, A. A. Affolder *et al.*, Phys. Rev. Lett. **84**, 5273 (2000), hep-ex/9912018.

378. DØ, V. M. Abazov *et al.*, arXiv:0901.1063.
379. ALEPH, DELPHI, L3 and OPAL, the LEPSUSY working group, Note LEPSUSYWG/04-07.1 (2004), http://lepsusy.web.cern.ch/lepsusy/Welcome.html.
380. CDF, T. Aaltonen *et al.*, CDF conference note **9439** (2008).
381. DØ, B. Abbott *et al.*, Phys. Rev. **D63**, 031101 (2000), hep-ex/0008024.
382. DØ, V. M. Abazov *et al.*, Phys. Lett. **B517**, 282 (2001), hep-ex/0106059.
383. CDF, D. E. Acosta *et al.*, Phys. Rev. **D65**, 091102 (2002), hep-ex/0110067.
384. CDF, D. E. Acosta *et al.*, Phys. Rev. **D69**, 052003 (2004).
385. CDF, D. E. Acosta *et al.*, Phys. Rev. **D71**, 012005 (2005), hep-ex/0410058.
386. DØ, V. M. Abazov *et al.*, Phys. Lett. **B622**, 265 (2005), arXiv:hep-ex/0505063.
387. DØ, V. M. Abazov *et al.*, Phys. Rev. **D75**, 092007 (2007), arXiv:hep-ex/0604020.
388. CDF, T. Aaltonen *et al.*, CDF conference note **9217** (2008).
389. CDF, T. Aaltonen *et al.*, CDF conference note **9221** (2008).
390. CDF, T. Aaltonen *et al.*, CDF conference note **9223** (2008).
391. CDF, T. Aaltonen *et al.*, CDF conference note **9313** (2008).
392. CDF, T. Aaltonen *et al.*, CDF conference note **9251** (2008).
393. CDF, T. Aaltonen *et al.*, CDF conference note **9479** (2008).
394. CDF, T. Aaltonen *et al.*, CDF conference note **9451** (2008).
395. CDF, T. Aaltonen *et al.*, CDF conference note **9464** (2008).
396. CDF, T. Aaltonen *et al.*, CDF conference note **9445** (2008).
397. DØ, V. M. Abazov *et al.*, arXiv:0903.0850.
398. CDF, T. Aaltonen *et al.*, arXiv:0903.0885.
399. M. Jezabek and J. H. Kühn, Phys. Lett. **B329**, 317 (1994), hep-ph/9403366.
400. G. Mahlon, hep-ph/9811219.
401. G. Mahlon, hep-ph/0011349.
402. E. E. Boos and A. V. Sherstnev, Phys. Lett. **B534**, 97 (2002), hep-ph/0201271.
403. M. Beneke *et al.*, hep-ph/0003033.
404. E. Boos, V. Bunichev, L. Dudko, and M. Perfilov, Phys. Lett. **B655**, 245 (2007), hep-ph/0610080.
405. DØ, V. M. Abazov *et al.*, Phys. Rev. Lett. **100**, 031804 (2008), arXiv:0710.2966.
406. J. Smith, W. L. van Neerven, and J. A. M. Vermaseren, Phys. Rev. Lett. **50**, 1738 (1983).
407. UA2, J. Alitti *et al.*, Nucl. Phys. **B400**, 3 (1993).
408. CDF, F. Abe *et al.*, Phys. Rev. **D55**, 5263 (1997), hep-ex/9702004.
409. DØ, V. M. Abazov *et al.*, Phys. Rev. **D69**, 111101 (2004), hep-ex/0308033.
410. DØ, V. M. Abazov *et al.*, Phys. Lett. **B641**, 423 (2006), arXiv:hep-ex/0607102.
411. CDF, D. E. Acosta *et al.*, Phys. Rev. Lett. **90**, 081802 (2003), hep-ex/0209030.
412. DØ, V. M. Abazov *et al.*, Phys. Rev. Lett. **100**, 211803 (2008), arXiv:0803.3256.
413. CDF, T. Aaltonen *et al.*, CDF conference note **9150** (2008).
414. J. F. Gunion, H. E. Haber, G. L. Kane, and S. Dawson, "The Higgs Hunter's Guide". Addison-Wesley, Reading, MA, USA (1990), 425p.
415. J. F. Gunion, H. E. Haber, G. L. Kane, and S. Dawson, hep-ph/9302272.
416. H.-J. He and C. P. Yuan, Phys. Rev. Lett. **83**, 28 (1999), hep-ph/9810367.
417. DØ, V. M. Abazov *et al.*, arXiv:0807.0859.
418. T. Han, M. Hosch, K. Whisnant, B.-L. Young, and X. Zhang, Phys. Rev. **D58**, 073008 (1998), hep-ph/9806486.
419. J. A. Aguilar-Saavedra, Acta Phys. Polon. **B35**, 2695 (2004), hep-ph/0409342.
420. ALEPH, A. Heister *et al.*, Phys. Lett. **B543**, 173 (2002), hep-ex/0206070.
421. DELPHI, J. Abdallah *et al.*, Phys. Lett. **B590**, 21 (2004), hep-ex/0404014.
422. L3, P. Achard *et al.*, Phys. Lett. **B549**, 290 (2002), hep-ex/0210041.

423. OPAL, G. Abbiendi *et al.*, Phys. Lett. **B521**, 181 (2001), hep-ex/0110009.
424. H1, D. M. South, Nucl. Phys. Proc. Suppl. **179-180**, 29 (2008), arXiv:0806.0069.
425. CDF, F. Abe *et al.*, Phys. Rev. Lett. **80**, 2525 (1998).
426. V. F. Obraztsov, S. R. Slabospitsky, and O. P. Yushchenko, Phys. Lett. **B426**, 393 (1998), hep-ph/9712394.
427. ZEUS, S. Chekanov *et al.*, Phys. Lett. **B559**, 153 (2003), hep-ex/0302010.
428. H1, A. Aktas *et al.*, Eur. Phys. J. **C33**, 9 (2004), hep-ex/0310032.
429. CDF, T. Aaltonen *et al.*, Phys. Rev. Lett. **101**, 192002 (2008), arXiv:0805.2109.
430. Y. P. Gouz and S. R. Slabospitsky, Phys. Lett. **B457**, 177 (1999), hep-ph/9811330.
431. A. A. Ashimova and S. R. Slabospitsky, Phys. Lett. **B668**, 282 (2008), hep-ph/0604119.
432. DØ, V. M. Abazov *et al.*, Phys. Rev. Lett. **99**, 191802 (2007), arXiv:hep-ex/0702005.
433. M. Hosch, K. Whisnant, and B. L. Young, Phys. Rev. **D56**, 5725 (1997), hep-ph/9703450.
434. CDF, T. Aaltonen *et al.*, CDF conference note **9440** (2008).
435. CDF, T. Aaltonen *et al.*, arXiv:0812.3400.
436. S. R. Slabospitsky and L. Sonnenschein, Comput. Phys. Commun. **148**, 87 (2002), hep-ph/0201292.
437. J. J. Liu, C. S. Li, L. L. Yang, and L. G. Jin, Phys. Rev. **D72**, 074018 (2005), hep-ph/0508016.
438. L. L. Yang, C. S. Li, Y. Gao, and J. J. Liu, Phys. Rev. **D73**, 074017 (2006), hep-ph/0601180.
439. J. J. Zhang *et al.*, arXiv:0810.3889.
440. ALEPH, DELPHI, L3, OPAL, the LEP Electroweak Working Group, arXiv:0712.0929.
441. DØ, V. M. Abazov *et al.*, Phys. Rev. Lett. **101**, 221801 (2008), arXiv:0807.1692.
442. D. O. Carlson, E. Malkawi, and C. P. Yuan, Phys. Lett. **B337**, 145 (1994), hep-ph/9405277.
443. E. Malkawi and C. P. Yuan, Phys. Rev. **D50**, 4462 (1994), hep-ph/9405322.
444. E. Boos, L. Dudko, and T. Ohl, Eur. Phys. J. **C11**, 473 (1999), hep-ph/9903215.
445. W. Bernreuther, M. Fücker, and Y. Umeda, Phys. Lett. **B582**, 32 (2004), hep-ph/0308296.
446. M. A. B. Bég, R. V. Budny, R. N. Mohapatra, and A. Sirlin, Phys. Rev. Lett. **38**, 1252 (1977).
447. M. A. B. Bég, R. V. Budny, R. Mohapatra, and A. Sirlin, Phys. Rev. Lett. **39**, 54 (1977).
448. S.-h. Nam, Phys. Rev. **D66**, 055008 (2002), hep-ph/0206037.
449. X.-l. Wang, Q.-l. Zhang, and Q.-p. Qiao, Phys. Rev. **D71**, 014035 (2005), hep-ph/0501145.
450. K. Fujikawa and A. Yamada, Phys. Rev. **D49**, 5890 (1994).
451. P. L. Cho and M. Misiak, Phys. Rev. **D49**, 5894 (1994), hep-ph/9310332.
452. M. Hosch, K. Whisnant, and B.-L. Young, Phys. Rev. **D55**, 3137 (1997), hep-ph/9607413.
453. C. Jessop, SLAC-PUB-9610.
454. DØ, V. M. Abazov *et al.*, Nature **429**, 638 (2004), hep-ex/0406031.
455. CDF, A. Abulencia *et al.*, Phys. Rev. **D73**, 111103 (2006), hep-ex/0511023.
456. CDF, A. Abulencia *et al.*, Phys. Rev. Lett. **98**, 072001 (2007), hep-ex/0608062.
457. DØ, V. M. Abazov *et al.*, Phys. Lett. **B617**, 1 (2005), hep-ex/0404040.
458. CDF, T. Aaltonen *et al.*, CDF conference note **9144** (2007).
459. DØ, V. M. Abazov *et al.*, Phys. Rev. Lett. **100**, 062004 (2008), arXiv:0711.0032.

460. E. W. Varnes, Private communication, 2008.
461. DØ, V. M. Abazov *et al.*, DØ conference note **5722** (2008).
462. CDF, T. Aaltonen *et al.*, CDF conference note **9215** (2009).
463. CDF, T. Aaltonen *et al.*, CDF conference note **9114** (2008).
464. CDF, T. Aaltonen *et al.*, CDF conference note **9431** (2008).
465. CDF, T. Aaltonen *et al.*, arXiv:0811.0344.
466. CDF, A. A. Affolder *et al.*, Phys. Rev. Lett. **84**, 216 (2000), hep-ex/9909042.
467. CDF, D. E. Acosta *et al.*, Phys. Rev. **D71**, 031101 (2005), hep-ex/0411070.
468. DØ, V. M. Abazov *et al.*, Phys. Rev. **D72**, 011104 (2005), arXiv:hep-ex/0505031.
469. CDF, A. Abulencia *et al.*, Phys. Rev. **D75**, 052001 (2007), hep-ex/0612011.
470. DØ, V. M. Abazov *et al.*, Phys. Rev. **D75**, 031102 (2007), arXiv:hep-ex/0609045.
471. DØ, V. M. Abazov *et al.*, arXiv:0901.0151.
472. J. Alwall *et al.*, Eur. Phys. J. **C49**, 791 (2007), hep-ph/0607115.
473. DØ, V. M. Abazov *et al.*, Phys. Rev. Lett. **100**, 192003 (2008), arXiv:0801.1326.
474. DØ, V. M. Abazov *et al.*, Phys. Lett. **B639**, 616 (2006), arXiv:hep-ex/0603002.
475. CDF, A. A. Affolder *et al.*, Phys. Rev. Lett. **86**, 3233 (2001), hep-ex/0012029.
476. CDF, D. E. Acosta *et al.*, Phys. Rev. Lett. **95**, 102002 (2005), hep-ex/0505091.
477. G. M. de Divitiis, R. Petronzio, and L. Silvestrini, Nucl. Phys. **B504**, 45 (1997), hep-ph/9704244.
478. J. L. Lopez, D. V. Nanopoulos, and R. Rangarajan, Phys. Rev. **D56**, 3100 (1997), hep-ph/9702350.
479. G. Eilam, A. Gemintern, T. Han, J. M. Yang, and X. Zhang, Phys. Lett. **B510**, 227 (2001), hep-ph/0102037.
480. H. Fritzsch and D. Holtmannspotter, Phys. Lett. **B457**, 186 (1999), hep-ph/9901411.
481. R. D. Peccei and X. Zhang, Nucl. Phys. **B337**, 269 (1990).
482. B. A. Arbuzov and M. Y. Osipov, Phys. Atom. Nucl. **62**, 485 (1999), hep-ph/9802392.
483. C.-X. Yue, G.-R. Lu, Q.-J. Xu, G.-L. Liu, and G.-P. Gao, Phys. Lett. **B508**, 290 (2001), hep-ph/0103081.
484. G. Eilam, J. L. Hewett, and A. Soni, Phys. Rev. **D44**, 1473 (1991).
485. G. Eilam, J. L. Hewett, and A. Soni, Phys. Rev. **D59**, 039901 (1998).
486. W.-S. Hou, Phys. Lett. **B296**, 179 (1992).
487. D. Atwood, L. Reina, and A. Soni, Phys. Rev. **D53**, 1199 (1996), hep-ph/9506243.
488. T. Han, K. Whisnant, B. L. Young, and X. Zhang, Phys. Lett. **B385**, 311 (1996), hep-ph/9606231.
489. T. Han and J. L. Hewett, Phys. Rev. **D60**, 074015 (1999), hep-ph/9811237.
490. F. del Aguila, J. A. Aguilar-Saavedra, and R. Miquel, Phys. Rev. Lett. **82**, 1628 (1999), hep-ph/9808400.
491. H. Fritzsch, Phys. Lett. **B224**, 423 (1989).
492. T. Han, R. D. Peccei, and X. Zhang, Nucl. Phys. **B454**, 527 (1995), hep-ph/9506461.
493. CDF, T. Aaltonen *et al.*, CDF conference note **8888** (2007).
494. CDF, T. Aaltonen *et al.*, CDF conference note **9496** (2008).
495. F. Borzumati, J.-L. Kneur, and N. Polonsky, Phys. Rev. **D60**, 115011 (1999), hep-ph/9905443.
496. M. S. Carena and H. E. Haber, Prog. Part. Nucl. Phys. **50**, 63 (2003), hep-ph/0208209.
497. J. S. Lee *et al.*, Comput. Phys. Commun. **156**, 283 (2004), hep-ph/0307377.
498. UA1, C. Albajar *et al.*, Phys. Lett. **B257**, 459 (1991).
499. UA2, J. Alitti *et al.*, Phys. Lett. **B280**, 137 (1992).
500. CDF, F. Abe *et al.*, Phys. Rev. Lett. **72**, 1977 (1994).
501. CDF, F. Abe *et al.*, Phys. Rev. Lett. **73**, 2667 (1994).

502. ALEPH, A. Heister *et al.*, Phys. Lett. **B543**, 1 (2002), hep-ex/0207054.
503. DELPHI, J. Abdallah *et al.*, Eur. Phys. J. **C34**, 399 (2004), hep-ex/0404012.
504. L3, P. Achard *et al.*, Phys. Lett. **B575**, 208 (2003), hep-ex/0309056.
505. OPAL, G. Abbiendi *et al.*, Eur. Phys. J. **C7**, 407 (1999), hep-ex/9811025.
506. LEP Higgs Working Group for Higgs boson searches, G. Abbiendi *et al.*, hep-ex/0107031.
507. M. Misiak *et al.*, Phys. Rev. Lett. **98**, 022002 (2007), hep-ph/0609232.
508. CDF, F. Abe *et al.*, Phys. Rev. **D54**, 735 (1996), hep-ex/9601003.
509. CDF, F. Abe *et al.*, Phys. Rev. Lett. **79**, 357 (1997), hep-ex/9704003.
510. CDF, A. A. Affolder *et al.*, Phys. Rev. **D62**, 012004 (2000), hep-ex/9912013.
511. DØ, B. Abbott *et al.*, Phys. Rev. Lett. **82**, 4975 (1999), hep-ex/9902028.
512. DØ, V. M. Abazov *et al.*, Phys. Rev. Lett. **88**, 151803 (2002), hep-ex/0102039.
513. J. A. Coarasa, J. Guasch, and J. Sola, hep-ph/9903212.
514. M. S. Carena, D. Garcia, U. Nierste, and C. E. M. Wagner, Nucl. Phys. **B577**, 88 (2000), hep-ph/9912516.
515. CDF, A. Abulencia *et al.*, Phys. Rev. Lett. **96**, 042003 (2006), hep-ex/0510065.
516. CDF, T. Aaltonen *et al.*, CDF conference note **9322** (2008).
517. U. Baur, M. Buice, and L. H. Orr, Phys. Rev. **D64**, 094019 (2001), hep-ph/0106341.
518. D. Chang, W.-F. Chang, and E. Ma, Phys. Rev. **D59**, 091503 (1999), hep-ph/9810531.
519. D. Chang, W.-F. Chang, and E. Ma, Phys. Rev. **D61**, 037301 (2000), hep-ph/9909537.
520. DØ, V. M. Abazov *et al.*, Phys. Rev. Lett. **98**, 041801 (2007), arXiv:hep-ex/0608044.
521. CDF, T. Aaltonen *et al.*, CDF conference note **8967** (2007).
522. CDF, T. Aaltonen *et al.*, CDF conference note **8104** (2006).
523. CDF, T. Aaltonen *et al.*, Phys. Rev. Lett. **102**, 042001 (2009), arXiv:0808.2167.
524. S. Heinemeyer, S. Kraml, W. Porod, and G. Weiglein, JHEP **09**, 075 (2003), hep-ph/0306181.
525. S. Heinemeyer, W. Hollik, A. M. Weber, and G. Weiglein, JHEP **04**, 039 (2008), arXiv:0710.2972.
526. CDF, A. Abulencia *et al.*, Phys. Rev. Lett. **96**, 022004 (2006), hep-ex/0510049.
527. CDF, A. Abulencia *et al.*, Phys. Rev. **D73**, 032003 (2006), hep-ex/0510048.
528. CDF, T. Aaltonen *et al.*, CDF conference note **9206** (2008).
529. CDF, T. Aaltonen *et al.*, arXiv:0809.4808.
530. CDF, T. Aaltonen *et al.*, CDF conference note **9414** (2008).
531. CDF, T. Aaltonen *et al.*, Phys. Rev. Lett. **100**, 062005 (2008), arXiv:0710.4037.
532. CDF, F. Abe *et al.*, Phys. Rev. Lett. **82**, 271 (1999), hep-ex/9810029.
533. CDF, F. Abe *et al.*, Phys. Rev. Lett. **82**, 2808 (1999).
534. DØ, B. Abbott *et al.*, Phys. Rev. Lett. **80**, 2063 (1998), hep-ex/9706014.
535. DØ, B. Abbott *et al.*, Phys. Rev. **D60**, 052001 (1999), hep-ex/9808029.
536. CDF, F. Abe *et al.*, Phys. Rev. Lett. **80**, 2767 (1998), hep-ex/9801014.
537. CDF, A. A. Affolder *et al.*, Phys. Rev. **D63**, 032003 (2001), hep-ex/0006028.
538. CDF, F. Abe *et al.*, Phys. Rev. Lett. **79**, 1992 (1997).
539. DØ, V. M. Abazov *et al.*, Phys. Lett. **B606**, 25 (2005), hep-ex/0410086.
540. CDF, T. Aaltonen *et al.*, Phys. Rev. **D75**, 111103 (2007), arXiv:0705.1594.
541. F. Fiedler, Habilitation thesis (2007),
    http://www.etp.physik.uni-muenchen.de/dokumente/thesis/habil_ffiedler.pdf.
542. CDF, A. Abulencia *et al.*, Phys. Rev. **D73**, 112006 (2006), hep-ex/0602008.
543. DØ, V. M. Abazov *et al.*, DØ conference note **5743** (2008).
544. DØ, V. M. Abazov *et al.*, DØ conference note **5746** (2008).

545. CDF, A. Abulencia *et al.*, Phys. Rev. **D74**, 032009 (2006), hep-ex/0605118.
546. CDF, A. Abulencia *et al.*, Phys. Rev. Lett. **96**, 152002 (2006), hep-ex/0512070.
547. DØ, V. M. Abazov *et al.*, Phys. Lett. **B655**, 7 (2007), arXiv:hep-ex/0609056.
548. CDF, A. Abulencia *et al.*, Phys. Rev. **D75**, 031105 (2007), hep-ex/0612060.
549. DØ, V. M. Abazov *et al.*, DØ conference note **5463** (2007).
550. CDF, T. Aaltonen *et al.*, CDF conference note **8959** (2007).
551. CDF, T. Aaltonen *et al.*, CDF conference note **8955** (2007).
552. CDF, T. Aaltonen *et al.*, CDF conference note **8951** (2008).
553. CDF, T. Aaltonen *et al.*, arXiv:0807.4652.
554. CDF, T. Aaltonen *et al.*, CDF conference note **9456** (2008).
555. F. A. Berends, H. Kuijf, B. Tausk, and W. T. Giele, Nucl. Phys. **B357**, 32 (1991).
556. CDF, T. Aaltonen *et al.*, CDF conference note **9427** (2008).
557. DØ, V. M. Abazov *et al.*, DØ conference note **5750** (2008).
558. DØ, V. M. Abazov *et al.*, Phys. Rev. Lett. **101**, 182001 (2008), arXiv:0807.2141.
559. CDF, A. Abulencia *et al.*, Phys. Rev. **D73**, 092002 (2006), hep-ex/0512009.
560. DØ, V. M. Abazov *et al.*, Phys. Rev. **D74**, 092005 (2006), arXiv:hep-ex/0609053.
561. DØ, V. M. Abazov *et al.*, Phys. Rev. **D75**, 092001 (2007), arXiv:hep-ex/0702018.
562. CDF, A. Abulencia *et al.*, Phys. Rev. **D75**, 071102 (2007), hep-ex/0612061.
563. CDF, A. Abulencia *et al.*, Phys. Rev. Lett. **99**, 182002 (2007), hep-ex/0703045.
564. CDF, T. Aaltonen *et al.*, CDF conference note **8669** (2007).
565. CDF, T. Aaltonen *et al.*, CDF conference note **9135** (2007).
566. CDF, T. Aaltonen *et al.*, arXiv:0812.4469.
567. http://www-cdf.fnal.gov/physics/new/top/systematics/.
568. CDF, T. Aaltonen *et al.*, CDF conference note **9165** (2008).
569. CDF, T. Aaltonen *et al.*, CDF conference note **9265** (2008).
570. CDF, T. Aaltonen *et al.*, Phys. Rev. Lett. **98**, 142001 (2007), hep-ex/0612026.
571. CDF, T. Aaltonen *et al.*, CDF conference note **8709** (2007).
572. CDF, T. Aaltonen *et al.*, arXiv:0811.1062.
573. CDF, T. Aaltonen *et al.*, CDF conference note **9450** (2008).
574. DØ, V. M. Abazov *et al.*, DØ conference note **5747** (2008).
575. ILC, J. Brau *et al.*, arXiv:0709.1893, ILC-REPORT-2007-001.
576. ILC, J. Brau *et al.*, arXiv:0712.1950.
577. ILC, T. Behnke *et al.*, arXiv:0712.2356.
578. W. Bernreuther, J. Phys. **G35**, 083001 (2008), arXiv:0805.1333.
579. DØ, V. M. Abazov *et al.*, DØ conference note **5742** (2008).
580. S. Frixione, M. L. Mangano, P. Nason, and G. Ridolfi, Phys. Lett. **B351**, 555 (1995), hep-ph/9503213.
581. CDF, DØ, the Tevatron Electroweak Working Group, arXiv:0803.1683.
582. ALEPH, DELPHI, L3, OPAL, SLD, the LEP Electroweak Working Group, the SLD Electroweak and Heavy Flavour Groups, hep-ex/0412015.
583. LEP Working Group for Higgs boson searches, R. Barate *et al.*, Phys. Lett. **B565**, 61 (2003), hep-ex/0306033.
584. CDF, DØ, the Tevatron New-Phenomena and Higgs working group, arXiv:0808.0534.